

Nonlinear couplings for quantum control of superconducting qubits and electrical/mechanical resonators

Kounalakis, Marios

DOI

[10.4233/uuid:7ffe6dfa-2a24-44d1-991f-7e1bbe2397d6](https://doi.org/10.4233/uuid:7ffe6dfa-2a24-44d1-991f-7e1bbe2397d6)

Publication date

2019

Document Version

Final published version

Citation (APA)

Kounalakis, M. (2019). *Nonlinear couplings for quantum control of superconducting qubits and electrical/mechanical resonators*. [Dissertation (TU Delft), Delft University of Technology]. TU Delft Casimir PhD series. <https://doi.org/10.4233/uuid:7ffe6dfa-2a24-44d1-991f-7e1bbe2397d6>

Important note

To cite this publication, please use the final published version (if applicable). Please check the document version above.

Copyright

Other than for strictly personal use, it is not permitted to download, forward or distribute the text or part of it, without the consent of the author(s) and/or copyright holder(s), unless the work is under an open content license such as Creative Commons.

Takedown policy

Please contact us and provide details if you believe this document breaches copyrights. We will remove access to the work immediately and investigate your claim.

**Nonlinear couplings for quantum control
of superconducting qubits and
electrical/mechanical resonators**

Nonlinear couplings for quantum control of superconducting qubits and electrical/mechanical resonators

Dissertation

for the purpose of obtaining the degree of doctor
at Delft University of Technology
by the authority of the Rector Magnificus prof.dr.ir. T.H.J.J. van der Hagen,
chair of the Board for Doctorates
to be defended publicly on
Thursday 19 December at 12:30 o'clock

by

Marios KOUNALAKIS

Master of Science in Physics, Leiden University, the Netherlands
born in Heraklion, Greece

This dissertation has been approved by the promotor.

Composition of the doctoral committee:

Rector Magnificus,	chairperson
Prof. dr. G. A. Steele,	Delft University of Technology, promotor
Prof. dr. L. Kuipers,	Delft University of Technology, promotor

Independent members:

Prof. dr. S. Kokkelmans,	Eindhoven University of Technology
Prof. dr. T. Kontos,	École Normal Supérieure
Prof. dr. B. M. Terhal,	Delft University of Technology
Prof. dr. ir. J. E. Mooij,	Delft University of Technology
Prof. dr. ir. H. S. J. van der Zant,	Delft University of Technology, Reserve member

Other members:

Prof. dr. Y. M. Blanter,	Delft University of Technology
--------------------------	--------------------------------



Printed by: Gildeprint, Enschede

Cover **Front:** The background SEM image depicts a transmon qubit behind an Aluminium airbridge with the focus on the Josephson junctions. Taken from one of my first chips together with A. Bruno. The idea to interleave Feynman diagrams with quantum circuits was inspired by C. Dickel. **Back:** SEM image of the same device with the focus on the airbridge. Overlaid with the constellations that are visible on the northeastern sky on a late August night in Crete.

Copyright © 2019 by M. Kounalakis
Casimir PhD Series, Delft-Leiden 2019-36

ISBN 978-90-8593-419-6

An electronic version of this dissertation is available at
<http://repository.tudelft.nl/>.

To the wonderful tragedies of my life,
Elektra and little Antigoni.

...and when one does not die for the other, we are already dead.

Tassos Leivaditis

Contents

Summary	xi
Samenvatting	xiii
1 Introduction	1
1.1 From Planck to superconducting qubits	2
1.2 Research context and scope of this thesis	4
1.2.1 Quantum simulation of many-body problems	5
1.2.2 Quantum control of mechanical resonators	6
1.2.3 Quantum control of thermally-populated resonators	7
1.3 Structure of the thesis	7
2 Theoretical description of quantum circuits	9
2.1 Classical description: from Lagrangian to Hamiltonian.	10
2.1.1 Method of nodes	10
2.1.2 LC oscillator	11
2.1.3 Coupled LC oscillators	12
2.1.4 Normal-mode analysis	13
2.2 Canonical quantisation: from variables to quantum operators	14
2.2.1 Quantum LC oscillator	14
2.2.2 Superconducting transmon qubits	15
2.2.3 Nonlinearly coupled transmon qubits	19
2.3 Modelling open quantum systems in time-domain	20
3 Circuit design and fabrication	23
3.1 Readout and control of transmon qubits	24
3.1.1 Frequency tuning and driving	24
3.1.2 Readout via coplanar waveguide resonators.	25
3.1.3 Qubit driving	30
3.2 Coupling transmon qubits	31
3.3 Chip fabrication	32
3.3.1 Base layer: Defining the capacitance network.	32
3.3.2 Josephson junctions	33
3.3.3 Air-bridge crossovers	35
3.3.4 Integration with printed circuit board.	36
4 Engineering tuneable qubit-qubit couplings	39
4.1 Introduction.	40
4.2 Main results.	41
4.2.1 Implementing nonlinear couplings	41

4.2.2	Tuneable single-photon hopping	43
4.2.3	Tuneable nonlinear cross-Kerr coupling	44
4.2.4	Qubit coherence.	46
4.3	Discussion.	47
4.4	Methods.	49
4.4.1	Chip fabrication	49
4.4.2	On-chip flux cross-talk calibration	50
4.4.3	Device parameters	50
4.5	Derivation of full circuit Hamiltonian	51
4.5.1	Analytical description in the harmonic limit	51
4.5.2	Hamiltonian description of the nonlinear circuit	53
4.5.3	Circuit quantisation in the harmonic oscillator basis	57
4.6	Measurement setup	58
4.7	Supplementary data	59
5	Quantum control of a mechanical resonator using three-body interactions with transmon qubits	63
5.1	Introduction.	64
5.2	Main results.	65
5.2.1	Motion-dependent qubit-qubit interaction.	65
5.2.2	Electromechanical system dynamics	66
5.2.3	Ground-state cooling	67
5.2.4	Mechanical Fock states and qubit-phonon entanglement	69
5.2.5	Multi-phonon quantum superpositions	71
5.3	Discussion.	72
5.4	Methods.	73
5.4.1	Numerical modelling	73
5.5	Lagrangian-Hamiltonian description of the circuit	74
5.5.1	Motion-dependent flux-tuneable Josephson energy	74
5.5.2	Flux-mediated interactions.	75
5.6	Circuit quantisation	77
5.6.1	Tripartite coupling	77
5.6.2	Radiation-pressure couplings.	78
5.6.3	Qubit-qubit couplings	78
5.6.4	Higher-order tripartite interactions	79
5.7	Protocols for arbitrary quantum state generation.	80
5.7.1	States with arbitrary complex coefficients.	80
5.7.2	States with arbitrary phonon number probability distributions	82
5.8	Validity for non-ideal system parameters	84
6	Flux-mediated optomechanics with a transmon qubit in the single-photon ultrastrong-coupling regime	87
6.1	Introduction.	88
6.2	Main results.	89
6.2.1	Electromechanical system	89
6.2.2	Ground-state cooling	92

6.2.3	Mechanical cat states	93
6.3	Discussion	95
6.4	Detailed analysis of the electromechanical system	96
6.4.1	Circuit Hamiltonian	96
6.4.2	Circuit quantisation and radiation-pressure coupling strength	96
6.4.3	Higher-order interaction terms	97
7	Controlling a hot radio-frequency resonator via dissipation engineering	99
7.1	Introduction	100
7.2	Main results	100
7.2.1	Circuit architecture and coupling mechanism	100
7.2.2	Ground-state cooling and Fock-state stabilisation	102
7.2.3	Time-domain experiments	104
7.3	Discussion	105
7.4	Extended author contribution statement	106
7.5	Experimental setup	106
7.6	Theory	106
7.6.1	Circuit Hamiltonian	106
7.6.2	Simulating the reflection measurement	109
7.6.3	Four wave mixing and cooling rate	111
7.7	Background subtraction	114
7.7.1	Network analysis	114
7.7.2	Measuring the microwave background	114
7.8	Fitting	116
7.8.1	Low-frequency mode dissipation	116
7.8.2	Circuit parameters	116
7.9	Supplementary experimental data	116
7.9.1	Low-frequency spectrum	116
7.9.2	Full time-dependent spectrum	119
8	Conclusions and outlook	121
8.1	Qubit-qubit interactions	122
8.2	Mechanical quantum states	123
8.3	Thermally-populated resonators	124
8.4	Epilogue	125
	Acknowledgements	127
	Curriculum Vitæ	131
	List of Publications	133
	References	135

Summary

As the title suggests, this thesis explores nonlinear couplings in superconducting circuits with the purpose of achieving tuneable interaction regimes between superconducting qubits, as well as enabling quantum control over mechanical and electrical resonators in the radio-frequency regime.

Chapter 1, contains a brief historical overview from the advent of quantum theory to the development of well-controlled quantum systems and superconducting qubits. The research context and scope of the thesis are presented, including an introduction of the research topics and the main research questions that this thesis aims to answer.

In chapter 2, I will introduce the theoretical framework for analysing superconducting circuits from a classical to a quantum description. The purpose is to provide the tools that are necessary for designing new circuits and modelling their quantum dynamics.

Chapter 3 concerns the experimental methods that are used to transform superconducting circuits from a theoretical construction into a physical reality. I will therefore discuss the design process and fabrication steps, focusing mainly on transmon-based devices.

Chapter 4, reports on the experimental realisation of a tuneable coupling scheme, giving rise to different interactions with adjustable ratios, between two transmon qubits. The tuneable capabilities of the device together with its versatile geometry and high coherence make it an interesting building block for analog quantum simulators of certain classes of complex problems.

Chapter 5, presents a theoretical proposal on controlling a mechanical resonator using two transmon qubits, by means of a tuneable three-body interaction. Firstly, the electromechanical circuit architecture giving rise to the tripartite coupling is analysed. Secondly, several protocols are performed numerically demonstrating ground-state cooling and the creation of mechanical quantum states, such as single-phonon and multi-phonon superposition states as well as qubit-phonon entanglement. Finally, different schemes for generating arbitrary quantum states are explored.

Chapter 6, relies on the same concept for coupling a mechanical resonator to a transmon qubit and explores the qubit-resonator system in the ultrastrong coupling regime, where the optomechanical coupling approaches or even exceeds the mechanical frequency. We find that for certain coupling strengths ground-state cooling is possible and devise a protocol for generating macroscopic quantum superposition states, known as “Shrödinger cats”, on the mechanical resonator.

Chapter 7, presents an experiment where a cold superconducting qubit is employed to readout and control a thermally populated radio-frequency resonator coupled via a strong dispersive coupling. By means of reservoir engineering we demonstrate ground-state cooling as well as the stabilisation of Fock states in the resonator.

In chapter 8, I will briefly conclude the main findings together with an outlook for future work on each topic.

Samenvatting

Zoals de titel suggereert, wordt in dit proefschrift afstelbaarheid van de koppeling tussen supergeleidende schakelingen bestudeerd. Ook wordt de mate waarin mechanische resonatoren in de kwantum regime gemanipuleerd kunnen worden onderzocht middels radiofrequentie elektrische resonatoren.

Hoofdstuk 1 bevat een kort historisch overzicht van de kwantumtheorie de ontwikkeling van goed gecontroleerde kwantumsystemen en supergeleidende qubits. Vervolgens wordt de onderzoekscontext en reikwijdte van het proefschrift gepresenteerd, inclusief een introductie van de onderzoeksthema's en de belangrijkste onderzoeksvragen die dit proefschrift beoogt te beantwoorden.

In hoofdstuk 2 zal ik het theoretische kader introduceren voor het analyseren van supergeleidende circuits van een klassieke naar een kwantumbeschrijving. Het doel is om een kader te bieden die nodig is voor het ontwerpen van nieuwe circuits en het modelleren van hun kwantumdynamiek.

Hoofdstuk 3 betreft de experimentele methoden die gebruikt kunnen worden om supergeleidende schakelingen te transformeren van een theoretische constructie tot een fysieke realisatie. Ik zal daarom het ontwerpproces en de fabricagestappen bespreken, voornamelijk gericht op op transmon gebaseerde apparaten.

Hoofdstuk 4, rapporteert over de experimentele realisatie van een afstelbare koppelingsschema, dat aanleiding geeft tot verschillende interacties met instelbare verhoudingen, tussen twee transmonqubits. De instelbare mogelijkheden van het apparaat samen met zijn veelzijdige geometrie en hoge coherentie maken het een interessante bouwsteen voor analoge kwantumsimulators die bepaalde soorten van complexe problemen bestudeerd.

Hoofdstuk 5 presenteert een theoretisch voorstel voor het besturen van een mechanische resonator met behulp van twee transmonqubits, door middel van een instelbare interactie van deze 3 systemen. Ten eerste wordt de architectuur van de elektromechanische schakeling geanalyseerd, wat aanleiding geeft tot een tripartiete koppeling. Ten tweede worden verschillende protocollen gesimuleerd die de koeling naar de grondtoestand en de creatie van mechanische kwantumtoestanden aantonen, zoals kwantum superpositie met één fonon en multi-fonon, evenals verstrengeling tussen qubit-fonon. Ten slotte worden verschillende schema's voor het genereren van willekeurige kwantumtoestanden onderzocht.

Hoofdstuk 6, betreft hetzelfde concept voor het koppelen van een mechanische resonator aan een transmon qubit en onderzoekt het qubit-resonatorsysteem in het ultrasnelle koppelingsregime, waar de optomechanische koppeling de mechanische frequentie benadert of zelfs overschrijdt. We vinden dat voor bepaalde koppelingssterktes grondtoestand koeling mogelijk is en ontwikkelen een protocol voor het genereren van macroscopische kwantum-superpositie, bekend als "Shrödinger katten", in de mechanische resonator.

Hoofdstuk 7 presenteert een experiment waarbij een koude supergeleidende qubit is gebruikt voor het uitlezen en besturen van een thermisch geoccupeerde radiofrequente resonator, gekoppeld via een sterke dispersieve koppeling. Door middel van reservoir engineering demonstreren we grondtoestand koeling evenals de stabilisatie van Fock-toestanden in de resonator.

In hoofdstuk 8 zal ik in het kort de belangrijkste bevindingen samenvatten met een kort vooruitblik op toekomstig werk over elk onderwerp.

1

Introduction

It is personalities, not principles, that move the age.

Oscar Wilde, "The Picture of Dorian Gray"

In this introductory chapter I will present the context as well as the scope of this thesis. I will begin with a historical overview (through my personal distorted prism) of the most important developments since the advent of quantum theory, that led to the development of superconducting qubits as a leading platform in quantum technologies. I will then present the main research themes to which this thesis contributes and the answers it aims to provide. Finally, I will present the thesis structure and sketch the highlights of each chapter.

1.1. From Planck to superconducting qubits

Quantum theory is one of the most precise and most tested theories describing the world at the tiniest scales. Historically, it started in 1900¹ with Planck who, largely influenced by earlier work of Boltzmann, proposed the idea that light can only be absorbed or emitted in little energy packets, termed *quanta* [1, 2]. This postulate led him to the explanation of the black-body radiation spectrum, which was one of the great mysteries at the time, and shook the grounds concerning our understanding about the nature of light thought till then to have a purely wave-like character. Soon after, in 1905, Einstein applied this concept to explain the photoelectric effect [3, 4], providing further evidence that quantum effects are not just a theoretical construct but play a crucial role in explaining physical phenomena. Furthermore, quantised energy levels provided the best explanation for the inherent stability of the atom and its structure [5], which was earlier observed in 1911 by Rutherford [6]. A period of great discoveries followed, most notably with the discovery of spin by Stern and Gerlach (1922)² and Compton scattering (1923) [8], in parallel with the construction of the theoretical framework of quantum mechanics by its founding fathers Bohr, Einstein, Heisenberg, Schrödinger, De Broglie, Born, Pauli and Dirac among others. This period up to 1930, when Dirac's textbook "The Principles of Quantum Mechanics" was published, laid the foundations for a solid new theory (unified with special relativity theory) that revolutionised modern science and philosophy. It had a huge impact on technology as well: it led to a better understanding of semiconductors and eventually to the realisation of transistors that form the building blocks of our computers, it enabled the construction of lasers, as well as novel imaging techniques, such as the MRI, to name only a few applications.

The acceptance of quantum theory as a complete description of the universe had ground-breaking implications about the nature of our reality, which was highlighted in the famous paper by Einstein, Podolsky and Rosen [9]. It predicted the possibility of nonlocal correlations between particles that have no classical analogue, what Schrödinger called *entanglement*. This implied the ability to influence the state of one particle just by measuring/manipulating the state of its entangled pair, no matter how far apart, even when they are not causally linked (violating local realism). For physicists this meant either a new paradigm shift concerning the nature of reality, or the need for a more fundamental description that satisfies local realism. In 1964 John Bell, highly influenced by the work of Bohm on nonlocal hidden-variable theories [10], came up with a theoretical framework³ to test experimentally the existence of nonlocal quantum correlations between pairs of particles [12]. This result was later confirmed by several experiments [13–15], laying the foundations for the coming "second quantum revolution" [16].

Quantum mechanics would keep puzzling physicists, however, on several accounts. One of the most profound questions concerned the absence of observable quantum phenomena in macroscopic objects, famously highlighted by the Schrödinger cat para-

¹Note that there have been scientific discoveries pointing at quantum effects before that, however, this was the first time the quantum hypothesis was used to produce quantitative results.

²Interestingly, it was realised five years later that it was spin they had actually discovered [7].

³Grete Hermann had made decisive contributions in this direction already in 1935 (see Ref. [11]), which unfortunately went unnoticed by the community until Bell rediscovered part of her work.

dox [17]. Since the early 80s there is growing consensus that decoherence happens as a result of entanglement of the quantum state with the infinite degrees of freedom of the environment/measurement apparatus, leading the system into *pointer states* that can be described as classical mixtures. The more quantum degrees of freedom the system possesses the faster this loss of coherence happens, therefore explaining why macroscopic systems are never observed in quantum superpositions (see Ref. [18] for an extensive review). However, there exist “special” macroscopic systems such as Bose-Einstein condensates where all degrees of freedom are “condensed” such that the system is described only by a single or a few collective variables. This is for example the case in superconductors where, below a critical temperature, boson-like pairs of electrons (Cooper-pairs) are condensed into a ground state described by a single wavefunction. This very notion led to the idea that quantum phenomena could be observed in superconducting circuits regardless of their size, provided they operate at low enough temperatures (for the condensation to happen) and are well-isolated from the environment [19, 20]. Additionally, the remarkable discovery of the Josephson effect [21] enabled the construction of Josephson junctions. These are nonlinear and (crucially) nondissipative inductors, consisting of two superconducting electrodes separated by an insulating barrier through which Cooper-pairs can tunnel. Experiments in the early 80s confirmed the existence of macroscopic quantum effects in these elements [22–24], paving the way for the birth of the first superconducting qubits in the late 90s.

In the meantime, theoretical advances in the emergent field of quantum information established the potential advantages of quantum coherent phenomena, such as superposition and entanglement, in cryptography and computing [25–28]. The developments in this field, apart from the outstanding technological implications, renewed the interest on the foundations of quantum theory for many physicists [29]. Moreover, the first experiments demonstrating quantum coherent phenomena and the manipulation of quantum states in well-isolated table-top experiments started to become a reality. The first experiments of this kind were performed in the labs of S. Haroche and D. Wineland using well-isolated atoms and ions in high-quality optical cavities and Pauli traps, respectively (see Nobel prize lectures [30, 31] for a review). These experiments enabled for the first time a more meticulous study of the dynamics of open quantum systems, establishing the role of decoherence, and demonstrated the ability to perform quantum gates (logical qubit operations) and controllably prepare quantum states by harnessing the interaction of light and matter.

Superconducting qubits started to develop into well-controlled quantum systems in the beginning of the 21st century. These are artificial atoms made out of capacitors and Josephson junctions (nonlinear inductors) that can be lithographically patterned on a 2D chip. They are categorised into charge [32–34], flux [35, 36] and phase qubits [37], depending on the interplay of charging and inductive energies in the circuit (see extensive reviews in Refs. [38–40]). Superconducting qubits can be electromagnetically coupled to high-quality-factor microwave resonators (in both 2D and 3D geometries) realising an alternative platform for studying light-matter interaction with superconducting circuits, that is widely known as circuit quantum electrodynamics (QED) [41]. The field benefited a lot from the already existing microwave technology, which, together with tremendous advances in nanofabrication over the last two decades, led superconducting qubits to

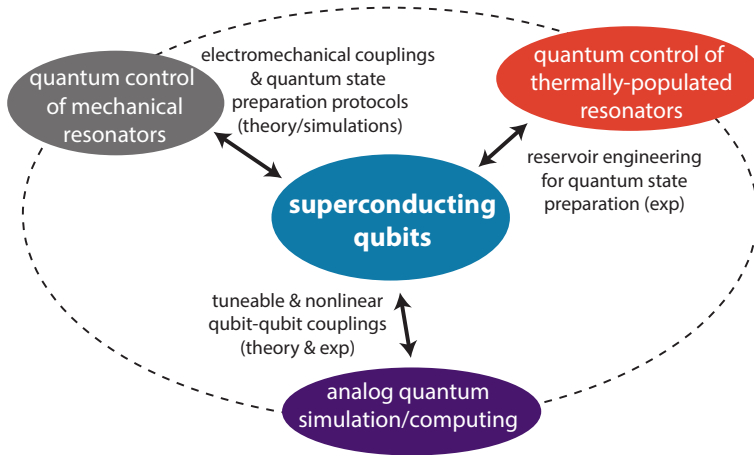


Figure 1.1: Schematic illustration of the research themes that are explored in this thesis.

become one of the most promising platforms for building a quantum computer. Among its most important advantages are the exquisite level of quantum control, flexibility in design and fabrication, as well as high coherence relative to qubit gates and interaction timescales. Additionally, these systems are very versatile with regard to coupling to other quantum systems, such as micromechanical devices and spins, making them ideal for hybrid approaches to quantum computing and communication [42]. They play a key role in developing quantum technologies, constituting one of the most well-funded research programs worldwide, both at an academic and industrial level [43].

1.2. Research context and scope of this thesis

Superconducting qubits (mainly transmons [44]) are at the very heart of this dissertation, which, as the title suggests, concerns the exploration of coupling schemes in circuit QED and hybrid electromechanical devices with the purpose of quantum control of qubits, phonons and photons. In the previous section I have given a historical background, from a personal perspective, of the most important discoveries preceding the development of superconducting qubits. Here, I will discuss their applications in technology and in tackling some of the fundamental questions regarding quantum mechanics that kept motivating my research during these four years. The curiosity-driven nature of the research led to the investigation of a wide spectrum of topics, which makes it difficult to define a single research question and I am going to refrain from inventing one. I will motivate each topic from my personal perspective, as I experienced it at the time, and try to narrow the discussion down to the objective research questions that this thesis aims to answer. Fig. 1.1 schematically depicts the three main themes to which this thesis contributes through the exploration of superconducting qubits, namely, analog quantum simulation, and quantum control of mechanical and electrical radio-frequency resonators.

1.2.1. Quantum simulation of many-body problems

A very exciting prospect for superconducting circuits is their potential contribution towards a better understanding of complex quantum phenomena, that typically occur in many-body problems. Many-body problems concern systems of strongly correlated particles where all the individual quantum degrees of freedom are equally important and, therefore, cannot be approximated by collective variables. Despite the impressive advances in analytical and numerical modelling techniques (which are typically problem-specific), such problems remain practically intractable due to the incapability of classical computer memory to keep up with their parameter space, d , which scales exponentially with the number of particles ($d \sim n^N$, where n is the number of individual degrees of freedom and N the number of particles). Being able to simulate them could solve long-time mysteries in physics such as the underlying mechanism behind high-temperature superconductors [45, 46] and colour confinement in quantum chromodynamics [47, 48], or even help with designing novel quantum materials and molecules in the field of quantum chemistry [49]. To get a feeling of the problem let us consider that currently our best supercomputers can simulate only $\lesssim 50$ interacting two-level particles/qubits [50–52].

As Richard Feynman pointed out in 1982, simulating quantum mechanical problems will eventually require the existence of *quantum simulators*, i.e. specially engineered well-controlled quantum systems onto which the problem of interest can be mapped [53]. Solving the problem can be summarised in three steps: quantum state preparation, controllable evolution for a variable time and, finally, readout of the relevant quantum observables [54]. This approach is interesting not only for solving complicated problems but also due to its exciting prospects for creating unexpected new phenomena that might not even exist in nature. The above discussion concerns *analog* quantum simulations, however, there also exist *digital* implementations that employ a sequence of discrete quantum operations/gates on the quantum bits to model the dynamics of interest. The digital errors in this case can be made small provided the gate times are fast enough [55]. A combination of both analog and digital schemes could provide a very powerful approach for building universal quantum simulators.

Of particular theoretical interest is a certain class of many-body problems, that concerns systems of interacting bosons on a lattice. The simplest one of these is the Bose-Hubbard model, where the system dynamics are governed by the interplay of on-site interactions with hopping of excitations. This model has traditionally been at the heart of simulating condensed-matter problems and is typically used as toy-model for studying quantum phase transitions. Bose-Hubbard models have been the cornerstone of quantum simulations with cold atoms [56], however, recently implementations with superconducting qubits have also been developed [57, 58]. In these implementations the qubits are engineered to have a dipole-dipole coupling that effectively simulates the “hopping” interaction, while the transmon anharmonicity effectively implements an “on-site” interaction. There also exist more complex versions of extended Hubbard models with additional *cross-Kerr* interactions, such that the existence of an excitation on a lattice site can make it more or less favourable for its neighbouring sites to become excited. When the excitations are confined within the qubit subspace, this model reduces to its analog for interacting spin systems, namely the Heisenberg XXZ model, which is one of the most commonly used toy-models for quantum magnetism. In this context,

the cross-Kerr interaction can be thought of as a longitudinal (ZZ) coupling that favours the parallel/antiparallel alignment of neighbouring spins, while the hopping interaction is equivalent to a transverse coupling (XX and YY).

Such many-body models are not integrable in lattice configurations (2D and above) and can only be simulated using approximate methods. Numerical simulations of driven extended Hubbard models predict exotic phenomena, such as photon crystalline and supersolid phases, which could be tested with superconducting circuits [59, 60]. Moreover, for certain coupling ratios, the XXZ interaction can be used to emulating gauge fields in the context of lattice gauge theories [61]. Experimental realisations of these couplings could also find application in quantum state transfer protocols or even in constructing alternative quantum computing schemes [62]. A very important tool in implementing these models experimentally would be the ability to tune the relative ratio between the two coupling strengths, as proposed in Refs. [59, 61]. One of the research questions in this thesis (studied in chapter 4) concerns the experimental implementation of such a coupling scheme with superconducting qubits, while maintaining the high coherence required for quantum simulations.

1.2.2. Quantum control of mechanical resonators

A very exciting prospect both for fundamental studies and technological applications is the ability to manipulate mechanical resonators at the quantum level. This is the main objective of the emerging field of optomechanics, which concerns the controllable interaction of light with mechanical elements [63, 64]. The coupling of motion to electromagnetic radiation is typically achieved by making one of the mirrors of an optical cavity moveable, or by suspending part of the capacitor in a microwave LC resonator such that its oscillations induce modulation of the electromagnetic field.

Of particular interest in this field is the possibility of addressing fundamental questions regarding the interplay of gravity and quantum mechanics. A unified theory of both remains elusive; whether gravity is emergent from quantum mechanics [65] or they are two different entities that possibly interfere with each other [66] is still an open question and a topic of intense research. Massive mechanical resonators, made of metallic drumheads or beams could play a role in elucidating some of these questions, e.g. by preparing them in mechanical superposition or entangled states and investigating potential gravity-induced decoherence mechanisms [67, 68].

From a technological perspective, these systems have many potential applications in quantum computing and quantum communication. For example, due to their long coherence times, relative to superconducting qubits, they can be used to store quantum information for longer timescales, playing the role of *quantum memories* [69]. Additionally, they can be coupled to a wide range of electromagnetic radiation, which makes them ideal for converting and transmitting quantum information, e.g. connecting different superconducting quantum computers (GHz regime) through optical fibers. Additionally, they can be coupled to many different quantum systems, such as spins, cold atoms and superconducting qubits, which makes them particularly interesting for hybrid approaches to quantum computing [42].

The absence of nonlinearity in these resonators makes it difficult to prepare quantum states by directly exciting them with an external source. Josephson-based supercon-

ducting circuits are particularly useful in this regard, as they provide a natural strong nonlinearity in the system while, at the same time, being nondissipative. Typically, however, due to the nature of the parametric coupling in such electromechanical systems, it is difficult to create a wide range of quantum states. In chapter 5 we theoretically examine the possibility of preparing arbitrary quantum states in a mechanical resonator using two directly coupled superconducting qubits instead of one linear electromagnetic mode, as typically realised in optomechanical setups. Chapter 6 can be considered as a spin-off of this project, where the main research question was whether using a single qubit (as opposed to a resonator) coupled to the mechanical resonator is sufficient for controlling it and preparing interesting quantum states. We demonstrate that this is the case, building on the analytical derivations in chapter 5 and performing numerical simulations of predicted experiments. Additionally, this work served as an investigation of the quantum dynamics of the interesting and largely unexplored *ultrastrong* coupling regime between a qubit and a mechanical resonator at single-photon levels.

1.2.3. Quantum control of thermally-populated resonators

Bringing any physical system into the quantum realm, where quantum effects are relevant or even dominate the dynamics, relies heavily on our ability to cool its degrees of freedom below the energy scale of thermal fluctuations $k_B T$. In solid state systems this is achieved through the use of $^3\text{He}/^4\text{He}$ cryogenic techniques which have enabled the discovery of novel quantum phenomena, such as superconductivity and the Josephson effect, as well as the experimental exploration of the energy structure of atoms and oscillators at the quantum level, leading to tremendous advances in quantum state engineering. With the lowest cryogenic temperatures achievable limited to a few mK, however, the employable transition frequencies must lie in the GHz regime or above, such that $k_B T < \hbar f$, making lower frequency systems very difficult to manipulate at the quantum level.

An interesting avenue for further cooling a system to its quantum groundstate is via dissipation engineering methods, originally developed in trapped ions [70] and later extended to solid-state systems and superconducting circuits in particular (see Ref. [71] for a thorough review). Despite the remarkable advances in quantum state engineering, controlling photons in quantum harmonic oscillators in the radio-frequency band remains a largely unexplored and challenging task. This constitutes the main research question explored in chapter 7, which led to experimental results demonstrating groundstate cooling and manipulation of quantum states in a thermally-populated radio-frequency resonator.

1.3. Structure of the thesis

The purpose of the first two chapters following this introduction is to introduce the most important theoretical and experimental tools that are required in order to answer the research questions described above. The rest of the chapters, except for the outlook chapter, constitute the core of the thesis which, in a nutshell, consists of the following three research themes:

1. In **chapter 4** we experimentally realise a tuneable coupling scheme between two superconducting transmon qubits, which can be used as a building block for analog quantum simulations of many-body problems. The novelty lies in the nature of the coupling, which allows for reaching and tuning *in situ* different interaction regimes while maintaining high coherence. The circuit is well-understood and explained with analytical modelling which together with its flexible design make it suitable for scaling up to larger implementations. These could be used for simulating the dynamics of complex models, ranging from extended Hubbard models to Heisenberg spin systems and lattice gauge theories. Additionally, the coupler could be used for realising two-qubit gates for quantum computing applications.
2. **Chapters 5 and 6** describe two theoretical proposals for controlling mechanical resonators using transmon qubits. These are inspired partially by the aforementioned tuneable coupling scheme of chapter 4 and the experimental advances in our group on coupling mechanical resonators to electromagnetic degrees of freedom using SQUIDs. In the first part (ch. 5) we propose a scheme for synthesizing multi-phonon quantum states in a tripartite coupling configuration involving two transmon qubits. Following the derivation of the circuit Hamiltonian and electromechanical couplings in the system, we provide further evidence for the validity of the scheme using real-world numerical simulations with parameters obtained from recent experiments. In the second part (ch. 6) we investigate the same coupling mechanism between a transmon qubit and a mechanical resonator and demonstrate the possibility of reaching optomechanical couplings that are larger than the mechanical frequency, in the so-called ultra-strong-coupling regime, at single-photon levels. We further demonstrate numerically the ability to cool the resonator via the qubit and propose a protocol for preparing massive mechanical superpositions by controllably tuning the coupling strength.
3. **Chapter 7** concerns the experimental realisation of a reservoir engineering scheme enabling quantum control in a thermally populated radio-frequency (170 MHz) resonator. This experiment was a result of a strong collaboration in the group led by my colleague M. F. Gely. The novelty of this work relies on the realisation of a strong dispersive coupling with a gigahertz superconducting qubit, despite the large frequency difference. The qubit, which was naturally cooled down by the dilution refrigerator hosting the device, was employed for readout and control of the low-frequency mode enabling the stabilisation of quantum states despite the strong presence of thermal effects.

2

Theoretical description of quantum circuits

*The mathematical sciences particularly exhibit order, symmetry and limitations;
and these are the greatest forms of the beautiful.*

Aristotle, "Metaphysics"

The purpose of this chapter is to present the theoretical methodology used in this thesis for designing and analysing electrical quantum circuits, as well as modelling their dynamics. First, a method for constructing the Lagrangian and Hamiltonian of linear circuits is described together with a mode analysis. We will then depart from this classical description to impose quantisation of the electromagnetic degrees of freedom and analyse nonlinear Josephson circuits, focusing on transmon qubits. The chapter concludes with a brief description of the necessary tools to simulate the evolution of interacting quantum systems in the presence of dissipation.

2.1. Classical description: from Lagrangian to Hamiltonian

In this section we will describe the methodology used to find the Lagrangian and Hamiltonian of an electrical circuit in the classical case. All circuits considered in this thesis are in the lumped element limit, i.e. the corresponding wavelength of their resonant modes (1-10 cm) is 2-3 orders of magnitude larger than their overall dimension ($\sim 100 \mu\text{m}$). We will first introduce the description of electromagnetic circuits in the node flux variable representation [72, 73]. This will allow us to define the circuit in terms of canonical conjugate variables, which is essential for finding its Hamiltonian and quantising it.

The Lagrangian of a system is a function of its generalised coordinates, their derivatives and time, and provides a compact description of the system dynamics [74]. It provides a powerful tool for exploiting the symmetries and conserved quantities of a system and its formulation, together with the further development of Hamiltonian mechanics, has revolutionised modern theoretical physics. Here, we will use it as a tool for analysing superconducting circuits at a classical level, finding their resonances, and deriving their underlying Hamiltonian with the purpose of reaching a quantum description. Note that a quantum description is also possible with the Lagrangian and the *path integral formulation* of quantum mechanics [75], however such methods are perhaps too sophisticated for the problems we are seeking to describe here.

2.1.1. Method of nodes

Electrical circuits consist of a network of “branches”, comprising elements such as capacitors and inductors, that are connected at “nodes”, as schematically depicted in Fig. 2.1. Knowledge of the branch variables, i.e. the currents flowing through and the voltages across its elements (or equivalently the corresponding charges and fluxes), is sufficient for constructing the capacitive and inductive energy of the circuit, \mathcal{E}_{cap} , \mathcal{E}_{ind} , and therefore the circuit Lagrangian [74],

$$\mathcal{L} = \mathcal{E}_{\text{cap}} - \mathcal{E}_{\text{ind}}. \quad (2.1)$$

Branch variables are not necessarily independent with each other as they are related via Kirchhoff’s laws. Formulating the dynamics of the circuit in terms of independent canonical variables is, however, necessary for obtaining its Hamiltonian and eventually imposing canonical quantisation.

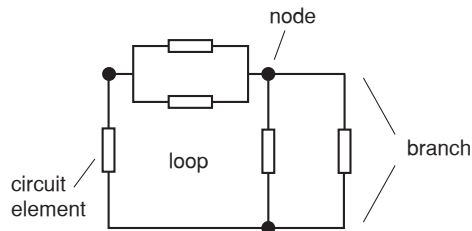


Figure 2.1: Schematic representation of an electrical circuit comprising a network of circuit elements that form “branches” connected at the “nodes” of the circuit.

An alternative description, incorporating Kirchhoff’s laws while using independent

variables can be achieved with the *method of nodes*, described in detail in Ref. [73]. In short, one starts with the prerequisite that every node should be connected to another node by at least one capacitive element. For example, if a branch contains only inductive elements, an additional capacitor needs to be assigned in parallel (corresponding to the parasitic capacitance of the inductor, or the capacitance of a Josephson junction). One then proceeds with defining a common node as the “ground”, which acts as a reference for all the other node flux variables. This construction comprising a set of branches that are connected such that there is a unique path from each node to the ground (via at least one capacitor) to avoid forming loops, is called the spanning tree. It is equivalent to a coordinate transformation that relates the branch variables to independent node variables¹. As an example, below we will follow this procedure to construct the Lagrangian for the simple case of the LC oscillator and the slightly more complex case involving coupled oscillators.

2.1.2. LC oscillator

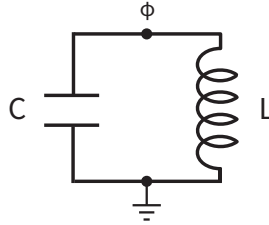


Figure 2.2: Circuit representation of the LC oscillator.

The most fundamental electrical circuit is the LC oscillator, consisting of a capacitor C in parallel to an inductor L (Fig. 2.2). Using the node variable representation is trivial in this case because of the simplicity of the circuit. Its Lagrangian is given by

$$\mathcal{L} = \frac{C\dot{\phi}^2}{2} - \frac{\phi^2}{2L}, \quad (2.2)$$

where the node flux variable ϕ is defined from the node potential V as $V(t) = \dot{\phi}$. The conjugate momentum, corresponding to the node charge, is then defined as $q = \frac{\partial \mathcal{L}}{\partial \dot{\phi}} = C\dot{\phi}$. The pair ϕ, q is a set of canonical coordinates satisfying Poisson bracket relations $\{\phi, q\} = 1$.

Following a Legendre transformation, we obtain the Hamiltonian

$$\mathcal{H} = \dot{\phi}q - \mathcal{L} = \frac{q^2}{2C} + \frac{\phi^2}{2L}, \quad (2.3)$$

and equations of motion

$$\dot{\phi} = \frac{\partial \mathcal{H}}{\partial q}, \quad \dot{q} = -\frac{\partial \mathcal{H}}{\partial \phi}. \quad (2.4)$$

¹Although here we focus on the node variable representation, one could equivalently formulate the Lagrangian and construct the Hamiltonian of the circuit using loop variables [76].

2.1.3. Coupled LC oscillators

Now we can explore the case of a more complicated circuit of coupled oscillators, shown in Fig. 2.3. The charging and inductive energies of the system are given by

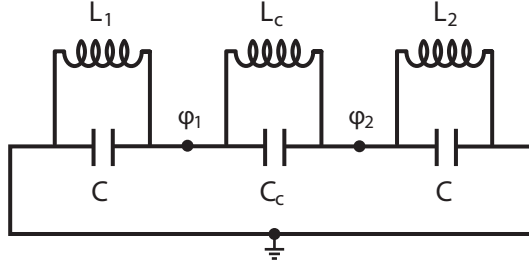


Figure 2.3: System of two coupled LC oscillators.

$$\mathcal{E}_{\text{charge}} = \frac{C}{2} \dot{\phi}_1^2 + \frac{C}{2} \dot{\phi}_2^2 + \frac{C_c}{2} (\dot{\phi}_1 - \dot{\phi}_2)^2, \quad (2.5)$$

and

$$\mathcal{E}_{\text{ind}} = -\frac{\phi_1^2}{2L_1} + \frac{\phi_2^2}{2L_2} + \frac{(\phi_1 - \phi_2)^2}{2L_c}, \quad (2.6)$$

where the node flux ϕ_i is related to the potential at node i according to $\dot{\phi}_i = V_i(t)$, as we discussed earlier. The system Lagrangian, therefore, is

$$\mathcal{L} = \mathcal{E}_{\text{charge}} - \mathcal{E}_{\text{ind}} = \frac{1}{2} \dot{\phi}^T [\mathbf{C}] \dot{\phi} - \frac{1}{2} \phi^T [\mathbf{L}^{-1}] \phi, \quad (2.7)$$

where

$$[\mathbf{C}] = \begin{bmatrix} C + C_c & -C_c \\ -C_c & C + C_c \end{bmatrix}, \quad (2.8)$$

is the capacitance matrix, and

$$[\mathbf{L}^{-1}] = \begin{bmatrix} 1/L_1 + 1/L_c & -1/L_c \\ -1/L_c & 1/L_2 + 1/L_c \end{bmatrix}, \quad (2.9)$$

is the inverse of the inductance matrix of the circuit, expressed in the node flux basis $\phi^T \doteq [\phi_1, \phi_2]$.

The conjugate momenta $q_i = \frac{\partial \mathcal{L}}{\partial \dot{\phi}_i}$, describing the charges associated with each node, can be determined by inverting the capacitance matrix, since $\mathbf{q} = [\mathbf{C}'] \dot{\phi}$. Therefore, the charging energy can also be expressed in terms of charge variables, as

$$\begin{aligned} \mathcal{E}_{\text{charge}} &= \frac{1}{2} \mathbf{q}^T \mathbf{C}^{-1} \mathbf{q} \\ &= \frac{1}{C(C + 2C_c)} \left[\frac{(C + C_c)}{2} q_1^2 + \frac{(C + C_c)}{2} q_2^2 + C_c q_1 q_2 \right]. \end{aligned} \quad (2.10)$$

Performing a Legendre transformation leads to the circuit Hamiltonian

$$\mathcal{H} = \sum_i \dot{\phi}_i q_i - \mathcal{L} = \frac{1}{2} \mathbf{q}^T \mathbf{C}^{-1} \mathbf{q} + \frac{1}{2} \phi^T [\mathbf{L}^{-1}] \phi. \quad (2.11)$$

2.1.4. Normal-mode analysis

With the capacitance and inductance matrices at hand we can already find the independent normal modes of oscillation in the circuit. These can be determined by the eigenvalues of the matrix $[\Omega^2] = [\mathbf{C}^{-1}][\mathbf{L}^{-1}]$, or by solving the characteristic/secular equation

$$[\mathbf{L}^{-1}] - \Omega^2 [\mathbf{C}] = 0. \quad (2.12)$$

It more informative, however, especially in the design process, to compute the corresponding eigenvectors in terms of the node variables as it can tell us where currents are flowing in the circuit when a certain mode is excited. The eigenvector corresponding to eigenfrequency Ω can be determined by computing the nullspace of the matrix $[\mathbf{L}^{-1}] - \Omega^2 [\mathbf{C}]$.

Following this procedure for the simple case of the circuit shown in Fig. 2.3, we find the following normal modes

$$\begin{aligned} \psi_+ &= a \phi_1 + b \phi_2, \\ \psi_- &= a \phi_1 - b \phi_2, \end{aligned} \quad (2.13)$$

where the coefficients a and b are equal for the case $L_1 = L_2 = L$. This case corresponds to two resonantly coupled LC oscillators, via a coupling inductor in parallel to a capacitor. The coupling element acts like a band-stop filter when the frequency of the other two is tuned to the filter frequency $\omega_1 = \omega_2 = 1/\sqrt{L_c C_c}$. At this point the coupling between the two oscillators are not coupled as a result of interference of currents flowing through the capacitor and the inductor. This concept of coupling is the topic of chapter 4, where a similar circuit is explored to couple two transmon qubits in the nonlinear case.

The normal-mode frequencies are

$$\begin{aligned} \omega_+ &= \sqrt{\frac{1}{LC}}, \\ \omega_- &= \sqrt{\frac{2L + L_c}{LL_c(C + 2C_c)}}. \end{aligned} \quad (2.14)$$

We plot the dependence of the normal-mode frequencies as a function of the coupling inductance L_c in Fig. 2.4(a). The two normal modes, corresponding to symmetric and antisymmetric combinations of the coupled oscillators (Eq. (2.13)), are schematically depicted in Figs. 2.4(b), (c). Note that the frequency of the symmetric mode ψ_+ is independent of L_c , as this mode does not involve currents flowing through the coupling elements. The normal-mode splitting, or equivalently the coupling between the two oscillators, is suppressed at the point where they are both on resonance with the coupling oscillator, i.e. at the “filter frequency” $1/\sqrt{L_c C_c}$ (dashed curve in Fig. 2.4(a)).

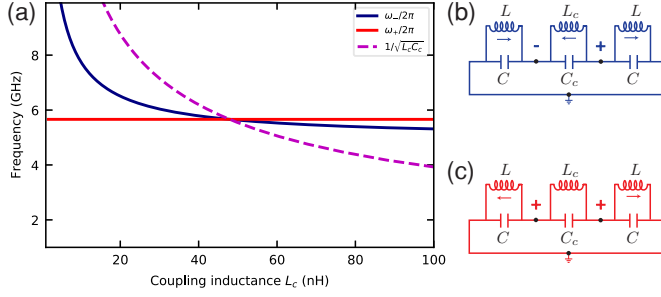


Figure 2.4: (a) Normal-mode frequencies of two resonantly coupled LC oscillators, as in Fig. 2.3, as a function of the coupling inductance L_c . The normal-mode splitting (blue and red curves) is suppressed at the point where the filter frequency of the coupler (dashed curve) is resonant with both oscillators. (b), (c) Corresponding normal modes of the circuit in the resonant case.

2.2. Canonical quantisation: from variables to quantum operators

The goal of this section is to present the procedure of *canonical quantisation* in the context of the circuits analysed in the previous section. Quantisation of the electromagnetic field imposes the following commutation relations $[\hat{\phi}_i, \hat{q}_j] = i\hbar\delta_{ij}$, where $\hat{\phi}_i, \hat{q}_i$ are the corresponding quantum operators for flux and charge at node i [73].

2.2.1. Quantum LC oscillator

The LC oscillator Hamiltonian in Eq. (2.3) can be described in terms of quantised excitations using the ladder operator method [77],

$$\hat{\phi} = \phi_{\text{ZPF}} (\hat{a} + \hat{a}^\dagger), \quad \hat{q} = q_{\text{ZPF}} i(\hat{a}^\dagger - \hat{a}), \quad (2.15)$$

where $\hat{a}^{(\dagger)}$ are ladder operators describing the annihilation (creation) of photons and satisfying bosonic commutation relations $[\hat{a}, \hat{a}^\dagger] = 1$. The zero-point fluctuations $\phi_{\text{ZPF}}, q_{\text{ZPF}}$, are a measure of the variance (or “quantum jitter” in Feynman’s words) of the observable flux or charge, when the system is in its lowest energy possible, i.e. its ground state. They are determined by the impedance $Z = \sqrt{L/C}$ of the corresponding mode

$$\phi_{\text{ZPF}} = \sqrt{\langle 0 | \hat{\phi}^2 | 0 \rangle} = \sqrt{\frac{\hbar Z}{2}}, \quad (2.16)$$

$$q_{\text{ZPF}} = \sqrt{\langle 0 | \hat{q}^2 | 0 \rangle} = \sqrt{\frac{\hbar}{2Z}}. \quad (2.17)$$

Promoting all canonical conjugate variables in Eq. (2.3) to quantum operators, using the above expressions, we find the Hamiltonian of the quantum harmonic oscillator (QHO)

$$\hat{\mathcal{H}}_{\text{QHO}} = \hbar\omega \left(\hat{a}^\dagger \hat{a} + \frac{1}{2} \right), \quad (2.18)$$

where $\omega = 1/\sqrt{LC}$ is its fundamental frequency.

A comment on normal-mode vs bare-mode basis

For more complicated circuits, such as the system of LC oscillators we analysed in section 2.1.3, it is important to reflect upon what we want to get out of this procedure. For example, if we are interested in finding the steady state of the coupled system (corresponding to the modes observed in a typical spectroscopic measurement), it makes sense to express the Hamiltonian in the normal-mode basis q_{\pm}, ψ_{\pm} ,

$$\begin{aligned}\hat{\mathcal{H}}_{\text{QHO}} &= \sum_{i=+,-} \left(\frac{\hat{q}_i^2}{2\tilde{C}_i} + \frac{\hat{\psi}_i^2}{2\tilde{L}_i} \right) \\ &= \sum_{i=+,-} \hbar\omega_i \left(\hat{a}_i^\dagger \hat{a}_i + \frac{1}{2} \right)\end{aligned}\quad (2.19)$$

where ω_i are the corresponding normal-mode frequencies, found in Eq. (2.14).

However, sometimes we might be interested in modelling experiments involving quenches, e.g. exciting one oscillator much faster than the mutual coupling and observing how this excitation propagates in time in the system. In cases like that it is more convenient to express the system in the bare basis of the uncoupled system, or some basis corresponding to a mode we can individually address in the experiment. For the coupled system of Fig. 2.3, the bare modes can be calculated for $C_c \rightarrow 0$, $L_c \rightarrow \infty$, such that $\psi_{+/-} \simeq \phi_{1/2}$. Provided there is no coupling between them, e.g. when they are sufficiently detuned, the bare modes could be individually addressed by local driving, which is typically realised via coplanar waveguides (CPW) capacitively connected to node 1 or 2 of the circuit². We will treat the circuit in the bare basis in the next section, where we will study the nonlinear case.

2.2.2. Superconducting transmon qubits

In this section we will introduce superconducting transmon qubits, which constitute the main element studied in this thesis. Building on the formalism we developed in the previous section, we will discuss how these nonlinear circuits are constructed from the Hamiltonian point of view and analyse them in two different bases. We will then review the example of the coupled oscillators of the previous section in the case of transmon qubits and nonlinear coupling elements.

Transmon as a weakly anharmonic oscillator

The transmon qubit is obtained from an LC oscillator by replacing the linear inductor with a nonlinear one, which is typically realised with a Josephson junction. The type of Josephson junctions considered here, which will be more extensively reviewed in the next chapter, consist of two superconducting electrodes that are separated by an insulating barrier. The potential energy that is stored in this circuit is described by the Josephson energy, $E_J \cos \delta$, where $\delta = \phi/\phi_0$ is the *gauge-invariant phase difference* across the junction and $\phi_0 = \hbar/2e$ is the reduced flux quantum [73]. The equivalent inductance of the junction is given by $L_J = \phi_0^2/E_J$.

²More details on the experimental realisation of CPW drivelines are given in the next chapter.

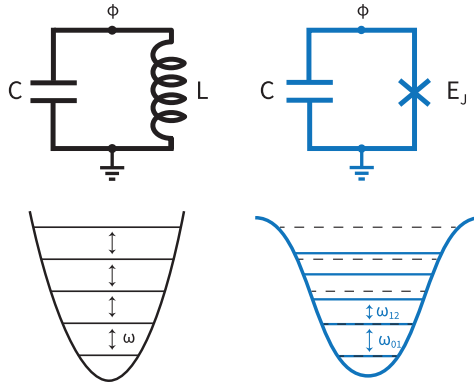


Figure 2.5: LC oscillator (black) and transmon (blue) circuit and potential. The cosine potential of the transmon leads to a 2π -periodic wavefunction in the flux coordinate ϕ (not shown). For large E_J/E_C ratios it is well-approximated by a Duffing oscillator potential with a negative anharmonicity $\omega_{12} - \omega_{01} \simeq -E_C/\hbar$.

Although a Josephson junction naturally forms a parallel LC circuit, albeit a nonlinear one, the transmon qubit is realised by additionally shunting the junction with a large capacitance [44], which minimises its charging energy $E_C = e^2/2C$, such that $E_J \gg E_C$.³ The transmon Hamiltonian is given by

$$\hat{\mathcal{H}}_T = 4E_C \hat{N}^2 - E_J \cos \hat{\delta}, \quad (2.20)$$

where $\hat{\delta}$, \hat{N} are quantum operators describing the phase difference and the discrete number of Cooper-pairs that participate in tunnelling across the junction, respectively. The nonlinear flux dependence of the Josephson inductance, in combination with the fact that quantum fluctuations become larger for higher excitations $\sqrt{\langle n | \hat{\phi}^2 | n \rangle} = \phi_{\text{ZPF}} \sqrt{2n+1}$, renders the system anharmonic with a negative anharmonicity $\omega_{12} - \omega_{01} \simeq -E_C/\hbar$, as depicted schematically in Fig. 2.5.

In the transmon limit $E_J/E_C \geq 50$, the zero-point fluctuations in the phase difference are very small $\phi_{\text{ZPF}}/\phi_0 = (2E_C/E_J)^{1/4} \ll 1$ and a perturbative expansion of the cosine potential to fourth order is sufficient (see Fig. 2.6 for a comparison with the exact Hamiltonian in the charge basis). The Hamiltonian is therefore well-approximated by that of a Duffing oscillator

$$\hat{\mathcal{H}}_T = 4E_C \hat{N}^2 + E_J \left(\frac{\hat{\delta}^2}{2} - \frac{\hat{\delta}^4}{24} \right). \quad (2.21)$$

The quantum operators in the harmonic oscillator basis are given by

$$\hat{N} = i \left(\frac{E_J}{32E_C} \right)^{1/4} (\hat{c}^\dagger - \hat{c}), \quad \hat{\delta} = \left(\frac{2E_C}{E_J} \right)^{1/4} (\hat{c} + \hat{c}^\dagger). \quad (2.22)$$

³The opposite limit, which we discuss more in the next section, is associated with charge noise sensitivity issues and less coherent qubits.

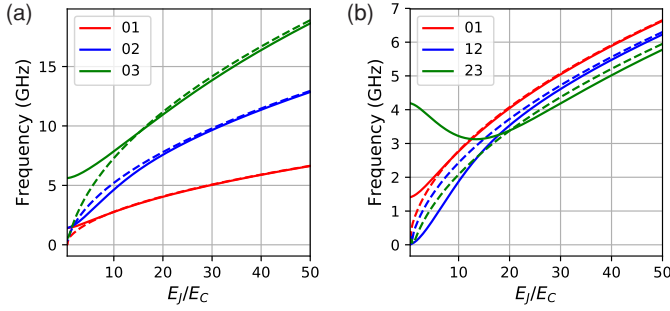


Figure 2.6: (a) First three energy transitions from the ground state vs E_J/E_C , obtained after diagonalising the transmon Hamiltonian in the charge basis (solid curves) and in the QHO basis using the Duffing oscillator approximation (dashed curves). (b) First three consecutive transitions in the same parameter space.

Replacing them in the equation above we have

$$\hat{\mathcal{H}}_T = \hbar\omega\hat{c}^\dagger\hat{c} - \frac{E_C}{2}\hat{c}^\dagger\hat{c}^\dagger\hat{c}\hat{c}, \quad (2.23)$$

where $\omega = (\sqrt{8E_JE_C} - E_C)/\hbar$ is the 0 – 1 transition frequency of the transmon, and we have neglected fast-oscillating terms $(\hat{c}^{(\dagger)})^n$ ($n \geq 2$).

Charge basis representation and the Cooper-pair Box

An exact description of the transmon dynamics can be obtained in the eigenbasis of the Cooper-pair number operator, $|N\rangle$. Unlike the total charge Q of the Cooper-pair condensate that is stored in the capacitance between the two superconducting islands, which can be treated as a continuous variable, the charge $2eN$ associated with the number of Cooper-pairs N tunnelling through the junction is a quantised integer number. This gives rise to the nonlinear current-phase relations discovered by Josephson [21, 73].

The Cooper-pair number operator in this basis is defined as

$$\hat{N} = \sum_N N|N\rangle\langle N|, \quad (2.24)$$

where the sum is from $-\infty$ to $+\infty$, although practically a cutoff at ~ 20 charge states is sufficient to describe the first three energy levels. Using the commutation relation $[\hat{\delta}, \hat{N}] = i$, we can also express the phase operator in the Cooper-pair basis as

$$e^{-i\hat{\delta}} = \sum_N |N+1\rangle\langle N|. \quad (2.25)$$

Noting that $2\cos\hat{\delta} = e^{i\hat{\delta}} + e^{-i\hat{\delta}}$, the transmon Hamiltonian in Eq. (2.20) becomes

$$\hat{\mathcal{H}}_T = 4E_C \sum_N N^2|N\rangle\langle N| - \frac{E_J}{2} \sum_N (|N+1\rangle\langle N| + |N\rangle\langle N+1|). \quad (2.26)$$

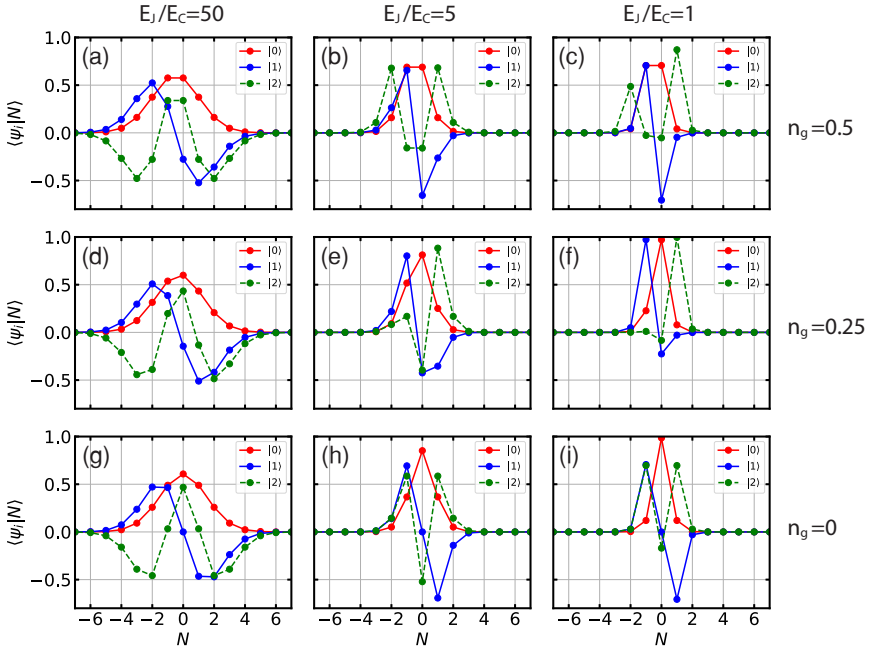


Figure 2.7: Wavefunctions of the first three energy levels in the Cooper-pair number space, obtained after diagonalising the Hamiltonian in Eq. (2.26) for different ratios of E_J/E_C and including different charge offsets $\tilde{N} \rightarrow (\tilde{N} - n_g \hat{I})$ (calculated for $-10 \geq N \geq 10$). In the transmon regime the shape of the wavefunction remains consistent for different values of n_g as shown in (a), (d) and (g). On the other hand the wavefunctions change dramatically as one enters the CPB regime.

In Fig. 2.6 we plot the first three transitions from the ground state, as obtained after diagonalising the transmon Hamiltonians in Eqs. (2.23) and (2.26). Note that the Duffing oscillator approximation (dashed curves) is in good agreement with the exact solution (solid curves) for large E_J/E_C ratios and begins to visibly diverge below $E_J/E_C \sim 20$. As the charging energy becomes comparable to the Josephson energy of the circuit, one enters the Cooper-pair Box (CPB) regime, where the qubit becomes sensitive to charge offsets caused by the environment, leading to small dephasing times [32, 78]. Experimentally it is possible to control this degree of freedom by applying a gate voltage such that the qubit operates at its charge-insensitive (to first order) points, which leads to significantly improved coherence times [34].

The improved version of the transmon qubit [44, 79], based on earlier theoretical work by Likharev and Zorin [80], cures the charge sensitivity issues by operating in the regime $E_J \gg E_C$ where the qubit states are immune to charge offsets over the whole range, therefore not requiring additional control circuitry. This regime is achieved by shunting the junction with a larger capacitance and forming a bigger Cooper-pair Box, perhaps better nicknamed as “Cooper-pair Crate”⁴. The suppression of the charge

⁴This more representative name was initially proposed by Prof. Jens Koch – *private discussion at the workshop “Quantum simulations and many-body physics with light” (Chania, Crete, June 2016)*.

noise sensitivity decreases exponentially with the ratio E_J/E_C , at the cost of a reduced anharmonicity (which however decreases only algebraically with this ratio), making the transmon a weakly-anharmonic qutrit that is well-approximated by the Duffing oscillator Hamiltonian in Eq. (2.23).

For a comparison of the two regimes, in Fig. 2.7 we plot the modulus squared of the first three eigenvectors of the charge qubit Hamiltonian (2.26) for different E_J/E_C ratios and charge offsets. The latter are included as an offset in the number operator, $\hat{N} \rightarrow (\hat{N} - n_g \hat{I})$, where n_g is a continuous variable. Note that as one goes deeper into the transmon regime, the ground and excited states are described by larger superpositions of Cooper-pair number states, making the shape of the wavefunctions unaffected by the existence of charge offsets. On the other hand, in the CPB limit ($E_C \geq E_J$) the states change dramatically as n_g is varied.

2.2.3. Nonlinearly coupled transmon qubits

In this section we will conclude the circuit quantisation analysis with the nonlinear version of the example of coupled oscillators system, studied in section 2.1.3, in the transmon limit (Fig. 2.8). This circuit has been proposed in Refs. [59, 61] for implementing tunable couplings between transmon qubits, as a building block for exploring experimentally complex problems by means of analog quantum simulations. An experimental realisation of a slightly more complicated version of this circuit is explored in chapter 4. Here we will review this circuit with the purpose of demonstrating how to apply the quantum analysis toolbox described in the previous sections in more complicated circuits.

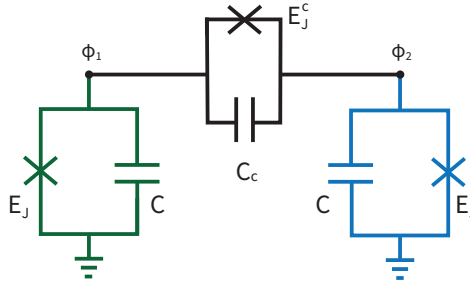


Figure 2.8: Coupled transmon qubits via a nonlinear transmon-like coupler.

The Hamiltonian of the coupled system is given by

$$\hat{H} = \sum_{i=1}^2 \hat{H}_T^{(i)} + \hat{H}_{\text{int}}, \quad (2.27)$$

where $\hat{H}_T^{(i)}$ describe the bare Hamiltonian of each transmon and

$$\hat{H}_{\text{int}} = \frac{4e^2 C_c}{C(C + 2C_c)} \hat{N}_1 \hat{N}_2 - E_J^c \cos\left(\frac{\hat{\phi}_1 - \hat{\phi}_2}{\phi_0}\right), \quad (2.28)$$

is the interaction Hamiltonian.

Expanding the inductive energy to $\mathcal{O}[\phi^4]$ and expressing the quantum operators describing charge and flux in the QHO basis (Eqs. (2.22)), the interaction Hamiltonian in the resonant case is

$$\hat{\mathcal{H}}_{\text{int}} \simeq J(\hat{c}_1^\dagger \hat{c}_2 + \hat{c}_1 \hat{c}_2^\dagger) - V \hat{c}_1^\dagger \hat{c}_1 \hat{c}_2^\dagger \hat{c}_2, \quad (2.29)$$

where

$$J = \frac{\omega}{2} \left(\frac{E_J^c}{E_J} - \frac{C_c}{C} \right) - 2E_C \frac{E_J^c}{E_J}, \quad V = 2E_C \frac{E_J^c}{E_J}, \quad (2.30)$$

are the coupling strengths describing hopping and cross-Kerr interactions, respectively. Note that we have neglected interaction terms involving more than one qubit excitations, e.g. correlated hopping $\hat{c}_i^\dagger \hat{c}_i^\dagger \hat{c}_i^\dagger \hat{c}_j$ or two-photon hopping $\hat{c}_i^\dagger \hat{c}_i^\dagger \hat{c}_j \hat{c}_j$, as well as fast-oscillating *counter-rotating* terms $[(\hat{c}_i \hat{c}_j)^\dagger]^n$ (assuming $J \ll \omega$).

In the charge basis, the interaction Hamiltonian is

$$\begin{aligned} \hat{\mathcal{H}}_{\text{int}} = & \frac{4e^2 C_c}{C(C + 2C_c)} \sum_{N_1} \sum_{N_2} N_1 |N_1\rangle \langle N_1| N_2 |N_2\rangle \langle N_2| \\ & - \frac{E_J^c}{2} \sum_{N_1} \sum_{N_2} (|N_1 + 1\rangle \langle N_1| N_2 \rangle \langle N_2 + 1| + |N_2 + 1\rangle \langle N_2| N_1 \rangle \langle N_1 + 1|), \end{aligned} \quad (2.31)$$

which can be readily diagonalised without any approximations. Working in this basis has the advantage of providing an exact description of the system, however, it becomes less favourable for larger circuits due to the large Hilbert space required (typically at least $-7 \leq N_i \leq +7$ up to the first 2-3 levels). Another disadvantage of working in this basis is that it becomes difficult to express and classify the different interaction terms in the circuit. For example, the existence of hopping and cross-Kerr coupling terms between the qubits is not directly evident from Eq. (2.31). Moreover, modelling time-domain experiments of open quantum systems is typically done in terms of the density matrix formalism [81, 82], for which ladder operators provide a more suitable basis to describe the interaction with the environment as we will see in the next section.

2.3. Modelling open quantum systems in time-domain

There exist a variety of computational techniques for describing the evolution of interacting open quantum systems. Such techniques provide a very important toolbox for understanding the observed dynamics in well-controlled time-domain experiments, as well as designing experiments in the context of quantum computing and quantum simulation, which involve the application of quantum gates and dissipation to the environment. Throughout this thesis, we will employ such techniques for modelling the quantum behaviour of superconducting circuits with the purpose of fitting time-domain measurements or benchmarking the validity of proposed experiments.

We utilise the simulation software toolbox provided by QuTiP [83], which describes the evolution of quantum systems under the framework of the Lindblad master equation

$$\dot{\rho} = \frac{i}{\hbar} [\rho, \hat{H}] + \sum_{i=1}^N \gamma^i (n_{\text{th}} + 1) \mathcal{L}[\hat{c}_i] \rho + \gamma_\phi^i \mathcal{L}[\hat{c}_i^\dagger \hat{c}_i] \rho + \gamma^i n_{\text{th}} \mathcal{L}[\hat{c}_i^\dagger] \rho, \quad (2.32)$$

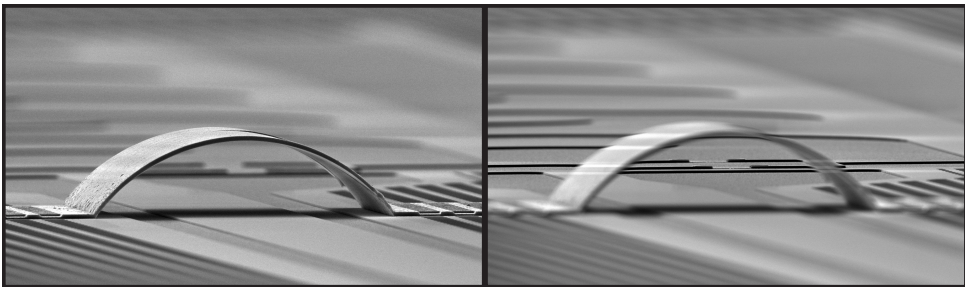
where ρ is the density matrix of the full quantum system. The trace-preserving Lindblad superoperators

$$\mathcal{L}[\hat{\sigma}]\rho \doteq (2\hat{\sigma}\rho\hat{\sigma}^\dagger - \hat{\sigma}^\dagger\hat{\sigma}\rho - \rho\hat{\sigma}^\dagger\hat{\sigma})/2, \quad (2.33)$$

describe the interaction of each circuit mode i with the environment, which is assumed to be a bath containing an infinite number of degrees of freedom [84]. Superconducting qubits typically operate at frequencies 4–8 GHz and are cooled down to their groundstate using dilution refrigerators operating at millikelvin temperatures, such that thermal excitations are vanishingly small $n_{\text{th}} = 1/[e^{\hbar\omega/k_B T} - 1] \lesssim 10^{-10}$. Under these conditions, dissipative processes manifest mainly as decay of excitations and phase information losses of superposition states, which are described by the first two Lindblad operators in Eq. (2.32) and quantified by the relaxation and dephasing rates, γ^i , γ_ϕ^i . In practical implementations, however, residual excitations of 1–10% are typically reported due to imperfect thermalisation and nonequilibrium quasiparticle excitations [85, 86]. Additionally, thermal effects due to the environment become significant when lower frequency modes ($\lesssim 1$ GHz) are considered. An additional Lindblad operator (last term in Eq. (2.32)) is therefore required to describe the thermal population due to the environment, which also causes an enhancement of the relaxation rate by $(n_{\text{th}} + 1)$.

3

Circuit design and fabrication



There is not a law under which any part of the universe is governed which does not come into play, and is touched upon in the chemistry of a candle.

Michael Faraday, "The Chemical History of a Candle"

The previous chapter was concerned with the theoretical description of superconducting circuits and the method of circuit quantisation. The goal of this chapter is to give an overview of the design and fabrication process that is necessary for an experimental realisation of these circuits, focusing mainly on transmon-based devices.

3.1. Readout and control of transmon qubits

In this section we will review the main aspects of control and readout of transmon qubits. We will start with a brief introduction of the necessary control lines for tuning the qubit frequency and for local driving. We will then discuss the most important design considerations for achieving optimal readout conditions.

3.1.1. Frequency tuning and driving

The dc-SQUID

An important element of control in superconducting circuits is the ability to tune the qubit/resonator frequencies as well as their couplings. As we discussed in the previous chapter, transmon qubits are realised using a capacitor in parallel to a Josephson junction, which introduces the required nonlinearity while being nondissipative. Tuning the qubit frequency $\omega \simeq \sqrt{8E_J E_C}/\hbar$ would require changing either its charging energy (hence the capacitance) or the Josephson energy (hence the inductance). Although a tuneable capacitance could be realised, for example using a vacuum-gap capacitor [87] with an additional voltage bias, typically qubit frequencies are tuned by changing the Josephson inductance. This is typically done by employing a dc superconducting quantum interference device (dc-SQUID), which consists of a superconducting loop that is interrupted by two Josephson junctions [88]. Applying a flux, Φ_b , through the loop changes the Josephson energy amplitude of the transmon as [44]

$$E_J = E_{J,\Sigma} |\cos(\pi\Phi_b/\Phi_0)| \sqrt{1 + a_J^2 \tan^2(\pi\Phi_b/\Phi_0)}, \quad (3.1)$$

where $\Phi_0 = h/2e$ is the magnetic flux quantum, $E_{J,\Sigma} = (E_{J,1} + E_{J,2})$ is the sum of the two junction Josephson energies, and $a_J = |E_{J,1} - E_{J,2}|/(E_{J,1} + E_{J,2})$ is the asymmetry of the SQUID.

When the junctions are identical the Josephson energy can be tuned down to zero, at half-integer flux quanta, forcing the qubit into the Cooper-pair box (CPB) regime, $E_J \lesssim E_C$. In Fig. 3.1(a) we plot the flux dependence of the first three consecutive transitions after diagonalising the transmon Hamiltonian in the charge basis (Eq. (2.26)), for typical parameters $E_C/h = 300$ MHz, $E_{J,\Sigma}/h = 20$ GHz and a symmetric SQUID ($a_J = 0$). Note that the approximation $\omega_{01} = (\sqrt{8E_J E_C} - E_C)/\hbar$ for the qubit frequency fails as we approach the CPB regime, which happens at $\Phi_b/\Phi_0 = 0.4$ for the parameters considered above. The optimal working point (dubbed as the *sweetspot*) is nevertheless at $\Phi_b = 0$, where the qubit is, to first order, insensitive to flux noise.

For comparison, in Fig. 3.1(b) we plot the flux dependence of the same transitions for an asymmetric SQUID ($a_J = 0.5$). One of the main advantages of using asymmetric junctions is the occurrence of a second flux insensitive point at $\Phi_b/\Phi_0 = 0.5$, which can be used when one wants to have two optimal working points in an experiment, e.g. one for interacting with one qubit and another for readout or driving. Other reasons for choosing asymmetric SQUIDs could be to avoid unwanted crossing with other qubits or circuit modes, or as a means to decrease flux noise overall for $a_J \rightarrow 1$ (although at the cost of limited tuneability) [89].

Tuning the SQUID requires the application of an out-of-plane magnetic field. This can be done with an external magnet, e.g. using a coil that is outside of the chip, as in

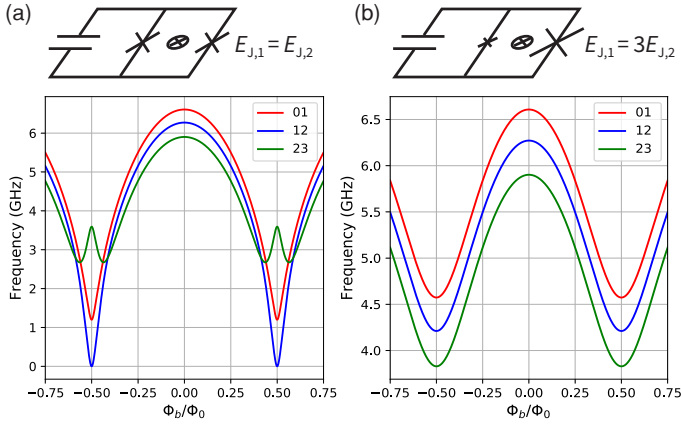


Figure 3.1: Transmon level transitions as a function of flux bias, obtained after diagonalising the Hamiltonian of Eq. (2.26) in the charge basis (at zero charge offset), assuming (a) a symmetric and (b) an asymmetric SQUID ($a_J = 0.5$). Parameters: $E_{J,\Sigma}/h = 20$ GHz, $E_C/h = 300$ MHz. In the symmetric case, the onset of the Cooper-pair box regime happens at $\Phi_b/\Phi_0 \simeq 0.4$.

the experiment discussed in chapter 7. However, this method is not very useful when operating multiple qubits on the same chip (as in chapter 4). In this case, where local flux control is desirable, one typically employs on-chip flux-lines, which can be realised with superconducting transmission lines that pass by close proximity to the transmon SQUID and are shorted to ground. Sending a current through the flux-line induces a pick-up flux on the loop which results in tuning of the Josephson energy amplitude and therefore the qubit frequency (see Fig. 3.2).

3.1.2. Readout via coplanar waveguide resonators

The input and output lines that are used for control and readout of the qubits are realised with coplanar waveguides (CPW) which are fabricated on the same chip. These are two-dimensional realisations of coaxial lines made out of superconducting material that consist of a long centre-pin that is shielded with a coaxial capacitance to ground. They can be used as transmission lines carrying the microwave (or DC) signals in and out of the device. CPWs can also function as superconducting resonators when boundary conditions are imposed [90, 91]. For example, if both ends of the centre-pin are capacitively connected to ground, a standing wave is formed with maximum voltage (zero current) at the two ends, realising a half-wave ($\lambda/2$) resonator. Alternatively, when one of the two ends is shorted to ground a quarter-wave ($\lambda/4$) resonator is formed. From a circuit point of view, these resonators can be described as the continuum limit of an infinite chain of LC oscillators (Fig. 3.3) [90, 92]. Their characteristic impedance $Z_0 = \sqrt{(\mathcal{L}_k + \mathcal{L}_g)/\mathcal{C}_g}$ is determined by the geometric and kinetic inductance \mathcal{L}_k , \mathcal{L}_g and capacitance \mathcal{C}_g per unit length. Typically, the lateral dimensions (widths of the centre-pin and gap to ground) are optimised for a 50 Ohm impedance in order to match to the characteristic impedance of the cables in the measurement setup.

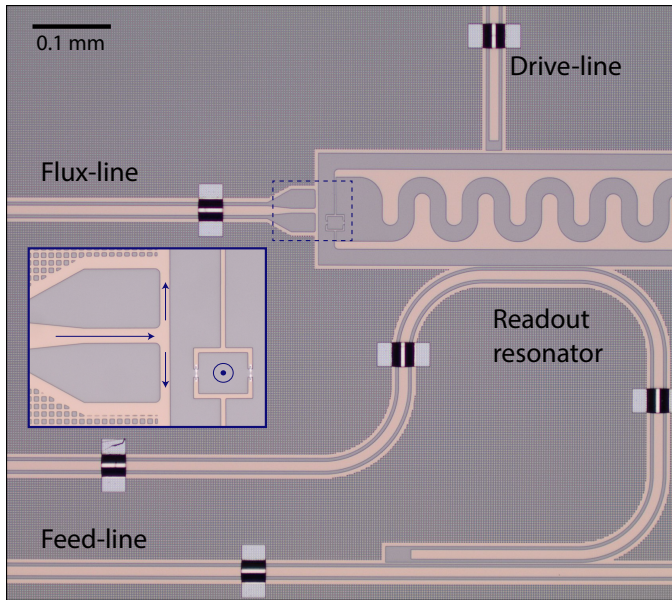


Figure 3.2: Optical microscope image of a superconducting transmon qubit and its control and readout circuitry. The transmon is measured via a dispersively coupled CPW resonator which is readout via a feed-line. A capacitively coupled drive-line is used to address its dipole moment, providing additional microwave (transversal) control. Flux-lines are realised using CPWs that are shorted to ground next to the SQUID (see inset), such that an applied DC current results in an out-of-plane flux through the loop changing its Josephson energy amplitude. Their geometry is also optimised for carrying microwave signals, e.g. for frequency modulation of the qubit.

CPW resonators offer many advantages, compared to lumped element realisations, due to their geometry which enhances the connectivity of distant circuit elements without compromising the simplicity in design and ease of fabrication. Following a stream of advances in nano-fabrication over the past decade, CPW resonators with very high-quality factors can be produced [93, 94], enabling the storage of fragile quantum states for more than a million oscillation cycles before decaying to the ground state. They can be easily coupled to transmon qubits (typically capacitively) realising an interesting platform for studying atom-light interaction at the quantum level. This field, called circuit quantum electrodynamics (QED) [41], is the solid-state analog of cavity QED using microwave photons instead of lasers and optical cavities. Transmon qubits, playing the role of artificial atoms, can be engineered to have very large dipole moments compared to those found in nature, e.g. Rydberg atoms, which, in combination with the strong nonlinearities provided by the Josephson junctions, lead to very strong coupling strengths. This is advantageous both from an engineering perspective, as quantum operations become faster, as well as for fundamental studies of light-matter interaction [95]. Transmission line resonators can also be used as “quantum buses” connecting distant qubits on the same chip and enabling high-fidelity two-qubit gates [96]. Another application of CPW resonators in circuit QED, as we will see below, is in performing

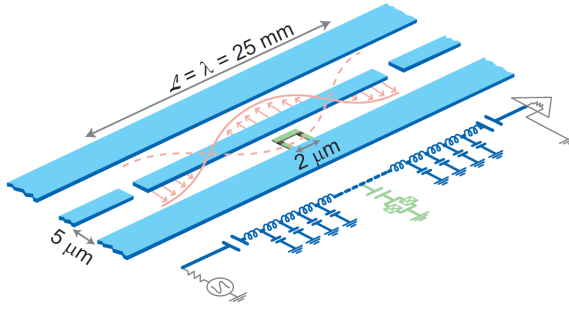


Figure 3.3: Minimal circuit QED setup consisting of a CPW resonator coupled to a transmon qubit via dipole-dipole interaction, that is maximised at the voltage antinodes of the transmission line. Figure adapted from Ref. [41]

qubit readout.

Dispersive readout

Determining the frequency of a mode can be done spectroscopically, by measuring the reflection of microwave signals impinging on the circuit, e.g. via an on-chip transmission line coupled capacitively to one of the superconducting islands (see drive-line in Fig. 3.2). A resonant microwave tone through the drive-line addresses its electric dipole moment, realising a transversal gate that leads to cyclic rotations from the ground to the first excited state. By sweeping the frequency of this tone and reading out the reflection of the signal with a spectrum analyser, the characteristic resonance and phase shift at the corresponding normal-mode frequency is observed in the steady state. Despite the simplicity of this direct readout method, it is not suited for more sophisticated schemes such as quantum-nondemolition (QND) measurements [97].

An alternative and more commonly utilised method for qubit readout in superconducting circuits, which is indirect and suitable for QND measurements, relies on measuring the microwave response of a resonator that is coupled to the qubit off-resonantly [41, 98]. Typically, one of the superconducting transmon islands is coupled capacitively to the open end (voltage antinode) of the CPW resonator, where voltage fluctuations are stronger, as schematically depicted in Fig. 3.3. This results in a dipole-dipole interaction, described by the Jaynes-Cummings model $\hbar g(\hat{c}^\dagger \hat{a} + \hat{a}^\dagger \hat{c})$ [99], where $\hat{a}^{(\dagger)}$, $\hat{c}^{(\dagger)}$ describe the annihilation (creation) of photons and qubit excitations, respectively. When the qubit is sufficiently detuned from the resonator ($\Delta_{\text{qr}} = \omega_r - \omega_q \gg g$) the interaction is effectively described by the following “dispersive” Hamiltonian

$$H/\hbar = \omega_q \hat{c}^\dagger \hat{c} - \frac{E_C}{2\hbar} \hat{c}^\dagger \hat{c}^\dagger \hat{c} \hat{c} + \omega_r \hat{a}^\dagger \hat{a} + \chi \hat{c}^\dagger \hat{c} \hat{a}^\dagger \hat{a}. \quad (3.2)$$

The dispersive coupling strength χ is approximately given by [44]

$$\chi = \frac{g^2 \alpha}{\Delta_{\text{qr}}(\Delta_{\text{qr}} + \alpha)}, \quad (3.3)$$

where $\alpha \sim -E_C/\hbar$ is the transmon anharmonicity.

This coupling, also referred to as “longitudinal” or “cross-Kerr” coupling, is particularly interesting as it can result in entanglement between the qubit and the resonator without excitation exchange. The dispersive interaction results in a resonator frequency shift ($\omega_r + \chi$) when the qubit is excited, which can be used to measure the qubit via the resonator [98]. The main advantage of this readout scheme is the fact that it can also be used for quantum nondemolition (QND) measurement of the qubit state in time-domain experiments [100]. Alternatively, one can also use the qubit as a photon meter of the resonator state [101, 102]¹. The CPW resonator can be measured by coupling it to a feed-line (for example capacitively as shown in Fig. 3.2) and measuring the transmission (or reflection) of a continuous wave (CW) microwave signal. The qubit can be detected by probing at the resonator frequency while scanning with another tone around the qubit frequency until a resonator shift in phase or amplitude is observed. The main design considerations for optimising the readout signal in such measurements are discussed below.

Design considerations

From a design perspective we have control over the coupling of the qubit to the readout resonator, g , their detuning Δ_{qr} (therefore also χ), as well as the external decay rate of the resonator due to its coupling to the feed-line. We can therefore optimise the readout conditions by appropriately choosing these parameters.

One important factor to consider is the enhancement of the qubit relaxation rate due to the presence of the resonator, known as the Purcell effect, which is given by $\kappa(g/\Delta_{\text{qr}})^2$ [103]. With relaxation times of state-of-the-art transmons approaching hundreds of microseconds this factor needs to be taken into account when designing to ensure it does not limit the qubit lifetime. Another consideration has to do with the validity of the dispersive Hamiltonian at high photon numbers in the resonator. As pointed out in Ref. [104], when the critical photon number $n_{\text{crit}} = \Delta_{\text{qr}}^2/(2g)^2$ is exceeded, the dispersive approximation (Eq. (3.2)) to the Jaynes-Cummings Hamiltonian breaks down and higher-order nonlinear terms need to be considered. Additionally, when $g \gg \kappa$, one needs to take into account the critical photon number, $n_\kappa = \kappa\Delta_{\text{qr}}/\chi^2$, above which the resonator becomes nonlinear due to higher-order dispersive shift contributions.

The signal-to-noise ratio (SNR) is a useful quantity to optimise for time-domain readout and is determined by the ratio of the measurement rate to the decay rate. When the probe frequency is resonant with the resonator, it is given by [105]

$$\text{SNR} = \eta \frac{\kappa}{\gamma} \frac{\bar{n}\chi^2}{(\kappa/2)^2 + \chi^2}, \quad (3.4)$$

where γ , κ are the qubit and resonator decay rates, \bar{n} the measurement photon number and $\eta = \frac{\hbar\omega_r}{k_B T_N}$ the measurement efficiency (where T_N is the noise temperature of the amplifier). The SNR is therefore maximised at $\kappa = 2\chi$, which determines our choice of g for a given detuning and anharmonicity. A thorough investigation of the SNR and

¹Note that this is the equivalent of the pioneering schemes developed in cavity QED experiments, where monitoring the phase shift of a beam of atoms sent through the cavity enables a non-demolition measurement of the photonic state [30, 97].

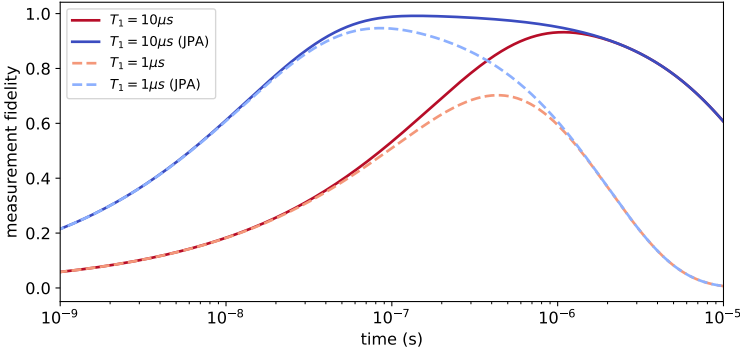


Figure 3.4: Theoretical modelling of the readout fidelity of a transmon as a function of time. The red and blue curves correspond to a measurement efficiency of 0.006 (assuming an amplifier noise temperature of 10 K) and 0.5 (assuming a quantum-limited parametric amplifier such as a JPA), respectively. The solid (dashed) curves are calculated assuming $T_1 = 10\mu\text{s}$ ($1\mu\text{s}$) for the qubit. Simulation parameters: $\omega_r = 7.5$ GHz, $\omega_q = 6.6$ GHz, $g = 40$ MHz, $\chi = 0.6$ MHz, $\kappa = 2\chi$, $\bar{n} = n_{\text{crit}}/2$.

measurement fidelity can be found in Ref. [105]. A simple model for the time evolution of the measurement fidelity is derived in Ref. [106] and is given by

$$F(t) = e^{-\frac{t}{2T_1}} \operatorname{erf} \left(\sqrt{\frac{t\text{SNR}}{2T_1}} \right), \quad (3.5)$$

where T_1 is the qubit lifetime, and $\operatorname{erf}(x) = \frac{2}{\sqrt{\pi}} \int_0^x dt e^{-t^2}$ is the error function. In Fig. 3.4 we plot $F(t)$ assuming an amplifier with a noise temperature of 10 K ($\eta = 0.006$) and an ideal quantum-limited Josephson parametric amplifier ($\eta = 0.5$), for two different qubit relaxation times.

Coupling to the feed-line

The coupling to the feed-line determines the external decay rate of the resonator κ_c . For capacitive coupling and measurement in transmission as in Fig. 3.2, the external quality factor can be determined from the transmission amplitude $|S_{21}|$, as [107]

$$Q_c = \frac{\omega}{\kappa_c} = \frac{\pi}{2|S_{21}|^2}. \quad (3.6)$$

The external quality factor Q_c is typically designed to be much smaller than the internal one ($Q_i \sim 10^5 - 10^6$) such that the total quality factor $Q = \frac{Q_c Q_i}{Q_c + Q_i} \simeq Q_c$ (around 10^4). Using the EM simulation software *Sonnet* [108] we calculate Q_c for different values of the resonator-feed-line coupler length, with a fixed gap between the central conductors. In Fig. 3.5 we plot Q_c as a function of coupler length for a resonator at 7.7 GHz and a gap of $12 \mu\text{m}$ ($2 \times 5 \mu\text{m}$ dielectric gap plus $2 \mu\text{m}$ of ground in between), assuming a $\lambda/2$ and a $\lambda/4$ resonator.

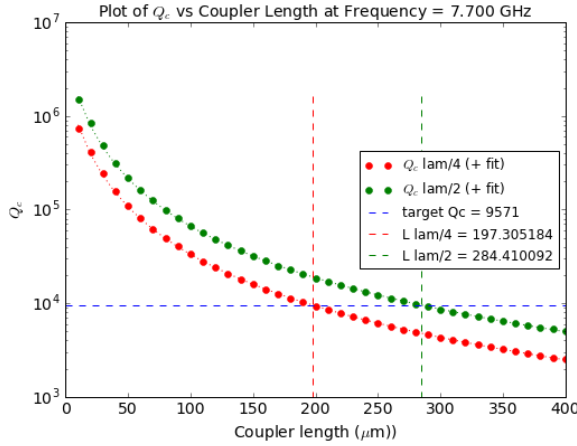


Figure 3.5: Calculated external quality factor for a $\lambda/4$ (red) and $\lambda/2$ (green) resonator ($\omega_r = 7.7$ GHz) as a function of the coupler length to the feed-line, using finite element simulations (*Sonnet*). The gap between the central conductors of the CPWs is fixed at $12 \mu\text{m}$.

Coupling to the qubit

Above we discussed the design process for the decay rate of the readout resonator. The capacitive coupling between the qubit and the resonator results in a dipole-dipole coupling strength determined by [44]

$$g = \frac{C_c}{C_*^2} \frac{1}{2\sqrt{Z_r Z_q}}, \quad (3.7)$$

where $Z_{q,r} = \sqrt{L_{q,r}/C_{q,r}}$ are the qubit and resonator impedances, C_c is the coupling capacitor, and $C_*^2 = C_c C_q + C_c C_r + C_q C_r$. The capacitance matrix of the coupled circuit is estimated via finite element electrostatic simulations using the *Ansoft Maxwell* software [109]. A design example is shown in Fig. 3.6. The software calculates the field distributions after imposing different charge excitations on each metallic island. This allows determining the capacitance matrix of the system introduced in section 2.1.3. The desired coupling capacitor C_c is determined for different gap sizes as well as coupler lengths between the central conductor of the CPW and the superconducting island of the transmon.

3.1.3. Qubit driving

Transversal control of the qubit (CW or pulsed) is performed using direct drive-lines that address the dipole moment of the transmon via capacitive coupling to one of the superconducting islands. Although the qubit can also be addressed via the readout resonators, using local drive-lines results in cleaner signal (in CW readout) and improved selectivity, i.e. less cross-talk, when multiple qubits are measured via the same feed-line. It comes at the cost of extra microwave lines on the chip, which inevitably becomes a

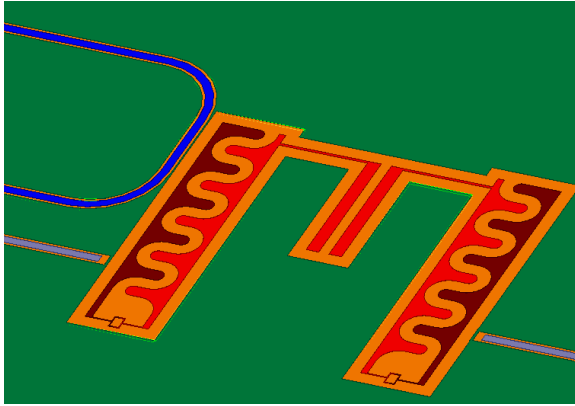


Figure 3.6: Capacitance network design (using 3D electrostatic field simulator *Maxwell*) of two capacitively coupled transmon qubits including dedicated readout resonators and drive-lines. The capacitance matrix is estimated by calculating the electric field distribution upon imposing different charge excitations on all transmon islands (light/dark red) and CPW centrepins (light/dark blue) relative to the ground plane (green).

problem with increasing number of qubits. 3D integration of superconducting circuits, however, promises to solve this issue [110, 111].

3.2. Coupling transmon qubits

In the previous section we covered the main aspects of readout and control of transmon qubits. Here, we will review the main tools that were used in this work for designing the couplings between qubits. We have already discuss this at a theoretical level in chapter 2, where we analysed the case of coupled oscillators and transmon qubits via capacitors and linear/nonlinear inductors. The focus in this section is more experimentally-oriented towards a practical implementation of two coupled qubits.

The simplest way to couple two transmons is via a commonly shared capacitance between their superconducting islands. A possible configuration, designed with *Maxwell*, is shown in Fig. 3.6. The desired capacitor can be obtained from the calculation of the capacitance matrix of the system (same procedure as described earlier for coupling to the qubit readout resonator). The design is optimised by iterating over the length and gap of the coupling capacitor and the results are typically accurate within a few fF (the level of accuracy depends a lot on choosing the right mesh). Designing the inductance of the Josephson junctions with similar finite element simulations is a seemingly worthless task due to fabrication-imposed limitations. The approach for designing these structures is currently limited to iterating between fabrication and measurement, as we will see in the next section.

An additional tool for determining the right coupling design is provided by circuit simulators. Although a theoretical description at the level of circuit quantisation is always more accurate, it can be a lengthy procedure requiring systematic analysis that can come at the cost of intuitive thinking and creativity. At the same time, as circuit complexity

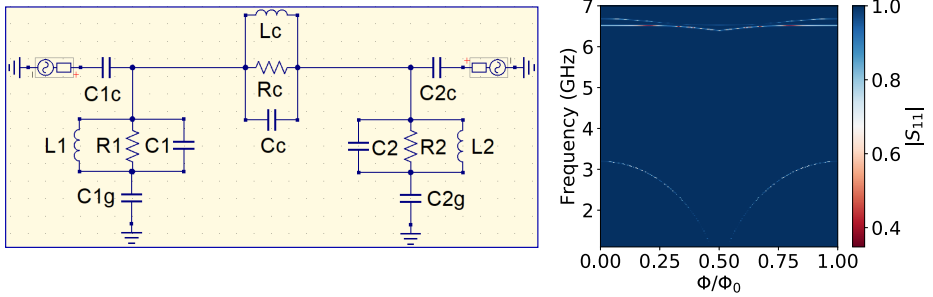


Figure 3.7: QUCS simulation of the system of two resonantly coupled LC oscillators (Fig. 2.3), with the addition of two capacitances to ground that introduce two additional nodes in the circuit. The microwave response of the system in reflection (S_{11}) is plotted versus $L_c \rightarrow L_{c,\min}/\cos(\pi\Phi/\Phi_0)$ as we vary Φ from 0 to Φ_0 . Note the appearance of a third mode, with maximum frequency around 3 GHz, as a result of adding the capacitances to ground C_{1g}, C_{2g} .

increases an analytical treatment can become extremely difficult. On the other hand, there exist software for modelling the microwave response and noise behaviour of classical circuits. One such example is *QUCS*, which is an open-source integrated circuit simulator including a graphical user interface [112]. An invaluable feature of this type of software is the ability to also test the microwave response of the designed circuit, close to the experimental conditions. For example, in Fig. 3.7 we explore a similar circuit to that of the coupled oscillators system studied in section 2.1.3, with the addition of resistors and microwave sources for readout. As in Fig. 2.3, we want to study the behaviour of the normal-mode frequencies as the coupling inductance is changed, however there are two main differences. Firstly, we use the linear analog of a SQUID inductance, i.e. we vary the flux Φ and the inductance changes as $L_c \rightarrow L_{c,\min}/\cos(\pi\Phi/\Phi_0)$ (using $L_{c,\min} = 28$ nH). Most importantly, however, the circuit features two more nodes at the point where the capacitances to ground C_{1g}, C_{2g} are connected. Interestingly this addition gives rise to a third mode ($f_{\max} \simeq 3$ GHz) in addition to the expected normal modes at 6-7 GHz. Despite lacking the option to add nonlinear inductors and the possibility of performing a quantum circuit analysis, such tools can be very useful in designing more complex circuits, for example, in predicting and anticipating unwanted modes. Recently an open-source Python library has been developed in our group, that allows the analysis of weakly nonlinear quantum circuits in terms of their normal modes while additionally treating dissipative elements [113].

3.3. Chip fabrication

In this section we will go through the basic fabrication steps that are required in order to realise the devices that were measured in this thesis.

3.3.1. Base layer: Defining the capacitance network

We will first discuss how the capacitive energy part of a circuit is physically realised. We use thin NbTiN superconducting films (maximum thickness of 200 nm) which are

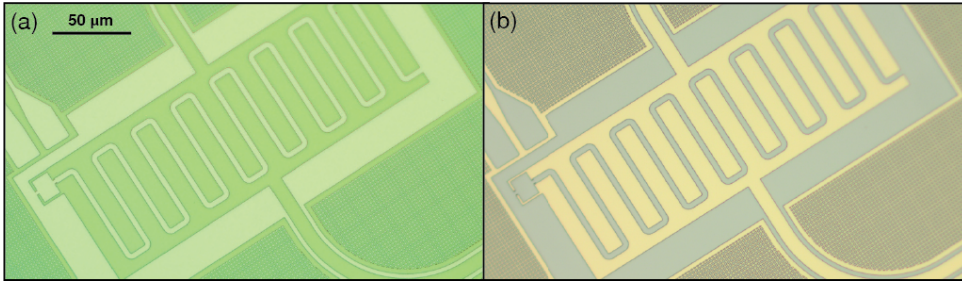


Figure 3.8: (a) Optical microscope image of a base layer pattern after exposure with the e-beam and development (ARP7700 resist on top of NbTiN). (b) Same picture taken after etching through the NbTiN (yellow) in the exposed parts (light blue corresponds to silicon) followed by cleaning of the leftover resist with PRS.

sputtered on top of a high-resistivity silicon substrate around $500\ \mu\text{m}$ thick. Intrinsic loss in these circuits are, to a large extent, due to two-level systems in the dielectric-metal interface. For this reason it is important to clean the surface of the substrate as much as possible before metal deposition, which is typically done by dipping it into hydrofluoric acid (HF) to remove the silicon oxides and hexamethyldisilazane (HMDS) treatment to render the surface hydrophobic just before sputtering [94, 114].

Defining the capacitance network of the device including CPW features, relies on etching away some parts of the superconducting film. We do this by spinning a resist layer and then writing using e-beam lithography where we want the metal to stay (for negative resists) or be removed (for positive resists). After baking and developing to remove the solvent (e.g. using MF321 for ARN7700 resist), we have created a mask on top of the metal (see Fig. 3.8). The uncovered NbTiN surface is etched away using Reactive Ion Etching with SF₆ and O₂ gas. The etch is carefully stopped as soon it arrives at the silicon surface by means of a laser endpoint detection, in order to avoid excessive substrate roughing and over-etching (which can make junction fabrication impossible) or under-etching. The remaining resist is then cleaned using hot PRS and we are left with the base layer of the device.

3.3.2. Josephson junctions

Josephson junctions, realising the nonlinear inductors of our qubits and couplers, consist of two superconducting layers separated by an insulator (SIS junctions). We fabricate them using the Dolan bridge technique [115], i.e. double-angle shadow evaporation of Aluminium (Al) with an oxidation step in between that forms the insulating layer of AlO_x. At first we spin a Polymethylglutarimide (PMGI) resist layer ($\sim 570\ \text{nm}$) followed by a Polymethylmethacrylate (PMMA) layer ($\sim 170\ \text{nm}$) and use e-beam lithography to define the pattern shown in Fig. 3.9(a), on top of the NbTiN pads base layer. Developing with MIBK:IPA 1:3 for 1 minute and MF321 for 12 seconds, results in two open pads separated by a bridge of resist. After that we clean the organic residues with oxygen plasma and remove any oxides with HF dip. This step is necessary in order to ensure a good contact at the Al to NbTiN interface. The evaporation consists of three main

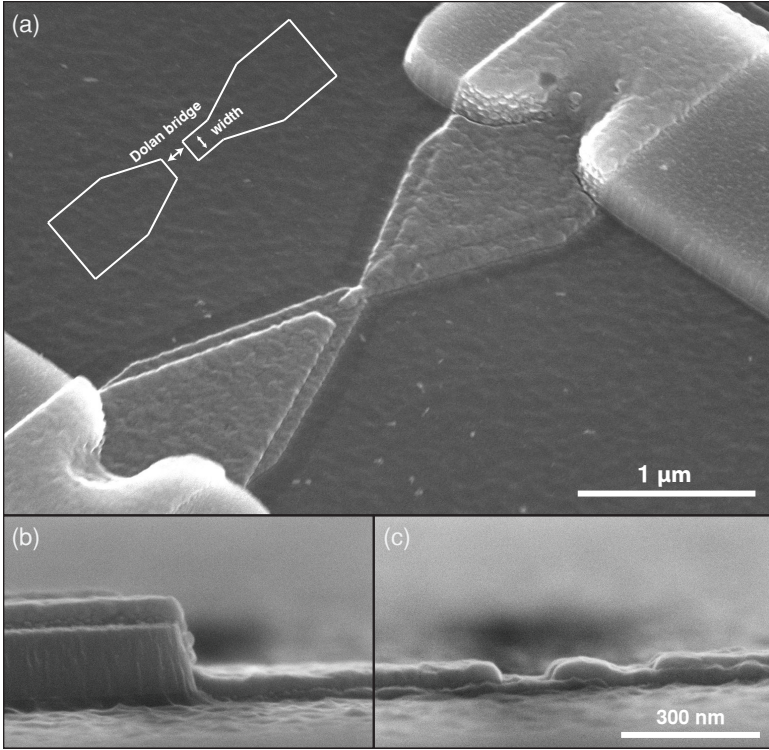


Figure 3.9: (a) Scanning electron microscope (SEM) image of an Al/AIO_x/Al Josephson junction fabricated on top of NbTiN pads on top of Si. The mask that is used is schematically depicted in the inset. (b), (c) Zoomed-in pictures taken from an angle almost parallel to the chip showing a more detailed view of the junction.

stages: evaporation of 30 nm of Al under an angle (here ~ 11 degrees), a controllable oxidation step (~ 1 mbar for 8 min.) to form a thin layer of AlO_x (time and pressure determine the thickness of the insulator) and a second evaporation of 50 nm of Al from the acute angle (169 degrees). The resulting junction after lifting-off the resist with Al on top (using NMP) is shown in Fig. 3.9.

The inductance of Josephson junctions, however, cannot be easily predicted and their fabrication comes with a lot of uncertainty due to their delicate nanometer-sized structure and the fact that small drifts in the machine settings over time can lead to big changes on the obtained junction inductances. Therefore, just before fabricating them in our devices, we prepare and measure several test junctions at room temperature with varying overlapping areas. We measure their normal state resistance at room temperature, R_N , from which we estimate the expected Josephson energy amplitude via the Ambegaokar-Baratoff formula [116]

$$E_J = \frac{h\Delta}{8e^2 R_N}, \quad (3.8)$$

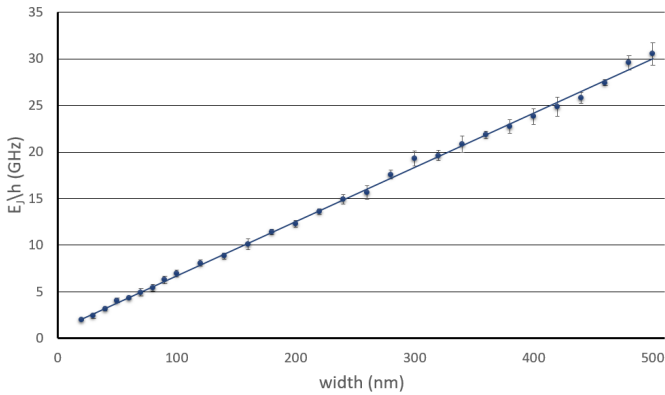


Figure 3.10: Josephson energy amplitude as a function of the width of the junction area extracted from room temperature measurements of the normal state resistance. Each data point is the average value of four identical junctions, fabricated on the same chip, with error bars indicating the standard deviation.

where Δ is the superconducting gap. We used the empirical formula $E_J/h \times R_N = 141 \text{ GHz/k}\Omega$, which is close to the expected value for Δ_{Al} . In Fig. 3.10, we plot E_J as a function of the width of the overlapping junction area after such a test evaporation. We sweep the width from 10 nm, below which the junctions are typically open (due to a combination of ebeam precision and Al grain size), up to 500 nm, above which we have more chances of shorted junctions (this is specific to the design we use and is typically due to the Dolan bridge failing after development). For each width value, four identically designed junctions on the same chip are measured and the calculated standard deviation is indicated by the error bars. Based on the linear fit results we design the junctions for the final experimental device.

3.3.3. Air-bridge crossovers

Last but not least, we fabricate air-bridges which are superconducting crossovers above CPWs, as shown in Fig. 3.11. When part of the ground plane is disconnected from the rest, e.g. due to an area being surrounded by CPWs, it can lead to the formation of slot modes that can couple to the qubit or resonator and could result in losses. Connecting all ground plane parts across the chip is therefore necessary to avoid this.

We follow a recipe similar to the ones used in Refs. [102, 117]. At first we spin a thick layer of PMGI and, following a baking step, we pattern with the e-beam two rectangular pads parallel to the CPW where we want to place the air-bridge, depicted with red colour in the inset of Fig. 3.11(a). After developing with a mixture of AZ400K and water, the resist on the pads is gone. We then bake for 5 minutes at 200-220°C, which results into a re-flow of the rectangular PMGI across the CPW into a more rounded structure. Finally, we spin and bake a bilayer of PMMA/MMA, and write a rectangular pattern (blue rectangle in the inset of Fig. 3.11(a)), which, after development with MIBK:IPA, opens a window across the CPW on top of the re-flown PMGI structure.

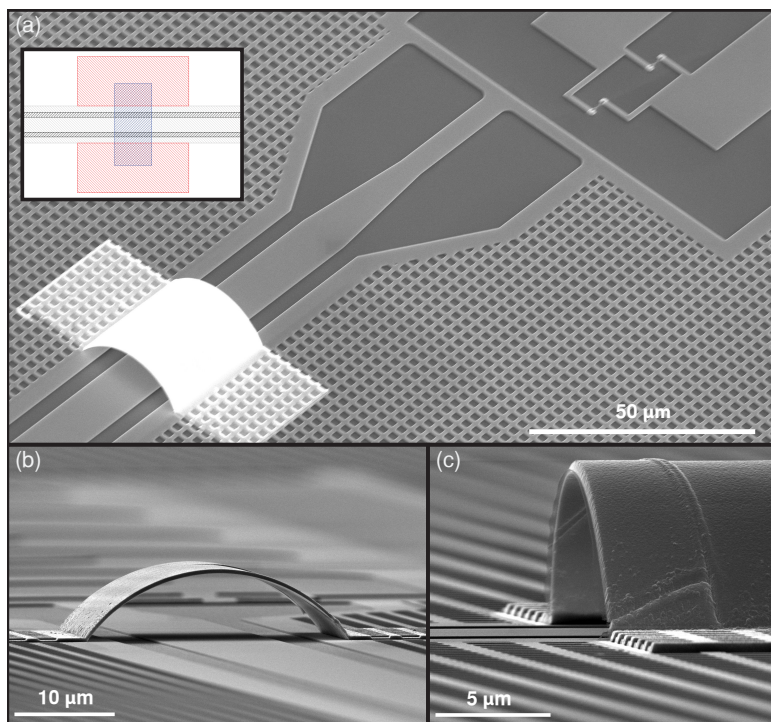


Figure 3.11: SEM images of Al air-bridges on top of CPW. The inset in (a) depicts the two masks that are used for e-beam patterning: red for PMGI and blue for PMMA (see text for details). (b), (c) Zoomed-in and angled SEM images showing more details of the crossover structures.

Finally, we remove organic residues and oxides using oxygen plasma cleaning and HF, and subsequently evaporate 400-500 nm of Al. The resulting structures are shown in Figs. 3.11(a)-(c).

3.3.4. Integration with printed circuit board

After the chip fabrication, we integrate the chips into a printed circuit board (PCB) that is used to connect the input/output lines to the cabling of the measurement setup. This is achieved with Rosenberg SMP connectors which are soldered into the PCB using silver paste and applying local heating with a heat gun. The “octobox” design is used, shown in Fig. 3.12 and described in Ref. [105]. Its Copper-made surface is first scratched using fiberglass scratch brush to remove surface oxides and facilitate wirebonding, and then cleaned with Acetone and IPA. The chip is placed in the centre of the PCB after applying vacuum grease and baking at 50°C to ensure uniformity. We connect the CPW features as well as the ground planes of the PCB to the chip using Al wirebonds, visible in the inset of Fig. 3.12.

The PCB can then be mounted directly to the mixing chamber of a dilution fridge, however, typically an additional sample holder with appropriate shielding is used, for

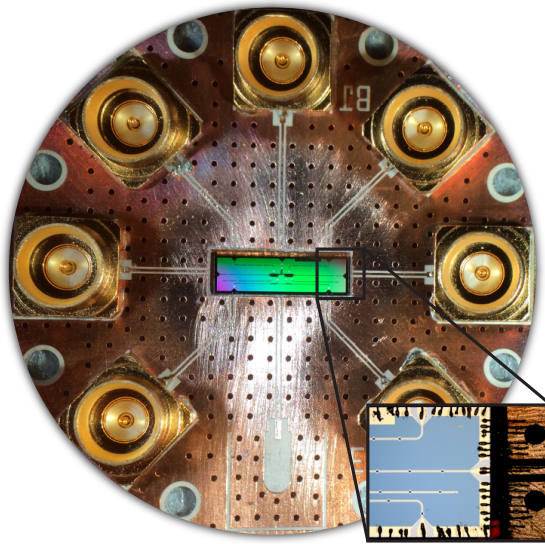


Figure 3.12: Chip mounted on the centre of a printed circuit board. The PCB lines are connected to the CPW launchers on the chip using Al wirebonds, which are also used to connect the ground planes together (see inset).

example as described in chapter 4. Shielding against magnetic fields (mainly produced by components inside the fridge) is important for eliminating flux noise effects on the qubits as well as the SQUID-based couplers. Additionally, radiation shielding is used for increasing the qubit performance. Typically, a Copper lid is screwed on top of the PCB in order to shape the electromagnetic environment of the device and ensure that any unwanted modes cannot couple to the circuit. The measurement setup including cabling and filtering for each experiment will be discussed in the corresponding chapter.

4

Engineering tuneable qubit-qubit couplings

A map of the world that does not include Utopia is not worth even glancing at, for it leaves out the one country at which Humanity is always landing. And when Humanity lands there, it looks out, and, seeing a better country, sets sail. Progress is the realisation of Utopias.

Oscar Wilde, "The Soul of Man under Socialism"

In this chapter, we present a superconducting circuit building block of two highly coherent transmons featuring in situ tuneable photon hopping (transverse) and cross-Kerr (longitudinal) couplings. The interactions are mediated via a nonlinear coupler, consisting of a large capacitor in parallel with a tuneable superconducting quantum interference device (SQUID). We demonstrate the working principle by experimentally characterising the system in the single- and two-excitation manifolds, and derive a full theoretical model that accurately describes the measurements. Both qubits have high coherence properties, with typical relaxation times in the range of 15 to 40 microseconds at all bias points of the coupler. This device could be used as a scalable building block in analog quantum simulators of extended Bose-Hubbard and Heisenberg XXZ models, and may also have applications in quantum computing such as realising fast two-qubit gates and perfect state transfer protocols.

This chapter has been published with minor differences in *npj Quantum Information* **4**, 38 (2018).

4.1. Introduction

Analog quantum simulations, where engineered systems emulate the behaviour of other, less accessible quantum systems in a controllable and measurable way [53], show significant promise for improving our understanding of complex quantum phenomena without the need for a full fault-tolerant quantum computer [118–121]. In this paradigm, the versatility of the simulator is determined by the range of interaction types and complexity accessible to the emulating quantum system. Promising avenues for pushing beyond what can be simulated with a classical machine include the study of highly interacting many-body systems [54, 122–125]. Superconducting circuit quantum electrodynamics (QED) is a very attractive platform for analog quantum simulation because of site-specific control and readout, and because of the flexible and engineerable system designs, which have led to the study of many interesting effects [57, 58, 102, 126–134]. Adding new components to the circuit QED design toolbox such as novel types of interactions can dramatically increase the range of phenomena that can be simulated [59–61]. For example, for exploring exotic effects, like quantum phase transitions in systems of strongly correlated particles, it is important to be able to access and rapidly tune between different many-body interaction regimes.

In situ tuneable couplers have been successfully realised in a variety of circuit QED architectures [135–144], in particular using the more coherent transmon design [44, 145–147]. In recent experiments, transmon arrays with tuneable exchange-type hopping interactions, have been employed to study many-body localisation phenomena of Bose-Hubbard and spin-1/2 XY models [57, 58]. However, moving beyond linear couplings to incorporate additional nonlinear interactions would enable the emulation of far more complex Hamiltonians. For example, nonlocal cross-Kerr interactions, present in extended Bose-Hubbard models [148, 149], introduce much richer many-body phase diagrams, leading to intriguing phenomena such as crystalline and supersolid phases of light as the ratio of the hopping and cross-Kerr coupling strengths is varied [59, 60]. In the qubit context, nonlinear cross-Kerr coupling, sometimes referred to as longitudinal coupling, is essential for engineering plaquette interactions in lattice gauge theories [61] and gives access to a large class of quantum-dimer and XYZ spin-model Hamiltonians.

Here, we demonstrate tuneable hopping and cross-Kerr interactions in a highly coherent two-transmon unit cell. Specifically, using a large capacitor in parallel with a tuneable nonlinear inductor as a coupling element, we are able to tune the ratio of the two coupling strengths, even suppressing hopping completely while maintaining a nonzero cross-Kerr coupling, giving access to different interaction regimes. We comprehensively characterise the energy landscape of this building block using different spectroscopic techniques. We show excellent agreement with a full theoretical model we have developed to describe the underlying circuit Hamiltonian including higher transmon excitation manifolds. Finally, we have thoroughly studied the qubit coherence as a function of the coupler bias, showing high relaxation times of 15–40 μs , and dephasing times reaching up to 40 μs at flux-insensitive operating points. Our work outlines a new recipe for building scalable analog quantum simulators of complex Hamiltonians using coupled transmon arrays, and our theoretical model provides an invaluable tool for designing and realising larger scale implementations.

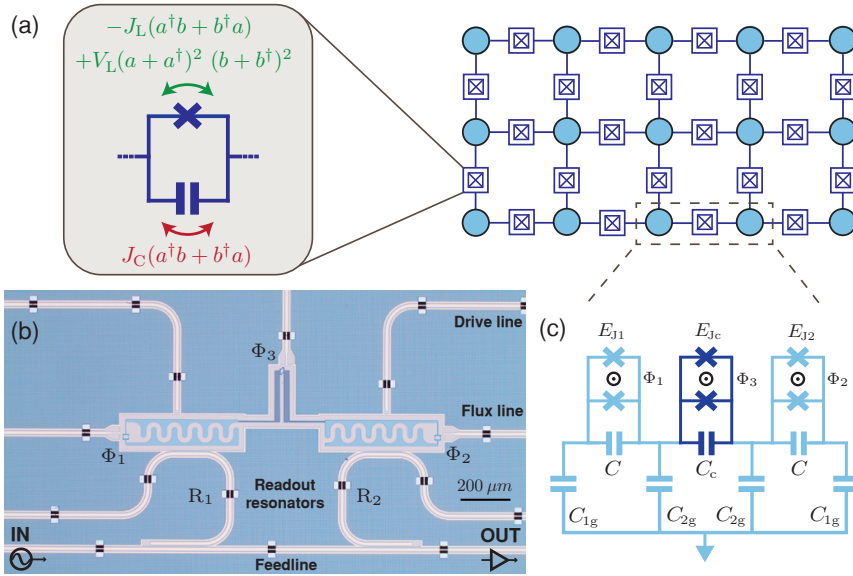


Figure 4.1: **Working principle and experimental device.** (a) A nonlinear coupler introducing hopping and cross-Kerr interactions between transmons (circles) on a circuit QED lattice. Photon hopping, mediated by the capacitor and the inductor (Josephson junction), can be coherently suppressed at the filtering condition ($J_L = J_C$), in analogy with the working principle of an LC filter. Tuning the nonlinear inductance can enable interesting regimes where cross-Kerr and photon-pair tunnelling dynamics are equivalent or even dominant over photon hopping processes. (b) Optical micrograph of the experimental device with added false-colour on the transmon-coupler superconducting islands. Qubit readout and microwave control is performed via dedicated resonators $R_{1,2}$ that are coupled to a common feed-line. Dedicated drive lines provide additional microwave control to each transmon. On-chip flux bias lines are used to tune the qubit frequencies and their mutual coupling. The scale bar corresponds to $200 \mu\text{m}$. (c) Circuit diagram of the implemented building block. The coupler (dark blue) is realised using a capacitor C_c in parallel with a tuneable nonlinear inductor (SQUID) that is galvanically connected with the two transmon qubits (light blue).

4.2. Main results

4.2.1. Implementing nonlinear couplings

The working principle of the coupler is similar to that of a band-stop LC filter, relying on the fact that its impedance $Z(\omega) = \frac{-i\omega}{C(\omega^2 - \omega_{LC}^2)}$ is infinite on resonance, as currents through the capacitor and the inductor interfere destructively. We implement a nonlinear analog of this circuit by using a nonlinear superconducting quantum interference device (SQUID) as the inductor, realising tuneable cross-Kerr and nearest-neighbour hopping interactions (Fig. 4.1(a)). The Josephson nonlinearity of the SQUID gives rise to tuneable higher-order nonlocal terms [148], including cross-Kerr interactions, which are equivalent to longitudinal $\hat{\sigma}_z \hat{\sigma}_z$ coupling in the qubit subspace. By contrast, the linear single-excitation hopping between the two sites is mediated by both the capacitor C_c at a constant rate J_C , and by the inductor at a tuneable rate $-J_L$. Because of interference between these two processes, the hopping strength tunes in a different way from the cross-Kerr coupling, making different many-body interaction regimes accessible. In

particular, at the point where the hopping rates cancel ($J_C = J_L$), we can access a purely nonlinear regime with zero linear interaction.

The nonlinear coupler is implemented in a circuit QED device of two superconducting transmon qubits, the basic building block required for future lattice implementations (Fig. 4.1(a)). The optical micrograph along with a circuit diagram of the device are shown in Figs. 4.1(b) and (c), respectively. Each transmon, consisting of two superconducting islands connected by an interdigitated capacitor C and a tuneable SQUID inductance, resonates at a plasma frequency $\omega \simeq (\sqrt{8E_J E_C} - E_C)/\hbar$, with Josephson energy E_J and charging energy $E_C = \frac{e^2}{2\tilde{C}}$, where \tilde{C} is the effective transmon capacitance (derived in section 4.5). Transmon frequencies can be independently tuned using on-chip flux lines ($\Phi_{1,2}$), and spectroscopy is performed through dispersively coupled readout resonators ($R_{1,2}$) measured via a common microwave feed-line (see Fig. 4.11 for the full measurement setup and Fig. 4.12 for qubit spectroscopy vs $\Phi_{1,2}$). Microwave drives are applied via either the resonators or dedicated drive-lines. The coupler capacitance C_C and flux-tuneable SQUID (Φ_3) connect galvanically to the two transmons.

The physics of the two-transmon building block is, to a good approximation, well described by an extended Bose-Hubbard model, which is a Heisenberg XXZ spin model in the qubit regime. To achieve this, we need to operate the qubits detuned from coupler resonances, so that coupler excitations do not participate directly in the system dynamics. Under this condition, the system can be described by a simplified two-transmon Hamiltonian:

$$\begin{aligned} \hat{\mathcal{H}}/\hbar = & \omega_1 \hat{a}^\dagger \hat{a} - U \hat{a}^\dagger \hat{a}^\dagger \hat{a} \hat{a} \\ & + \omega_2 \hat{b}^\dagger \hat{b} - U \hat{b}^\dagger \hat{b}^\dagger \hat{b} \hat{b} \\ & + J(\hat{a}^\dagger \hat{b} + \hat{b}^\dagger \hat{a}) \\ & + V \hat{a}^\dagger \hat{a} \hat{b}^\dagger \hat{b}, \end{aligned} \quad (4.1)$$

where $\hat{a}^{(\dagger)}$, $\hat{b}^{(\dagger)}$ are bosonic annihilation (creation) operators for each transmon in the uncoupled basis, with on-site nonlinearity $U = \frac{E_C}{2\hbar}$. The interaction between the two sites can be described by hopping of single excitations at a rate

$$J = J_C - J_L = \frac{\sqrt{8E_J E_C}}{2\hbar} \left(\frac{C_C}{4C_{\text{eff}}} - \frac{E_J^c}{4E_J} \right), \quad (4.2)$$

and a cross-Kerr coupling strength

$$V = -\frac{E_J^c E_C}{8\hbar E_J}. \quad (4.3)$$

The capacitive coupling J_C is fixed and determined by the ratio of the coupling capacitor C_C to an effective capacitance C_{eff} , which depends on the circuit network (see Eq. (4.32)). The interaction strengths J_L and V are determined by tuning the Josephson energy of the coupling SQUID, $E_J^c = E_J^{c(\text{max})} \cos(\pi\Phi_3/\Phi_0)$.

Importantly, the cross-Kerr coupling V is different from the diagonal coupling that can be observed in linearly coupled transmon architectures, where the self-Kerr nonlinearity of each transmon leads to an effective cross-Kerr coupling between the normal

modes of the system. Such effective diagonal coupling scales with the hopping interaction strength and vanishes at $J = 0$ [150], making it impossible to tune the ratio J/V independently. In our design, however, the cross-Kerr interaction results directly from the nonlinearity of the coupling junction and tunes to zero at a different coupler bias from the linear hopping interaction, giving access to different interaction regimes. As Φ_3 is tuned towards the filtering condition ($J_L \sim J_C$), the linear hopping term is suppressed more rapidly than the nonlinear cross-Kerr coupling, allowing access to the $J \ll V$ regime. By contrast, when $\Phi_3 \sim 0.5 \Phi_0$, the cross-Kerr coupling is suppressed ($V = J_L = 0$) and the dynamics are dominated by single-photon hopping at a rate J_C .

In the full treatment of the quantum circuit, the nonlinear inductance also gives rise to correlated hopping and two-photon tunnelling correction terms, which play a role in the higher-excitation manifold. These terms may also lead to interesting physical phenomena, which we return to in the discussion section. We derive the full quantum model in section 4.5, along with a classical normal mode analysis providing supporting intuition for the full system behaviour.

4.2.2. Tuneable single-photon hopping

We demonstrate our ability to tune the linear single-photon hopping interaction between the two transmons, by measuring qubit-qubit avoided crossings, in Fig. 4.2. The top panels show example crossings, as qubit 1 is tuned on resonance with the other at ~ 6.6 GHz, in three different coupling scenarios, $J_L > J_C$ in Fig. 4.2(a), $J = 0$ ($J_L = J_C$) in Fig. 4.2(b), and the J_C -dominated regime in Fig. 4.2(c). The measurements in Figs. 4.2(a), (c) are performed via readout resonator R_2 , while in the zero coupling case (Fig. 4.2(b)) we measure via R_1 . The range of typical coupling strengths that can be achieved with this device is illustrated in Fig. 4.2(d), where we plot $|J|/2\pi$ vs calibrated coupler bias Φ_3 . We note that we have measured larger coupling strengths, up to 140 MHz, when operating at different qubit frequencies ~ 5.4 GHz (see Fig. 4.9). The linear coupling is suppressed when the qubit frequencies are equal to the filter frequency $1/\sqrt{L_C C_C}$, which here takes place around $\Phi_3 \sim 0.3 \Phi_0$. Note that a higher transition of a lower-frequency *sloshing* mode of the circuit, crossing with the qubits around this point, limits the observed on-off ratio in this device to ~ 10 (see Fig. 4.9). This low-frequency mode, hybridising with the qubits, is associated with currents flowing only through the coupling inductor, and could be avoided with slightly different design parameters (see Fig. 4.10). Additional avoided crossing measurements in the regime where the linear coupling gets suppressed and reverses sign are plotted in Fig. 4.14, with spectroscopy on both qubits.

For a more complete characterisation of the tuneable hopping interaction, we fit the experimentally measured coupled-qubit spectrum with our theoretical model of the quantum circuit. More specifically, in Fig. 4.2(e), we fix the qubits on resonance and plot the normal-mode splitting between the dressed states $|+\rangle = \frac{|01\rangle + |10\rangle}{\sqrt{2}}$ and $|-\rangle = \frac{|01\rangle - |10\rangle}{\sqrt{2}}$, as we tune the calibrated coupler flux bias. The blue and red curves are theory fits of the single-excitation manifold to the quantum circuit Hamiltonian (Eq. (4.17)), showing excellent agreement with the experimentally obtained spectrum. The parameters obtained from this fit, which neglects higher-order couplings of each transmon to the low-frequency sloshing mode, are listed in Table 4.1. Note that the antisymmetric mode

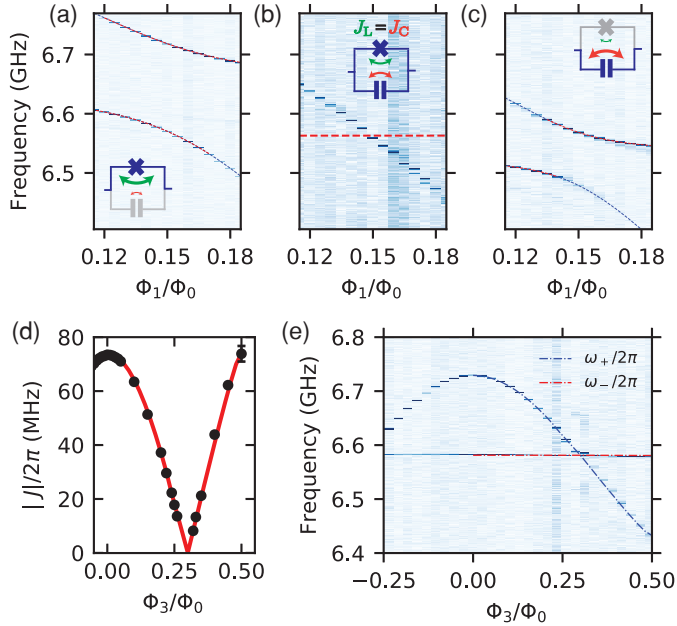


Figure 4.2: **Tuneable linear coupling and single-photon hopping suppression.** Top: Avoided crossings for (a) inductive, (b) zero and (c) capacitive coupling regimes. In all three cases, the frequency of qubit 2 is set around 6.6 GHz ($\Phi_2 = 0$), while we tune qubit 1 through resonance. Qubit spectroscopy is performed via readout resonator R_2 in (a) and (c), and via R_1 in (b). The coupling elements that participate more strongly to the qubit-qubit interaction are indicated in the insets. (d) Linear coupling strength $|J|$ obtained from a series of fitted avoided crossings, at different values of calibrated coupler flux bias Φ_3 . (e) Eigenspectrum of the coupled qubit system on resonance vs Φ_3 , fitted with a simplified circuit theory model (the fitting parameters are listed in Table 4.1). The normal-mode splitting gets suppressed at the crossover between inductively and capacitively dominated coupler regimes ($\Phi_3/\Phi_0 \simeq 0.3$). Cross-talk effects between the different flux channels have been calibrated out experimentally.

frequency $\omega_-/2\pi$ is unaffected by coupler tuning, which reflects the fact that this mode is only associated with charge oscillations across the qubit junctions (see Fig. 4.8).

4.2.3. Tuneable nonlinear cross-Kerr coupling

As already discussed, a key feature of our implementation which differentiates it from previous tuneable couplers, is the nonlinear cross-Kerr interaction which can be tuned into different coupling regimes relative to the hopping strength and does not zero when J does. This cross-Kerr coupling, which in different contexts is referred to as $\sigma_z\sigma_z$, longitudinal [151], or dispersive [41], does not involve excitation hopping processes. Its presence, however, does influence the dynamics as the occupation at one site can alter the energy level spectrum of a neighbouring site, in a process analogous to photon scattering [59].

In a coupled two-qubit system, the effect of cross-Kerr interaction can be seen as a shift of the energy level of the $|11\rangle$ state and can be determined spectroscopically

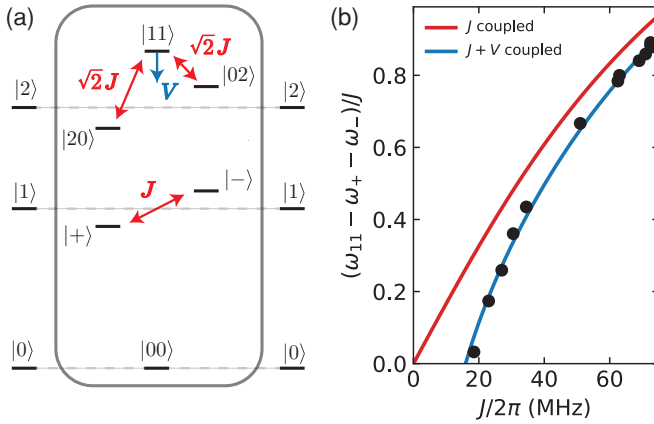


Figure 4.3: **Observation of nonlinear cross-Kerr coupling in spectroscopy.** (a) Level schematic of two coupled transmons up to the two-excitation manifold. At the single-photon level, the linear coupling J results in an avoided crossing between the dressed states $|+\rangle = \frac{|01\rangle + |10\rangle}{\sqrt{2}}$ and $|-\rangle = \frac{|01\rangle - |10\rangle}{\sqrt{2}}$. As J becomes comparable to the transmon anharmonicity, the $|02\rangle$, $|20\rangle$ and $|11\rangle$ levels mix with each other, resulting in an effective repulsion of $|11\rangle$. On the other hand, a qubit-qubit interaction with negative cross-Kerr coupling results in lowering the energy of $|11\rangle$. (b) Combined two-tone spectroscopy data (black dots) showing $\frac{\omega_{11} - \omega_- - \omega_+}{J}$ vs J . The red curve is theory prediction assuming only hopping interaction between two transmons ($V = 0$), while the blue one shows simulation results obtained by taking into account also the higher-order nonlinear contributions, $\frac{V}{4}(a + a^\dagger)^2(b + b^\dagger)^2$, which include the dominant cross-Kerr term. The parameters used are listed in Table 4.1.

from the transition energies relative to the ground state $\omega_{11} - \omega_- - \omega_+$. For weakly anharmonic systems, such as the transmon, this picture becomes more complicated in the presence of linear hopping (Fig. 4.3(a)). A three-state analysis at the two-excitation manifold reveals that $|11\rangle$, $|02\rangle$ and $|20\rangle$ also couple to each other, resulting in an effective upwards repulsion of the $|11\rangle$ state [152], which scales as $\sim J^2/E_C$ [150]. Because the direction of this effect competes with the negative cross-Kerr shift, when the effects are similar in size, it can hinder the observation of cross-Kerr coupling in an individual spectroscopy measurement. To separate the two effects, it is therefore necessary to measure the shift for different coupling levels.

We experimentally demonstrate the presence of cross-Kerr interaction between the two transmons, by measuring transitions in the two-excitation manifold of the coupled system. More specifically, we extract the frequency shift of $|11\rangle$ at different couplings from a series of two-tone spectroscopy measurements (see Fig. 4.13), focusing on the inductively dominated regime $0 \leq \Phi_3/\Phi_0 \leq 0.25$. In order to distinguish between the negative cross-Kerr shift and the positive shift from linear coupling J , we plot $\frac{\omega_{11} - \omega_- - \omega_+}{J}$ as a function of J , in Fig. 4.3(b). The red curve is theoretical prediction assuming only hopping interaction ($V = 0$) between the two transmons. The blue curve shows numerical results after diagonalising the transmon-transmon Hamiltonian with the full nonlinear coupling terms $\frac{V}{4}(a + a^\dagger)^2(b + b^\dagger)^2$, which includes the dominant cross-Kerr interaction. We use the parameters listed in the second column of Table 4.1, which differ slightly from the fitted parameters of Fig. 4.2(e) to accommodate the effects of

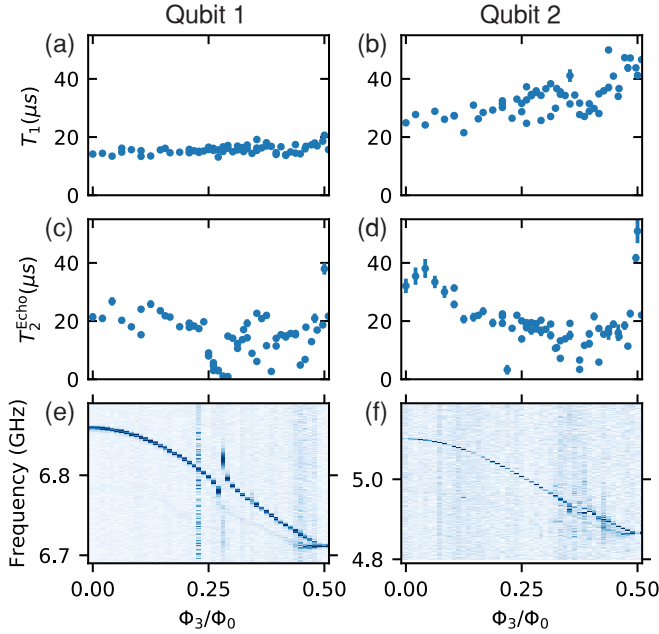


Figure 4.4: **Observation of high qubit coherence vs coupler flux bias.** (a), (b) T_1 measurements showing high energy-relaxation times ($15 - 40\mu s$) for the whole range of coupler bias, with the qubits detuned at their top and bottom sweetspots. (c), (d) Respective measurements of T_2^{Echo} decay times vs Φ_3/Φ_0 . High coherence is observed except for the points where a lower sloshing circuit mode crosses the qubits (see text for details). (e), (f) Respective spectroscopy of both qubits vs Φ_3/Φ_0 . As the inductance of the coupler is varied the qubit frequencies change as expected from theory. The 0-3 transition of the lower circuit sloshing mode crossing both qubits at $\Phi_3/\Phi_0 \sim 0.28$ and $\Phi_3/\Phi_0 \sim 0.38$ is also clearly seen.

extra higher-order terms (see later in Fig. 4.5). At $J = 0$ ($\Phi_3 \sim 0.3 \Phi_0$) the cross-Kerr coupling $|V|/2\pi$ is around 4 MHz, and it reaches a maximum of 10 MHz at $\Phi_3 = 0$. We were unable to explore the region $J/2\pi < 20$ MHz in this device, due to a higher transition of the lower frequency sloshing mode hybridising with the qubits (see Fig. 4.9).

4.2.4. Qubit coherence

Maintaining high coherence for all interaction strengths is an essential requirement for future implementations based on our building block device. In Fig. 4.4, we investigate the individual qubit properties as a function of the coupler bias, with the transmons far detuned from each other by ~ 1.8 GHz, at their flux insensitive top and bottom sweetspots ($\Phi_1 = 0$, $\Phi_2/\Phi_0 = 0.5$). In Figs. 4.4(a), (b), we demonstrate high relaxation times T_1 ($15 - 40 \mu s$) over the entire coupling range. We also report a systematic study of dephasing times in our device, obtained from spin-echo measurements (Figs. 4.4(c), (d)). T_2^{Echo} times are large overall, reaching up to $40 \mu s$, except for the points where the qubits hybridise with the lower frequency sloshing mode (at $\Phi_3/\Phi_0 \sim 0.28$ and $\Phi_3/\Phi_0 \sim 0.38$ as shown in Figs. 4.4(e), (f)). Note that the qubit frequency shifts of ~ 200 MHz in

Figs. 4.4(e), (f) are due to inherent changes to the Josephson energy of each transmon as E_J^c is varied, which we derive in section 4.5. Repeated long Ramsey measurements were performed at $\Phi_3 = 0$, showing a beating pattern consistent with charge dispersion in the transmon regime [44, 85]. A measurement analysis with fits to the double sinusoidal decay pattern reveals qubit dephasing times T_2^* of 10 – 30 μs for qubit 1 and 25 – 40 μs for qubit 2, around the flux insensitive points.

4.3. Discussion

Our work demonstrates a key building block for circuit QED devices capable of exploring a rich vein of many-body physics in extended Hubbard models. In the context of driven nonlinear arrays, a chemical potential term, $\mu = \omega_q - \omega_d$, could be straightforwardly implemented by coherently driving the transmons through the drive lines at a frequency ω_d , which would enable the study of rich many-body phase diagrams with all J , V , μ tuneable [59, 60]. It may also be possible to implement topological pumping of interacting photons, by modulating the frequency of each transmon, to study bosonic transport of Fock states in a nonlinear array configuration [153]. In realisations where higher-excitation manifolds might be explored, additional higher-order terms arising from the junction nonlinearity should be considered. For example, in our implementation, the nonlinearity of the medium leads to correlated hopping terms,

$$\frac{V}{6} \left(\hat{a}^\dagger (\hat{n}_a + \hat{n}_b) \hat{b} + \hat{b}^\dagger (\hat{n}_a + \hat{n}_b) \hat{a} \right), \quad (4.4)$$

such that a photon can hop between sites, on the condition that another photon is present. Additional contributions at higher excitation manifolds involve photon-pair tunnelling processes

$$\frac{V}{4} (\hat{a}^\dagger \hat{a}^\dagger \hat{b} \hat{b} + \hat{a} \hat{a} \hat{b}^\dagger \hat{b}^\dagger), \quad (4.5)$$

which might lead to exotic phenomena such as fractional Bloch oscillations [154]. These contributions are explicitly derived in the section 4.5, following a full quantum mechanical treatment of our circuit. In Fig. 4.5, we plot the coupled system eigenspectrum up to the two-excitation manifold, based on our full theoretical model including all next-to-leading order terms, which is found to be in excellent agreement with our data obtained at high powers.

Our circuit can also be used to study many-body effects in spin models. When the transmon anharmonicity is much larger than the coupling strength ($E_C \gg J$), a truncation to the qubit subspace is justified, and the transmon-transmon interaction is described by a Heisenberg XXZ Hamiltonian

$$2J(\hat{\sigma}_x \hat{\sigma}_x + \hat{\sigma}_y \hat{\sigma}_y) + V \hat{\sigma}_z \hat{\sigma}_z. \quad (4.6)$$

The coupling strengths available in this device are $J/2\pi \sim 8 - 140$ MHz, $V/2\pi \sim 0 - 10$ MHz, with orders of magnitude lower qubit decay rates (3 – 15 kHz). In a slightly different design, with a larger coupling capacitor C_c , it would also be possible to further explore the $J \ll V$ regime (see Fig. 4.10). One could then simulate an Ising

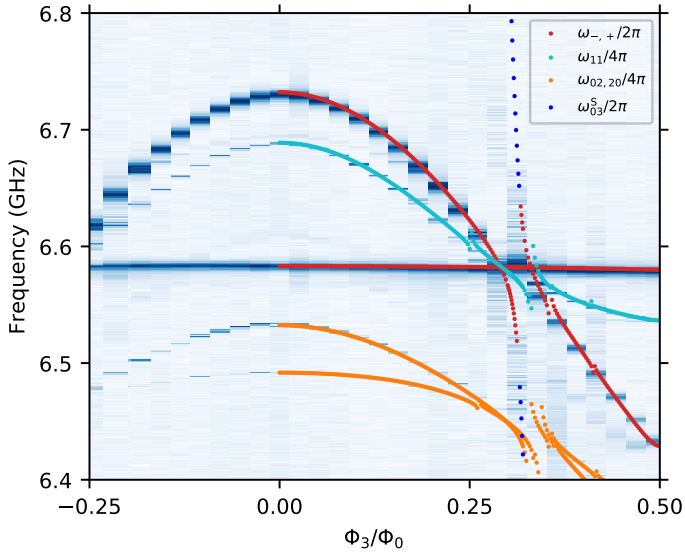


Figure 4.5: **Full theoretical model of the higher excitation manifold of the device.** Measurement of the coupled system eigenspectrum (as Fig. 4.2(e)) at higher powers. Dots show theoretical calculations using the full quantum circuit Hamiltonian including all next-to-leading order transmon-transmon coupling terms and the sloshing mode contributions, for the parameters listed in Table 4.1. Simulations are performed using a Hilbert space dimension of $N = 15^3$.

$\hat{\sigma}_z \hat{\sigma}_z$ interaction Hamiltonian ($J = 0$), with antiferromagnetic couplings of ~ 10 MHz. Additionally, time modulated magnetic fluxes threaded through the coupler SQUID can enable a large set of spin-spin interactions (e.g. pure $\hat{\sigma}_x \hat{\sigma}_x$ or $\hat{\sigma}_y \hat{\sigma}_y$) [155], therefore, giving access to emulating the dynamics of almost any spin model and exploring their phase diagrams. Connecting the coupler to four transmons on a lattice could enable simulating models with topological order such as the famous toric code [155]. Our circuit could also be employed to engineer plaquette terms in lattice gauge theories or ring-exchange interactions in dimer models, where a longitudinal coupling much larger than the hopping term is required in order to emulate effective fields on the lattice [61]. Moreover, a similar architecture, featuring $\hat{\sigma}_z \hat{\sigma}_z$ coupling between transmons has been proposed theoretically for the realisation of a microwave single-photon transistor [156].

In order to scale this circuit to larger lattice sizes, future experiments could take an approach where each transmon is connected to couplers via the same superconducting island, with the other island used for drive control and readout. Using a two-island transmon design has the advantages of reducing or eliminating the number of possible current loops involving current flow across qubit junctions, as well as allowing spurious flux cross-talk to be eliminated by linear compensation techniques (see Methods). Our coherence measurements (Fig. 4.4) suggest that this coupler design can be realised without significantly limiting qubit coherence times, showing promise for scaling up to larger lattice sizes.

In conclusion, the implemented circuit increases the range of available interactions and phenomena that can be explored with circuit QED analog quantum simulators. We

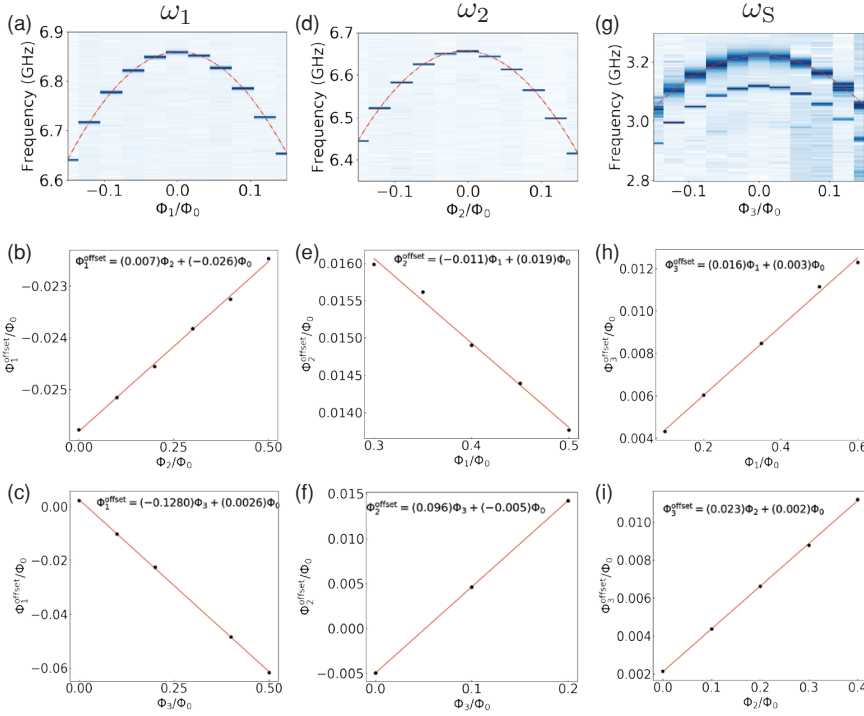


Figure 4.6: **Characterisation and calibration of on-chip flux cross-talk between all bias channels.** (a) Frequency dependence of qubit 1 vs uncalibrated flux channel 1, around its top sweetspot (for $\Phi_2/\Phi_0 = 0.5$, $\Phi_3 = 0$). The top sweetspot is centred at some offset value Φ_1^{offset} , which can vary depending on the applied flux on the other channels, in the presence of on-chip cross talk. (b) Dependence of Φ_1^{offset} on the applied flux in channel 2. Each dot is obtained from a full transmon Hamiltonian fit with Φ_1^{offset} as a parameter, for different Φ_2 values (Φ_3 is constant). A linear fit determines the dependence of Φ_1^{offset} on Φ_2 . (c) Dependence of Φ_1^{offset} on Φ_3 for constant Φ_2 . The same procedure is followed for determining Φ_2^{offset} vs (Φ_1, Φ_3) in (d)-(f) and Φ_3^{offset} vs (Φ_1, Φ_2) in (g)-(i). The extracted cross-talk coefficients are then used to make all flux channels orthogonal in the experiment.

have demonstrated hopping and cross-Kerr interactions with *in situ* tuneability between two transmon qubits in a flexible and scalable superconducting circuit. The observed decay rates are orders of magnitude lower than the coupling strengths, making this a viable platform for analog quantum simulation experiments. Moreover, our full theoretical model of the quantum circuit is in excellent agreement with the measurements, providing a powerful tool for designing future larger scale implementations.

4.4. Methods

4.4.1. Chip fabrication

The capacitive network of superconducting islands and ground plane, together with readout and control lines are defined on a thin NbTiN film [157] on top of a high resistivity Si substrate. The film is patterned using e-beam lithography on ARN7700

resist and etched with SF₆/O₂ plasma reactive-ion etching. Josephson junctions are then fabricated on each SQUID using Al-AIO_x-Al shadow evaporation following e-beam lithography patterning on a PMGI/PMMA lift-off mask and HF dip to remove surface oxides on the NbTiN contact pads. Finally, after an e-beam patterning and reflowing PMGI step, followed by a second e-beam patterning of a MAA/PMMA resist stack, we evaporate Al air-bridges which are used as cross-overs above all lines in order to ensure a uniform ground plane.

4.4.2. On-chip flux cross-talk calibration

Due to the compact geometry of our device, on-chip cross-talk between all flux channels is quite significant and extra care is required in order to decouple them. This requirement is vital for independent control, especially for larger scale implementations where such effects could become a major experimental challenge. We employ a systematic calibration procedure (see Fig. 4.6) which is enabled by the fact that the frequency of the lower circuit sloshing mode (3.2 GHz at flux insensitive point) is directly associated with tuning the coupling strength via Φ_3 . There is therefore one circuit degree of freedom corresponding to each bias channel. We track spectroscopically the frequency of each degree of freedom (e.g. qubit 1) around its flux insensitive point (top sweetspot) and determine the flux offset as we vary the other two channels (2 and 3). Repeating this for all three degrees of freedom and flux channels we were able to measure and calibrate all cross-talk effects, making all flux bias channels $\Phi_{1,2,3}$ orthogonal. Note that the calibration method employed here allows us to distinguish between the on-chip flux cross-talk effects from the intrinsic qubit frequency shifts that are expected by varying the coupling inductance. The latter are deliberately not calibrated out in order to be able to fit the measurement data in Fig. 4.2(e) and Fig. 4.5 with the full circuit theory Hamiltonian, however we could straightforwardly compensate for them if required.

4.4.3. Device parameters

Parameter	Fitting of the single-excitation manifold (Fig. 4.2(e))	Full nonlinear circuit model (Figs. 4.3(b) & 4.5)
E_J/h (GHz)	22.99	23.01
C (fF)	39	39
C_{1g} (fF)	60.5	61
C_{2g} (fF)	87	87
$E_J^{c(\max)}/h$ (GHz)	7.33	7.75
$E_J^{c(\min)}/h$ (GHz)	0.37	0.39
C_c (fF)	18	20

Table 4.1: Table of device parameters.

The device parameters are presented in Table 4.1. In the first column, we list the circuit parameters obtained by fitting the resonantly coupled transmon-transmon spectrum in the single-excitation manifold (Fig. 4.2(e)) with a simplified circuit model

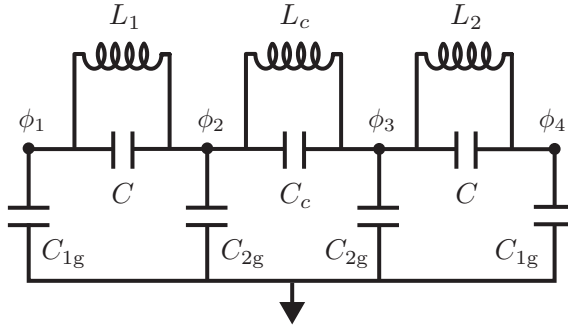


Figure 4.7: **Harmonic limit of the circuit diagram shown in Fig. 4.1, where each Josephson element is approximated by a linear inductor.**

that neglects any higher-order couplings to the sloshing mode. The parameters in the second column are used in our full numerical model that includes all next-to-leading order terms in the circuit Hamiltonian (Eq. (4.17)), to describe the obtained data at higher excitation manifolds (Fig. 4.5).

4.5. Derivation of full circuit Hamiltonian

Here, we analytically derive the full Hamiltonian that describes the two-transmon coupled system including all circuit degrees of freedom. We begin with a Lagrangian description of the circuit in the harmonic limit and proceed with the Hamiltonian formulation and canonical quantisation, following the methodology described in Ref. [72, 158].

4.5.1. Analytical description in the harmonic limit

An intuitive picture about the circuit and the relevant degrees of freedom can be drawn in the harmonic limit, where all Josephson elements are approximated by linear inductors, $L_i = \left(\frac{\phi_0}{2\pi}\right)^2 \frac{1}{E_J^i}$, as shown in Fig. 4.7. The charging and inductive energies of the linearised system are

$$\begin{aligned} \mathcal{E}_{\text{charge}} = & \frac{C}{2}(\dot{\phi}_2 - \dot{\phi}_1)^2 + \frac{C_c}{2}(\dot{\phi}_3 - \dot{\phi}_2)^2 + \frac{C}{2}(\dot{\phi}_4 - \dot{\phi}_3)^2 \\ & + \frac{C_{1g}}{2}(\dot{\phi}_1^2 + \dot{\phi}_4^2) + \frac{C_{2g}}{2}(\dot{\phi}_2^2 + \dot{\phi}_3^2), \end{aligned} \quad (4.7)$$

and

$$\mathcal{E}_{\text{ind}} = \frac{(\phi_1 - \phi_2)^2}{2L_1} + \frac{(\phi_3 - \phi_4)^2}{2L_2} + \frac{(\phi_2 - \phi_3)^2}{2L_c}, \quad (4.8)$$

where the node flux ϕ_i is related to the potential at node i as $\dot{\phi}_i = V_i$. The system Lagrangian, therefore, is

$$\mathcal{L} = \mathcal{E}_{\text{charge}} - \mathcal{E}_{\text{ind}} = \frac{1}{2}\dot{\phi}^T[\mathbf{C}]\dot{\phi} - \frac{1}{2}\phi^T[\mathbf{L}^{-1}]\phi, \quad (4.9)$$

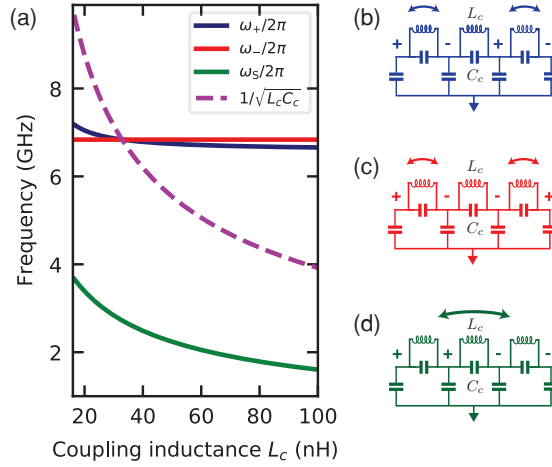


Figure 4.8: **Normal modes of the resonantly coupled transmon-transmon system in the harmonic limit.** (a) Normal-mode frequencies as a function of the coupling inductance. The normal-mode splitting (blue and red curves) is suppressed at the point where the filter frequency (dashed curve) is resonant with both transmons. The sloshing mode frequency (green curve) vanishes at the limit of no inductive coupling ($L_c \rightarrow \infty$). (b) - (d) Schematic representation of the circuit charge oscillations associated with each normal mode. Note that the symmetric mode is associated with charge oscillations across the transmon inductors only and therefore its frequency $\omega_-/2\pi$ is independent of the coupling inductance L_c as shown in (a).

where

$$[\mathbf{C}] = \begin{bmatrix} C + C_{1g} & -C & 0 & 0 \\ -C & C + C_{2g} + C_c & -C_c & 0 \\ 0 & -C_c & C + C_{2g} + C_c & -C \\ 0 & 0 & -C & C + C_{1g} \end{bmatrix}, \quad (4.10)$$

is the capacitance matrix, and

$$[\mathbf{L}^{-1}] = \begin{bmatrix} 1/L_1 & -1/L_1 & 0 & 0 \\ -1/L_1 & 1/L_1 + 1/L_c & -1/L_c & 0 \\ 0 & -1/L_c & 1/L_2 + 1/L_c & -1/L_2 \\ 0 & 0 & -1/L_2 & 1/L_2 \end{bmatrix}, \quad (4.11)$$

is the inverse of the inductance matrix of the circuit, expressed in the node flux basis $\phi^T \doteq [\phi_1, \phi_2, \phi_3, \phi_4]$.

Solving the characteristic/secular equation in the resonantly coupled case ($L_1 = L_2$)

$$[\mathbf{L}^{-1}] - \Omega^2[\mathbf{C}] = 0, \quad (4.12)$$

yields the following normal modes (up to normalisation factors)

$$\begin{aligned}
 \phi_1 - a \phi_2 - a \phi_3 + \phi_4, \\
 \phi_1 - b \phi_2 + b \phi_3 - \phi_4, \\
 \phi_1 + c \phi_2 - c \phi_3 - \phi_4, \\
 \phi_1 + d \phi_2 + d \phi_3 + \phi_4
 \end{aligned} \tag{4.13}$$

where the coefficients a , b , c , d depend on the geometry of the circuit.

The first two normal modes correspond to symmetric and antisymmetric combinations of the coupled transmons as schematically depicted in Figs. 4.8(b), (c). The third term corresponds to a sloshing mode associated with charge oscillations across the coupling element (Fig. 4.8(d)). The last term describes a zero-frequency rigid mode, corresponding to all capacitors charging up simultaneously. The normal-mode frequencies of the linearised circuit are plotted in Fig. 4.8(a) as a function of the coupling inductance L_c , for our device parameters. Note that the normal-mode splitting and, subsequently, the coupling between the two transmons is suppressed at the point where they are both on resonance with the filter frequency $1/\sqrt{L_c C_c}$ (dashed curve in Fig. 4.8(a)).

4.5.2. Hamiltonian description of the nonlinear circuit

The inductive energy of the nonlinear circuit (Fig. 4.1(c)) is

$$\begin{aligned}
 \mathcal{E}_{\text{ind}} &= -E_J^{(1)} \cos(\phi_1 - \phi_2) - E_J^{(2)} \cos(\phi_3 - \phi_4) - E_J^c \cos(\phi_2 - \phi_3) \\
 &= -E_J^{(1)} \cos \psi_A - E_J^{(2)} \cos \psi_B - E_J^c \cos \left(\frac{\psi_A - \psi_B}{2} - \psi_S \right),
 \end{aligned} \tag{4.14}$$

where, in the second step, we have expressed it using the transmon and sloshing mode variables $\psi_A \doteq \phi_1 - \phi_2$, $\psi_B \doteq \phi_4 - \phi_3$ and $\psi_S \doteq \frac{1}{2}(\phi_1 + \phi_2 - \phi_3 - \phi_4)$ (expressed in units of the reduced flux quantum $\phi_0 = \hbar/2e$). The first two terms describe the Josephson energy of each transmon, while the third one describes the inductive coupling between them, as well as the inductive energy of the sloshing mode. Here, $\psi_{A,B}$ correspond to the uncoupled transmon modes in the limit $C_c = 0$, $L_c \rightarrow \infty$.

Defining $\psi_R \doteq \frac{1}{2}(\phi_1 + \phi_2 + \phi_3 + \phi_4)$ and performing a change of basis from ϕ^T to $\psi^T = [\psi_R, \psi_S, \psi_B, \psi_A]$, the capacitance matrix transforms as

$$[\mathbf{C}'] = \begin{bmatrix} \frac{C_{1g}+C_{2g}}{8} & 0 & \frac{C_{1g}-C_{2g}}{8} & \frac{C_{1g}-C_{2g}}{8} \\ 0 & \frac{C_{1g}+C_{2g}+2C_c}{8} & \frac{-C_{1g}+C_{2g}+2C_c}{8} & \frac{C_{1g}-C_{2g}-2C_c}{8} \\ \frac{C_{1g}-C_{2g}}{8} & \frac{-C_{1g}+C_{2g}+2C_c}{8} & C + \frac{C_{1g}+C_{2g}+C_c}{4} & \frac{-C_c}{4} \\ \frac{C_{1g}-C_{2g}}{8} & \frac{C_{1g}-C_{2g}-2C_c}{8} & \frac{-C_c}{4} & C + \frac{C_{1g}+C_{2g}+C_c}{4} \end{bmatrix}, \tag{4.15}$$

Therefore, the system Lagrangian, expressed in the mode variable basis ψ , is

$$\mathcal{L} = \frac{1}{2} \dot{\psi}^T [\mathbf{C}'] \dot{\psi} + E_J^{(1)} \cos \psi_A - E_J^{(2)} \cos \psi_B - E_J^c \cos \left(\frac{\psi_A - \psi_B}{2} - \psi_S \right). \tag{4.16}$$

The conjugate momenta $Q_i = \frac{\partial \mathcal{L}}{\partial \dot{\psi}_i}$, describing the charges associated with each mode, can be determined by inverting the capacitance matrix, since $\mathbf{Q} = [\mathbf{C}'] \dot{\psi}$. Performing a Legendre transformation $\mathcal{H} = \sum_i \dot{\psi}_i Q_i - \mathcal{L}$ and promoting all variables to

operators, satisfying $[\hat{\psi}_i, \hat{Q}_i] = i\hbar$, we obtain the full circuit Hamiltonian:

$$\begin{aligned} \hat{H} = & \frac{\hat{Q}_R^2}{2\tilde{C}_R} + \frac{\hat{Q}_S^2}{2\tilde{C}_S} + \frac{\hat{Q}_A^2}{2\tilde{C}} + \frac{\hat{Q}_B^2}{2\tilde{C}} + \frac{C_c C_{1g}^2}{4\text{Det}[C']} \hat{Q}_A \hat{Q}_B + \frac{1}{\tilde{C}_{ABS}} \hat{Q}_S (\hat{Q}_A - \hat{Q}_B) \\ & + \frac{1}{\tilde{C}_{ABR}} \hat{Q}_R (\hat{Q}_A + \hat{Q}_B) - E_J^{(1)} \cos \hat{\psi}_A - E_J^{(2)} \cos \hat{\psi}_B - E_J^c \cos \left(\frac{\hat{\psi}_A - \hat{\psi}_B}{2} - \hat{\psi}_S \right), \end{aligned} \quad (4.17)$$

where

$$\tilde{C} = \frac{4\text{Det}[C']}{(C_{1g} C_{2g} (C_{1g} + C_{2g}) + C_{1g} (C_{1g} + 2C_{2g}) C_c + C (C_{1g} + C_{2g}) (C_{1g} + C_{2g} + 2C_c))}, \quad (4.18)$$

$$\tilde{C}_S = \frac{2(C_{1g} (C_{2g} + 2C_c) + C (C_{1g} + C_{2g} + 2C_c))}{(4C + C_{1g} + C_{2g} + 2C_c)}, \quad (4.19)$$

$$\tilde{C}_R = \frac{2C_{1g} C_{2g} + 2C (C_{1g} + C_{2g})}{(4C + C_{1g} + C_{2g})}, \quad (4.20)$$

$$\tilde{C}_{ABS} = \frac{2(C_{1g} (C_{2g} + 2C_c) + C (C_{1g} + C_{2g} + 2C_c))}{(C_{2g} - C_{1g} + 2C_c)}, \quad (4.21)$$

$$\tilde{C}_{ABR} = \frac{2C_{1g} C_{2g} + 2C (C_{1g} + C_{2g})}{C_{2g} - C_{1g}}, \quad (4.22)$$

and

$$\text{Det}[C'] = \frac{(C_{1g} C_{2g} + C (C_{1g} + C_{2g})) (C_{1g} (C_{2g} + 2C_c) + C (C_{1g} + C_{2g} + 2C_c))}{4} \quad (4.23)$$

is the determinant of the capacitance matrix.

Inductive coupling contributions

The linear contributions to the inductive coupling, arising from the first-order expansion of $E_J^c \cos \left(\frac{\hat{\psi}_A - \hat{\psi}_B}{2} - \hat{\psi}_S \right)$, are,

$$\begin{aligned} \frac{E_J^c}{2!} \left(\frac{\hat{\psi}_A - \hat{\psi}_B}{2} - \hat{\psi}_S \right)^2 = & -\frac{E_J^c}{4} \hat{\psi}_A \hat{\psi}_B - \frac{E_J^c}{2} (\hat{\psi}_A - \hat{\psi}_B) \hat{\psi}_S \\ & + \frac{E_J^c}{2} \left[\left(\frac{\hat{\psi}_A}{2} \right)^2 + \left(\frac{\hat{\psi}_B}{2} \right)^2 + \hat{\psi}_S^2 \right], \end{aligned} \quad (4.24)$$

where the first term corresponds to a direct dipole-dipole interaction between the transmons due to the coupling inductor, and the second results in an indirect transmon-transmon coupling via the off-resonant sloshing mode. The last terms describe a linear contribution to the inductive energy of each mode.

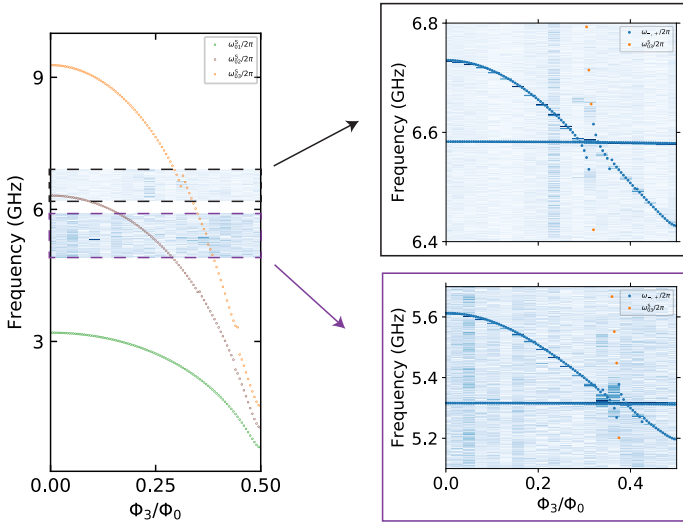


Figure 4.9: **Higher-order sloshing mode transition interference with the qubit-qubit spectrum.** The left plot shows the expected frequency dependence of the sloshing mode and its higher levels on the coupler bias Φ_3/Φ_0 . On the right we show data and theory fit of the coupled qubit spectrum in the single-excitation manifold for two different frequency operating points (at the top and bottom sweetspots of qubit 2 and 1, respectively). The higher 0 – 3 sloshing mode transition always crosses with the qubits around the zero coupling region, for our particular choice of circuit parameters. Note that the range of available coupling strengths is larger when operating at ~ 5.4 GHz.

The second-order nonlinear contributions ($\mathcal{O}[\psi^4]$) are

$$\begin{aligned}
 \frac{E_J^c}{4!} \left(\frac{\hat{\psi}_A - \hat{\psi}_B}{2} - \hat{\psi}_S \right)^4 &= \frac{E_J^c}{96} (\hat{\psi}_A^3 \hat{\psi}_B + \hat{\psi}_B^3 \hat{\psi}_A) - \frac{E_J^c}{64} \hat{\psi}_A^2 \hat{\psi}_B^2 \\
 &\quad - \frac{E_J^c}{16} (\hat{\psi}_A - \hat{\psi}_B)^2 \hat{\psi}_S^2 + \frac{E_J^c}{12} (\hat{\psi}_A - \hat{\psi}_B) \hat{\psi}_S^3 \\
 &\quad \frac{E_J^c}{4!} \left[\left(\frac{\hat{\psi}_A}{2} \right)^4 + \left(\frac{\hat{\psi}_B}{2} \right)^4 + \hat{\psi}_S^4 \right], \quad (4.25)
 \end{aligned}$$

where the first direct transmon-transmon coupling term describes correlated hopping processes including small corrections to the linear coupling, and the second term contains the cross-Kerr contribution. In our design, the sloshing mode is at much lower frequency than the transmons, therefore the third term is not directly relevant, however, the fourth term results in qubit coupling to the 0 – 3 transition of the sloshing mode, which was observed in spectroscopy near the zero coupling region. As we show in Fig. 4.9, this transition always crosses around the zero coupling region, even when operating at different qubit frequencies. This is an undesired effect which arises due to the fact that the two-island transmon design introduces four nodes in our circuit. A possible solution to this, would be to carefully engineer where these higher transitions occur and make sure that they do not cross with the qubits at the critical operation points. For example,

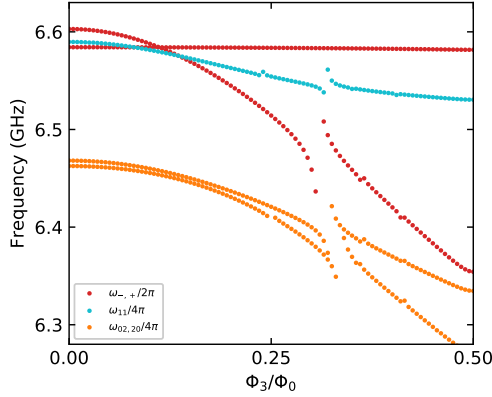


Figure 4.10: **Controlling the higher sloshing mode level crossings with an alternative circuit design.** Theoretical calculations of the coupled system energy level spectrum, demonstrate that using a slightly bigger coupling capacitor ($C_c = 30$ fF), would enable experimental accessibility to regimes where $V \gg J$ and $J = 0$ without other transitions interfering.

as we show in Fig. 4.10, a zero linear coupling regime could be reached for a slightly different circuit design with a larger coupling capacitor C_c .

Notice that, all the self-inductive terms to infinite order $\mathcal{O}(\psi_A^2, \psi_B^2, \psi_S^2, \psi_A^4, \psi_B^4, \psi_S^4, \dots)$ result in the following contribution to the Hamiltonian

$$-E_J^c \cos \hat{\psi}_S - E_J^c \left(\cos \frac{\hat{\psi}_A}{2} + \cos \frac{\hat{\psi}_B}{2} \right). \quad (4.26)$$

The first term describes the Josephson energy of the sloshing mode, while the rest two terms account for a correction to the transmon Josephson energies as E_J^c is tuned. This change accounts for the measured transmon frequency shifts vs coupler bias Φ_3 , shown in Figs. 4.4(e), (f).

Capacitive coupling contributions and mode variable elimination

The two transmons couple directly via their charge degrees of freedom as $\frac{C_c C_{1g}^2}{4 \text{Det}[C^j]} \hat{Q}_A \hat{Q}_B$. Additionally they couple together indirectly via the off-resonant sloshing mode, as described by the term $\frac{1}{C_{ABS}} \hat{Q}_S (\hat{Q}_A - \hat{Q}_B)$.

The mode variable Q_R has no inductive energy associated with it and only contributes to the analytical dynamics in (4.17) by coupling with the transmons via the term $\frac{1}{C_{ABR}} \hat{Q}_R (\hat{Q}_A + \hat{Q}_B)$. Notably, this coupling would vanish if the two islands of each transmon had exactly the same capacitances to ground ($C_{1g} = C_{2g}$). In our design there is a small asymmetry ($C_{1g} \neq C_{2g}$), therefore, this contribution should be taken into account for an accurate theoretical description of the circuit. It is possible, however, to eliminate this variable, while taking into account the stray contributions to the coupling between the two transmons. To illustrate this, we rewrite these coupling

terms as

$$\begin{aligned} \frac{1}{\tilde{C}_{ABR}} \hat{Q}_R (\hat{Q}_A + \hat{Q}_B) &= \left(\frac{\hat{Q}_R}{\sqrt{2\tilde{C}_R}} + \sqrt{\frac{\tilde{C}_R}{2\tilde{C}_{ABR}^2}} (\hat{Q}_A + \hat{Q}_B) \right)^2 - \frac{\tilde{C}_R}{2\tilde{C}_{ABR}^2} (\hat{Q}_A + \hat{Q}_B)^2 \\ &= \frac{\hat{Q}_R^2}{\tilde{C}_R} - \frac{\tilde{C}_R}{2\tilde{C}_{ABR}^2} (\hat{Q}_A^2 + \hat{Q}_B^2) - \frac{\tilde{C}_R}{\tilde{C}_{ABR}^2} \hat{Q}_A \hat{Q}_B. \end{aligned} \quad (4.27)$$

The first term is derived following a redefinition of the rigid mode $\hat{Q}_R = f(\hat{Q}_R, \hat{Q}_A, \hat{Q}_B)$. This zero frequency mode has no contribution to the equations of motion of all the other modes and can, therefore, be eliminated. The second term accounts for a renormalisation of the transmon charging energies, while the last term accounts for a small contribution to the direct capacitive coupling, which can be absorbed into a redefinition of J_C . We have therefore eliminated one variable which reduces the computational power required for numerical modelling and makes the theoretical description of the circuit more elegant.

4.5.3. Circuit quantisation in the harmonic oscillator basis

The Hamiltonian describing the uncoupled system is given by

$$\mathcal{H}_0 = 4E_C \hat{N}_A^2 - E_J^{(1)} \cos \hat{\psi}_A + 4E_C \hat{N}_B^2 - E_J^{(2)} \cos \hat{\psi}_B, \quad (4.28)$$

where $E_C = \frac{e^2}{2C}$ is the charging energy of each transmon and $\hat{N}_{A,B} = \frac{\hat{Q}_{A,B}}{2e}$ is the number operator associated with Cooper-pairs tunnelling through each junction [158].

Introducing annihilation (creation) operators $\hat{a}^{(\dagger)}, \hat{b}^{(\dagger)}$ such that

$$\begin{aligned} \hat{N}_A &= i \left(\frac{E_J^{(1)}}{32E_C} \right)^{1/4} (\hat{a}^\dagger - \hat{a}), & \hat{\psi}_A &= \left(\frac{2E_C}{E_J^{(1)}} \right)^{1/4} (\hat{a} + \hat{a}^\dagger), \\ \hat{N}_B &= i \left(\frac{E_J^{(2)}}{32E_C} \right)^{1/4} (\hat{b}^\dagger - \hat{b}), & \hat{\psi}_B &= \left(\frac{2E_C}{E_J^{(2)}} \right)^{1/4} (\hat{b} + \hat{b}^\dagger), \end{aligned} \quad (4.29)$$

the uncoupled two-transmon Hamiltonian can be approximated as two independent Duffing oscillators [44]

$$\mathcal{H}_0 = \hbar\omega_1 \hat{a}^\dagger \hat{a} - \frac{E_C}{2} \hat{a}^\dagger \hat{a}^\dagger \hat{a} \hat{a} + \hbar\omega_2 \hat{b}^\dagger \hat{b} - \frac{E_C}{2} \hat{b}^\dagger \hat{b}^\dagger \hat{b} \hat{b}, \quad (4.30)$$

at frequencies $\omega_{1,2} = \sqrt{8E_J^{(1,2)} E_C} - E_C$. Note that the sloshing mode can also be approximately described by the transmon Hamiltonian, however this approximation ceases to be valid as E_J^C is tuned to zero.

Linear coupling

When the two transmons are resonant ($E_J^{(1)} = E_J^{(2)} \doteq E_J$), the linear coupling terms $\hat{Q}_A \hat{Q}_B$, $\hat{\psi}_A \hat{\psi}_B$, result in a dipole-dipole interaction of the form

$$J(\hat{a}^\dagger + \hat{a})(\hat{b} + \hat{b}^\dagger). \quad (4.31)$$

In the case where $J \ll \omega$ this is equivalent to single photon hopping $J(\hat{a}^\dagger \hat{b} + \hat{b}^\dagger \hat{a})$, following a rotating wave approximation (RWA). Moreover, in the qubit subspace this is also equivalent to $2J(\hat{\sigma}_x^1 \hat{\sigma}_x^2 + \hat{\sigma}_y^1 \hat{\sigma}_y^2)$, where $\sigma_{x,y}$ are Pauli operators. The coupling strength is given by

$$J = \frac{\sqrt{8E_J E_C}}{2} \left(\frac{e^2 C_{1g}^2 C_c}{8E_C \text{Det}[\mathbf{C}']} - \frac{E_J^c}{4E_J} \right). \quad (4.32)$$

As we have already discussed, small contributions to J need to be considered as the two transmons additionally couple via the off-resonant sloshing mode ($(\hat{Q}_A - \hat{Q}_B)\hat{Q}_S$ and $(\hat{\psi}_A - \hat{\psi}_B)\hat{\psi}_S$ terms). We include these contributions, as well as higher order corrections, by diagonalising the full circuit Hamiltonian (4.17) in our theoretical modelling of the experimental data.

4

Nonlinear coupling

The first term in (4.25) describes correlated photon hopping terms,

$$\frac{V}{6} (\hat{a}^\dagger \hat{n}_a \hat{b} + \hat{a} \hat{n}_a \hat{b}^\dagger + \hat{b}^\dagger \hat{n}_b \hat{a} + \hat{b} \hat{n}_b \hat{a}^\dagger), \quad (4.33)$$

where

$$V = -\frac{E_J^c E_C}{8E_J}. \quad (4.34)$$

This term, also leads to a small correction to the dipole-dipole coupling $J \rightarrow J - \frac{V}{6}$.

The second term in (4.25) results in cross-Kerr coupling

$$V \hat{a}^\dagger \hat{a} \hat{b}^\dagger \hat{b}, \quad (4.35)$$

and photon-pair tunnelling processes

$$\frac{V}{4} (\hat{a}^\dagger \hat{a}^\dagger \hat{b} \hat{b} + \hat{a} \hat{a} \hat{b}^\dagger \hat{b}^\dagger). \quad (4.36)$$

4.6. Measurement setup

The measurement setup including the wiring diagram and an optical micrograph of the full $2 \text{ mm} \times 7 \text{ mm}$ chip is shown in Fig. 4.11. Our device was mounted on a printed circuit board (PCB) at the mixing chamber plate of a dilution refrigerator (fridge temperature $\sim 20 \text{ mK}$). The sample was shielded against external magnetic fields, using a pair of cryogenic mu-metal shields as well as aluminium layers, and infrared radiation, using an additional copper can coated with a mixture of silicon carbide and Stycast 2850 [159]. Cryogenic attenuators and home-build eccosorb filters were used in all microwave lines, resulting in a total attenuation of $\sim 60 \text{ dB}$ for each line. For the DC flux bias lines we use home-build eccosorb filters and commercial low-pass filters (VLFX) with 1.35 GHz frequency cutoff. The input line additionally has a 10 GHz low-pass filter, and the output signal passes through 3 circulators, connected in series, before being amplified using cryogenic (HEMT) and room-temperature amplifiers. The signal is then demodulated, amplified and registered with a data acquisition card.

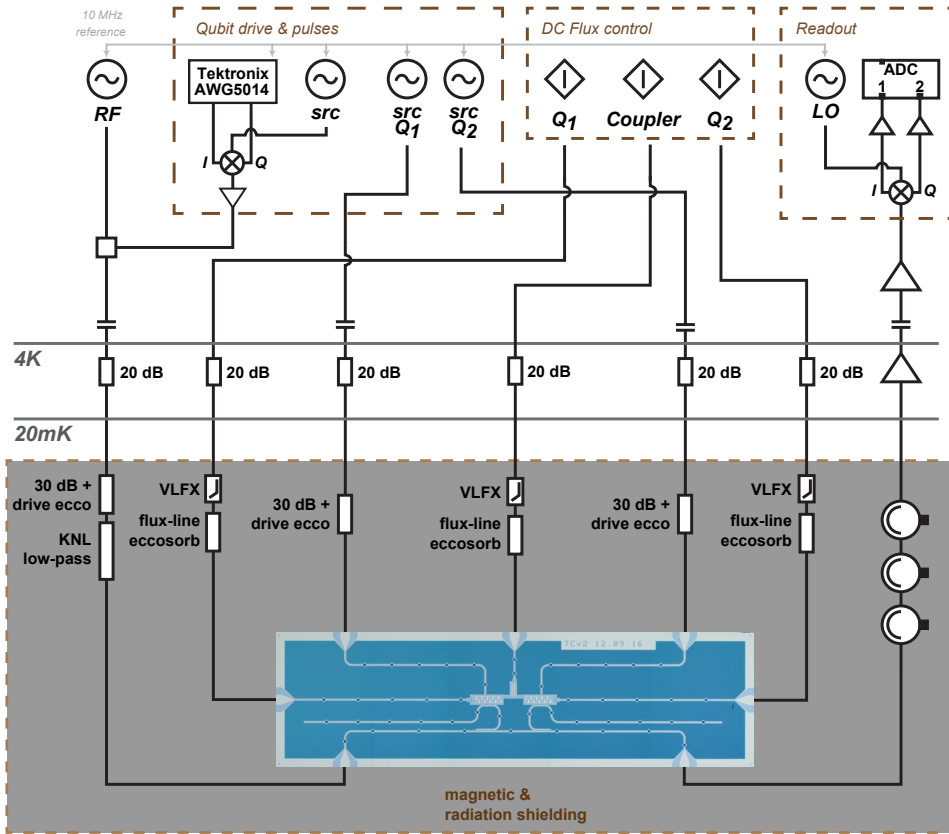


Figure 4.11: Schematic of the measurement setup including microwave and DC wiring to our 2 mm × 7 mm chip.

4.7. Supplementary data

In order to determine the cross-Kerr couplings of Fig. 4.3, spectroscopically, we need to access the two-excitation manifold in the resonantly coupled system (Fig. 4.13(a)). However, directly exciting the even states with one source is difficult because of the transmon selection rules [92]. This could, in principle, be achieved via single-tone spectroscopy at very high powers (as in Fig. 4.5), however this results in broadening and Stark shifting of the coupled qubits frequencies, causing some uncertainty in our measurements. We therefore perform two-tone spectroscopy, where we read out via one resonator and sweep the drive frequencies of two microwave tones (f_{S1} and f_{S2}) applied through each drive-line, as shown in Fig. 4.13(b). The bright vertical lines, correspond to the dressed state transition frequencies $\omega_{+}/2\pi$, $\omega_{-}/2\pi$, which can be easily excited with each source. The diagonal 45° lines correspond to two-photon transitions to $|02\rangle$, $|20\rangle$ and $|11\rangle$ as different photons from each source combine together to excite these states. Each data point in Fig. 4.3(b) is extracted from a series of similar two-tone

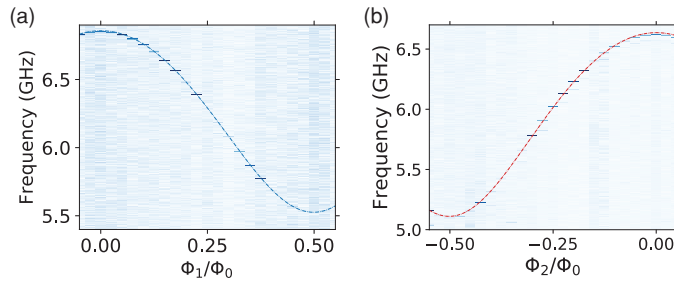


Figure 4.12: **Frequency tuning of the two qubits.** Each qubit is driven via its dedicated flux bias line. Raw data including theory fits are shown. All flux channels have been made orthogonal following the calibration procedure described in Fig. 4.6.

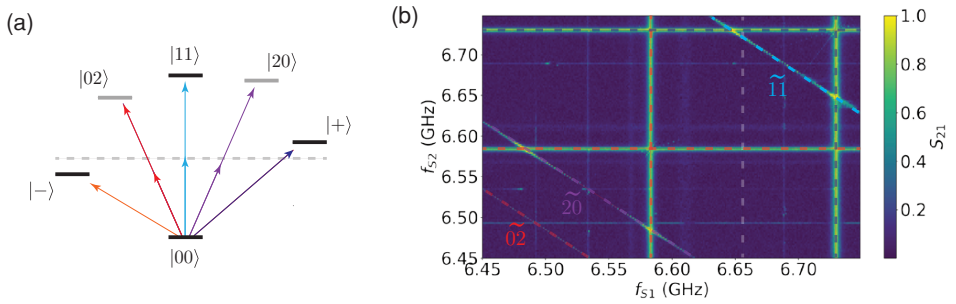


Figure 4.13: **Two-tone spectroscopy.** (a) Level diagram of the coupled two-transmon system on resonance. Higher level transitions are prohibited by selection rules and therefore two-tone spectroscopy is required to probe the two-excitation manifold. (b) Two-tone spectroscopy of the coupled system at $\Phi_3/\Phi_0 = 0$. Vertical and horizontal lines correspond to the 01 and 10 transitions, while diagonal lines correspond to two-photon transitions.

spectroscopy measurements.

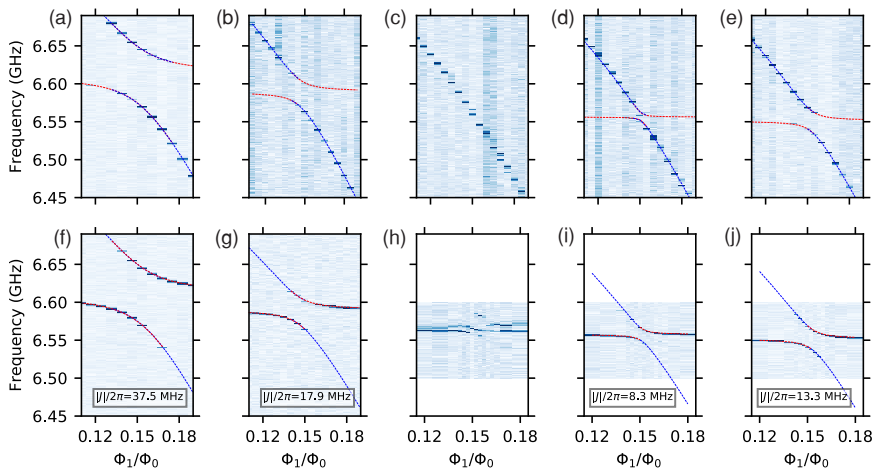


Figure 4.14: **Detailed avoided crossings around the normal-mode splitting suppression point, as we tune from an inductively dominated towards a capacitively dominated coupling regime.** The top row (a)-(e) shows qubit spectroscopy data via resonator R_1 as qubit 1 is tuned on resonance with qubit 2, for different values of coupler bias $\Phi_3/\Phi_0 = 0.25, 0.26, 0.3, 0.32, 0.33$ (from left to right). The bottom figures (f)-(j) correspond to the same measurement with qubit spectroscopy via resonator R_2 . The insets show the extracted linear coupling strengths from qubit-qubit avoided crossing fits.

5

Quantum control of a mechanical resonator using three-body interactions with transmon qubits

Every difficulty in life presents us with an opportunity to turn inward and to invoke our own submerged inner resources. The trials we endure can and should introduce us to our strengths. Dig deeply. You possess strengths you might not realize you have. Find the right one. Use it.

Epictetus, "The Art of Living"

In this chapter, we propose a scheme for controlling a radio-frequency mechanical resonator at the quantum scale using two superconducting transmon qubits that can be integrated on the same chip. Specifically, we consider two qubits coupled via a capacitor in parallel to a superconducting quantum interference device (SQUID), which has a suspended mechanical beam embedded in one of its arms. Following a theoretical analysis of the quantum system, we find that this configuration, in combination with an in-plane magnetic field, can give rise to a tuneable three-body interaction in the single-photon strong-coupling regime, while enabling suppression of the stray qubit-qubit coupling. Using state-of-the-art parameters and qubit operations at single-excitation levels, we numerically demonstrate the possibility of ground-state cooling as well as high-fidelity preparation of mechanical quantum states and qubit-phonon entanglement, i.e. states having negative Wigner functions and obeying non-classical correlations.

This chapter has been published with minor differences in *npj Quantum Information* 5, 100 (2019).

5.1. Introduction

The ability to control massive mechanical objects at the quantum level constitutes a very interesting task for many technological applications, ranging from microwave-to-optical conversion to quantum memories, as well as fundamental studies regarding the quantum-classical divide [63, 64, 66–68, 160–164]. The rapid development of cavity optomechanics over the last decade has enabled the exploration of mechanical resonators in regimes where quantum effects become prominent. One approach relies on resonant coupling of acoustic phonons to microwave excitations via piezoelectric materials [165, 166], however, the amplitude of the lattice vibrations in these systems is very small, limiting their applications. On the other hand, in typical opto- and electromechanical setups, low-frequency mechanical resonators are controlled via parametric coupling to an optical or microwave cavity [167–171]. The mechanical elements in these systems are usually realised with metal drumheads or beams, which are characterised by large quality factors and large mass, making them also prime candidates for experimental tests of gravity-induced wavefunction collapse theories [66–68, 160].

Following the pioneering work on acoustic resonators [165], recently, quantum superpositions of the ground and first excited state were for the first time generated in a parametrically coupled mechanical resonator [172]. In this approach, a superconducting qubit is used to create the excitation, which decays into a microwave resonator on a different chip and subsequently transferred to the mechanical element via an effective linearised interaction. It is recognised, however, that this method has severe limitations as it relies on strong driving, which is challenging with qubits, and suffers from unavoidable losses during the state transfer between different chips, limiting the fidelity of the prepared state [173]. A different scheme, implemented in the optical domain, uses entanglement and post-selective measurements to generate single-photon states [174], although the non-deterministic nature of the protocol in combination with low count rates limits the types of states that can be prepared.

A promising route towards high-fidelity mechanical quantum control is the ability to operate in the single-photon strong-coupling regime, where interaction times are faster than dissipation processes, which however still remains an experimental challenge for far-detuned parametrically coupled mechanical resonators [173, 175]. Operating in this regime is predicted to give rise to non-classical photon correlations [176] and non-Gaussian states [177, 178], as well as macroscopic mechanical superpositions [179]. Moreover, using the radiation-pressure coupling to qubits can lead to the creation of mechanical Schrödinger cat states [180, 181]. Generating Fock states in this regime could also be enabled using an additional microwave resonator to create an effective tripartite coupling, as predicted in Ref. [181], although this approach is limited to low state preparation fidelities mainly due to the limitations of capacitive coupling and stray qubit-resonator interaction. In spite of the experimental and theoretical advances in the field, high-fidelity quantum state preparation of mechanical systems appears to be limited to a small class of engineerable states which are, to a large degree, architecture-dependent.

Here, we analyse a new scheme for synthesizing generic mechanical states by employing tuneable three-body interactions between two superconducting qubits and a mechanical resonator in the single-photon strong-coupling regime. The coupling relies

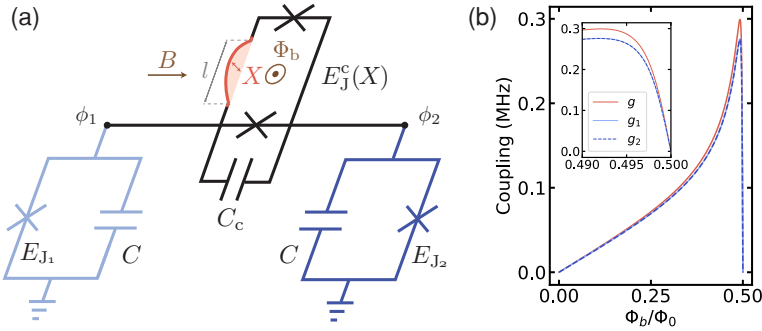


Figure 5.1: **Tripartite coupling architecture.** (a) Circuit diagram of the electromechanical system comprising two transmon qubits directly coupled via a SQUID coupler with an embedded beam that can oscillate out of plane. Tuning the coupler to its filter frequency, where linear currents through the capacitor and the SQUID cancel out, and applying an in-plane magnetic field B , results in a dominant tripartite coupling as the beam oscillations modulate the qubit-qubit interaction. (b) Flux-mediated couplings as a function of flux bias Φ_b for in-plane magnetic field $B = 10$ mT and circuit parameters used in this work. The red curve represents the tripartite coupling strength, while the solid/dashed blue curves correspond to the radiation-pressure coupling of the beam with each qubit.

on embedding a suspended micrometer-long beam in one of the arms of a superconducting quantum interference device (SQUID) in combination with an externally applied magnetic field [182–185]. We find that by connecting two superconducting transmon qubits directly via this mechanical SQUID, a tuneable three-body interaction arises as the qubit-qubit flux-mediated coupling is modulated by the mechanical displacement. Importantly, the detrimental exchange-type interaction between the two qubits can be suppressed by adding a capacitor in parallel to the SQUID, as discussed in the previous chapter. Using state-of-the-art parameters, reported in recent experiments [185], we numerically demonstrate the possibility of high-fidelity coherent quantum control of the beam, from ground-state cooling to fast and high-fidelity preparation of mechanical Fock states, as well as maximally entangled states of qubits and phonons. Finally, we devise a protocol consisting of qubit flux-pulsing and post-selective measurements for synthesizing multi-phonon superposition states, extending the quantum control toolbox and the plurality of engineerable quantum states in radio-frequency mechanical resonators.

5.2. Main results

5.2.1. Motion-dependent qubit-qubit interaction

The proposed circuit, shown in Fig. 5.1(a), comprises two transmon qubits coupled directly via a superconducting quantum interference device (SQUID) shunted by a capacitor, C_c . This tuneable coupling scheme has recently been realised in circuit QED setups using transmons [186] and LC resonators [187]. The coupling is controlled by tuning the Josephson energy of the SQUID, $E_J^c(\Phi_b) = E_{J,\Sigma}^c |\cos(\pi\Phi_b/\Phi_0)|$, with an out-of-plane flux bias, Φ_b , where $\Phi_0 = h/2e$ is the magnetic flux quantum and $E_{J,\Sigma}^c$ is the sum of the two junction Josephson energies in the SQUID. The mechanical part of the circuit con-

sists of a beam of length l that is embedded in one of the arms of the SQUID loop and can oscillate out of plane. By applying an in-plane external magnetic field B , the loop can pick up an additional flux $\beta_0 BlX$ due to the beam displacement X , resulting in a flux-tunable and motion-dependent Josephson energy $E_J^c = E_{J,\Sigma}^c |\cos(\pi\Phi_b/\Phi_0 + \alpha X)|$, where $\alpha = \pi\beta_0 Bl/\Phi_0$ and β_0 is a geometric factor depending on the mode shape (for the first mechanical mode, considered here, $\beta_0 \simeq 1$) [184, 185, 188].

The Hamiltonian describing the circuit in Fig. 5.1(a) is

$$H = \frac{P^2}{2m} + \frac{m\omega_m^2 X^2}{2} + \sum_{i=1}^2 \left[\frac{Q_i^2}{2\tilde{C}_i} - E_{J_i} \cos\left(\frac{\phi_i}{\phi_0}\right) \right] + \frac{C_c}{C_1 C_2} Q_1 Q_2 - E_J^c(X) \cos\left(\frac{\phi_1 - \phi_2}{\phi_0}\right), \quad (5.1)$$

where $\{X, P\}$ and $\{\phi_i, Q_i\}$ are conjugate variable pairs describing the mechanical and the electrical degrees of freedom at circuit node i , and $\phi_0 = \Phi_0/(2\pi)$ is the reduced flux quantum. The first four terms describe the uncoupled system of the mechanical resonator and two transmon qubits, where m , ω_m denote the mass and frequency of the beam and E_{J_i} , \tilde{C}_i represent the Josephson energy and loaded capacitance of each transmon, respectively (see section 5.5). The last two terms describe the qubit-qubit interaction via their charge and flux degrees of freedom, Q_i and ϕ_i .

The core of this proposal relies on the fact that the dynamical displacement of the beam results in a modulation of the superconducting current through the coupling SQUID and its Josephson energy, which mediates the qubit-qubit interaction. Taking into account the finite asymmetry of the SQUID loop, which is present in any realistic scenario, this results in a motion-dependent Josephson energy,

$$E_J^c(X) = E_{J,\Sigma}^c [c_J \cos(\pi\Phi_b/\Phi_0) - s_J \sin(\pi\Phi_b/\Phi_0)\alpha X], \quad (5.2)$$

where $c_J = \sqrt{1 + a_J^2 |\tan(\pi\Phi_b/\Phi_0)|}$ and $s_J = (1 - a_J^2)/c_J$ are correction factors due to the SQUID asymmetry a_J . Note that the above expression is valid for $\pi\Phi_b/\Phi_0 \gg \alpha X$ and relies on the assumption that $\alpha X \ll 1$ (for a full derivation see section 5.5.1). For the parameters considered here, which are compatible with values reported in recent experiments using micrometer-long Al beams and sub-Tesla magnetic fields [185], we have $\alpha X \sim 10^{-5} - 10^{-6}$, therefore this is a valid assumption.

5.2.2. Electromechanical system dynamics

The Hamiltonian of the system can be expressed in second quantisation form, as

$$\hat{H} = \hat{H}_0 + \hat{H}_{\text{int}}, \quad (5.3)$$

$$\hat{H}_0 = \hbar\omega_m \hat{b}^\dagger \hat{b} + \sum_{i=1}^2 \hbar\omega_i \hat{c}_i^\dagger \hat{c}_i - \frac{E_{C_i}}{2} \hat{c}_i^\dagger \hat{c}_i^\dagger \hat{c}_i \hat{c}_i, \quad (5.4)$$

$$\hat{H}_{\text{int}} = \hbar g (\hat{c}_1^\dagger \hat{c}_2 + \hat{c}_1 \hat{c}_2^\dagger) (\hat{b} + \hat{b}^\dagger) - \sum_{i=1}^2 \hbar g_i \hat{c}_i^\dagger \hat{c}_i (\hat{b} + \hat{b}^\dagger) + \hat{H}'_{12}, \quad (5.5)$$

where $\hat{b}^{(\dagger)}$ and $\hat{c}_i^{(\dagger)}$ are bosonic operators describing the annihilation (creation) of phonons and qubit excitations, respectively (see section 5.6). The effective electromechanical frequencies are ω_m and $\omega_i = \frac{1}{\hbar} \left(\sqrt{8\tilde{E}_{J_i} E_{C_i}} - E_{C_i} \right)$, where \tilde{E}_{J_i} is the modified transmon Josephson energy due to the coupler. The classical analysis together with a full quantum mechanical treatment of the circuit, including higher-order nonlinear interaction terms, is presented in sections 5.5 and 5.6.

The first term in Eq. (5.5) describes a three-body interaction involving hopping of qubit excitations together with mechanical displacements of the beam. The coupling strength is given by

$$g = \frac{\alpha \sqrt{Z_1 Z_2}}{2\phi_0^2} s_J E_{J,\Sigma}^c \sin(\pi\Phi_b/\Phi_0) X_{\text{ZPF}}, \quad (5.6)$$

where $Z_i = \frac{\hbar}{e^2} \sqrt{E_{C_i}/2\tilde{E}_{J_i}}$ denote the transmon impedances, and $X_{\text{ZPF}} = \sqrt{\hbar/(2m\omega_m)}$ is the zero-point motion of the mechanical resonator. The next interaction term describes the radiation-pressure interaction between each qubit and the beam with coupling strength $g_{1(2)} = g \sqrt{Z_{1(2)}/Z_{2(1)}}$. The electromechanical coupling strengths are plotted in Fig. 5.1(b) as a function of the out-of-plane flux bias Φ_b . Close to a half-integer flux quantum, $E_J^c(X)$ is maximally susceptible to mechanical motion which maximises the electromechanical coupling. Note that all couplings become zero exactly at a half-integer flux quantum due to the finite SQUID asymmetry a_J . In our calculations an asymmetry of 0.01 is included, reflecting a 2% spread in junction fabrication targeting.

The last term in Eq. (5.5) describes the qubit-qubit interaction

$$\hat{H}'_{12} = \hbar(J_C - J_L)(\hat{c}_1^\dagger \hat{c}_2 + \hat{c}_1 \hat{c}_2^\dagger) + \hbar V \hat{c}_1^\dagger \hat{c}_1 \hat{c}_2^\dagger \hat{c}_2, \quad (5.7)$$

where J_C , J_L are exchange-type coupling strengths arising from the coupling capacitor and SQUID, respectively, and V is the cross-Kerr coupling strength, which is minimised at $\Phi_b \simeq \Phi_0/2$ (see Eq. (5.44)). A significant advantage of this architecture for realising tripartite interactions, compared to relying exclusively on capacitive coupling [181], is that any stray linear coupling between the qubits can be suppressed with the right choice of coupling capacitance C_c [186, 187]. This makes the three-body interaction dominant and ensures the ability to manipulate the state of each qubit individually by local driving, which is crucial for the state engineering protocols discussed below.

5.2.3. Ground-state cooling

Mechanical resonators realised using vibrating beams and drumheads lie in the radio-frequency regime (~ 10 MHz), where thermal fluctuations are dominant even at millikelvin temperatures, achieved with conventional cryogenic techniques. An essential element of control is, therefore, the ability to cool these systems to their quantum ground state before manipulating them further. Typically, electromechanical experiments employ a ‘‘cold’’ microwave cavity (~ 10 GHz), which is coupled to the mechanical element via an effective linearised interaction in the many-photon regime, and cooling is enabled by red-sideband driving [168]. However, in a system comprised of qubits, cooling the

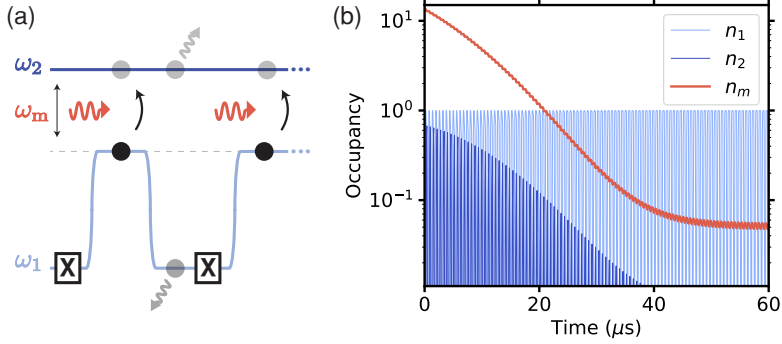


Figure 5.2: **Ground-state cooling.** (a) Schematic of the time-domain protocol to cool the mechanical resonator to its ground state using the three-body interaction. In each cycle, qubit 1 is excited with a microwave pulse, then its frequency is tuned at $\omega_1 = \omega_2 - \omega_m$ for a variable time Δt_{cool} followed by a reset on both qubits. (b) Numerical results after ~ 100 cycles demonstrating cooling to a 0.05 phonon occupancy for a 10 MHz resonator at $T = 10$ mK ($n_{\text{th}} \simeq 20$) using the system parameters presented in Table 5.1.

mechanical resonator via sideband driving can be a challenging task, requiring multiple tones and eventually limited by the critical number of photons in the Josephson junction [189, 190].

Here, we show that it is possible to overcome the challenges of sideband cooling with qubits by employing a time-domain protocol to cool the mechanical resonator to its quantum ground state, using the three-body interaction. The scheme, depicted in Fig. 5.2(a), consists of a sequence of single-qubit operations which, combined with the tripartite interaction, enable the transfer of the thermal phonons to the environment in a stroboscopic fashion, as described below. At first, we bring one qubit (q_1) to its excited state and then tune its frequency such that $\omega_1 = \omega_2 - \omega_m$. Since $g \ll \omega_m$ the interaction ($\hat{c}_1 \hat{b} \hat{c}_2^\dagger + \text{H.c.}$) is resonant at this condition, such that a phonon combined with the excitation in q_1 can be transferred to the other qubit (q_2) after variable time Δt_{cool} . The cycle is then completed by reinitialising both qubits using active reset protocols [191–193]. A similar scheme has also been realised recently for detecting microwave photons in a superconducting resonator, using tripartite interactions with a transmon qubit and a dissipative mode [194].

In Fig. 5.2(b) we plot the average number of phonons and qubit excitations as a function of time after ~ 100 cooling cycles, for a mechanical beam oscillating at $\omega_m/(2\pi) = 10$ MHz and a tripartite coupling strength $g/(2\pi) \simeq 0.3$ MHz. At the end of the protocol the mechanical resonator is cooled down to the ground state with a phonon occupancy of 0.05, assuming an environment temperature of $T = 10$ mK ($n_{\text{th}} \simeq 20$). The qubit ($\omega_1/(2\pi) = 7$ GHz) is excited with a 200 ns Gaussian pulse, while the reset and cooling times are set to $\Delta t_{\text{reset}} = \Delta t_{\text{cool}} = 200$ ns. The cooling time would be best optimised by choosing a short time for large thermal occupation and then increase the time as the resonator cools, since phonons swap faster for higher occupations. For simplicity, here, we considered a fixed time and found that for these

parameters, a 200 ns time is sufficient. Furthermore, we have assumed an in-plane magnetic field $B = 10$ mT which is well-below the critical field for thin Al beams [195] and does not compromise the qubit coherence [196]. All system parameters used in the simulations are listed in Table 5.1.

Parameter	Value
$\omega_m/(2\pi)$	10 MHz
$\omega_{1,2}/(2\pi)$	~ 7 GHz
$g/(2\pi)$	0.3 MHz
B	10 mT
Φ_b	$0.495 \Phi_0$
l	$14.7 \mu\text{m}$
X_{ZPF}	33 fm
β_0	1
C_c	9.7 fF
$E_{J,\Sigma}^c/E_{J_i}$	~ 10
E_{C_i}/h	320 MHz
n_{th} (T)	~ 20 (10 mK)
T_1, T_2	$30 \mu\text{s}$
Q_m	10^6

Table 5.1: Parameter set used in the numerical simulations.

5.2.4. Mechanical Fock states and qubit-phonon entanglement

Following ground-state preparation, we present a protocol which employs the tripartite coupling to deterministically generate mechanical Fock states and maximally entangled states. As schematically depicted in the inset of Fig. 5.3(a), it consists of preparing q_2 in the excited state and tuning it to $\omega_2 = \omega_1 + \omega_m$, such that the interaction ($\hat{c}_1^\dagger \hat{b}^\dagger \hat{c}_2 + \text{H.c.}$) is resonant. Ideally, assuming unitary evolution $U(t)$ under the tripartite interaction, the state would evolve as

$$U(t)|0_1 0_m 1_2\rangle = \cos(gt)|0_1 0_m 1_2\rangle - i \sin(gt)|1_1 1_m 0_2\rangle. \quad (5.8)$$

The evolution of the average number of phonons and qubit excitations, starting from an attainable mechanical state of 0.05 thermal phonons and including system dissipation (see Methods) is plotted in Fig. 5.3(a). We consider the full interaction Hamiltonian presented in Eq. (5.5), including next-to-leading order non-linear correction (see section 5.6), for the simulation parameters shown in Table 5.1. In Fig. 5.3(b) we plot the Wigner function of the final state in the mechanical resonator, after time $t = \pi/(2g)$, revealing a single-phonon Fock state with 97% (99%) fidelity, starting from an attainable (ideal) ground state. Higher phonon states could also be prepared by resetting and repeating the protocol with modified transfer times $t_n = n_m^{-1/2} \pi/(2g)$.

The quantum state preparation scheme described above, can also be used to generate bipartite and tripartite maximally entangled states between the mechanical resonator and

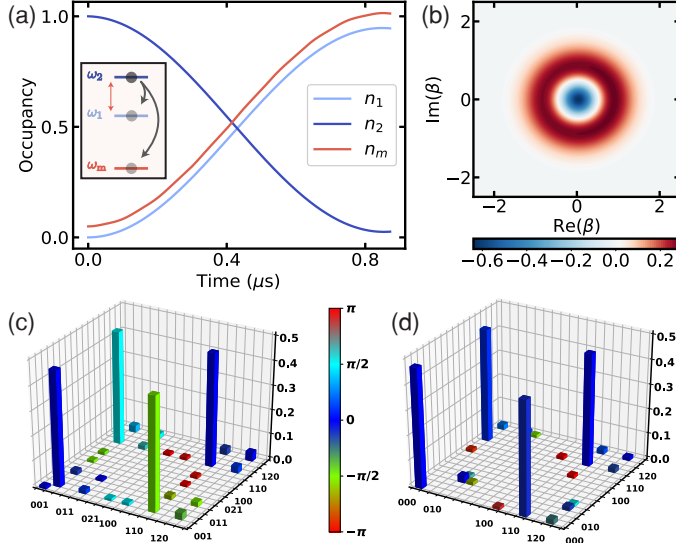


Figure 5.3: Protocol for Fock-state preparation and maximally entangled states of phonons and qubit excitations. (a) Time evolution after exciting qubit 2 and tuning into the operating point $\omega_2 = \omega_1 + \omega_m$ (schematically presented in the inset) such that the interaction ($\hat{c}_1 b \hat{c}_2^\dagger + \text{H.c.}$) is resonant. Starting from a phonon occupancy of 0.05, a mechanical Fock state is generated with 97% fidelity after time $t = \pi/(2g)$. (b) Wigner function of the resulting mechanical state. (c) Density matrix of a Greenberger–Horne–Zeilinger state that is generated in the middle of the protocol, at $t = \pi/(4g)$. The notation $(0_1 0_m 1_2)$ is used in labelling and only matrix elements with a magnitude larger than 0.005 are shown. (d) Resulting density matrix after repeating the same protocol with qubit 2 initialised in the superposition state $\frac{1}{\sqrt{2}}(|0_2\rangle + |1_2\rangle)$, leading to a Bell state with 96% fidelity.

the qubits. In particular, in the middle of the above protocol, at $t = \pi/(4g)$, the system is in a Greenberger–Horne–Zeilinger (GHZ) state

$$|\psi\rangle_f = \frac{1}{\sqrt{2}} (|0_1 0_m 1_2\rangle - i |1_1 1_m 0_2\rangle), \quad (5.9)$$

with 98% fidelity, with the corresponding density matrix shown in Fig. 5.3(c). Such states are particularly interesting for applications in quantum information [197, 198] and fundamental tests of quantum theory [199]. Using the same protocol for q_2 in a superposition state $\frac{1}{\sqrt{2}}(|0_2\rangle + |1_2\rangle)$, the Bell state

$$|\psi\rangle_f = \left(\frac{1}{\sqrt{2}} (|0_1 0_m\rangle + |1_1 1_m\rangle) \right) |0_2\rangle, \quad (5.10)$$

is generated after time $\pi/(2g)$ with 96% fidelity (98% for ideal ground state), as depicted in Fig. 5.3(d). The prepared state is a maximally entangled pair of a phonon and a qubit excitation, which could be utilised as a testbed for checking the validity of quantum mechanics at macroscopic scales without requiring tomography of the mechanical state [200, 201]. Such states might also be suitable for integrating transmon qubits into

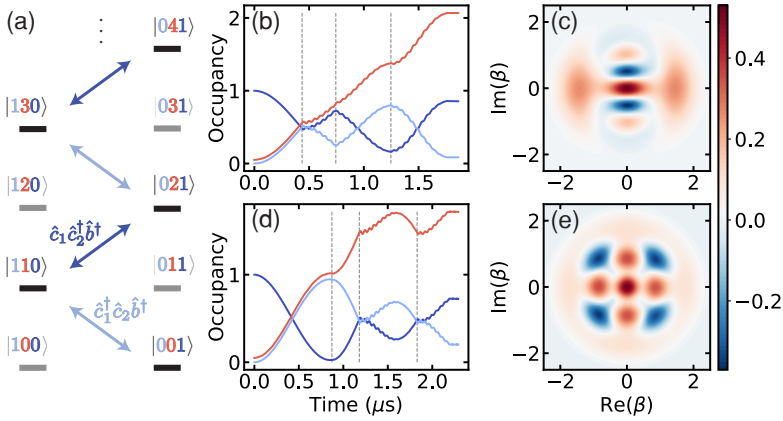


Figure 5.4: **Synthesizing multi-phonon quantum superposition states.** (a) Level diagram of the system indicating the resonant three-body interactions when the qubits are tuned such that $\omega_2^\pm = \omega_1 \pm \omega_m$. (b), (d) Evolution of phonon and qubit populations after exciting qubit 2 and alternating the qubit frequencies to ω_2^\pm , where the dashed vertical lines denote the application of a square tuning flux pulse. An attainable mechanical state of 0.05 phonons is taken initially. (c), (e) Wigner functions of the resulting states $\frac{1}{2}(|0\rangle + \sqrt{2}|2\rangle + |4\rangle)$ and $\frac{1}{\sqrt{2}}(|0\rangle + |4\rangle)$ with preparation fidelities 98% and 97% (following post-selection on $|0_1 1_2\rangle$), respectively.

other platforms such as spins, cold atoms, or even optical photons, via the mechanical resonator [202–205]. They could also provide possibilities for entangling the mechanical resonator with other physical systems via the transmon.

5.2.5. Multi-phonon quantum superpositions

We now extend the protocol described above to create multi-phonon quantum superposition states in the mechanical resonator, simply by flux-pulsing the qubits. In the protocols discussed previously, the qubit frequencies are tuned at $\omega_2 = \omega_1 + \omega_m$ such that the states $|0_1 n_m 1_2\rangle$ and $|1_1 (n+1)_m 0_2\rangle$ are coupled. However, when tuned at $\omega_2 = \omega_1 - \omega_m$ the interaction term $(\hat{c}_1 \hat{b}^\dagger \hat{c}_2^\dagger + \text{H.c.})$ becomes resonant, which couples $|0_1 (n+1)_m 1_2\rangle$ and $|1_1 n_m 0_2\rangle$. Therefore, by interchanging the qubit frequencies with flux-tuning pulses during each cycle it could be possible to create higher phonon Fock states and multi-phonon quantum superposition states, as depicted schematically in Fig. 5.4(a).

As a proof-of-concept, using the same simulation parameters as above (Table 5.1), we demonstrate the creation of superposition states $|\psi_m\rangle' = \frac{1}{2}(|0\rangle + \sqrt{2}|2\rangle + |4\rangle)$ and $|\psi_m\rangle'' = \frac{1}{\sqrt{2}}(|0\rangle + |4\rangle)$, after exciting qubit 2 and applying three flux pulses that interchange the qubit frequencies at variable times t_1, t_2 and t_3 . Figs. 5.4(b), (d) show the evolution of the qubit and resonator occupancy, starting from an attainable mechanical state of 0.05 phonons. The dashed lines indicate the times that a flux-tuning pulse is applied. The corresponding Wigner functions at the end of each protocol, following post-selection on $|0_1 1_2\rangle$, are shown in Figs. 5.4(c), (e), with preparation fidelities 98% and 97%, respectively. After preparation, the states evolve naturally as

$U(t)|\psi_m\rangle' = (\alpha|0\rangle + \beta e^{-in\omega_m t}|n\rangle + \gamma e^{-im\omega_m t}|m\rangle)$ including dissipation, which is however not a limiting factor because of the long lifetimes of these mechanical resonators [185]. Readout of the prepared states including Wigner tomography could be performed using similar techniques to the ones developed in Ref. [206].

The scheme described above enables the generation of interesting classes of multi-phonon superposition states, such as the ones shown in Fig. 5.4, requiring only flux-tuning pulses and a projective measurement at the end. As we show in section 5.7.2, by including a projective measurement after each step of the protocol, it is possible to generate states with arbitrary phonon number probability distributions, although constrained in the relative phases of the superpositions. Furthermore, we find that quantum superpositions with arbitrary complex coefficients can also be generated with this platform by additionally employing the qubit-qubit interaction in a controllable fashion to perform exchange-type and C-Phase gates between the two qubits (see section 5.7.1). This would enable the creation of truly arbitrary states, similar to those produced in resonantly coupled qubit-resonator systems [206, 207], with the trade-off of increased complexity in the protocol. Alternatively, using the radiation-pressure coupling with one qubit in combination with a sequence of driving pulses, could enable the creation of mechanical Schrödinger cat states as discussed in Ref. [181].

5.3. Discussion

A reconciliation of quantum mechanics and general relativity remains elusive at a theoretical level, however, there exist several proposals for testing the quantum-classical boundary with mechanical resonators offering an ideal testbed. More specifically, it has been theorised that a massive object in quantum superposition results in two coexisting space-time geometries, leading to issues with the unitary evolution, which eventually causes it to collapse [66, 68]. Importantly, this relies on the zero-point motion X_{ZPF} being much larger than the approximate size of the nucleus (~ 1 fm), which is the case in our system ($X_{\text{ZPF}} = 33$ fm). The collapse timescale t_G is inversely proportional to the mass of the object, resulting in $t_G \sim 1 - 10$ s for the parameters considered here ($m \sim 1$ pg), therefore the resonator coherence time should be larger than that. Recent advances in strain engineering techniques can enable the enhancement of beam quality factors up to $Q_m \sim 10^9$ [208], leading to relaxation times of hundreds of seconds, which would be sufficient for observing gravitational effects. Moreover, the ability to prepare a large variety of superposition states could offer an additional tool in testing such theories. The proposed architecture provides a very versatile platform in this regard, enabling not only generic quantum state preparation, but also with high fidelity, which has so far been a very challenging task.

Our approach combines the best of both worlds of two very versatile systems, namely the exquisite level of quantum control of qubits in circuit quantum electrodynamics [41], with the long lifetimes and flexibility of mechanical elements in coupling to electromagnetic radiation. The high-fidelity generation of hybrid entangled states of phonons and qubit excitations, which have no classical analogue, may provide alternative routes for testing the limits of quantum theory at macroscopic scales [199–201]. Additionally, such states are of particular importance in enabling quantum technologies with hybrid quantum systems, from quantum simulation to quantum computing and communica-

tion [42], and could also be used for coupling qubit excitations with other systems such as optical photons, cold atoms, or spin systems [202–205].

Furthermore, we have tested the robustness of our proposal against several imperfections that may occur in a realistic experimental scenario (see section 5.8). The most important limitation would be the presence of a considerable amount of flux noise, resulting in stray qubit-qubit coupling; for example, adding a fluctuation of $\delta\Phi_b = 1 - 10 \mu\Phi_0$ results in 0.1 – 1 MHz added qubit-qubit coupling J , respectively. We find that for $J < 1$ MHz the fidelity of the cooling and quantum state preparation protocols is not compromised (Fig. 5.8), therefore $\delta\Phi_b < 10 \mu\Phi_0$ is required, which is compatible with observations in similar devices [89, 209]. We note that despite the steep slope of the tripartite coupling g versus flux bias for $\Phi_b/\Phi_0 > 0.495$ (Fig. 5.1(b)), the tripartite coupling never changes by more than 1% for $\delta\Phi_b < 10 \mu\Phi_0$. Another possible experimental limitation is the deviation from the target qubit frequencies due to imperfect flux tuning pulses. We have studied the effect of this imperfection and find that targeting the qubit frequencies within 100 kHz is sufficient for high-fidelity quantum state preparation (see Fig. 5.9). Additionally, we have studied the robustness of the protocol against qubit coherence and we find that high-fidelity quantum state preparation can be obtained for relaxation and dephasing times $T_{1,2} \gtrsim 10 \mu\text{s}$, which are typical in the superconducting qubit community and compatible with 10 mT magnetic fields [196].

In conclusion, we have analysed a hybrid circuit architecture featuring strong and tuneable flux-mediated electromechanical interactions between a mechanical resonator and two superconducting transmon qubits. Using state-of-the-art parameters, we find that the coupled system can operate in the single-photon strong-coupling regime, which has been a long-standing goal in the field of optomechanics. We have proposed and numerically demonstrated several protocols for achieving ground-state cooling and preparing multi-phonon quantum superposition states as well as hybrid entanglement with high fidelities, which has been a tremendous challenge so far. Moreover, the proposed schemes for quantum manipulation are applicable to a wider range of tripartite quantum systems where a lower frequency mode, that is not directly accessible, is within the tuning range of the two other controllable modes. Our work significantly extends the quantum control toolbox of parametrically coupled radio-frequency mechanical resonators and provides a versatile on-chip interface with transmon-based processors, offering rich opportunities for technological applications as well as fundamental tests of quantum mechanics.

5.4. Methods

5.4.1. Numerical modelling

We model the dynamical evolution of the system, including environmental dissipation, with the Lindblad master equation

$$\begin{aligned} \dot{\rho} = & \frac{i}{\hbar}[\rho, \hat{H}] + (n_{\text{th}} + 1)\gamma_m \mathcal{L}[\hat{b}]\rho + n_{\text{th}}\gamma_m \mathcal{L}[\hat{b}^\dagger]\rho \\ & + \sum_{i=1}^2 \frac{1}{T_1} \mathcal{L}[\hat{c}_i]\rho + \frac{1}{T_2} \mathcal{L}[\hat{c}_i^\dagger \hat{c}_i]\rho, \end{aligned} \quad (5.11)$$

which is numerically solved using QuTiP [83]. Here, $\mathcal{L}[\hat{\rho}] \doteq (2\hat{\rho}\hat{\rho}^\dagger - \hat{\rho}^\dagger\hat{\rho} - \hat{\rho}\hat{\rho}^\dagger\hat{\rho})/2$ are superoperators describing each dissipation process, and $n_{\text{th}} = 1/[\exp(\hbar\omega_m/(k_B T)) - 1]$ is the thermal phonon number at temperature T . More specifically, we consider qubit decay and dephasing times $T_1 = T_2 = 30 \mu\text{s}$, which are consistent with measured values in a similar tuneable coupling transmon architecture (see Fig. 4.4 in chapter 4). The coupling of the mechanical mode to the environment is determined by $\gamma_m = \omega_m/Q$, where the quality factor $Q = 10^6$ is chosen in agreement with experimental observations in recently fabricated SQUID-embedded beams [185]. For completeness, we additionally include $\mathcal{O}(\phi^4 X)$ terms in the interaction Hamiltonian (see section 5.6), which nevertheless cause insubstantial corrections to the system dynamics. We model the mechanical resonator using forty levels and each transmon as a three-level system (including an anharmonicity of $E_{C_i}/h \simeq 320$ MHz). The same parameters, shown in Table 5.1, were considered in all the simulations.

5.5. Lagrangian-Hamiltonian description of the circuit

The Lagrangian describing the electromechanical system in Fig. 5.1(a) is

$$\begin{aligned} \mathcal{L} = & \frac{m\dot{X}^2}{2} - \frac{m\omega_m^2 X^2}{2} + \sum_{i=1}^2 \left[\frac{1}{2} C_i \dot{\phi}_i^2 + E_{J_i} \cos\left(\frac{\phi_i}{\phi_0}\right) \right] \\ & + \frac{1}{2} C_c (\dot{\phi}_1 - \dot{\phi}_2)^2 + E_J^c \cos\left(\frac{\phi_1 - \phi_2}{\phi_0}\right), \end{aligned} \quad (5.12)$$

where X , ϕ_i are variables representing the beam displacement and the flux on circuit node i [158], respectively, and $\phi_0 = \hbar/2e$ is the reduced flux quantum. C_i , C_c and E_{J_i} , E_J^c denote the capacitances and Josephson energies of each transmon and the coupler, respectively, and m , ω_0 are the mass and frequency of the beam. Following a Legendre transformation $H = \sum_i \phi_i Q_i - \mathcal{L}$ we obtain the system Hamiltonian

$$H = \frac{P^2}{2m} + \frac{m\omega_m^2 X^2}{2} + \sum_{i=1}^2 \left[\frac{Q_i^2}{2\tilde{C}_i} - E_{J_i} \cos\left(\frac{\phi_i}{\phi_0}\right) \right] + \frac{C_c}{C_1 C_2} Q_1 Q_2 - E_J^c \cos\left(\frac{\phi_1 - \phi_2}{\phi_0}\right), \quad (5.13)$$

where $P = \frac{\partial \mathcal{L}}{\partial \dot{X}}$ is the mechanical conjugate momentum and $Q_i = \frac{\partial \mathcal{L}}{\partial \dot{\phi}_i}$ are the electrical conjugate momenta representing charges on each circuit node. $\tilde{C}_2 = C_2 + \frac{C_1 C_c}{C_1 + C_c}$ and $\tilde{C}_1 = C_1 + \frac{C_2 C_c}{C_2 + C_c}$ denote the modified transmon capacitances due to the coupling capacitance C_c .

5.5.1. Motion-dependent flux-tuneable Josephson energy

If the two junctions of the SQUID are identical, the total Josephson energy is $E_J^c(\Phi_b) = E_{J,\Sigma}^c |\cos(\pi\Phi_b/\Phi_0)|$, where $E_{J,\Sigma}^c$ is the sum of the Josephson energies of each junction. In the presence of an in-plane magnetic field, B , the SQUID loop can pick up an additional flux, $\beta_0 B l X$, due the beam displacement, where l is the length of the suspended arm and β_0 is a geometric constant associated with the mode shape of the beam (for the first mechanical mode $\beta_0 \sim 1$) [185, 188]. Therefore, the flux- and motion-dependent

Josephson energy reads

$$E_J^c = E_{J,\Sigma}^c |\cos(\pi\Phi_b/\Phi_0 + \alpha X)|, \quad (5.14)$$

where $\alpha = \pi\beta_0 Bl/\Phi_0$ and $\Phi_0 = h/2e$ is the magnetic flux quantum. Using basic trigonometry and expanding to lowest order in X , assuming $\pi\Phi_b/\Phi_0 \gg \alpha X$, we find

$$E_J^c \simeq E_{J,\Sigma}^c [\cos(\pi\Phi_b/\Phi_0)(1 - \alpha^2 X^2) - \sin(\pi\Phi_b/\Phi_0)\alpha X], \quad (5.15)$$

The above approximation holds for $\alpha X_{ZPF} \ll 1$, which is valid for the beams considered in similar experiments and small magnetic fields ($B < 1$ T) [185].

In the above, the case of a symmetric SQUID $E_{J,1}^c = E_{J,2}^c$ is considered, however in realistic devices a finite asymmetry needs to be taken into account. The Josephson energy is therefore more accurately described by

$$E_J^c(\Phi_b, X) = E_{J,\Sigma}^c [\cos^2(\pi\Phi_b/\Phi_0 + \alpha X) + a_J^2 \sin^2(\pi\Phi_b/\Phi_0 + \alpha X)]^{1/2}, \quad (5.16)$$

where $a_J = |(E_{J,1}^c - E_{J,2}^c)/(E_{J,1}^c + E_{J,2}^c)|$ is the SQUID asymmetry [44]. For $\pi\Phi_b/\Phi_0 \gg \alpha X$, we have

$$\begin{aligned} \cos^2(\pi\Phi_b/\Phi_0 + \alpha X) &\simeq \cos^2(\pi\Phi_b/\Phi_0) - 2\alpha X \cos(\pi\Phi_b/\Phi_0) \sin(\pi\Phi_b/\Phi_0), \\ \sin^2(\pi\Phi_b/\Phi_0 + \alpha X) &\simeq \sin^2(\pi\Phi_b/\Phi_0) + 2\alpha X \cos(\pi\Phi_b/\Phi_0) \sin(\pi\Phi_b/\Phi_0). \end{aligned} \quad (5.17)$$

Substituting into Eq. (5.16), yields

$$E_J^c = E_{J,\Sigma}^c [1 + a_J^2 \tan^2(\pi\Phi_b/\Phi_0)]^{1/2} \cos(\pi\Phi_b/\Phi_0) \left[1 - \alpha X \frac{(1 - a_J^2) \tan(\pi\Phi_b/\Phi_0)}{1 + a_J^2 \tan^2(\pi\Phi_b/\Phi_0)} \right]^{1/2}, \quad (5.18)$$

which can further be simplified, assuming $\alpha X \frac{(1 - a_J^2) \tan(\pi\Phi_b/\Phi_0)}{1 + a_J^2 \tan^2(\pi\Phi_b/\Phi_0)} \ll 1$, into

$$E_J^c \simeq E_{J,\Sigma}^c [c_J \cos(\pi\Phi_b/\Phi_0) - s_J \sin(\pi\Phi_b/\Phi_0)\alpha X] + \mathcal{O}[X^2], \quad (5.19)$$

where $c_J = \sqrt{1 + a_J^2 \tan^2(\pi\Phi_b/\Phi_0)}$ and $s_J = (1 - a_J^2)/c_J$. The higher order terms

$$\mathcal{O}[X^2] = E_{J,\Sigma}^c \frac{s_J \sin^2(\pi\Phi_b/\Phi_0)}{2c_J \cos(\pi\Phi_b/\Phi_0)} \alpha^2 X^2, \quad (5.20)$$

are considered in the analysis below, however, as we will see later, they do not affect the system dynamics for the parameters used in this work.

5.5.2. Flux-mediated interactions

Expanding the last term in Eq. (5.13) up to $\mathcal{O}[\phi^4 X^2]$, in combination with Eq. (5.19), yields the following flux-mediated interaction terms

$$H_{\text{int}}^{(\text{flux})} = H_{3\text{-body}} + H_{\text{RP}} + H^{\{\phi^2\}} + H^{\{\phi^4\}} + H^{\{\phi^4 X\}} + H^{\{\phi^2 X^2\}} + H^{\{\phi^4 X^2\}}. \quad (5.21)$$

The first term describes a three-body interaction, between the two qubits and the beam

$$H_{3\text{-body}} = \alpha E_{J,\Sigma}^c s_J \sin(\pi\Phi_b/\Phi_0) \frac{\phi_1\phi_2}{\phi_0^2} X, \quad (5.22)$$

while the second term

$$H_{\text{RP}} = -\alpha E_{J,\Sigma}^c s_J \sin(\pi\Phi_b/\Phi_0) \frac{(\phi_1^2 + \phi_2^2)}{2\phi_0^2} X, \quad (5.23)$$

describes a radiation-pressure type coupling of the mechanical mode with each qubit.

The next two terms describe flux-mediated qubit-qubit interactions, where

$$H^{\{\phi^2\}} = -E_{J,\Sigma}^c c_J \cos(\pi\Phi_b/\Phi_0) \frac{\phi_1\phi_2}{\phi_0^2}, \quad (5.24)$$

is a linear dipole coupling term, and

$$H^{\{\phi^4\}} = E_{J,\Sigma}^c c_J \cos(\pi\Phi_b/\Phi_0) \left(-\frac{\phi_1^2\phi_2^2}{4\phi_0^4} + \frac{\phi_1^3\phi_2 + \phi_1\phi_2^3}{6\phi_0^4} \right), \quad (5.25)$$

is a nonlinear interaction including cross-Kerr as well as pair- and correlated-hopping terms.

The last three terms

$$H^{\{\phi^4 X\}} = \alpha E_{J,\Sigma}^c s_J \sin(\pi\Phi_b/\Phi_0) \frac{(\phi_1 - \phi_2)^4}{24\phi_0^4} X, \quad (5.26)$$

$$H^{\{\phi^2 X^2\}} = -\alpha^2 E_{J,\Sigma}^c \frac{s_J \sin^2(\pi\Phi_b/\Phi_0)}{2c_J \cos(\pi\Phi_b/\Phi_0)} \frac{(\phi_1 - \phi_2)^2}{2\phi_0^2} X^2, \quad (5.27)$$

and

$$H^{\{\phi^4 X^2\}} = \alpha^2 E_{J,\Sigma}^c \frac{s_J \sin^2(\pi\Phi_b/\Phi_0)}{2c_J \cos(\pi\Phi_b/\Phi_0)} \frac{(\phi_1 - \phi_2)^4}{24\phi_0^4} X^2, \quad (5.28)$$

describe nonlinear tripartite interactions, which are much weaker and do not contribute significantly to the dynamics compared to the leading order electromechanical terms of Eq. (5.22) and (5.23).

In addition, the last term in Eq. (5.13) leads to corrections in the bare subsystem Hamiltonians. More specifically, the inductive energy term

$$E_{J,\Sigma}^c c_J \cos(\pi\Phi_b/\Phi_0) \left(\frac{\phi_1^2 + \phi_2^2}{2\phi_0^2} - \frac{\phi_1^4 + \phi_2^4}{24\phi_0^4} \right), \quad (5.29)$$

results in an effective qubit Josephson energy

$$\tilde{E}_{J_i} = E_{J_i} + E_{J,\Sigma}^c c_J \cos(\pi\Phi_b/\Phi_0), \quad (5.30)$$

while the potential energy term

$$E_{J,\Sigma}^c \alpha X s_J \sin(\pi\Phi_b/\Phi_0) \quad (5.31)$$

leads to a displaced rest position

$$X_0 = \frac{\alpha E_{J,\Sigma}^c s_J \sin(\pi\Phi_b/\Phi_0)}{2m\omega_m}. \quad (5.32)$$

The latter does not affect the dynamics and can be absorbed in a redefinition of $X \rightarrow (X - X_0)$.

5.6. Circuit quantisation

We now switch to a quantum mechanical description of the circuit, promoting all canonical variables to quantum operators

$$\begin{aligned} \hat{X} &= X_{\text{ZPF}} (\hat{b} + \hat{b}^\dagger), \quad \hat{P} = P_{\text{ZPF}} i(\hat{b}^\dagger - \hat{b}), \\ \hat{\phi}_i &= \sqrt{\frac{\hbar Z_i}{2}} (\hat{c}_i + \hat{c}_i^\dagger), \quad \hat{Q}_i = \sqrt{\frac{\hbar}{2Z_i}} i(\hat{c}_i^\dagger - \hat{c}_i), \end{aligned} \quad (5.33)$$

where $\hat{c}_i^{(\dagger)}$ and $\hat{b}^{(\dagger)}$ are ladder operators describing the annihilation (creation) of photons and phonons, respectively, and satisfy bosonic commutation relations $[\hat{c}_i, \hat{c}_j^\dagger] = \delta_{ij}$ and $[\hat{b}, \hat{b}^\dagger] = 1$. The zero-point fluctuations in the mechanical displacement and momentum are given by $X_{\text{ZPF}} = \sqrt{\hbar/(2m\omega_m)}$ and $P_{\text{ZPF}} = \sqrt{\hbar m\omega_m/2}$, respectively. $Z_i = \frac{\hbar}{e^2} \sqrt{E_{C_i}/2\tilde{E}_{J_i}}$ denotes the impedance of each transmon, where $E_{C_i} = \frac{e^2}{2C_i}$ is its charging energy. Since the qubits are in the transmon regime [44], $\tilde{E}_{J_i} \gg E_{C_i}$, the uncoupled electromechanical system is well-described by

$$\hat{H}_0 = \hbar\omega_m \hat{b}^\dagger \hat{b} + \sum_{i=1}^2 \hbar\omega_i \hat{c}_i^\dagger \hat{c}_i - \frac{E_{C_i}}{2} \hat{c}_i^\dagger \hat{c}_i^\dagger \hat{c}_i \hat{c}_i, \quad (5.34)$$

with qubit frequencies $\omega_i = \frac{1}{\hbar} \left(\sqrt{8\tilde{E}_{J_i} E_{C_i}} - E_{C_i} \right)$.

5.6.1. Tripartite coupling

Following Eq. (5.22) we can now write the Hamiltonian operator describing the three-body interaction

$$\begin{aligned} \hat{H}_{3\text{-body}} &= \hbar g (\hat{c}_1 + \hat{c}_1^\dagger)(\hat{c}_2 + \hat{c}_2^\dagger)(\hat{b} + \hat{b}^\dagger), \\ &= \hbar g (\hat{c}_1^\dagger \hat{c}_2 + \hat{c}_1 \hat{c}_2^\dagger)(\hat{b} + \hat{b}^\dagger), \end{aligned} \quad (5.35)$$

where, in the second step, we have made a rotating-wave approximation (RWA) to neglect fast rotating terms $\hat{c}_1 \hat{c}_2 \hat{b}^{(\dagger)}$ and $\hat{c}_1^\dagger \hat{c}_2^\dagger \hat{b}^{(\dagger)}$, which do not contribute to the dynamics since $\omega_1, \omega_2 \gg \omega_m, g$. The tripartite coupling strength is given by

$$g = \frac{\alpha \sqrt{Z_1 Z_2}}{2\phi_0^2} E_{J,\Sigma}^c \sin(\pi\Phi_b/\Phi_0) X_{\text{ZPF}}. \quad (5.36)$$

5.6.2. Radiation-pressure couplings

The radiation-pressure interaction between each qubit and the beam, in Eq. (5.23), can be expressed in second quantisation form as

$$\hat{H}_{\text{RP}} = \hbar g_1 \hat{c}_1^\dagger \hat{c}_1 (\hat{b} + \hat{b}^\dagger) + \hbar g_2 \hat{c}_2^\dagger \hat{c}_2 (\hat{b} + \hat{b}^\dagger), \quad (5.37)$$

following a RWA. The radiation-pressure coupling strengths are given by

$$g_i = \frac{\alpha Z_i}{2\phi_0^2} E_{\text{J},\Sigma}^c \sin(\pi\Phi_b/\Phi_0) X_{\text{ZPF}}. \quad (5.38)$$

5.6.3. Qubit-qubit couplings

Following circuit quantisation and a RWA, the linear qubit-qubit interaction Hamiltonian in Eq. (5.24) becomes

$$H^{\{\phi^2\}} = -\hbar J_{\text{L}} (\hat{c}_1^\dagger \hat{c}_2 + \hat{c}_1 \hat{c}_2^\dagger) \quad (5.39)$$

where

$$J_{\text{L}} = \frac{\sqrt{Z_1 Z_2}}{2\phi_0^2} E_{\text{J},\Sigma}^c \cos(\pi\Phi_b/\Phi_0), \quad (5.40)$$

The qubits also couple via their charge degrees of freedom ($Q_1 Q_2$ term in Eq. (5.13)), which results in the same type of linear interaction with coupling strength

$$J_{\text{C}} = \frac{C_{\text{c}}}{2C_1 C_2} (Z_1 Z_2)^{-1/2}. \quad (5.41)$$

Combining these together leads to an overall exchange-type interaction

$$H_{12} = \hbar (J_{\text{C}} - J_{\text{L}}) (\hat{c}_1^\dagger \hat{c}_2 + \hat{c}_1 \hat{c}_2^\dagger), \quad (5.42)$$

which can be suppressed at the desired operating point (Φ_b) with the right choice of coupling capacitor C_{c} .

The nonlinear interaction between the two transmons in Eq. (5.25) is given by

$$\begin{aligned} \hat{H}^{\{\phi^4\}} &= \frac{\hbar V}{4} (\hat{c}_1^\dagger + \hat{c}_1)^2 (\hat{c}_2^\dagger + \hat{c}_2)^2 \\ &\quad + \frac{\hbar J_{n_1}}{3} (\hat{c}_1^\dagger + \hat{c}_1)^3 (\hat{c}_2^\dagger + \hat{c}_2) \\ &\quad + \frac{\hbar J_{n_2}}{3} (\hat{c}_1^\dagger + \hat{c}_1) (\hat{c}_2^\dagger + \hat{c}_2)^3. \end{aligned} \quad (5.43)$$

The first term, following a RWA, results in a cross-Kerr interaction, $V \hat{c}_1^\dagger \hat{c}_1 \hat{c}_2^\dagger \hat{c}_2$, with coupling strength

$$V = -\frac{\hbar Z_1 Z_2}{4\phi_0^4} E_{\text{J},\Sigma}^c \cos(\pi\Phi_b/\Phi_0). \quad (5.44)$$

Additionally the same term yields a pair-hopping interaction $\frac{V}{4}(\hat{c}_1^\dagger \hat{c}_1^\dagger \hat{c}_2 \hat{c}_2 + \text{H.c.})$, which however is not contributing to the dynamics for single-excitation levels. Finally, the other two terms in Eq. (5.43) result in correlated hopping interactions $[\hat{c}_1^\dagger (J_{n_1} \hat{c}_1^\dagger \hat{c}_1 + J_{n_2} \hat{c}_2^\dagger \hat{c}_2) \hat{c}_2 + \text{H.c.}]$, with

$$J_{n_{1(2)}} = -\frac{\hbar \sqrt{Z_{1(2)}^3 Z_{2(1)}}}{24\phi_0^4} E_{J,\Sigma}^c \cos(\pi\Phi_b/\Phi_0), \quad (5.45)$$

which contribute to the linear coupling in Eq. (5.42) as $J \rightarrow J + J_{n_1} + J_{n_2}$.

5.6.4. Higher-order tripartite interactions

The next-to-leading order electromechanical interactions are given by

$$\begin{aligned} \hat{H}^{\{\phi^4 X\}} &= \hbar g_{\phi_1^2 \phi_2^2 x} (\hat{c}_1^\dagger + \hat{c}_1)^2 (\hat{c}_2^\dagger + \hat{c}_2)^2 (\hat{b} + \hat{b}^\dagger) \\ &+ \hbar g_{\phi_1^3 \phi_2 x} (\hat{c}_1^\dagger + \hat{c}_1)^3 (\hat{c}_2^\dagger + \hat{c}_2) (\hat{b} + \hat{b}^\dagger) \\ &+ \hbar g_{\phi_1 \phi_2^3 x} (\hat{c}_1^\dagger + \hat{c}_1) (\hat{c}_2^\dagger + \hat{c}_2)^3 (\hat{b} + \hat{b}^\dagger), \end{aligned} \quad (5.46)$$

with nonlinear coupling strengths

$$g_{\phi_1^2 \phi_2^2 x} = \frac{\hbar \alpha Z_1 Z_2}{16\phi_0^4} E_{J,\Sigma}^c \sin(\pi\Phi_b/\Phi_0) X_{\text{ZPF}}, \quad (5.47)$$

$$g_{\phi_1^3 \phi_2 x} = \frac{\hbar \alpha Z_1^{3/2} Z_2^{1/2}}{24\phi_0^4} E_{J,\Sigma}^c \sin(\pi\Phi_b/\Phi_0) X_{\text{ZPF}}, \quad (5.48)$$

and

$$g_{\phi_1 \phi_2^3 x} = \frac{\hbar \alpha Z_1^{1/2} Z_2^{3/2}}{24\phi_0^4} E_{J,\Sigma}^c \sin(\pi\Phi_b/\Phi_0) X_{\text{ZPF}}. \quad (5.49)$$

The last two terms also lead to a small correction of the tripartite coupling strength $g \rightarrow g + 3g_{\phi_1^3 \phi_2 x} + 3g_{\phi_1 \phi_2^3 x}$. These terms, although weaker, are not negligible (since they are of the same order or larger than dissipation rates) and they are included in simulating the system dynamics.

The $\mathcal{O}[\phi^2 X^2]$ terms in Eq. (5.27) can be written as,

$$\hat{H}^{\{\phi^2 X^2\}} = \sum_{i,j} \hbar g_{\phi_i \phi_j x^2} \hat{c}_i^\dagger \hat{c}_j (\hat{b} + \hat{b}^\dagger)^2 \quad (5.50)$$

where

$$g_{\phi_i \phi_j x^2} = \frac{\alpha^2 \sqrt{Z_i Z_j}}{2\phi_0^2} E_{J,\Sigma}^c \frac{s_j \sin^2(\pi\Phi_b/\Phi_0)}{2c_j \cos(\pi\Phi_b/\Phi_0)} X_{\text{ZPF}}^2. \quad (5.51)$$

For the parameters used in this work ($\alpha X_{\text{ZPF}} \sim 10^{-6}$) the coupling is negligible and does not affect the system dynamics (the same holds for the even weaker $\mathcal{O}[\phi^4 X^2]$ terms). Interestingly, however, for $i = j$ we find a dispersive (cross-Kerr) interaction $\hat{c}_i^\dagger \hat{c}_i \hat{b}^\dagger \hat{b}$ of each qubit with the resonator, which is active even when the qubits are far detuned and could potentially be employed for phonon-sensitive measurements of the mechanical state [173].

5.7. Protocols for arbitrary quantum state generation

5.7.1. States with arbitrary complex coefficients

In the main text we demonstrated a protocol for creating multi-phonon quantum superposition states by alternating the qubit frequencies such that different parts of the tripartite interaction become resonant. By controlling the interaction times and post-selecting on the qubit state at the end of the protocol, we showed the possibility of creating interesting classes of superposition states with high fidelity. However, this protocol alone is not sufficient for generating mechanical superposition states $|\psi\rangle = \sum_{n=0}^N c_n |n_m\rangle$ with arbitrary complex coefficients c_n , since there is no phase degree of freedom to control in the protocol. This is due to the fact that the coupling constant g is not an adjustable complex number and in practical implementations the interaction time is the only parameter that can be varied.

However, there is another tuning knob that can be employed by taking advantage of the qubit-qubit exchange-type interaction $J (\hat{c}_1^\dagger \hat{c}_2 + \hat{c}_1 \hat{c}_2^\dagger)$. Detuning the qubits by $\Delta = |\omega_1 - \omega_2| \gg \omega_m$, while tuning the coupling SQUID such that there is a finite exchange-type coupling strength $J \geq \Delta$, results in a resonant qubit-qubit interaction that couples $|0_1 1_2\rangle$ and $|1_1 0_2\rangle$. For example, starting from $|0_1 1_2\rangle$ one would end up with state $[\cos(Jt)|0_1 1_2\rangle - i \sin(Jt)|1_1 0_2\rangle]$ after time t (at $t = \pi/(2J)$ this realises a SWAP gate). Furthermore, by detuning the qubit frequencies such that $\Delta > J$ it is also possible to introduce a relative phase between the qubit states $|0_1 1_2\rangle$ and $|1_1 0_2\rangle$ (C-Phase gate), as in Ref. [210]. Combining this gate with the resonant qubit-qubit interaction, acting on $|0_1 1_2\rangle$ would result in

$$U_J(t, \theta)|0_1 1_2\rangle = \cos(Jt)|0_1 1_2\rangle - i e^{i\theta} \sin(Jt)|1_1 0_2\rangle. \quad (5.52)$$

We note that our system, is analogous to the one studied theoretically by Law and Eberly [207] and experimentally by Hofheinz et al. [206]. The system studied in these references considers a resonator that is controllably coupled to a qubit (with local qubit driving) via a resonant exchange-type interaction (Jaynes-Cummings). It is shown that an arbitrary resonator state can be generated by interleaving the Jaynes-Cummings evolution with qubit driving. The two-qubit states $|0_1 1_2\rangle$ and $|1_1 0_2\rangle$ in our system can be mapped to the single qubit basis $|0\rangle$ and $|1\rangle$ considered in Law and Eberly. Furthermore, the tripartite interaction can be mapped to the qubit-resonator Jaynes-Cummings interaction, where in our system we additionally have the possibility of realising the equivalent of a counter-rotating Jaynes-Cummings interaction by exchanging the qubit frequencies. The equivalent of qubit driving can then be performed by controlling the evolution under the exchange qubit-qubit interaction U_J described in Eq. (5.52).

We will consider the case where an arbitrary state $|\psi\rangle_m = \sum_{n=0}^N a_n |n_m\rangle$ is generated following post-selection from the arbitrary entangled state $|\psi\rangle = \sum_{n=0}^{N-1} (a_n |0_1 n_m 1_2\rangle + b_n |1_1 n_m 0_2\rangle) + a_N |0_1 N_m 1_2\rangle$. That is, if we can create the above state $|\psi\rangle$ with arbitrary complex coefficients, it is then straightforward to collapse it to $|\psi\rangle_m$ following post-selection on the $|0_1 1_2\rangle$ qubit state. Inspired by Refs. [206, 207], let us now consider the problem of generating the arbitrary state $|\psi\rangle$ from the inverse point of view, i.e. by proving that it is always possible to empty it. Suppose we start from $|\psi\rangle = \sum_{n=0}^{N-1} (a_n |0_1 n_m 1_2\rangle + b_n |1_1 n_m 0_2\rangle) + a_N |0_1 N_m 1_2\rangle$ (Fig. 5.5(a)). Then by apply-

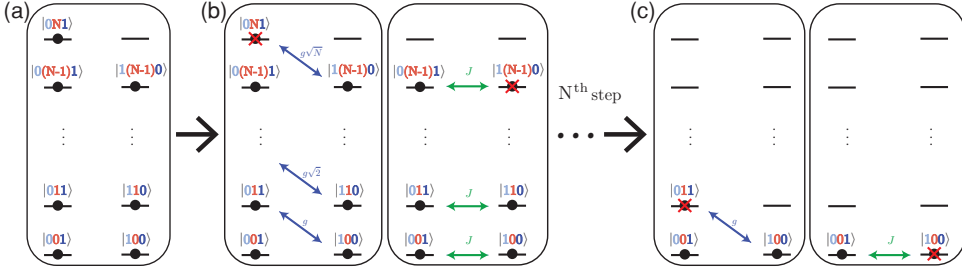


Figure 5.5: **Protocol for arbitrary state generation.** (a) The protocol is calculated in reverse by emptying an arbitrary entangled state $|\psi\rangle = \sum_{n=0}^{N-1} (a_n|0_1 n_m 1_2\rangle + b_n|1_1 n_m 0_2\rangle) + a_N|0_1 N_m 1_2\rangle$ (from this state it is always possible to obtain an arbitrary mechanical state by post-selecting on $|0_1 1_2\rangle$). (b) The first step of the protocol is shown, which consists of two substeps: At first we turn on the (inverse of the) C-Phase gate and the tripartite interaction $\hat{U}(t) = e^{i(\hat{c}_1^\dagger \hat{b} \hat{c}_2 + \text{H.c.})t}$ such that all population from $|0_1 N_m 1_2\rangle$ is emptied to $|1_1 (N-1)_m 0_2\rangle$. Then, by applying another C-Phase gate in combination with resonant qubit-qubit interaction for a variable time it is possible to empty $|1_1 (N-1)_m 0_2\rangle$ to $|0_1 (N-1)_m 1_2\rangle$. (c) Following this procedure N times it is possible to empty the original state in (a) and end up in $|0_1 0_m 1_2\rangle$.

ing the (inverse of the) C-Phase gate and the tripartite interaction $\hat{U}^\dagger(t) = e^{i(\hat{c}_1^\dagger \hat{b} \hat{c}_2 + \text{H.c.})t}$ for phase θ_A and time t_A , the probability amplitude of state $|0_1 N_m 1_2\rangle$ becomes

$$a_N \rightarrow a_N \cos(g\sqrt{N}t_A) + ie^{\theta_A} b_{N-1} \sin(g\sqrt{N}t_A). \quad (5.53)$$

By appropriately choosing θ_A and t_A , it is possible to make the above probability amplitude zero, such that all phonons occupying the state $|0_1 N_m 1_2\rangle$ are transferred to $|1_1 (N-1)_m 0_2\rangle$ (see Fig. 5.5(b)).

The step above also results in incomplete transfer of phonons between states $|0_1 n_m 1_2\rangle$ and $|1_1 (n-1)_m 0_2\rangle$ (for $n < N$), after which we are left with the state $|\psi\rangle' = \sum_{n=0}^{N-1} (a'_n|0_1 n_m 1_2\rangle + b'_n|1_1 n_m 0_2\rangle)$. Now by combining the (inverse of the) C-Phase gate and resonant qubit-qubit interaction $U_J^\dagger(t_J, \theta_J)|\psi\rangle'$ the probability amplitude of state $|1_1 (N-1)_m 0_2\rangle$ becomes

$$b_{N-1} \rightarrow b_{N-1} \cos(Jt_J) + ie^{\theta_J} a_{N-1} \sin(Jt_J), \quad (5.54)$$

which can be made zero by appropriately choosing θ_J and t_J such that all phonons occupying $|1_1 (N-1)_m 0_2\rangle$ are transferred to $|0_1 (N-1)_m 1_2\rangle$ (see Fig. 5.5(b)). By applying the above two steps N times it is possible to completely empty the initial state, leading the system to $|0_1 0_m 1_2\rangle$ (Fig. 5.5(c)). Therefore, reversing the problem, it is possible to generate any arbitrary mechanical state $|\psi\rangle_m = \sum_{n=0}^N a_n |n_m\rangle$ by creating the arbitrary entangled state

$$\prod_{j=N}^1 \hat{U}_{\theta_{A_j}} \hat{U}(t_{A_j}) \hat{U}_J(t_{J_j}, \theta_{J_j}) |0_1 0_m 1_2\rangle = \sum_{n=0}^{N-1} (a_n |0_1 n_m 1_2\rangle + b_n |1_1 n_m 0_2\rangle) + a_N |0_1 N_m 1_2\rangle, \quad (5.55)$$

and post-selecting on $|0_1 1_2\rangle$.

5.7.2. States with arbitrary phonon number probability distributions

The protocol presented in the previous section can enable the creation of any mechanical quantum state with arbitrary coefficients. Although this protocol is experimentally feasible, it can become complex as it requires a lot of additional tuning to realise the C-Phase and exchange-type gates between the qubits. Here we describe an alternative protocol that only employs the tripartite interactions, therefore requiring only alternating between the qubit frequencies, and post-selective measurements at each step. Reducing the complexity of tuning pulses comes at the cost of not being able to create states with arbitrary complex coefficients, although it is possible to generate states with arbitrary phonon number probability distributions as we see below.

The protocol relies on initially preparing the two qubits in an arbitrary entangled state (Fig. 5.6(a)). Assuming the resonator is in the ground state, the tripartite system is initially described by the following wavefunction

$$|\psi\rangle_0 = (\alpha|0_11_2\rangle + \beta|1_10_2\rangle)|0_m\rangle, \quad (5.56)$$

where α, β are complex numbers that can be chosen arbitrarily and are related by $|\alpha|^2 + |\beta|^2 = 1$. As described in the previous section, one can prepare this state by activating the exchange-type qubit-qubit interaction $U_J(t, \theta)$. This can be done by detuning the qubits sufficiently such that their frequency difference is much greater than the mechanical frequency, and at the same time smaller than the direct qubit-qubit coupling, i.e. $J \geq |\omega_1 - \omega_2| \gg \omega_m$, which can be adjusted by changing the flux Φ_b on the coupling SQUID.

The next step, schematically depicted in Fig. 5.6(b), consists of the following three substeps:

1. Flux pulse into resonance condition $\omega_2^+ = \omega_1 + \omega_m$ for variable time t_1
2. Flux pulse into resonance condition $\omega_2^- = \omega_1 - \omega_m$ for variable time t_2 ,
3. Projective measurement on one of the qubits and post-selection on $|0_11_2\rangle$.

The initial wavefunction is transformed into

$$|\psi\rangle_1 = \hat{P}\hat{U}_B(t_2)\hat{U}_A(t_1)|\psi\rangle_0, \quad (5.57)$$

where $\hat{P} = |0_11_2\rangle\langle 0_11_2|$ and $\hat{U}_{A,B}(t_{1,2}) = e^{-i\hat{H}_{A,B}t_{1,2}}$, with interaction Hamiltonians $\hat{H}_A = \hat{c}_1^\dagger \hat{b}^\dagger \hat{c}_2 + \text{H.c.}$ and $\hat{H}_B = \hat{c}_1 \hat{b}^\dagger \hat{c}_2^\dagger + \text{H.c.}$, respectively.

Below we derive the resulting wavefunction after each substep:

1. $\hat{U}_A(t_1)|\psi\rangle_0 = \alpha(\cos(gt_1)|0_10_m1_2\rangle - i\beta \sin(gt_1)|1_11_m0_2\rangle) + \beta|1_10_m0_2\rangle,$
2. $\hat{U}_B(t_2)\hat{U}_A(t_1)|\psi\rangle_0 = \alpha \cos(gt_1)|0_10_m1_2\rangle + \beta (\cos(gt_2)|1_10_m0_2\rangle + \sin(gt_2)|0_11_m1_2\rangle) + \alpha \sin(gt_1) \left(\cos(g\sqrt{2}t_2)|1_11_m0_2\rangle + \sin(g\sqrt{2}t_2)|0_12_m1_2\rangle \right)$
3. $\hat{P}\hat{U}_B(t_2)\hat{U}_A(t_1)|\psi\rangle_0 = \frac{1}{P} [\alpha \cos(gt_1)|0_m\rangle + \beta \sin(gt_2)|1_m\rangle + \alpha \sin(gt_1) \sin(g\sqrt{2}t_2)|2_m\rangle] |0_11_2\rangle,$ (5.58)

where P is a normalisation factor determined by the Born rule.

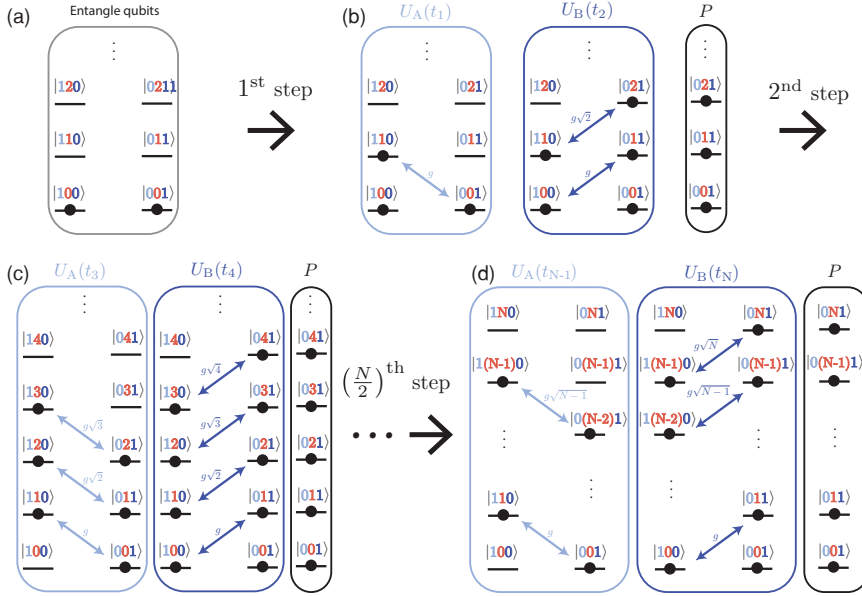


Figure 5.6: **Protocol for generating states with arbitrary phonon number probability distributions using flux pulsing and projective measurements.** (a) Assuming the mechanical resonator is in the ground state, we can start the protocol with the qubits in an entangled state. This can be achieved by letting the qubits interact for a variable time without interacting with the resonator, e.g. by tuning the system such that the condition $J \geq |\omega_1 - \omega_2| \gg \omega_m$ is satisfied. (b) The first step of the protocol is shown, which consists of three substeps: At first we turn on the interaction $\hat{H}_A = \hat{c}_1^\dagger \hat{b}^\dagger \hat{c}_2 + \text{H.c.}$, by bringing the system in the resonance condition $\omega_2^+ = \omega_1 + \omega_m$, for variable time t_1 (light blue frame). Then, by tuning to $\omega_2^- = \omega_1 - \omega_m$, the system evolves according to $\hat{H}_B = \hat{c}_1 \hat{b} \hat{c}_2^\dagger + \text{H.c.}$ for a different time t_2 (dark blue frame). Finally, we measure either qubit 1 or 2 and post-select on the outcome $|1_1 0_2\rangle$ (black frame). The freedom in choosing the coefficients of the initial two-qubit state together with the choice of interaction times t_1 and t_2 give enough degrees of freedom for generating a superposition state with arbitrary phonon number probability distribution up to the third level. (c) Second step of the protocol leading to a superposition state up to the fifth level. (d) General case for creating states with arbitrary phonon number probability distribution up to N , following $N/2$ steps.

Evidently, following this first step one has enough degrees of freedom (α, t_1, t_2) to create states with arbitrary phonon number probability distribution up to three levels, $|\psi\rangle_1 = \sum_{n=0}^2 c_n |n_m\rangle |0_1 1_2\rangle$. Following a second step (Fig. 5.6(c)), we find

$$\begin{aligned} \hat{P} \hat{U}_B(t_4) \hat{U}_A(t_3) |\psi\rangle_1 &= |0_1 1_2\rangle \{ c_0 \cos(gt_3) |0_m\rangle + c_1 \cos(g\sqrt{2}t_3) \cos(gt_4) |1_m\rangle \\ &\quad + (c_0 \sin(gt_3) \sin(g\sqrt{2}t_4) + c_2 \cos(g\sqrt{3}t_3) \cos(g\sqrt{2}t_4)) |2_m\rangle \\ &\quad + c_1 \sin(g\sqrt{2}t_3) \sin(g\sqrt{3}t_4) |3_m\rangle + c_2 \cos(g\sqrt{4}t_4) |4_m\rangle \}. \end{aligned} \quad (5.59)$$

The addition of two more variables t_3, t_4 enables the creation of states with arbitrary phonon number probability distribution up to $|4\rangle$.

Suppose we start from an arbitrary mechanical state $|\psi\rangle = \sum_{n=0}^{N-2} c_n |n_m\rangle |0_1 1_2\rangle$,

which can be created by applying the above protocol $(N/2 - 1)$ times. Then, following another step we have

$$\prod_{j=N/2}^1 \hat{P}\hat{U}_B(t_{2j})\hat{U}_A(t_{2j-1})|\psi\rangle_0 = \hat{P}\hat{U}_B(t_{N-1})\hat{U}_A(t_N) \left(\sum_{n=0}^{N-2} c_n |n\rangle |0_1 1_2\rangle \right) = \sum_{n=0}^N c'_n |n\rangle |0_1 1_2\rangle, \quad (5.60)$$

where the new coefficients are determined by the previous ones according to the following relations:

$$c'_0 = c_0 \cos(gt_{N-1}) \quad (5.61)$$

$$c'_1 = c_1 \cos(g\sqrt{2}t_{N-1}) \cos(gt_N) \quad (5.62)$$

$$c'_2 = c_0 \sin(gt_{N-1}) \sin(g\sqrt{2}t_N) + c_2 \cos(g\sqrt{3}t_{N-1}) \cos(g\sqrt{2}t_N) \quad (5.63)$$

⋮
⋮
⋮

$$c'_n = c_{n-2} \sin(g\sqrt{n-1}t_{N-1}) \sin(g\sqrt{n}t_N) + c_n \cos(g\sqrt{n+1}t_{N-1}) \cos(g\sqrt{n}t_N) \quad (5.64)$$

⋮
⋮
⋮

$$c'_{N-1} = c_{N-3} \sin(g\sqrt{N-2}t_{N-1}) \sin(g\sqrt{N-1}t_N) \quad (5.65)$$

$$c'_N = c_{N-2} \sin(g\sqrt{N-1}t_{N-1}) \sin(g\sqrt{N}t_N). \quad (5.66)$$

Therefore, applying this protocol $N/2$ times can lead to the creation of states with arbitrary phonon number probability distribution up to $|N\rangle$.

5.8. Validity for non-ideal system parameters

Although in the simulations we have considered realistic parameters taken from recent experiments, we realise that in an experimental scenario system parameters such as the qubit coherence may significantly deviate from the ones considered in Table 1. Although bad qubit coherence may not affect the success of the cooling protocol, it can pose limits on the quantum state preparation protocols. We have therefore examined the dependence of the fidelity of the prepared quantum state in Fig. 5.3 to the ideal evolution $|\psi_{\text{ideal}}\rangle = U(t)|0_1 0_m 1_2\rangle = \cos(gt)|0_1 0_m 1_2\rangle - i \sin(gt)|1_1 1_m 0_2\rangle$ on the qubit coherence. In Fig. 5.7 we plot the evolution of the fidelity of the prepared density matrix ρ to the ideal one $\rho_{\text{ideal}} = |\psi_{\text{ideal}}\rangle\langle\psi_{\text{ideal}}|$, for different values of T_1 (assuming $T_2 = T_1$). The dashed curves correspond to e^{-t/T_1} . We find that high-fidelity state preparation ($> 90\%$) can be achieved with qubit coherence times of $T_1, T_2 \sim 10 \mu\text{s}$ which are standard in the superconducting qubit community and achievable in the presence of 10 mT magnetic fields [196].

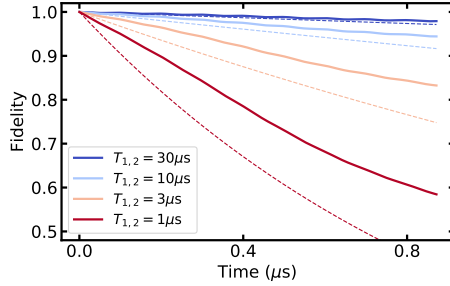


Figure 5.7: **Effect of qubit coherence on quantum state preparation.** Evolution of the fidelity of the prepared state to the ideal state, $\cos(gt)|0_1 0_m 1_2\rangle - i \sin(gt)|1_1 1_m 0_2\rangle$, using the protocol presented in Fig. 5.3, for different values of relaxation and pure dephasing times (assuming $T_1 = T_2$). The dashed curves correspond to e^{-t/T_1} for each case.

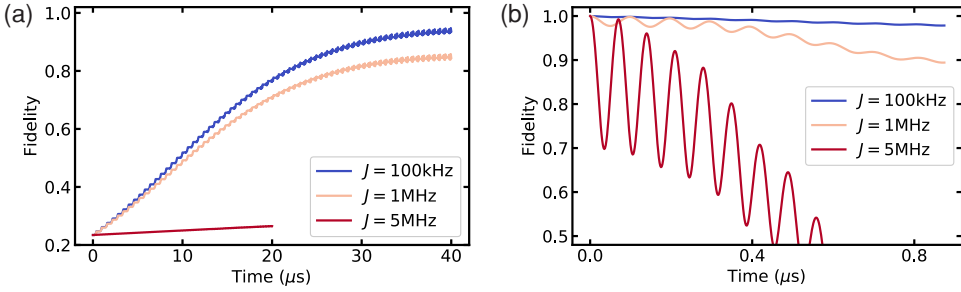


Figure 5.8: **Effect of flux bias fluctuations and stray qubit-qubit coupling on ground-state cooling and quantum state preparation.** (a) Evolution of the fidelity of the prepared mechanical state to the vacuum state using the cooling protocol of Fig. 5.2, for different values of qubit-qubit coupling $J = 100$ kHz, 1 MHz and 5 MHz, corresponding to flux bias fluctuations of $\delta\Phi_b/\Phi_0 = 10^{-6}$, 10^{-5} and 5×10^{-5} , respectively. The same number of cooling steps were used in all simulations, where for $J = 5$ MHz a cooling step of 100 ns instead of 200 ns was chosen as an optimal cooling time. (b) Evolution of the fidelity of the prepared state to the ideal state, $\cos(gt)|0_1 0_m 1_2\rangle - i \sin(gt)|1_1 1_m 0_2\rangle$, following the protocol used in Fig. 5.3, for the same variations on J and $\delta\Phi_b/\Phi_0$ as in (a).

One effect that is not considered in the main text is that of fluctuations on the flux bias channel $\delta\Phi_b$. These can occur as a result of environmental magnetic field noise or noise of the current source used for biasing the flux line. Given the stability of our current sources and assuming flux noise levels reported in similar devices [89, 209], we estimate such fluctuations to be around $\delta\Phi_b/\Phi_0 \sim 10^{-6}$ during the course of the preparation protocols. The most important effect of flux fluctuations would be to introduce a stray qubit-qubit exchange-type coupling as $J_L \propto E_{J,\Sigma}^c \cos(\pi(\Phi_b + \delta\Phi_b)/\Phi_0)$. More specifically, adding a fluctuation of $\delta\Phi_b/\Phi_0 \sim 10^{-6}$ would result in $J_L \rightarrow J_L + 100$ kHz, while $\delta\Phi_b/\Phi_0 \sim 10^{-5}$ and $\delta\Phi_b/\Phi_0 \sim 10^{-4}$ translate to additional coupling of 1 and 10 MHz, respectively. The latter would be detrimental for the state preparation protocols as it is of the order of the mechanical frequency. Note that the effect of flux noise on the qubit-qubit coupling is also amplified by our choice of a large coupling Josephson

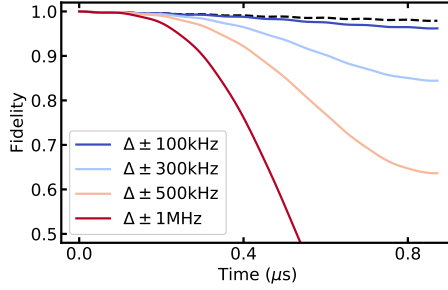


Figure 5.9: **Effect of imperfect flux pulsing on quantum state preparation.** Evolution of the fidelity of the prepared state to the ideal state using the protocol presented in Fig. 5.3, for different variations of the qubit-qubit detuning Δ . The black dashed curve corresponds to no variation, i.e. $\Delta = \omega_m$.

energy amplitude $E_{J,\Sigma}^c/h = 200$ GHz. In Fig. 5.8 we plot the effect of a finite qubit-qubit coupling on the cooling and quantum state preparation protocols. We find that for $J < 1$ MHz (therefore $\delta\Phi_b < 10 \mu\Phi_0$) it is possible to maintain high-fidelity quantum state preparation. Note that despite the sharp dependence of the tripartite coupling on the flux bias (Fig. 5.1), this change is less than 0.1% in the case of $\delta\Phi_b < 10 \mu\Phi_0$.

Additionally, in Fig. 5.9 we examine the effect of imperfect qubit flux pulsing on the fidelity of the prepared quantum state. We find that the fidelity of the protocol is sensitive to this parameter and that targeting the qubit frequencies within ~ 100 kHz is required for high-fidelity quantum state preparation.

6

Flux-mediated optomechanics with a transmon qubit in the single-photon ultrastrong-coupling regime

*All things will be in everything; nor is it possible for them to be apart,
but all things have a portion of everything.*

Anaxagoras (Fragments)

In this chapter, we propose a scheme for controlling a radio-frequency mechanical resonator at the quantum level using a single superconducting qubit. Similar to the previous chapter, the circuit consists of a transmon qubit connected in parallel to a superconducting quantum interference device (SQUID) with an embedded mechanical beam in one of its arms. By considering a longer beam we enable the study of the resonator-qubit system in the ultrastrong-coupling regime, where the optomechanical coupling is comparable to or even larger than the mechanical frequency. We investigate the dynamics of the driven system for a range of coupling strengths and find an optimum regime for ground-state cooling, consistent with previous theoretical investigations considering linear cavities. Furthermore, we numerically demonstrate a protocol for generating hybrid discrete- and continuous-variable entanglement as well as mechanical Schrödinger cat states, which can be realised within the current state of the art.

This chapter appears with minor differences in arxiv:1911.05550.

6.1. Introduction

The rapid progress in the field of cavity optomechanics and electromechanics over the last decade has enabled the study of massive micro- and nano-mechanical objects in the quantum regime, paving the way for several technological applications as well as fundamental tests of quantum mechanics [63, 67, 202]. Important advances include ground-state cooling of mechanical resonators [167, 168], ponderomotive squeezing [211–213], coherent state transfer [214], as well as preparation of quantum states [172, 174]. Such optomechanical setups consist of a mechanical drum or beam resonator that is parametrically coupled to a higher-frequency optical or microwave cavity via radiation-pressure. Typically the coupling g_0 is lower than the decay rate of the cavity κ , limiting the ability to manipulate the mechanical element at single-photon levels. A strong linearised interaction is effectively achieved by driving the cavity with thousands or even millions of photons, which however leads to unresolved heating issues [168, 215, 216] and makes it difficult to couple to artificial atoms working in the single-photon regime. Growing efforts in the field are focusing on reaching the single-photon strong-coupling regime, $g_0 > \kappa$, which holds great promise for high-fidelity mechanical state preparation. An even more intriguing prospect is the possibility of reaching the *single-photon ultrastrong-coupling* regime, where g_0 additionally approaches or even exceeds the mechanical frequency ω_M , leading to interesting phenomena such as photon blockade and non-classical mechanical states [176–179, 217].

A promising playground for enhancing the single-photon coupling is flux-mediated optomechanics, in which a vibrating mechanical element parametrically modulates the inductance of a LC microwave cavity. This can be realised by integrating a mechanical beam into the arms of a superconducting quantum interference device (SQUID), which leads to radiation-pressure type coupling between the beam resonator and the cavity flux degree of freedom [161, 184, 188, 218]. A recent experiment has confirmed the viability of this approach using linear SQUID cavities [185], however, reaching the single-photon strong-coupling still remains a challenge. One limitation of this setup was the suppression of the flux susceptibility, which is proportional to the optomechanical coupling, due to the geometric inductance being a considerable fraction of the total inductance of the linear SQUID. Another limitation of this scheme is related to the fact that the optomechanical coupling is maximised when the applied flux through the SQUID is close to a half-integer flux quantum, which is where the cavity frequency becomes zero. Moreover, the absence of a strong non-linear element, such as a qubit, can limit the range of states that can be created.

Here we show that it is possible to circumvent these issues in a modified circuit that incorporates a superconducting transmon qubit [44] coupled to the mechanical resonator via a flux-mediated radiation-pressure interaction in the single-photon ultrastrong-coupling regime. Using parameters obtained from recent experiments [185], we investigate the possibility of cooling the resonator via sideband driving of the qubit and find that ground-state cooling is possible with less than one drive photons, circumventing the issues associated with strong driving and qubits. Furthermore, we devise a protocol for creating hybrid Bell-cat entanglement and mechanical Schrödinger cat states using flux-pulsing and qubit operations, enabled by the ability to tune the coupling independently of the qubit frequency. Our results pave the way for the successful

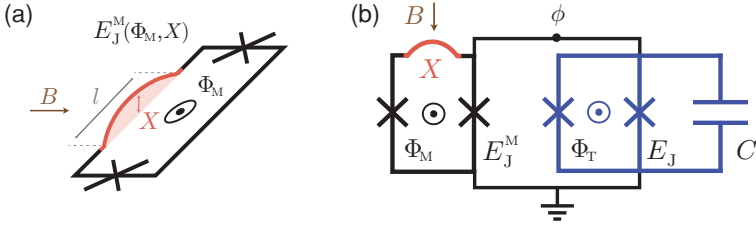


Figure 6.1: **Proposed circuit architecture.** (a) Schematic representation of the mechanical SQUID comprising a suspended beam that is embedded in the arms of a SQUID loop and can mechanically oscillate out of plane. Upon application of an in-plane magnetic field any mechanical displacement leads to a pick-up flux in the SQUID, resulting in a motion-dependent Josephson inductance. (b) The proposed circuit incorporates a flux-tunable transmon qubit connected in parallel to the mechanical SQUID, leading to a tuneable radiation-pressure coupling between the mechanical resonator and the qubit.

on-chip integration of mechanical elements with state-of-the-art transmon-based processors and the manipulation of mechanical motion at single-photon levels, enabling technological applications and fundamental studies of quantum theory.

6.2. Main results

6.2.1. Electromechanical system

The mechanical part of the circuit comprises a suspended beam embedded in a SQUID loop that can oscillate out of plane, as schematically depicted in Fig. 6.1(a). Upon application of an in-plane magnetic field (B) the loop picks up a flux due to the beam displacement (X) which results in a flux-mediated optomechanical interaction between the SQUID cavity and the mechanical oscillator, as recently realised in Ref. [185]. Here, we extend this setup by directly connecting it to a superconducting transmon qubit [44], formed by a second SQUID in parallel to a capacitor C . We refer to the two SQUIDs as the *transmon* and the *mechanical* SQUID, which can be tuned independently by applying locally an out-of-plane flux bias Φ_T and Φ_M , respectively. In an experimental scenario this could be realised via dedicated on-chip flux lines, see e.g. Ref. [186] for a realisation in a similar architecture. The corresponding Josephson energies are given by $E_J = E_{J,\max} |\cos(\pi\Phi_T/\Phi_0)|$ and $E_J^M(X) = E_{J,\max}^M |\cos(\pi(\Phi_M + \beta_0 B l X)/\Phi_0)|$, where $\Phi_0 = h/2e$ is the flux quantum, l is the beam length and β_0 is a geometric factor depending on the mechanical mode shape [185, 188]. The above expression for E_J^M is valid for a symmetric SQUID, i.e. when the two junctions are identical. Including a finite asymmetry a_J and assuming $\Phi_M, \Phi_0 \gg \beta_0 B l X$ (see Appendix), we have

$$E_J^M \simeq E_{J,\max}^M [c_J \cos(\pi\Phi_M/\Phi_0) - s_J \sin(\pi\Phi_M/\Phi_0) \alpha X], \quad (6.1)$$

where $c_J = \sqrt{1 + a_J^2 \tan^2(\pi\Phi_M/\Phi_0)}$, $s_J = (1 - a_J^2)/c_J$ are correction factors due to the SQUID asymmetry and we have defined $\alpha \doteq \pi\beta_0 B l / \Phi_0$.

The electromechanical system is described by the Hamiltonian

$$\hat{H} = \hat{H}_0 + \hat{H}_{\text{int}}, \quad (6.2)$$

$$\hat{H}_0 = \hbar\omega_M \hat{b}^\dagger \hat{b} + \hbar\omega_T \hat{c}^\dagger \hat{c} - \frac{E_C}{2} \hat{c}^\dagger \hat{c}^\dagger \hat{c} \hat{c}, \quad (6.3)$$

$$\hat{H}_{\text{int}} = \hbar g_0 \hat{c}^\dagger \hat{c} (\hat{b} + \hat{b}^\dagger) + \hat{H}'_{\text{int}}, \quad (6.4)$$

where $\hat{b}^{(\dagger)}$ and $\hat{c}^{(\dagger)}$ are bosonic operators describing the annihilation (creation) of phonons and qubit excitations, respectively. The effective transmon frequency is given by $\omega_T = \left(\sqrt{8\tilde{E}_J E_C} - E_C \right) / \hbar$, where $\tilde{E}_J = E_J + E_{J,\text{max}}^M c_J |\cos(\pi\Phi_M/\Phi_0)|$ is the modified transmon Josephson energy due to the mechanical SQUID and $E_C = e^2/2C$ is its charging energy. A detailed derivation of the circuit Hamiltonian is presented in the Appendix.

The qubit is predominantly coupled to the beam via the radiation-pressure interaction, described by the first term in Eq. (6.4), with single-photon coupling strength

$$\begin{aligned} g_0 &= \frac{\partial\omega_T}{\partial\Phi_M} \frac{\partial\Phi_M}{\partial X} X_{\text{ZPF}} \\ &= -\frac{\alpha Z}{2\phi_0^2} s_J E_{J,\text{max}}^M \sin(\pi\Phi_M/\Phi_0) X_{\text{ZPF}}, \end{aligned} \quad (6.5)$$

where X_{ZPF} is the zero-point mechanical motion, $Z = \frac{\hbar}{e^2} \sqrt{E_C/2\tilde{E}_J}$ is the transmon impedance and $\phi_0 = \Phi_0/2\pi$ is the reduced flux quantum.

The second term in Eq. (6.4) describes higher-order contributions to the interaction Hamiltonian (see Appendix for details)

$$\hat{H}'_{\text{int}} = \hbar g'_0 \hat{c}^\dagger \hat{c}^\dagger \hat{c} \hat{c} (\hat{b} + \hat{b}^\dagger) + \hbar g''_0 \hat{c}^\dagger \hat{c} (\hat{b} + \hat{b}^\dagger)^2. \quad (6.6)$$

The first part is a non-linear correction to the interaction, stemming from the transmon anharmonicity, with coupling strength

$$g'_0 = \alpha \hbar Z^2 s_J E_{J,\text{max}}^M \sin(\pi\Phi_M/\Phi_0) X_{\text{ZPF}} / (16\phi_0^4). \quad (6.7)$$

Although this term does not impact the dynamics at single-photon levels, it contributes to the radiation-pressure coupling as $g_0 \rightarrow g_0 + 2g'_0$. The second part stems from a higher-order expansion of E_J^M to $\mathcal{O}[X^2]$, resulting in a coupling strength

$$g''_0 = \frac{\alpha^2 Z s_J}{4\phi_0^2 c_J} E_{J,\text{max}}^M \tan(\pi\Phi_b/\Phi_0) \sin(\pi\Phi_b/\Phi_0) X_{\text{ZPF}}^2, \quad (6.8)$$

which is three orders of magnitude smaller than g_0 for the parameters considered here. For the sake of completeness we include all terms of \hat{H}'_{int} in the simulations, which however lead to negligible effects on the system dynamics.

The dependence of the radiation-pressure coupling strength g_0 , as well as that of the qubit frequency, on the flux bias Φ_M is plotted in Fig. 6.2(a), for the parameters

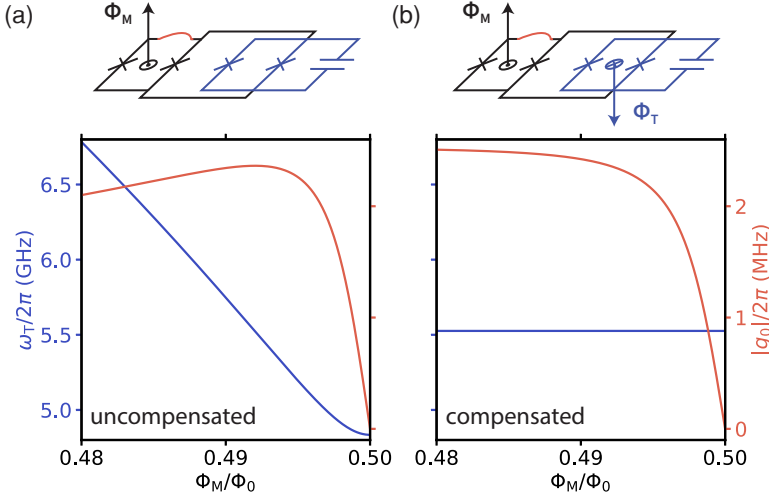


Figure 6.2: **Tuneable radiation-pressure coupling.** (a) The orange curve corresponds to the single-photon optomechanical coupling as a function of the flux bias on the mechanical SQUID (Φ_M), while the blue curve depicts the corresponding transmon frequency dependence. The coupling becomes zero at $\Phi_M/\Phi_0 = 0.5$ as a result of a finite SQUID asymmetry. (b) Same plot in the case where an additional flux Φ_T is applied on the transmon SQUID (tuning E_J from 3 to 10 GHz), such that the qubit frequency remains constant while the coupling is tuned.

shown in Table 6.1. The coupling is maximised at the point where the slope of the qubit frequency $\partial\omega_T/\partial\Phi_M$ is maximum, close to a half-integer flux quantum. Note that the coupling becomes exactly zero at half-integer flux quanta, as a result of the finite asymmetry of the SQUID (s_J factor in Eq. (6.5)), which is here chosen to be $a_J = 0.01$, reflecting a 2% fabrication error in junction targeting. Notably, the Josephson inductance of each junction in the SQUID ($L_J = 2\phi_0^2/E_{J,\max}^M$) is chosen to be much smaller than its expected geometric inductance ($L_g \sim 300$ pH), such that the screening parameter $\beta_L = L_g/(\pi L_J) \sim 0.06$ [219] is negligible and does not limit the achievable coupling strengths as in Ref. [185].

Another comparative advantage of this proposal is the additional flux-bias degree of freedom provided by the transmon SQUID. More specifically, in implementations using a single SQUID, the frequency of the qubit (or SQUID cavity) becomes zero at the point of maximum coupling $\Phi_M \simeq \Phi_0/2$, as shown in Fig. 6.2(a). Using a second SQUID, however, entirely circumvents this issue as the minimum qubit frequency is set by E_J and can be non-zero even at $\Phi_M = \Phi_0/2$. Most importantly, it allows to turn the optomechanical coupling on and off while keeping the qubit frequency constant by appropriately adjusting Φ_T , as depicted in Fig. 6.2(b). This can also ensure that the qubit remains in the transmon regime $E_J \gg E_C$, where it is insensitive to charge noise [44], for the entire coupling range.

We model the dynamical evolution of the system, using the Lindblad master equation

$$\begin{aligned} \dot{\rho} = & \frac{i}{\hbar}[\rho, \hat{H}] + (n_{\text{th}} + 1)\gamma_m \mathcal{L}[\hat{b}]\rho + n_{\text{th}}\gamma_m \mathcal{L}[\hat{b}^\dagger]\rho \\ & + \frac{(n_{\text{th}}^\top + 1)}{T_1} \mathcal{L}[\hat{c}]\rho + \frac{n_{\text{th}}^\top}{T_1} \mathcal{L}[\hat{c}^\dagger]\rho + \frac{1}{T_2} \mathcal{L}[\hat{c}^\dagger \hat{c}]\rho, \end{aligned} \quad (6.9)$$

where $\mathcal{L}[\hat{o}]\rho = (2\hat{o}\rho\hat{o}^\dagger - \hat{o}^\dagger\hat{o}\rho - \rho\hat{o}^\dagger\hat{o})/2$ are superoperators describing each dissipation process, and $n_{\text{th}} = 1/[\exp(\hbar\omega_m/(k_{\text{M}}T)) - 1]$ is the thermal phonon number at temperature T . We use the solver package provided by QuTiP [83], including realistic dissipation rates. More specifically, we consider qubit decay and dephasing times $T_1 = T_2 = 10 \mu\text{s}$ which are consistent with measured values in a similar tuneable coupling transmon architecture [186] and with transmons operating in 10 mT magnetic fields [196]. We additionally include a thermal transmon occupation $n_{\text{th}}^\top = 5\%$ (effective temperature of 90 mK), corresponding to realistic experimental conditions [85, 189]. The coupling of the mechanical mode to the environment is determined by $\gamma_m = \omega_m/Q$, where the quality factor $Q = 10^6$ is chosen in agreement with experimental observations in recently fabricated SQUID-embedded beams [185].

Parameter	Value
$\omega_{\text{M}}/(2\pi)$	1 MHz
$\omega_{\text{T}}/(2\pi)$	5.53 GHz
$ g_0 /(2\pi)$	≤ 2.4 MHz
$E_{\text{J,max}}^{\text{M}}/h$	200 GHz
E_{J}/h	3-10 GHz
E_{C_i}/h	280 MHz
B	10 mT
Φ_{M}/Φ_0	0.49-0.5
l	147 μm
β_0	1
n_{th}	~ 200 (10mK)
T_1, T_2	10 μs
Q_{M}	10^6

Table 6.1: Parameter set used in the numerical simulations.

6.2.2. Ground-state cooling

Manipulating the mechanical oscillator at the quantum level requires the ability to cool it down to its ground state, where thermal effects are suppressed. In typical optomechanical setups, this is achieved via a red-detuned continuous-wave (CW) tone on the electromagnetic resonator [167, 168]. This leads to an effective linearised interaction that is used to transfer phonons to the resonator, which eventually decay. Typically the single-photon coupling is small and thousands of drive photons are required, therefore the success of these schemes relies heavily on the resonator being linear. CW ground-state cooling via a transmon qubit has the additional disadvantage of the pump power

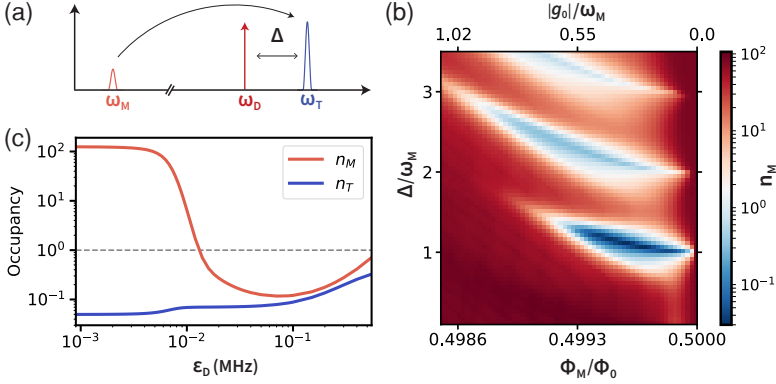


Figure 6.3: **Ground-state cooling.** (a) Sideband cooling scheme where a red-detuned drive is applied on the qubit. (b) Steady-state phonon occupancy as a function of the detuning Δ and flux bias Φ_M corresponding to different ratios of $|g_0|/\omega_M$ (shown in the top horizontal axis), for a driving amplitude of $\mathcal{E}_D = 70$ kHz. (c) Cooling as a function of \mathcal{E}_D near the optimal condition of $|g_0| \simeq \omega_M/4$ found in (b). We additionally include a 5% thermal transmon occupancy, which limits the ground-state cooling to a phonon occupancy of $\sim 10\%$.

being limited by the critical photon number in Josephson junctions [190]. These issues could be circumvented in a time-domain scheme, by employing an additional qubit and combining tripartite photon-phonon SWAP gates with qubit reset [220], which is however outside the scope of this study.

We investigate the possibility of cooling the beam via sideband driving on the transmon qubit, as depicted in Fig. 6.3(a). More specifically, we add a driving term $\hat{H}_D/\hbar = \mathcal{E}_D(\hat{c}^\dagger e^{-i\omega_D t} + \hat{c}e^{i\omega_D t})$ to the system Hamiltonian, where \mathcal{E}_D and ω_D denote the amplitude and frequency of the driving tone, respectively. We numerically solve the Lindblad equation (6.9) for the set of parameters listed in Table 6.1. In Fig. 6.3(b) we plot the steady-state occupancy in the mechanical resonator as a function of the detuning $\Delta = \omega_T - \omega_D$ and single-photon coupling strength for $\mathcal{E}_D = 70$ kHz. The cooling resonances observed at multiples of $\Delta = \omega_M - g_0^2/\omega_M$, are in accordance with predictions for weakly driven optomechanical systems in the single-photon strong-coupling regime [221]. We find an optimal cooling regime around $|g_0| = \omega_M/4$, leading to a phonon occupancy of 3% (assuming a perfectly thermalised transmon $n_{\text{th}}^T = 0$). As expected, ground-state cooling with a qubit becomes impossible in the limit of small coupling $|g_0| \ll \omega_m$, or when $|g_0| \sim \omega_M$ where the two modes hybridise. In Fig. 6.3(c), we plot the steady-state phonon occupancy as we vary the amplitude of the drive, for the optimal cooling condition found in (b) and including a transmon thermal occupancy of $n_{\text{th}}^T = 5\%$, leading to $n_M^{\text{min}} \simeq 10\%$ at $\mathcal{E}_D = 70$ kHz.

6.2.3. Mechanical cat states

An important feature of the proposed circuit is that it allows for fast tuning of the optomechanical coupling. Practically this can be achieved by applying flux pulses via dedicated on-chip lines, as short as a few nanoseconds, i.e. much shorter than the

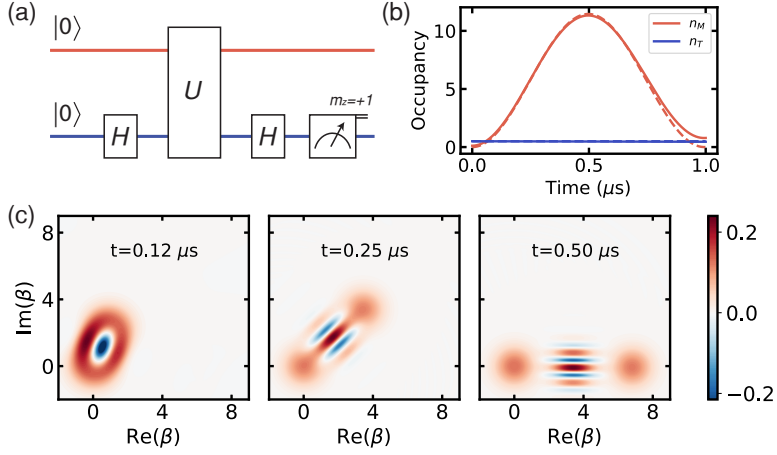


Figure 6.4: Generating mechanical cat states. (a) Description of the protocol. In the first step, with the coupling turned off ($\Phi_M/\Phi_0 = 0.5$), the qubit is prepared in the superposition state $|+\rangle_T$ by applying a Hadamard gate. The optomechanical coupling is turned on ($\Phi_M/\Phi_0 = 0.49$) for a variable time such that the system evolves under the radiation-pressure interaction $U(t) = e^{-ig_0 t \hat{c}^\dagger \hat{c}(\hat{b} + \hat{b}^\dagger)}$. The coupling is then turned off and a second Hadamard gate is applied on the qubit, followed by a measurement in the computational basis. Measuring the qubit in the ground or excited state results in even or odd Schrödinger cat states in the mechanical oscillator. (b) Evolution of the system excitations after preparing the qubit in a superposition state and turning on the interaction. The blue curve corresponds to the qubit excitation number while the orange curve depicts the phonon number evolution for one cycle ($t = 1/\omega_M$), including 0.1 and 0.05 thermal phonon and qubit occupancy, respectively, as obtained from Fig. 6.3(c). The dashed curves correspond to the ideal evolution of the system without dissipation. (c) Wigner functions of the mechanical resonator at different times following the protocol in (a) and projecting on $|0\rangle_T$. At $t = 1/2\omega_M$ an even cat state is created with 98% (93%) fidelity, starting from an ideal (attainable) ground state.

interaction timescales. One can then use the qubit for creating interesting mechanical states as discussed below.

In Fig. 6.4(a) we describe an experimentally feasible protocol for generating macroscopic superposition states on the beam resonator. In the first step, starting from the ground-state $|0\rangle_T|0\rangle_M$ and with the coupling off ($\Phi_M/\Phi_0 = 0.5$), a Hadamard gate is applied on the qubit, which creates the superposition state $|+\rangle_T = \frac{1}{\sqrt{2}}(|0\rangle + |1\rangle)_T$. The second step consists of flux-pulsing the mechanical SQUID to $\Phi_M/\Phi_0 = 0.49$ and letting the system evolve for a variable time under the radiation-pressure interaction $U(t) = e^{-ig_0 t \hat{c}^\dagger \hat{c}(\hat{b} + \hat{b}^\dagger)}$. The evolution of excitations in the system after one cycle ($t = 1/\omega_M$) is plotted in Fig. 6.4(b), assuming thermal occupancies of 10% and 5% for the beam and the qubit, respectively. The operation of $U(t)$ results in a coherent displacement on the mechanical resonator depending on the qubit being in the excited state, i.e.

$$U(t)|+\rangle_T|0\rangle_M = \frac{1}{\sqrt{2}}(|0\rangle_T|0\rangle_M + |1\rangle_T|\beta\rangle_M), \quad (6.10)$$

where $|\beta\rangle_M$ denotes a coherent mechanical state of amplitude $\beta = \sqrt{n_M}$.

The state created above resembles a hybrid Bell-cat state featuring discrete-continuous variable entanglement [222, 223] and can also be written as

$$|\psi\rangle_{\text{TM}} = \frac{1}{\sqrt{2}}|+\rangle_{\text{T}}(|0\rangle + |\beta\rangle)_{\text{M}} + |-\rangle_{\text{T}}(|0\rangle - |\beta\rangle)_{\text{M}}. \quad (6.11)$$

Turning off the coupling and applying a second Hadamard gate on the qubit, transforms the state into

$$|\psi\rangle_{\text{TM}} = \frac{1}{2\sqrt{2}}|0\rangle_{\text{T}}(|0\rangle + |\beta\rangle)_{\text{M}} + |1\rangle_{\text{T}}(|0\rangle - |\beta\rangle)_{\text{M}}. \quad (6.12)$$

By performing a projective measurement on the qubit, the beam collapses in a macroscopic superposition $|0 \pm \beta\rangle$, depending on whether the qubit is measured in its ground or excited state. This state corresponds to an even/odd Schrödinger cat state displaced by $\beta/2$. In Fig. 6.4(c) we plot the evolution of the even cat state after repeating the above protocol and conditioning on $|0\rangle_{\text{T}}$. The size of the cat state is maximum at half a cycle and is determined by $\beta_{\text{max}} = 2|g_0|/\omega_{\text{M}}$. The fidelity of the prepared state to the ideal Schrödinger cat state is 93% and is mainly limited by the finite thermal occupancy of the initial ground state. Assuming no initial thermal occupancy we find 98% cat state fidelity, while for ideal evolution without dissipation the fidelity is 99.8%. All higher order interaction terms in Eq. (6.6) are included in the simulations.

6.3. Discussion

In summary, we have analysed a hybrid system involving a superconducting transmon qubit parametrically coupled to a mechanical beam via radiation-pressure in the ultrastrong-coupling regime, where the coupling strength exceeds the mechanical frequency at the single-photon level. A similar system, considering a carbon nanotube coupled to a transmon qubit, was studied recently in Ref. [224], however it relies on unrealistically optimistic parameters and high magnetic fields ($B = 500$ mT) to reach the ultrastrong-coupling regime. We use experimentally feasible parameters, which have been reported in recent experiments combining Aluminium beams with SQUIDs [185], and small magnetic fields that do not compromise the performance of transmon qubits below $\sim 10 \mu\text{s}$ [196]. We have demonstrated numerically the possibility of ground-state cooling, by sideband driving below the single-photon level, for a range of achievable coupling strengths. Additionally, we have investigated the dynamics of the coupled system in the ultrastrong-coupling regime and devised a protocol for preparing mechanical Schrödinger cat states with high fidelity.

Our proposed circuit architecture provides a versatile platform for integrating transmon qubits with long-lived mechanical resonators, and may find interesting applications in hybrid quantum technologies [42]. The prepared Bell-cat states are particularly interesting for several quantum computing schemes and error correcting protocols [225–228]. Additionally, the radiation-pressure interaction can also be employed to prepare mechanical Gottesman–Kitaev–Preskill states, which are useful for fault-tolerant error correction schemes [229, 230]. Finally, the prepared macroscopically distinct massive superposition states are ideally suited for testing fundamental aspects of quantum theory and its relation to gravity [66, 68].

6.4. Detailed analysis of the electromechanical system

6.4.1. Circuit Hamiltonian

The Lagrangian describing the electromechanical circuit in Fig. 6.1(b) is

$$\begin{aligned} \mathcal{L} = & \frac{m\dot{X}^2}{2} - \frac{m\omega_M^2 X^2}{2} + \frac{1}{2}C\dot{\phi}^2 \\ & + [E_J + E_J^M(X)] \cos\left(\frac{\phi}{\phi_0}\right), \end{aligned} \quad (6.13)$$

where X , ϕ are variables representing the beam displacement and the node flux, respectively, and $\phi_0 = \hbar/2e$ is the reduced flux quantum. C denotes the total capacitance of the transmon and Josephson junctions, which are added in parallel. Following a Legendre transformation we obtain the system Hamiltonian

$$\begin{aligned} H = & \frac{P^2}{2m} + \frac{m\omega_M^2 X^2}{2} \\ & + \frac{Q^2}{2C} - [E_J + E_J^M(X)] \cos\left(\frac{\phi}{\phi_0}\right), \end{aligned} \quad (6.14)$$

where $\{X, P\}$ and $\{\phi, Q\}$ are conjugate variable pairs describing the mechanical and the electrical degrees of freedom, respectively.

The optomechanical coupling between the resonator and the qubit can be determined by analysing the term $E_J^M(X) \cos\left(\frac{\phi}{\phi_0}\right)$ in the above equation. The motion-dependent Josephson energy of the mechanical SQUID is given by

$$\begin{aligned} E_J^M(\Phi_b, X) = & E_{J,\max}^M [\cos^2(\pi\Phi_b/\Phi_0 + \alpha X) \\ & + a_J^2 \sin^2(\pi\Phi_b/\Phi_0 + \alpha X)]^{1/2}, \end{aligned} \quad (6.15)$$

where a_J is the SQUID asymmetry. Following the analysis presented in Ref. [220], for $\alpha X \ll 1, \pi\Phi_b/\Phi_0$, this expression can be approximated by

$$E_J^M \simeq E_{J,\max}^M [c_J \cos(\pi\Phi_b/\Phi_0) - s_J \sin(\pi\Phi_b/\Phi_0)\alpha X], \quad (6.16)$$

up to $\mathcal{O}[X]$, where $c_J = \sqrt{1 + a_J^2 \tan^2(\pi\Phi_M/\Phi_0)}$ and $s_J = (1 - a_J^2)/c_J$.

6.4.2. Circuit quantisation and radiation-pressure coupling strength

The first term in Eq. (6.16) results in an effective transmon Josephson energy given by

$$\tilde{E}_J = E_J + E_{J,\max}^M c_J \cos(\pi\Phi_M/\Phi_0), \quad (6.17)$$

which is responsible for the qubit frequency change as a function of Φ_M , shown in Fig. 6.2(a). The second term, combined with an expansion of the cosine term in Eq. (6.14) up to $\mathcal{O}[\phi^4]$, yields the optomechanical interaction Hamiltonian

$$H_{\text{int}} = -\alpha E_{J,\max}^M s_J \sin(\pi\Phi_M/\Phi_0) X \left(\frac{\phi^2}{2\phi_0^2} - \frac{\phi^4}{24\phi_0^4} \right). \quad (6.18)$$

We can express the interaction Hamiltonian in second quantisation form by promoting all canonical variables to quantum operators

$$\begin{aligned}\hat{X} &= X_{\text{ZPF}} (\hat{b} + \hat{b}^\dagger), \quad \hat{P} = P_{\text{ZPF}} i(\hat{b}^\dagger - \hat{b}), \\ \hat{\phi} &= \sqrt{\frac{\hbar Z}{2}} (\hat{c} + \hat{c}^\dagger), \quad \hat{Q} = \sqrt{\frac{\hbar}{2Z}} i(\hat{c}^\dagger - \hat{c}),\end{aligned}\quad (6.19)$$

where $\hat{b}^{(\dagger)}$, $\hat{c}^{(\dagger)}$ are ladder operators describing the annihilation (creation) of phonons and qubit excitations, respectively, satisfying bosonic commutation relations $[\hat{c}, \hat{c}^\dagger] = 1$ and $[\hat{b}, \hat{b}^\dagger] = 1$. The zero-point fluctuations in the mechanical displacement and momentum are given by $X_{\text{ZPF}} = \sqrt{\hbar/(2m\omega_M)}$ and $P_{\text{ZPF}} = \sqrt{\hbar m\omega_M/2}$, respectively. $Z = \frac{\hbar}{e^2} \sqrt{E_C/2\tilde{E}_J}$ denotes the transmon impedance, where $E_C = \frac{e^2}{2C}$ is its charging energy, and the qubit frequency is given by $\omega = \frac{1}{\hbar} \left(\sqrt{8\tilde{E}_J E_C} - E_C \right)$.

Replacing the classical variables in Eq. (6.18) with the quantum operators introduced in Eq. (6.19) we have

$$\hat{H}_{\text{int}}/\hbar = g_0 \hat{c}^\dagger \hat{c} (\hat{b} + \hat{b}^\dagger) + g'_0 \hat{c}^\dagger \hat{c} \hat{c} (\hat{b} + \hat{b}^\dagger), \quad (6.20)$$

following a rotating wave approximation (RWA) where fast rotating terms $(\hat{c}^{(\dagger)})^n$ are neglected. The first term describes a radiation-pressure interaction between the qubit and the resonator with coupling strength

$$g_0 = \frac{\alpha Z}{2\phi_0^2} E_{\text{J,max}}^{\text{M}} \sin(\pi\Phi_{\text{M}}/\Phi_0) X_{\text{ZPF}}. \quad (6.21)$$

The second term is a higher-order correction to the interaction, stemming from the transmon anharmonicity, with coupling strength

$$g'_0 = \alpha \hbar Z^2 s_{\text{J}} E_{\text{J,max}}^{\text{M}} \sin(\pi\Phi_{\text{M}}/\Phi_0) X_{\text{ZPF}} / (16\phi_0^4). \quad (6.22)$$

This term is included in the simulations although it does not lead to substantial contribution in the system dynamics, however, it leads to a correction of the radiation pressure coupling $g_0 \rightarrow g_0 + 2g'_0$.

6.4.3. Higher-order interaction terms

The next-to-leading order correction in the expansion of $E_{\text{J}}^{\text{M}}(X)$ in Eq. (6.16) is given by

$$E_{\text{J}}^{\text{M}}\{\mathcal{O}[X^2]\} = -E_{\text{J,max}}^{\text{M}} \frac{s_{\text{J}} \sin^2(\pi\Phi_{\text{b}}/\Phi_0)}{2c_{\text{J}} \cos(\pi\Phi_{\text{b}}/\Phi_0)} \alpha^2 X^2. \quad (6.23)$$

This term, combined with a second-order expansion of the cosine in Eq. (6.14), yields the following interaction

$$H_{\text{int}}^{\{\phi^2 X^2\}} = E_{\text{J,max}}^{\text{M}} \frac{s_{\text{J}} \sin^2(\pi\Phi_{\text{b}}/\Phi_0)}{2c_{\text{J}} \cos(\pi\Phi_{\text{b}}/\Phi_0)} \alpha^2 X^2 \frac{\phi^2}{2\phi_0}, \quad (6.24)$$

which can be written in second quantisation form (following a RWA) as

$$H_{\text{int}}^{\{\phi^2 X^2\}}/\hbar = g_0'' \hat{c}^\dagger \hat{c} (\hat{b} + \hat{b}^\dagger)^2. \quad (6.25)$$

The coupling strength of this interaction is given by

$$g_0'' = \frac{\alpha^2 Z s_J}{4\phi_0^2 c_J} E_{J,\text{max}}^M \tan(\pi\Phi_b/\Phi_0) \sin(\pi\Phi_b/\Phi_0) X_{\text{ZPF}}^2. \quad (6.26)$$

The maximum value of this coupling strength is $g_0'' \simeq 5$ kHz around $\Phi_M/\Phi_0 = 0.497$ for the parameters considered in this work. For the sake of completeness we include this interaction in the simulations, however, we do not observe any significant impact on the fidelity of the cooling and quantum state preparation protocols.

7

Controlling a hot radio-frequency resonator via dissipation engineering

*L'homme n'est rien de lui-même. Il n'est qu'une chance infinie.
Mais il est le responsable infini de cette chance.*

Albert Camus, "Carnets II"

As we saw in the previous chapters, superconducting circuits operate in the gigahertz regime such that their fundamental frequencies are above the energy scale of thermal fluctuations. This lower bound is set by the achievable temperatures using state-of-the-art cryogenic techniques, which are of the order of 1-10 mK. In this chapter, we describe an experiment where we were able to overcome this limitation and achieve quantum control over a megahertz radio-frequency resonator by means of dissipation engineering techniques. Specifically, using a gigahertz superconducting qubit dispersively coupled to the hot resonator, we were able to detect its quantised energy structure and perform ground-state cooling as well as stabilise Fock states. Releasing the resonator from our control, we were also able to observe its re-thermalisation with nanosecond resolution. This work extends circuit QED in the radio-frequency regime, enabling the exploration of thermodynamics at the quantum scale and interfacing electrical circuits with spin systems or macroscopic mechanical oscillators that operate at similar frequencies.

7.1. Introduction

Detecting and manipulating single photons becomes more difficult at lower frequencies because of thermal fluctuations. A hot environment randomly creates and annihilates photons causing decoherence in addition to creating statistical mixtures of states from which quantum state preparation is challenging. This can be mitigated by using a colder system as a heat sink, to extract the entropy created by the environment. Such a scheme, known as reservoir engineering, was first developed in trapped ions [70], where hot degrees of freedom are cooled via the atomic transitions of ions.

Using superconducting electronics, circuit quantum electrodynamics (QED) has made extensive use of reservoir engineering to cool, but also manipulate electromagnetic fields at the quantum level. With the prospect of building a quantum computer, or to demonstrate fundamental phenomena, experiments have shown the cooling or reset of qubits to their ground state [193, 231, 232], also in the megahertz regime [233], quantum state stabilisation [234–236], and quantum error correction [237]. Using superconducting circuits, reservoir engineering is commonplace in electromechanical systems [168, 238], but with weak nonlinearity, such schemes have only limited quantum control [171, 173] compared to typical circuit QED systems. Despite the many applications of quantum state engineering in circuit QED, obtaining control over the quantum state of a hot resonator, where the environment temperature is a dominant energy scale, remains a largely unexplored and challenging task.

We directly observe the quantisation of radio-frequency electromagnetic fields in a thermally-excited megahertz photonic resonator, and manipulate its quantum state using reservoir engineering. Specifically, we cool the 173 MHz resonator to 90% ground-state occupation, and stabilise one- and two-photon Fock states. Releasing the resonator from our control, we observe its re-thermalisation with photon-number resolution.

We use the paradigm of circuit QED, where a resonator can be read out and controlled by dispersively coupling it to a superconducting qubit. Achieving this with a GHz qubit and MHz photons is challenging, since in a conventional circuit QED architecture the coupling would be far too weak [239]. To overcome this, we present a circuit enabling a very strong interaction, resulting in a cross-Kerr coupling larger than the qubit and resonator dissipation rates, despite an order of magnitude difference in their resonance frequencies.

7.2. Main results

7.2.1. Circuit architecture and coupling mechanism

The circuit (Fig. 7.1(a)) comprises of a Josephson junction ($L_J = 41$ nH) connected in series to a capacitor ($C_L = 11$ pF) and a spiral inductor ($L = 28$ nH). At low frequencies, the parasitic capacitance of the spiral inductor is negligible, and the equivalent circuit (Fig. 7.1(b)) has a first transition frequency $\omega_L = 2\pi \times 173$ MHz. At gigahertz frequencies, C_L behaves as a short, and the capacitance of the spiral inductor $C_H = 40$ fF becomes relevant instead. The resulting parallel connection of L_J , L and C_H (Fig. 7.1(c)) has a first transition frequency $\omega_H = 2\pi \times 5.91$ GHz. The two modes share the Josephson junction. The junction has an inductance that varies with the current fluctuations traversing it, and consequently the resonance frequency of

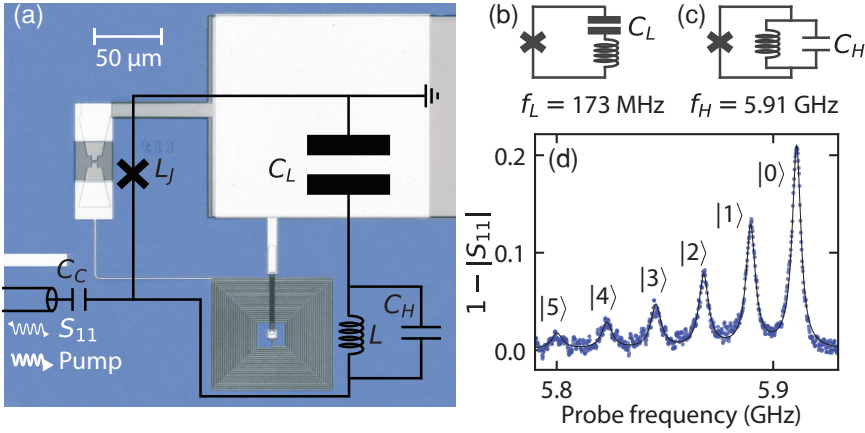


Figure 7.1: **Cross-Kerr coupling between a transmon qubit and radio-frequency resonator.** (a) False-colored optical micrograph of the device overlaid with the equivalent lumped element circuit. (b), (c) Effective circuit at low and high frequencies. At low (high) frequencies, the femtofarad (picofarad) capacitances of the circuit are equivalent to open (short) circuits, and the device is equivalent to a series (parallel) JJ-inductor-capacitor combination. The circuit has thus two modes, a 173 MHz resonator and a 5.9 GHz qubit. (d) Microwave response $|S_{11}|$. Through cross-Kerr coupling, quantum fluctuations of a photon number state $|n = 0, 1, \dots\rangle$ in the resonator shift the qubit transition frequency. Peak heights are proportional to the occupation of state $|n\rangle$, and we extract a thermal occupation $n_{\text{th}} = 1.6$ in the resonator corresponding to a temperature of 17 mK.

the high-frequency (HF) mode shifts as a function of the number of excitations in the low-frequency (LF) mode and vice versa. This cross-Kerr interaction is quantified by the shift per photon $\chi = 2\sqrt{A_H A_L}$, where the anharmonicity of the LF and HF mode $A_L = h \times 495$ kHz and $A_H = h \times 192$ MHz are given by

$$A_L = -\frac{e^2}{2C_L} \left(\frac{L_J}{L + L_J} \right)^3, \quad A_H = -\frac{e^2}{2C_H} \left(\frac{L}{L + L_J} \right). \quad (7.1)$$

The system is described by the Hamiltonian

$$\begin{aligned} \hat{H} = & \hbar\omega_H \hat{a}^\dagger \hat{a} + \hbar\omega_L \hat{b}^\dagger \hat{b} \\ & - \frac{A_H}{2} \hat{a}^\dagger \hat{a}^\dagger \hat{a} \hat{a} - \frac{A_L}{2} \hat{b}^\dagger \hat{b}^\dagger \hat{b} \hat{b} \\ & - \chi \hat{a}^\dagger \hat{a} \hat{b}^\dagger \hat{b}, \end{aligned} \quad (7.2)$$

where \hat{a} (\hat{b}) is the annihilation operator for photons in the HF (LF) mode. The second line describes the anharmonicity or Kerr nonlinearity of each mode. The last term describes the cross-Kerr interaction. The dependence of the HF mode resonance on the number of photons in the LF mode becomes apparent by combining it with the first term as $(\hbar\omega_H - \chi \hat{b}^\dagger \hat{b}) \hat{a}^\dagger \hat{a}$.

The cross-Kerr interaction manifests as photon-number splitting [101] in the measured microwave reflection S_{11} (Fig. 7.1(d)). Distinct peaks correspond to the first

transition frequency of the HF mode $|g, n\rangle \leftrightarrow |e, n\rangle$, with frequencies $\omega_H - n\chi/\hbar$ where $\chi/\hbar = 21$ MHz. We label the eigenstates of the system $|j, n\rangle$, with $j = g, e, f, \dots$ ($n = 0, 1, 2, \dots$) corresponding to excitations of the HF (LF) mode. The amplitude of peak n is proportional to

$$P_n \kappa_{\text{ext}} / \kappa_n, \quad (7.3)$$

where P_n is the occupation of photon-number level $|n\rangle$ in the LF mode and $\kappa_{\text{ext}}/\kappa_n$ is the ratio of external coupling $\kappa_{\text{ext}}/2\pi = 1.6 \cdot 10^6 \text{ s}^{-1}$ to the total line-width κ_n of peak n . From the Bose-Einstein distribution of peak heights P_n , we extract the average photon occupation $n_{\text{th}} = 1.6$ corresponding to a mode temperature of 17 mK.

The resolution of individual photon peaks is due to the condition $\kappa_n \ll \chi/\hbar$. The peak line-widths increase with n following $\kappa_n = \kappa(1 + 4n_{\text{th}}^{(H)}) + 2\gamma(n + (1 + 2n)n_{\text{th}})$, where $\kappa/2\pi = 3.7 \cdot 10^6 \text{ s}^{-1}$ is the dissipation rate of the HF mode, $n_{\text{th}}^{(H)} \simeq 0.09$ its thermal occupation, and $\gamma/2\pi = 23 \cdot 10^3 \text{ s}^{-1}$ is the dissipation rate of the LF mode (obtained through time-domain measurement Fig. 7.4). The condition $\kappa_n \ll A_H/\hbar$ makes the HF mode an inductively-shunted transmon qubit [44], making it possible to selectively drive the $|g, n\rangle \leftrightarrow |e, n\rangle$ and $|e, n\rangle \leftrightarrow |f, n\rangle$ transitions. Despite its low dissipation rate γ , the LF mode has a line-width of a few MHz (measured with two-tone spectroscopy, Fig. 7.10) which originates in thermal processes such as $|g, n\rangle \rightarrow |e, n\rangle$ occurring at rates $\sim \kappa n_{\text{th}}^{(H)}$ larger than γ . The LF mode line-width is then an order of magnitude larger than A_L , making it essentially a harmonic oscillator that we will refer to as the resonator.

7.2.2. Ground-state cooling and Fock-state stabilisation

The junction nonlinearity enables transfer of population between states by coherently pumping the circuit at a frequency ω_p . The cosine potential of the junction imposes four-wave mixing selection rules, only allowing interactions that involve 4 photons. One such interaction is

$$\hat{H}_{\text{int}} = -\hbar g \sqrt{n+1} |f, n\rangle \langle g, n+1| + h.c., \quad (7.4)$$

activated when driving at the energy difference between the two coupled states $\omega_p = 2\omega_H - \omega_L - (2n\chi + A_H)/\hbar$. This process, enabled by a pump photon, annihilates a photon in the resonator and creates two in the transmon. The number of photons involved in the interaction is four, making it an allowed four-wave mixing process. The induced coupling rate is $g = A_H^{\frac{3}{4}} A_L^{\frac{1}{4}} \xi_p$, where $|\xi_p|^2$ is the amplitude of the coherent pump tone measured in number of photons.

We use this pump tone in combination with the large difference in mode relaxation rates to cool the megahertz resonator to its ground state (Fig. 7.2(a)). The pump drives transitions between $|g, 1\rangle$ and $|f, 0\rangle$ at a rate g . The population of $|g, 1\rangle$, transferred to $|f, 0\rangle$, subsequently decays at a rate 2κ to the ground state $|g, 0\rangle$. Cooling occurs when the thermalisation rate of the resonator $n_{\text{th}}\gamma$ is slower than the rate $C\gamma$ at which excitations are transferred from $|g, 1\rangle$ to $|g, 0\rangle$, where $C = 2g^2/\kappa\gamma$ is the cooperativity (proportional to cooling-pump power).

For different cooling pump strengths, we measure S_{11} (Fig. 7.2(b)). The pump frequency is adapted at each power since the AC-stark effect increasingly shifts the qubit

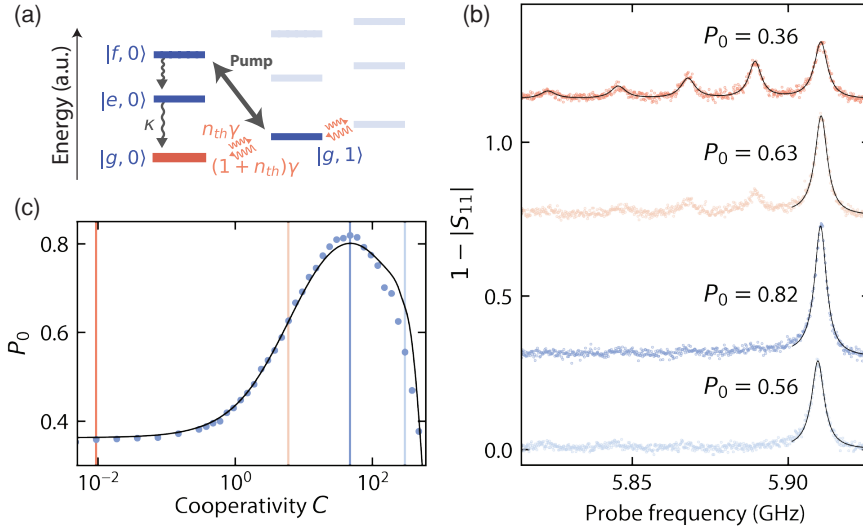


Figure 7.2: **Ground-state cooling of the radio-frequency resonator.** (a) Energy ladder of the coupled transmon qubit and resonator. Meandering arrows indicate relaxation and thermal processes. The resonator is cooled by driving a transition (black arrow) that transfers excitations from the resonator to the qubit, where they are quickly dissipated. (b) Photon-number spectroscopy of the resonator for different cooperativities C (proportional to cooling-pump power). $C = 0.01, 6, 47, 300$ from top to bottom. Ground-state occupations P_0 are extracted from Lorentzian fits (black curves). (c) Vertical lines indicate the the datasets of panel (b). A simulation (curve) predicts the measured (dots) high- C decrease of P_0 through the off-resonant driving of other sideband transitions.

frequency as a function of power. The data is fitted to a sum of complex Lorentzians, with amplitudes given by Eq. (7.3) and line-widths κ_n , from which P_n is extracted. Thermal effects lead to the ratio $P_{n+1}/P_n = n_{\text{th}}/(1+n_{\text{th}})$ between neighboring photon-number states for $n \geq 1$, and the cooling pump changes the ratio of occupation of the first two states

$$\frac{P_1}{P_0} \simeq \frac{n_{\text{th}}}{1 + n_{\text{th}} + C}. \quad (7.5)$$

The ground-state occupation hence increases with cooperativity and we attain a maximum $P_0 = 0.82$. At higher cooperativity, P_0 diminishes due to the off-resonant driving of other four-wave mixing processes such as $|f, n+1\rangle\langle g, n| + h.c.$ which tend to raise the photon number of the resonator. This effect is simulated using an adaptive rotating-wave approximation [240] (Fig. 7.2(c)).

Neighbouring four-wave mixing processes are measured by sweeping the pump frequency whilst monitoring the spectrum (Fig. 7.3(a)). When cooling with a single pump they eventually limit performance, but can be resonantly driven to our advantage. By driving multiple cooling interactions $|g, n\rangle \leftrightarrow |f, n-1\rangle$, less total pump power is required to reach a given ground-state occupation, hence minimizing off-resonant driving. By maximizing the ground-state peak amplitude as a function of the power and frequency of four cooling tones, we achieve $P_0 = 0.90$ (Fig. 7.3(b)).

By combining cooling $|g, n\rangle \leftrightarrow |f, n-1\rangle$ and raising $|g, n\rangle \leftrightarrow |f, n+1\rangle$ tones (inset

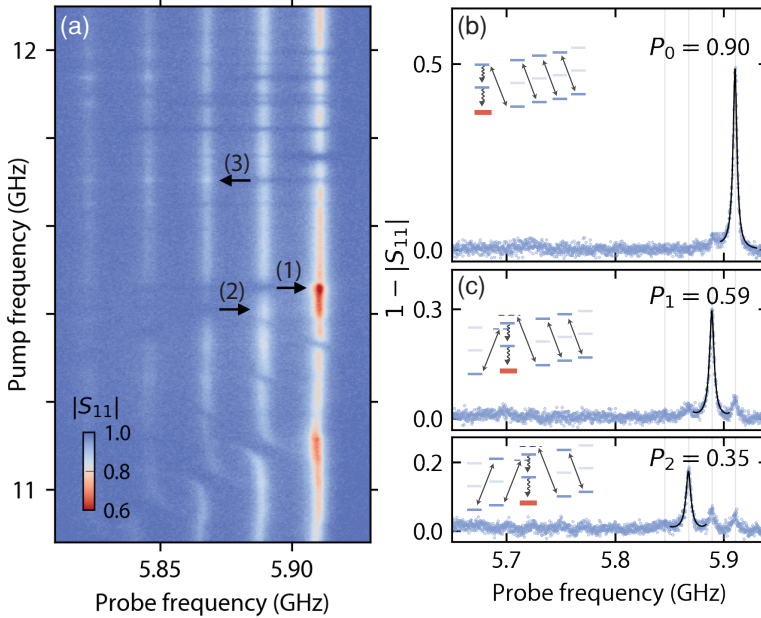


Figure 7.3: **Enhanced cooling and Fock-state stabilisation using multiple tones.** (a) $|S_{11}|$ as a function of pump and probe frequency. Vertical lines correspond to the photon-number-split qubit frequencies. Horizontal and diagonal features appear at pump frequencies enabling the transfer of population between Fock states of the resonator. Arrows indicate three example transitions: **(1)** the cooling transition of Fig. 7.2, **(2)** the transition $|g, 2\rangle \leftrightarrow |f, 1\rangle$ transferring $|2\rangle$ to $|1\rangle$, and **(3)** the transition $|g, 1\rangle \leftrightarrow |f, 2\rangle$ which raises $|1\rangle$ to $|2\rangle$. (b) By simultaneously driving four cooling transitions ($|g, n+1\rangle \leftrightarrow |f, n\rangle$), cooling is enhanced to $P_0 = 0.9$. (c) Using these transitions in conjunction with raising transitions $|g, n\rangle \leftrightarrow |f, n+1\rangle$, we stabilise Fock states 1 and 2 with 59% and 35% fidelity. We fit a sum of complex Lorentzians to the spectrum, showing only the relevant Lorentzian (black curve) whose amplitude provides P_n . Off-resonant driving results in population transfer to higher energy states visible as features in the lower frequencies of the spectrum.

7

of Fig. 7.3(c)), we demonstrate stabilisation of higher Fock states, non-Gaussian states commonly considered as nonclassical phenomena [241]. The optimum frequencies for the raising and cooling tones adjacent to the stabilised state were detuned by a few MHz from the transition frequency (see dashed lines in the inset of Fig. 7.3(c)), otherwise one pump tone would populate the $|f\rangle$ level, diminishing the effectiveness of the other.

7.2.3. Time-domain experiments

Finally we investigate dynamics in a photon resolved manner (Fig. 7.4). Whilst probing S_{11} at a given frequency, we switch the cooling or single photon stabilisation pumps on and off for intervals of $50 \mu\text{s}$. We perform this for a sequence of probe frequencies, resulting in S_{11} as a function of both frequency and time (see full spectrum in Fig. 7.11). The spectrum is fitted at each time to extract P_n as a function of time. After reaching the steady state, the pumps are turned off and we observe the thermalisation process

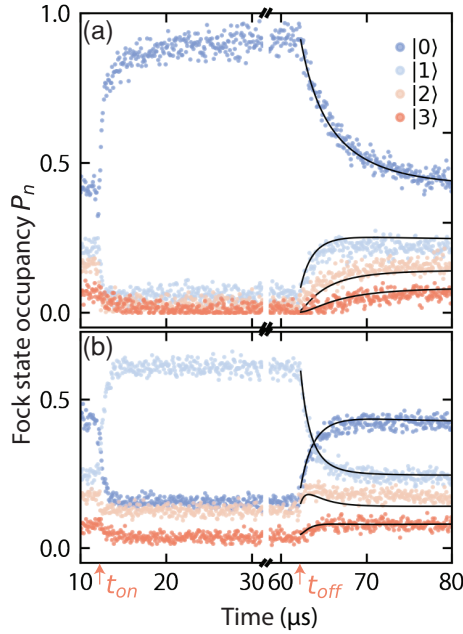


Figure 7.4: **Fock-state-resolved thermalisation-dynamics of the resonator.** At t_{on} , pumps are turned on and the resonator evolves into the ground state (a) or a single photon state (b). At t_{off} , control is released and we observe photon-number resolved thermalisation of the resonator. The extracted Fock-state occupation (dots) is fitted to Eq. 7.6 (black curve).

which follows the semi-classical master equation

$$\begin{aligned} \dot{P}_n = & -n\gamma(n_{\text{th}} + 1)P_n + n\gamma n_{\text{th}}P_{n-1} \\ & - (n + 1)P_n\gamma n_{\text{th}} + (n + 1)P_{n+1}\gamma(n_{\text{th}} + 1) . \end{aligned} \quad (7.6)$$

7.3. Discussion

Our circuit QED architecture enables the readout and manipulation of a radio-frequency resonator at the quantum level. Utilizing the fast readout methods of circuit QED, single-shot readout or the tracking of quantum trajectories could enable even finer resolution of thermodynamic effects at the quantum scale. Coupling many of these devices together could enable the exploration of many-body effects in Bose-Hubbard systems with dynamically tunable temperatures [242, 243]. This circuit architecture could also be used to interface circuit quantum electrodynamics with different physical systems in the MHz frequency range, such as spin systems [244] or macroscopic mechanical oscillators[168]. Finally, this circuit could enable sensing of radio frequency radiation with quantum resolution, a critical frequency range for a number of applications, from nuclear magnetic resonance imaging to radio astronomy.

7.4. Extended author contribution statement

The work presented in this chapter was a result of a strong collaboration with M.F.Gely, who is also a PhD student in the group. As the manuscript will appear as a chapter in both PhD theses, I include here an extended description of my contribution to the work presented, which involves: helping with the design and fabrication of Josephson junctions; contributing to the initial tune-up of the device and spectroscopic measurements described in Figs. 7.1, 7.2, 7.3, 7.9 and 7.10; co-performing the time-domain experiments described in Figs. 7.4 and 7.11.

7.5. Experimental setup

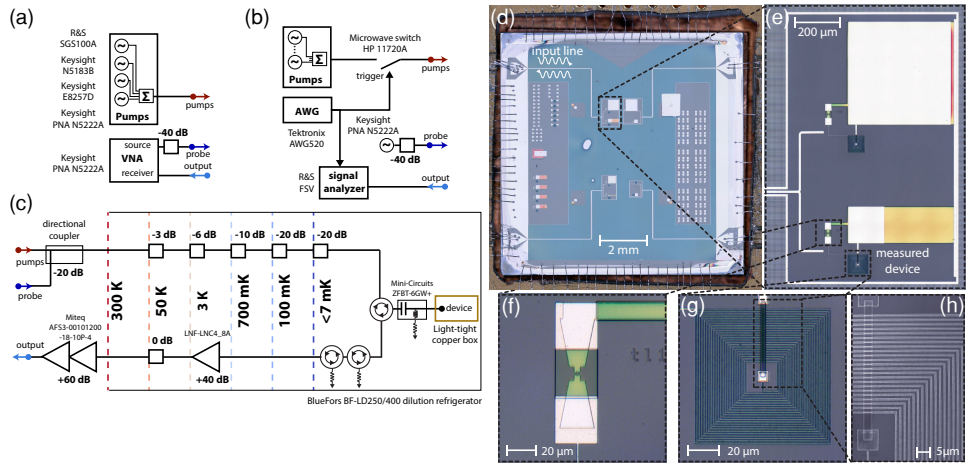


Figure 7.5: **Experimental setup and device.** (a) Room temperature setup for spectroscopy experiments, (b) Room temperature setup for time-domain experiments. These setups are connected to the fixed setup shown in (c). (c) Cryogenic setup. (d) Optical image of the chip, wire-bonded to a surrounding printed circuit board (PCB). The PCB is mounted in a copper box which is cooled below 7 mK (*i.e.* under the range of our fridge thermometry) in our dilution refrigerator. (e) Optical image of the two circuits connected to the measured feed-line. Due to a small cross-Kerr to line-width ratio, photon-number splitting was not achieved in the top device, where the low (high) mode was designed to resonate at ~ 50 MHz (~ 7.2 GHz). (f) Optical image of the SQUID, under a protective a-Si:H layer to avoid damage from Ar milling in the last step. (g), (g) Optical and SEM image of the 23-turn spiral inductor which has a $1.5 \mu\text{m}$ pitch and a 500 nm wire width.

7.6. Theory

7.6.1. Circuit Hamiltonian

In this section, we derive the Hamiltonian for the circuit shown in Fig. 7.6(a) using the black-box quantisation method [245]. This method allows the systematic derivation of the resonance frequency $\bar{\omega}_m$ and anharmonicity A_m of the different modes m of a circuit from the admittance $Y(\omega) = 1/Z(\omega)$ across the Josephson junction if we replace the latter by a linear inductor $L_J = \hbar^2/4e^2 E_J$. The resonance frequencies $\bar{\omega}_m$ are the zeros

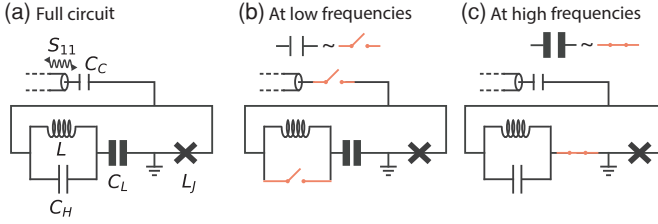


Figure 7.6: The circuit studied in this work (a) and approximate circuits for the low-frequency (b) and high-frequency regime (c).

of the admittance $Y(\bar{\omega}_m) = 0$, and the anharmonicities are given by

$$A_m = -\frac{2e^2}{L_J \bar{\omega}_m^2 (\text{Im} Y'(\bar{\omega}_m))^2}. \quad (7.7)$$

The idea is to quantify through A_m the amount of current traversing the Josephson junction for an excitation in mode m . The Hamiltonian of the circuit is then

$$\hat{H} = \sum_m \hbar \bar{\omega}_m \hat{a}_m^\dagger \hat{a}_m + \underbrace{E_J [1 - \cos \hat{\varphi}] - E_J \frac{\hat{\varphi}^2}{2}}_{\text{junction nonlinearity}}, \quad (7.8)$$

where $\hat{\varphi} = \sum_m (2A_m/E_J)^{1/4} (\hat{a}_m^\dagger + \hat{a}_m)$.

In the circuit of Fig. 7.6(a), there are two modes, a high-frequency one and a low-frequency one. By comparing to a black-box quantisation of the full circuit, we find that taking the approximation of $C_H \simeq 0$, $C_C \simeq 0$ for the low-frequency mode and $C_L \simeq \infty$ for the high-frequency mode results in corrections of only 0.2, 1.2, 0.3 and 2.1 % in the value of ω_L , ω_H , A_L and A_H respectively. It is therefore a good approximation, which has the additional advantage of producing simple analytical equations for the frequencies and anharmonicities of the circuit. Starting with the low-frequency mode shown in Fig. 7.6(b), we find the (imaginary part of the) admittance across the linearized junction to be

$$\text{Im} Y(\omega) = \frac{1}{\omega L_J} \frac{\left(\frac{\omega}{\omega_L}\right)^2 - 1}{1 - (\omega \sqrt{LC_L})^2}, \quad (7.9)$$

yielding the resonance frequency

$$\omega_L = \frac{1}{\sqrt{(L + L_J)C_L}}. \quad (7.10)$$

Taking the derivative of the imaginary part of the admittance at $\omega = \omega_L$ yields:

$$\text{Im} \frac{\partial Y}{\partial \omega}(\omega_L) = 2C_L \left(\frac{L + L_J}{L_J}\right)^2 \quad (7.11)$$

Substituting this into Eq. (7.7) yields

$$A_L = -\frac{e^2}{2C_L} \left(\frac{L_J}{L + L_J} \right)^3. \quad (7.12)$$

Turning to the high-frequency mode shown in Fig. 7.6(c), we find the (imaginary part of the) admittance across the linearized junction to be

$$\text{Im}Y(\omega) = C_H \omega \left(1 - \frac{\omega_H^2}{\omega^2} \right), \quad (7.13)$$

yielding the resonance frequency

$$\omega_H = \sqrt{\frac{L + L_J}{LL_J C_H}}. \quad (7.14)$$

Taking the derivative of the imaginary part of the admittance at $\omega = \omega_H$ yields:

$$\text{Im} \frac{\partial Y}{\partial \omega}(\omega_H) = 2C_H \quad (7.15)$$

Substituting this into Eq. (7.7) yields

$$A_H = -\frac{e^2}{2C_H} \left(\frac{L}{L + L_J} \right). \quad (7.16)$$

A Taylor expansion of the junctions cosine potential is justified if the anharmonicities are weak and only a few photons populate the circuit. Whilst numerical calculations in this work consider the 8-th order expansion, much understanding can be gleaned by stopping the expansion at the fourth-order

$$\begin{aligned} \hat{H}_{4,\text{diag}} = & \hbar\omega_H \hat{a}^\dagger \hat{a} - \frac{A_H}{2} \hat{a}^\dagger \hat{a}^\dagger \hat{a} \hat{a} \\ & + \hbar\omega_L \hat{b}^\dagger \hat{b} - \frac{A_L}{2} \hat{b}^\dagger \hat{b}^\dagger \hat{b} \hat{b} \\ & - \chi \hat{a}^\dagger \hat{a} \hat{b}^\dagger \hat{b}, \end{aligned} \quad (7.17)$$

where χ is the cross-Kerr coupling: the amount by which the high-mode transition shifts as a result of adding an excitation in the low mode and vice versa. We defined the first transition frequencies of both modes

$$\begin{aligned} \hbar\omega_H &= \hbar\bar{\omega}_H - A_H - \frac{\chi}{2}, \\ \hbar\omega_L &= \hbar\bar{\omega}_L - A_L - \frac{\chi}{2}. \end{aligned} \quad (7.18)$$

In Eq. (7.17), we have neglected terms in the expansion which are off-diagonal in the Fock basis and do not modify the eigenenergies to leading order perturbation theory. The eigenfrequencies of the system are summarized in the energy diagram of Fig. 7.7

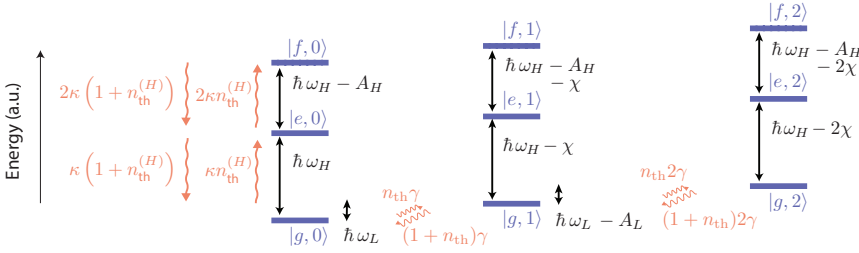


Figure 7.7: **Detailed energy diagram of the system.** We depict the first three levels of both high and low mode along with their dissipation and thermalisation rates. Transition energies are written with $\hbar = 1$.

7.6.2. Simulating the reflection measurement

We now introduce a driving term in the Hamiltonian and consider losses to both the environment and the measurement port. Following input-output theory [246, 247], the quantum Langevin equation for $\hat{a}(t)$ is

$$\frac{d}{dt}\hat{a}(t) = \frac{i}{\hbar}[\hat{H}_{\text{undr}}, \hat{a}(t)] - \frac{\kappa}{2}\hat{a}(t) + \sqrt{\kappa_{\text{ext}}}\tilde{a}_{\text{in}}(t). \quad (7.19)$$

The undriven Hamiltonian \hat{H}_{undr} corresponds to that of Eq. (7.8), where the degree of expansion of the nonlinearity is yet unspecified. The microwave reflection (in the time-domain) is given by

$$S_{11}(t) = \frac{\tilde{a}_{\text{out}}(t)}{\tilde{a}_{\text{in}}(t)} = 1 - \sqrt{\kappa_{\text{ext}}}\frac{\hat{a}(t)}{\tilde{a}_{\text{in}}(t)}, \quad (7.20)$$

where $\tilde{a}_{\text{in}}(t)$ ($\tilde{a}_{\text{out}}(t)$) is the incoming (outgoing) field amplitude, κ_{ext} (κ) is the external (total) coupling rate of the high-frequency mode. The coupling of the low mode to the feed-line $\gamma_{\text{ext}}/2\pi = 2s^{-1}$ is much smaller than the coupling of the high mode to the feed-line $\kappa_{\text{ext}}/2\pi = 1.63 \cdot 10^6 s^{-1}$, we therefore assume that a drive tone only affects the high-frequency mode. For a coherent drive, characterized by a drive frequency ω_d and an incoming power P_{in} (equal to the average power $\langle P(t) \rangle$ of the oscillating input signal), the wave amplitude is

$$\tilde{a}_{\text{in}}(t) = \sqrt{\frac{P_{\text{in}}}{\hbar\omega_d}}e^{-i\omega_d t}, \quad (7.21)$$

and the drive term can be incorporated in the Hamiltonian of the system

$$\begin{aligned} \frac{d}{dt}\hat{a}(t) &= \frac{i}{\hbar}[\hat{H}_{\text{undr}} + \hat{H}_{\text{drive}}, \hat{a}(t)] - \frac{\kappa_{\text{ext}}}{2}\hat{a}(t), \\ \text{where } \hat{H}_{\text{drive}} &= i\hbar\epsilon_d (e^{-i\omega_d t}\hat{a}^\dagger(t) - e^{i\omega_d t}\hat{a}(t)), \\ \epsilon_d &= \sqrt{\frac{\kappa_{\text{ext}}P_{\text{in}}}{\hbar\omega_d}}. \end{aligned} \quad (7.22)$$

Additionally, we also remove the time-dependence in the drive Hamiltonian by moving to a frame rotating at ω_d with the unitary transformation $U_{\text{probe}} = e^{i\omega_d t \hat{a}^\dagger \hat{a}}$,

$$\frac{d}{dt} \hat{a} = \frac{i}{\hbar} [U_{\text{probe}}^\dagger \hat{H}_{\text{undr}} U_{\text{probe}} + \tilde{H}_{\text{drive}}, \hat{a}] - \frac{\kappa_{\text{ext}}}{2} \hat{a}, \quad (7.23)$$

where $\hat{a} e^{i\omega_d t} = \hat{a}(t)$ and

$$\tilde{H}_{\text{drive}} = -\hbar\omega_d \hat{a}^\dagger \hat{a} + i\hbar\epsilon_d (\hat{a}^\dagger - \hat{a}). \quad (7.24)$$

In this rotating frame, the reflection coefficient becomes

$$\hat{S}_{11}(\omega_d) = 1 - \frac{\kappa_{\text{ext}}}{\epsilon_d} \hat{a}, \quad (7.25)$$

of which we measure the expectation value when probing the system. From now on, and in the main text we use the shorthand $S_{11}(\omega_d) = \langle \hat{S}_{11}(\omega_d) \rangle$.

The evolution of the density matrix of the system ρ is described by the Lindblad master equation

$$\begin{aligned} \frac{d}{dt} \rho = & -\frac{i}{\hbar} [H_{4,\text{diag}} + \hat{H}_{\text{drive}}, \rho] \\ & + \kappa(n_{\text{th}}^{(H)} + 1) \mathcal{L}[\hat{a}] + \kappa n_{\text{th}}^{(H)} \mathcal{L}[\hat{a}^\dagger] \\ & + \gamma(n_{\text{th}} + 1) \mathcal{L}[\hat{b}] + \gamma n_{\text{th}} \mathcal{L}[\hat{b}^\dagger], \end{aligned} \quad (7.26)$$

which we solve numerically using the QuTiP simulation toolbox [83]. Note that the internal dissipation of the high mode κ_{int} , is added to the external dissipation rate to constitute its total dissipation rate $\kappa = \kappa_{\text{int}} + \kappa_{\text{ext}}$. The low mode is attributed a dissipation rate γ . The average thermal occupation of the two modes are denoted by $n_{\text{th}}^{(H)}$ and n_{th} for the high and low mode respectively.

The expectation value of the reflection coefficient is given by

$$S_{11}(\omega_d) = \text{Tr} \left[\rho \left(1 - \frac{\kappa_{\text{ext}} \hat{a}}{\epsilon_d} \right) \right]. \quad (7.27)$$

In search for an analytical form for S_{11} , we may treat the driven part of the density matrix as a perturbation (for small probe powers), i.e. we may write $\rho = \rho_{\text{unpert}} + \epsilon_d \rho_{\text{pert}}$, where ρ_{unpert} is the unperturbed (diagonal) density matrix and ρ_{pert} is the perturbed density matrix (expressed in units of time). As explained in the supplementary material of Ref. [189], after analytically solving the Lindblad equation, we arrive to a solution

$$\begin{aligned} S_{11}(\omega_d) = & 1 - (P_g - P_e) \sum_n P_n \frac{\kappa_{\text{ext}}}{i\Delta_{g,n} + \kappa_{g,n}} \\ & - (P_e - P_f) \sum_n P_n \frac{2\kappa_{\text{ext}}}{i\Delta_{e,n} + \kappa_{e,n}}, \end{aligned} \quad (7.28)$$

where $\kappa_{g,n} = \kappa(1 + 4n_{\text{th}}^{(H)}) + 2\gamma(n + (1 + 2n)n_{\text{th}})$,

$\kappa_{e,n} = \kappa(3 + 8n_{\text{th}}^{(H)}) + 2\gamma(n + (1 + 2n)n_{\text{th}})$.

This corresponds to a sum of Lorentzian functions, each associated to high-mode level i and a low-mode level n , with line-width $\kappa_{i,n}$ centred around $\Delta_{i,n} = 0$, where

$$\begin{aligned}\Delta_{g,n} &= \omega_{\text{H}} - n\chi/\hbar - \omega_{\text{d}} , \\ \Delta_{e,n} &= \omega_{\text{H}} - (n\chi - A_{\text{H}})/\hbar - \omega_{\text{d}} .\end{aligned}\quad (7.29)$$

When fitting data, we use Eq. (7.28) whilst fixing $\Delta_{i,n}$ with a diagonalisation of the Hamiltonian Eq. (7.8) Taylor expanded to the 8-th order. Note that in the main text we use the notation $\kappa_{g,n} = \kappa_n$.

7.6.3. Four wave mixing and cooling rate

Adding a pump tone driving the high mode with frequency ω_{p} and strength ϵ_{p} transforms the system Hamiltonian into [236],

$$\begin{aligned}\hat{H}_{4,\text{dr}} &= \hbar\bar{\omega}_{\text{H}}\hat{a}^\dagger\hat{a} + \hbar\bar{\omega}_{\text{L}}\hat{b}^\dagger\hat{b} + E_{\text{J}}[1 - \cos\tilde{\varphi}] - \frac{E_{\text{J}}}{2}\tilde{\varphi}^2 \\ \text{where } \tilde{\varphi} &= (2A_{\text{H}}/E_{\text{J}})^{1/4}(\hat{a}^\dagger + \hat{a}) + (2A_{\text{L}}/E_{\text{J}})^{1/4}(\hat{b}^\dagger + \hat{b}) \\ &+ (2A_{\text{H}}/E_{\text{J}})^{1/4}(\tilde{\xi}_{\text{p}}^* + \tilde{\xi}_{\text{p}}),\end{aligned}\quad (7.30)$$

where the pump field amplitude $\tilde{\xi}_{\text{p}}$ (assuming $|\omega_{\text{H}} - \omega_{\text{p}}| \gg \kappa$) is given by

$$\tilde{\xi}_{\text{p}} \simeq \epsilon_{\text{p}} e^{-i\omega_{\text{p}}t} \left(\frac{1}{\omega_{\text{p}} - \bar{\omega}_{\text{H}}} + \frac{1}{\omega_{\text{p}} + \bar{\omega}_{\text{H}}} \right), \quad (7.31)$$

and the Hamiltonian is expressed in the displaced frame of the pump. We now Taylor expand the cosine nonlinearity to fourth-order, neglecting terms which are off-diagonal in the Fock basis except when they depend on $\tilde{\xi}_{\text{p}}$, yielding

$$\hat{H}_{4,\text{pumped}} = \hat{H}_{4,\text{diag}} + \hat{H}_{\text{p}}, \quad (7.32)$$

where $\hat{H}_{4,\text{diag}}$ is given by Eq. (7.17). \hat{H}_{p} contains terms which are dependent on the pump power and frequency. In Table 7.1 we summarise the most relevant terms used in this work, along with the approximate pumping frequency ω_{p} that is required to eliminate their time-dependence (the complete set of terms can be found in Ref. [189]). As shown in the next paragraph, this occurs when the pump frequency matches the transition frequency between the two states coupled by the interaction term.

We now move to the interaction picture through the unitary transformation

$$U_{\text{int}} = e^{i\hat{H}_{4,\text{diag}}t/\hbar}, \quad (7.33)$$

$\omega_p \simeq$	prefactor	interaction
Stark shift		
	$-2A_H \xi_p ^2$	$\hat{a}^\dagger \hat{a}$
	$-\chi \xi_p ^2$	$\hat{b}^\dagger \hat{b}$
Heating interactions		
$(\omega_H + \omega_L)/2$	$-A_H^{\frac{3}{4}} A_L^{\frac{1}{4}} (\tilde{\xi}_p^*)^2$	$\hat{a} \hat{b} + \hat{a}^\dagger \hat{b}^\dagger$
$\omega_H + 2\omega_L$	$-\chi \tilde{\xi}_p^*/2$	$\hat{a} \hat{b}^2 + \hat{a}^\dagger (\hat{b}^\dagger)^2$
$2\omega_H + \omega_L$	$-A_H^{\frac{3}{4}} A_L^{\frac{1}{4}} \tilde{\xi}_p^*$	$\hat{a}^2 \hat{b} + (\hat{a}^\dagger)^2 \hat{b}^\dagger$
Cooling interactions		
$(\omega_H - \omega_L)/2$	$-A_H^{\frac{3}{4}} A_L^{\frac{1}{4}} (\tilde{\xi}_p^*)^2$	$\hat{a} \hat{b}^\dagger + \hat{a}^\dagger \hat{b}$
$\omega_H - 2\omega_L$	$-\chi \tilde{\xi}_p^*/2$	$\hat{a} (\hat{b}^\dagger)^2 + \hat{a}^\dagger \hat{b}^2$
$2\omega_H - \omega_L$	$-A_H^{\frac{3}{4}} A_L^{\frac{1}{4}} \tilde{\xi}_p^*$	$\hat{a}^2 \hat{b}^\dagger + (\hat{a}^\dagger)^2 \hat{b}$

Table 7.1: **Employed four-wave mixing terms.** Terms become time-independent around the frequency ω_p given in the left column.

$\hat{H}_{4,\text{diag}}$ is diagonal in the Fock state basis $\{|j, n\rangle\}_{\substack{n=0,1,2,\dots \\ j=g,e,f,\dots}}$

$$\hat{H}_0 = \sum_{\substack{n=0,1,2,\dots \\ j=g,e,f,\dots}} \hbar \epsilon_{j,n} |j, n\rangle \langle j, n| ,$$

$$\text{where } \epsilon_{j,n} = n\omega_L - \frac{A_L}{2\hbar} (n^2 - n) \quad (7.34)$$

$$+ j\omega_H - \frac{A_H}{2\hbar} (j^2 - j)$$

$$- nj\chi/\hbar .$$

To determine \hat{H}_p in this frame, it suffices to know the expression of annihilation operators in this frame. We will take as an example the term we use for cooling, which reads in the interaction picture

$$U_{\text{int}} \left(-A_H^{\frac{3}{4}} A_L^{\frac{1}{4}} (\tilde{\xi}_p^*)^2 \hat{a}^2 \hat{b}^\dagger \right) U_{\text{int}}^\dagger + h.c. \quad (7.35)$$

$$= -A_H^{\frac{3}{4}} A_L^{\frac{1}{4}} (\tilde{\xi}_p^*)^2 (U \hat{a} U^\dagger)^2 (U \hat{b} U^\dagger)^\dagger + h.c. .$$

Since \hat{H}_0 is diagonal, exponentiating it only requires exponentiating each of the diagonal elements, and the annihilation operators in the interaction picture are

$$\begin{aligned}
U_{\text{int}}\hat{a}U_{\text{int}}^\dagger &= \sum_{\substack{n=0,1,\dots \\ j=g,e,\dots}} \sqrt{j+1} e^{-(\epsilon_{n,j+1}-\epsilon_{n,j})t/\hbar} |j, n\rangle \langle j+1, n| \\
U_{\text{int}}\hat{b}U_{\text{int}}^\dagger &= \sum_{\substack{i=0,1,\dots \\ j=g,e,\dots}} \sqrt{n+1} e^{-(\epsilon_{j,n+1}-\epsilon_{j,n})t/\hbar} |j, n\rangle \langle j, n+1| .
\end{aligned} \tag{7.36}$$

Note that if the system were harmonic, these expressions would simplify to $e^{-i\omega_{\text{H}}t}\hat{a}$ and $e^{-i\omega_{\text{L}}t}\hat{b}$. If we substitute Eqs. (7.36) into Eq. (7.35), one of the terms we obtain is

$$-\hbar g e^{i(\omega_{\text{p}}-(2\omega_{\text{H}}-A_{\text{H}}/\hbar-\omega_{\text{L}}))t} |g, 1\rangle \langle f, 0| + h.c. , \tag{7.37}$$

where we defined the interaction strength

$$g = \sqrt{2} A_{\text{H}}^{\frac{3}{4}} A_{\text{L}}^{\frac{1}{4}} |\xi_{\text{p}}|/\hbar . \tag{7.38}$$

By choosing the pump frequency $\omega_{\text{p}} = 2\omega_{\text{H}} - A_{\text{H}}/\hbar - \omega_{\text{L}}$, the term becomes time-independent, making it more relevant than the other terms of \hat{H}_{P} . More generally, we can engineer the cooling interactions

$$-\hbar g \sqrt{n+1} |f, n\rangle \langle g, n+1| + h.c. , \tag{7.39}$$

by choosing the pump frequencies

$$\omega_{\text{p}} = 2\omega_{\text{H}} - 2n\chi/\hbar - A_{\text{H}}/\hbar - \omega_{\text{L}} . \tag{7.40}$$

Rather than lowered, the number of excitations in the low mode can also be raised using interactions of the form

$$-\hbar g \sqrt{n+1} |f, n+1\rangle \langle g, n| + h.c. , \tag{7.41}$$

which are realized by choosing the pump frequencies

$$\omega_{\text{p}} = 2\omega_{\text{H}} - 2(n+1)\chi/\hbar - A_{\text{H}}/\hbar + \omega_{\text{L}} . \tag{7.42}$$

In all the cooling experiments discussed here, we employed the interaction described by Eq. (7.39). For sufficiently weak pumping strengths such that $2\kappa \gg \sqrt{n}g$, the cooling rate of the low-frequency mode is given by [189]

$$\Gamma_{n \rightarrow n-1} = \frac{2ng^2 P_g}{\kappa(1 + \frac{3}{2}n_{\text{th}}^{(H)})} \frac{1}{1 + (\frac{\Delta}{\kappa})^2} , \tag{7.43}$$

where $\Delta = \omega_{\text{p}} - (2\omega_{\text{H}} - 2n\chi/\hbar - A_{\text{H}}/\hbar - \omega_{\text{L}})$. The ratio of the cooling rate to γ , is defined as the cooperativity

$$C = \frac{\Gamma_{1 \rightarrow 0}}{\gamma} = \frac{2g^2}{\kappa\gamma(1 + \frac{3}{2}n_{\text{th}}^{(H)})} \frac{1}{1 + (\frac{\Delta}{\kappa})^2} . \tag{7.44}$$

7.7. Background subtraction

7.7.1. Network analysis

Most of our data analysis relies on fitting a sum of complex Lorentzians (see Eq. (7.28)), to the measured microwave reflection S_{11} in both phase and amplitude. The signal we acquire is affected by the imperfections of the microwave equipment used to carry the signals to and from the device.

These can be modeled by a two port network with s parameters s_{11}, s_{22} , corresponding to the reflections at the VNA ports (reflected back to the VNA) and at the device (reflected back to the device) respectively, and s_{21}, s_{12} , corresponding to the attenuation chain from the VNA to the device and the amplification chain from the device to the VNA respectively.

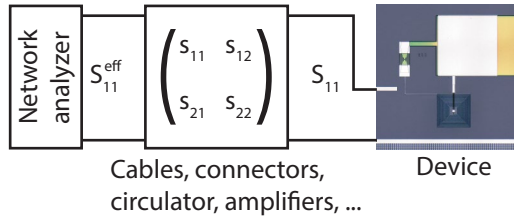


Figure 7.8: **Effective microwave network.** We do not directly have access to the reflection at our device S_{11} . We measure an effective reflection coefficient S_{11}^{eff} , affected by the imperfect microwave equipment between the network analyzer and device described by an s -matrix.

We hence measure with our VNA the effective microwave reflection

$$S_{11}^{\text{eff}} = s_{11} + \frac{s_{12}s_{21}}{1 - s_{22}S_{11}} S_{11} \quad (7.45)$$

Note that these s parameters are generally frequency dependent. We make the approximation $s_{11}, s_{22} \ll s_{12}, s_{21}$, meaning we attribute most of the measured microwave background to the frequency dependent transmission of the attenuation and amplification chain. The signal we want to measure is now proportional to a so-called “microwave background”

$$S_{11}^{\text{eff}} \simeq s_{12}s_{21}S_{11}, \quad (7.46)$$

which we have to experimentally measure.

7.7.2. Measuring the microwave background

As shown in Fig. 7.9, when probing the system at high power the device response is $S_{11} = 1$, allowing us to extract the microwave background $s_{12}s_{21}$. This phenomenon is a consequence of super-splitting as explained in [248], which we will briefly summarize here.

To understand super-splitting, we have to truncate the high mode to a two-level system constituted of its two first levels $|g\rangle$ and $|e\rangle$. In the Bloch sphere, the probe tone will cause rotations around the y -axis and $1 - S_{11}$ corresponds to the projection of the state vector on the x -axis. For driving rates faster than κ , the state vector will

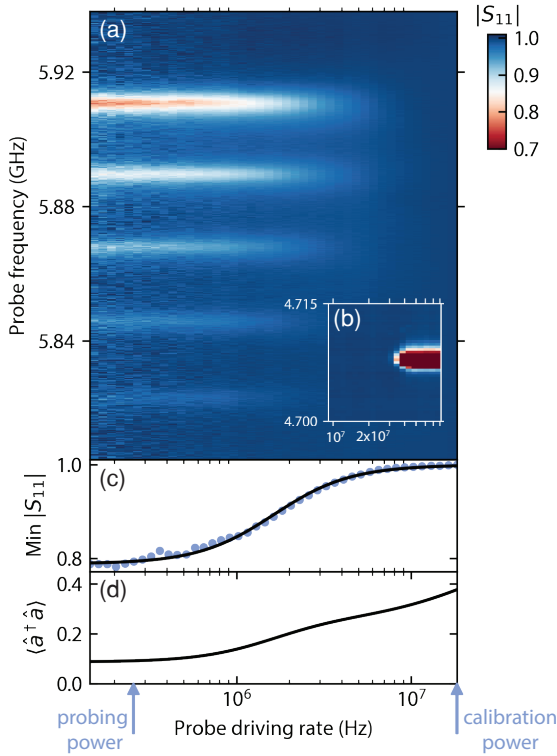


Figure 7.9: **High-probe-power behaviour.** (a) $|S_{11}|$ as a function of probe frequency and probe power. (b) At higher powers, the system starts to resonate at a different frequency, corresponding to the junction being replaced by an open circuit. (c) Depth of the $n = 0$ peak extracted from data (blue dots) and numerical steady-state calculation. As the probe driving rate exceeds κ , the peaks vanish. We use the disappearance of peaks at the high power indicated by an arrow to acquire a microwave background that is subtracted (divided) in phase (amplitude) from all datasets. (d) Population in the high mode as a function of probe power as extracted from simulation. We used this information to choose the probing power indicated by an arrow for all other experiments. It is as high as possible to increase signal to noise ratio, but low enough to not populate the high mode.

rapidly rotate around the y -axis yielding a zero projection on the x -axis hence $S_{11} = 1$ and no peak. For driving rates slower than κ , random decays of the state vector will be very likely to occur before the state vector can rotate around the y -axis, yielding a non zero projection on the x -axis and a dip in the microwave reflection. A signature of this effect is the splitting of the absorption peak in two for large probe powers. Whilst our signal to noise does not allow the resolution of this feature, it is present in the fitted simulation, supporting this explanation.

At even higher power, the system starts to resonate at a different frequency, corresponding to the junction being replaced by an open circuit when the current traversing the junction exceeds the critical current. This effect is shown in the inset, Fig. 7.9(b).

We use the disappearance of peaks at a high power indicated by the arrow “cali-

brating power” to acquire a microwave background that is subtracted (divided) in phase (amplitude) to all datasets.

$$\frac{S_{11}^{\text{eff}}}{s_{12}s_{21}} \simeq S_{11} . \quad (7.47)$$

7.8. Fitting

Here, we summarize our fitting routine. We start by extracting γ from the time-domain data, which will be used in the formula for the linewidth κ_n in all subsequent fits. By fitting the microwave reflection S_{11} to a sum of Lorentzians (see Eq. (7.28)), we get access to the peaks linewidths and amplitudes which allows us to determine κ , κ_{ext} and $n_{\text{th}}^{(H)}$. By fitting S_{11} to the eigenfrequencies obtained from a diagonalisation of the Hamiltonian of Eq. (7.8), we determine the values of the circuit elements. The occupation of the low mode n_{th} is determined separately for each individual experiment. Each step is detailed in the subsections below.

7.8.1. Low-frequency mode dissipation

We start by fitting the thermalisation from the ground-state measured in time-domain (Fig. 7.11(a)) to determine γ . Since the line-width of the $S_{11}(t)$ peaks is a function of γ and n_{th} , we start by postulating these two values to extract a first estimate of the time evolution of P_n . By fitting the evolution of P_n to the rate equation of Eq. (7.6), we extract a new value for γ and n_{th} . We then repeat this process many times, each time using the new values γ and n_{th} to fit $S_{11}(t)$, until we converge to $\gamma/2\pi = 23.5 \cdot 10^3 \text{ s}^{-1}$.

7.8.2. Circuit parameters

The frequency of the system transitions (and hence the circuit parameters) is determined by fitting a numerical steady-state calculation of S_{11} , following a diagonalisation of the Hamiltonian in Eq. (7.8). In this fit we additionally impose that the transition frequency $|g, 0\rangle \leftrightarrow |g, 1\rangle$ matches the value measured in two-tone spectroscopy (Fig. 7.10(a)). The fitted circuit parameters are summarised in Table 7.2.

7.9. Supplementary experimental data

7.9.1. Low-frequency spectrum

We monitor the height of the $|g, 0\rangle \leftrightarrow |e, 0\rangle$, whilst sweeping the frequency of a secondary pump tone. As shown in Figs. 7.10(a), (b), this allows us to easily measure the anharmonicity of the high mode and the frequency of the low mode.

The line-width of the low-mode peak is considerably larger than the previously determined low-mode dissipation rate $\gamma/2\pi = 23 \cdot 10^3 \text{ s}^{-1}$. If the line-width was equal to γ , we would expect to see photon number splitting, distinct peaks separated by the low-mode anharmonicity A_L , corresponding to the transitions $|g, n\rangle \leftrightarrow |g, n+1\rangle$. To understand why this is not the case, we fit a steady-state numerical computation of a pumped and probed Hamiltonian

$$\begin{aligned} \hat{H} = & -A_H(\hat{a}^\dagger)^2\hat{a}^2 + \hbar(\omega_L - \omega_p)\hat{b}^\dagger\hat{b} - A_L(\hat{b}^\dagger)^2\hat{b}^2 \\ & + i\hbar\epsilon_d(\hat{a}^\dagger - \hat{a}) + i\hbar\epsilon_p(\hat{b}^\dagger - \hat{b}) , \end{aligned} \quad (7.48)$$

Quantity	Symbol	Value	Equation
Hamiltonian parameters			
Dressed high-mode frequency	ω_H	$2\pi \times 5.911$ GHz	$\bar{\omega}_H + A_H/\hbar + \chi/2\hbar$
Dressed low-mode frequency	ω_L	$2\pi \times 173$ MHz	$\bar{\omega}_L + A_L/\hbar + \chi/2\hbar$
Bare high-mode frequency	$\bar{\omega}_H$	$2\pi \times 6.113$ GHz	$\sqrt{\frac{L+L_J}{L L_J C_L}}$
Bare low-mode frequency	$\bar{\omega}_L$	$2\pi \times 182$ MHz	$\frac{1}{\sqrt{(L+L_J)C_L}}$
High-mode anharmonicity	A_H	$\hbar \times 192$ MHz	$\frac{e^2}{2C_H} \left(\frac{L}{L+L_J} \right)$,
Low-mode anharmonicity	A_L	$\hbar \times 495$ kHz	$\frac{e^2}{2C_L} \left(\frac{L_J}{L+L_J} \right)^3$,
Cross-Kerr	χ	$\hbar \times 21.29$ MHz	$2\sqrt{A_L A_H}$
Dissipation rates			
High-mode dissipation rate	κ	$2\pi \times 3.70$ MHz	
External coupling rate	κ_{ext}	$2\pi \times 1.63$ MHz	
Low-mode dissipation rate	γ	$2\pi \times 23.50$ kHz	
Low-mode external coupling rate	γ_{ext}	$2\pi \times 1.99$ Hz	
High-mode quality factor	Q_H	1599	ω_H/κ
High-mode external quality factor	$Q_H^{(\text{ext})}$	3617	$\omega_H/\kappa_{\text{ext}}$
Low-mode quality factor	Q_L	7348	ω_L/γ
Low-mode external quality factor	$Q_L^{(\text{ext})}$	87×10^6	$Z_0 \sqrt{\frac{C_L}{L+L_J}} \left(\frac{C_c}{C_L} \right)^2$
Thermal parameters			
High-mode temperature	T_H	112 mK	
Low-mode temperature	T_L	17 mK	
High-mode occupation number	$n_{\text{th}}^{(H)}$	0.09	$\frac{1}{e^{\frac{\hbar\omega_H}{k_B T_H}} - 1}$
Low-mode occupation number	n_{th}	1.62	$\frac{1}{e^{\frac{\hbar\omega_L}{k_B T_L}} - 1}$
Circuit parameters			
Josephson energy	E_J	$\hbar \times 4.01$ GHz	$\frac{\hbar^2 \bar{\omega}_H^2 \bar{\omega}_L^2}{8(\bar{\omega}_H \sqrt{A_L} + \bar{\omega}_L \sqrt{A_H})^2}$
Josephson inductance	L_J	41 nH	$\frac{\hbar^2}{4e^2 E_J}$
Low-mode capacitance	C_L	11.1 pF	$\frac{e^2 \sqrt{A_L} \bar{\omega}_H^3}{2(\bar{\omega}_L \sqrt{A_H} + \bar{\omega}_H \sqrt{A_L})^3}$
High-mode capacitance	C_H	40.7 fF	$\frac{e^2 \bar{\omega}_L}{2(\sqrt{A_H A_L} \bar{\omega}_H + A_H \bar{\omega}_L)}$
High-mode inductance	L	28.2 nH	$\frac{2\sqrt{A_H} (\bar{\omega}_L \sqrt{A_H} + \bar{\omega}_H \sqrt{A_L})^2}{e^2 \sqrt{A_L} \bar{\omega}_H^3 \bar{\omega}_L}$
Coupling capacitor	C_c	0.95 fF	$C_H \sqrt{\frac{\kappa_{\text{ext}} L L_J}{Z_0 (L+L_J)}}$
Feed-line impedance	Z_0	50 Ω	

Table 7.2: Fitted system parameters.

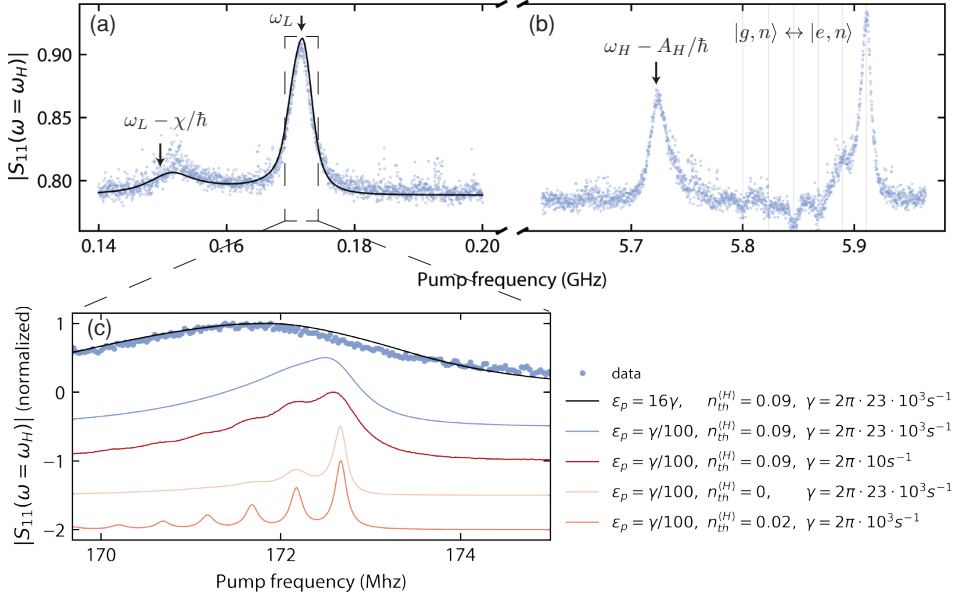


Figure 7.10: **Two-tone measurement of the anharmonicity and lower mode spectrum.** (a) We sweep a pump tone around the low-mode frequency (x-axis) whilst monitoring the depth of the $n = 0$ peak $|S_{11}(\omega = \omega_H)|$ (y-axis). We observe two peaks, separated by χ corresponding to the transitions $|g, n\rangle \leftrightarrow |g, n+1\rangle$ at $\omega_p = \omega_L$ and $|e, n\rangle \leftrightarrow |e, n+1\rangle$ at $\omega_p = \omega_L - \chi/\hbar$. A steady-state numerical computation is shown as a black curve and data as blue points. (b) By performing the same measurement around the high-mode frequency, we measure a peak corresponding to $|e, 0\rangle \leftrightarrow |f, 0\rangle$ at $\omega_p = \omega_H - A_H/\hbar$. These two datasets provide a measurement of ω_L and A_H . (c) The line-width of the low mode was found to be significantly broader than γ , with no accessible photon-number resolution. By varying simulation parameters as detailed in the legend, we explore the origin of this broad line-width.

including the collapse operators $\kappa(n_{\text{th}}^{(H)} + 1)\mathcal{L}[\hat{a}]$, $\kappa n_{\text{th}}^{(H)}\mathcal{L}[\hat{a}^\dagger]$, $\gamma(n_{\text{th}} + 1)\mathcal{L}[\hat{b}]$, $\gamma n_{\text{th}}\mathcal{L}[\hat{b}^\dagger]$. The only free parameter is the pumping strength $\epsilon_p \sim 16 \times \gamma$, the probe strength was taken to be negligibly small with respect to all other rates in the model. By varying simulation parameters, we can then explore the origin of this broad line-width. These results are summarized in Fig. 7.10(c). Reducing the pumping strength ϵ_p will suppress what is usually referred to as ‘power broadening’, at the expense of the signal-to-noise ratio, but does not reveal photon-number splitting. By reducing γ to a negligibly small rate, photon number splitting can only be glimpsed behind a line-width broadening induced by the process $|g, n\rangle \rightarrow |e, n\rangle$ which occurs at a rate $\kappa n_{\text{th}}^{(H)}$. This becomes clear if we instead keep $\gamma/2\pi = 23 \cdot 10^3 \text{ s}^{-1}$ and take the limit $n_{\text{th}}^{(H)} = 0$, making the first two peaks apparent. As derived in Eq. (7.28), the line-width of a thermally populated anharmonic oscillator broadens significantly with its thermal occupation, which is responsible in this case for the disappearance (broadening) of peaks $n \geq 2$. By reducing both γ and $n_{\text{th}}^{(H)}$, photon-number resolution would become visible.

7.9.2. Full time-dependent spectrum

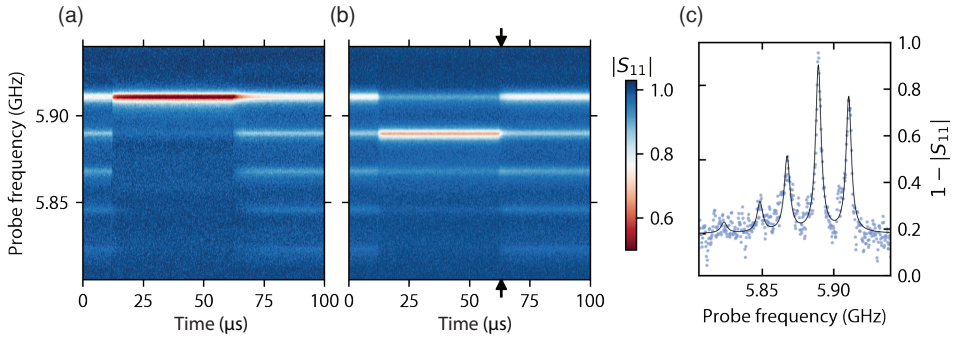


Figure 7.11: **Full time-dependent spectrum.** Time and probe frequency dependence of $|S_{11}|$ for both ground-state cooling (a) and the one-photon-state stabilisation (b). By fitting these datasets using Eq. (7.28), in both frequency and time, we construct the plots shown in Fig. 7.4. (c) line cut of the data set B (indicated by arrows in B) is shown as blue dots, the black line corresponds to a fit. The relatively low signal-to-noise ratio is responsible for the large noise in probability of Fig. 7.4.

8

Conclusions and outlook

*Earth, stream and tree return to the sea
Waves sweep the sand from my island,
from me.*

King Crimson, "Islands"

This thesis constitutes a small contribution to the stock of knowledge concerning superconducting qubits and their applications for quantum simulation as well as quantum control of mechanical and thermally-populated electromagnetic resonators in the radio-frequency range. Here I will summarise the main findings and give a personal reflection on possible further research directions for extending this work.

8.1. Qubit-qubit interactions

In chapter 4 we explored the possibility of realising experimentally a tuneable coupler for superconducting qubits that allows tuning into different interaction regimes. The coupling scheme is relevant for simulating a variety of many-body problems by means of analog quantum simulation and could be used for performing two-qubit gates. We demonstrated the experimental feasibility of this scheme, while maintaining high coherence of the qubits. Additionally we performed a thorough theoretical analysis of the circuit Hamiltonian that helped to understand some unexpected features and how to avoid them, which is valuable for future implementations especially when more circuit elements are involved.

More specifically, this work provided a very small step towards realising the first analog quantum simulations of extended Hubbard and Heisenberg XXZ models in solid-state platforms. Useful results, testing theoretical predictions, will eventually be obtained in more complex configurations in 2D geometries using tens of qubits and coupling elements. Scaling up, however, unavoidably leads to complexity. For example, the number of readout and control lines on the chip need to increase leading to spatial crowding. This is an issue that is currently being addressed by the community with the development of 3D integration methods that could allow for example the readout circuitry to be part of a separate chip that is connected in parallel to the quantum processor [110, 111]. Additionally, due to fabrication errors in targeting of Josephson junctions, the qubit frequencies cannot be reliably produced within the range of coupling strengths. Therefore, frequency tuning the qubits on and out of resonance is required in order to activate the interactions, which may lead to frequency crowding issues, e.g. qubit frequencies interfering with higher level transitions of nearby modes. Another possible issue is that of flux cross-talk, which concerns the unwanted flux tuning of SQUIDs as one tunes another flux channel, for example, due to unanticipated on-chip current paths in configurations using fluxlines (see Ref. [249] for AC and DC cross-talk calibration methods). In chapter 4 we demonstrated a reliable procedure for calibrating out these effects, which, however, might become very complex when tens of qubits and couplers are concerned.

The situation can become a lot easier by using off-resonant, fixed frequency qubits that can be made to interact via flux modulation on the coupling SQUIDs [250]. Apart from the advantage of coupling qubits that are far off-resonant to interact otherwise, this approach is interesting for generating interactions that are not possible in standard resonant coupling schemes, such as squeezing. For example, as proposed in Ref. [251], using our coupler with appropriate AC flux modulation at the sum or difference of the qubit frequencies, one can realise all possible interaction terms of the XYZ Heisenberg model. Such a scheme gets rid of much of the complexity concerning the control circuitry, flux cross-talk and frequency crowding, while enhancing the number of interactions at hand. We have made some preliminary tests of this concept using the device measured in chapter 4, which we show in Fig. 8.1. This is a very simple situation where the two qubits are off-resonant (at their top sweetspots) and an AC current is applied on top of the DC biasing on the coupler SQUID, while reading out one qubit via its dedicated resonator. When the modulation frequency matches the qubit frequency difference we additionally observe a second peak at the frequency of the other qubit,

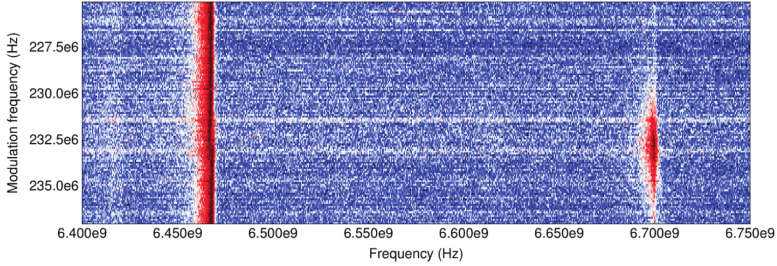


Figure 8.1: **Generating qubit-qubit interactions via flux modulation on the coupling SQUID in the device studied in chapter 4.** The qubits are tuned at their top sweetspots and the coupler is current-biased (DC) slightly off-resonant from its sweetspot. An additional AC current is applied through the coupler fluxline, modulating the flux on the SQUID. Readout is performed on the lower frequency qubit (~ 6.47 GHz) via its dedicated readout resonator. When the modulation frequency matches the qubit frequency difference (~ 233 MHz) a second peak is observed at the frequency of the other qubit, indicating transverse coupling between them.

indicating transverse qubit-qubit coupling. Further measurements with frequency modulation at the sum of the qubit frequencies could demonstrate squeezing interactions and, in combination with the always-on cross-Kerr (ZZ) coupling, the complete set of interactions required for simulating arbitrary spin models.

8.2. Mechanical quantum states

The main research question explored in chapter 5 was whether it would be possible to achieve generic quantum state preparation in a low-frequency mechanical resonator that is parametrically coupled to an electromagnetic mode. We showed that this could be achieved in a tuneable coupling architecture, using a SQUID-embedded mechanical resonator as a coupling element between two transmon qubits. We found that this configuration can give rise to a three-body interaction that is linear in all the modes and much stronger than decay rates, assuming typical parameters reported in experiments. We numerically demonstrated the ability to cool the mechanical resonator to its ground state and prepare generic quantum states using time-domain protocols that are typical in state-of-the-art superconducting qubit experiments.

In chapter 6 we used a similar coupling scheme between one qubit and a mechanical resonator and demonstrated the possibility of achieving ultrastrong couplings that are even larger than the resonator frequency, in the single-photon regime. Furthermore, we performed numerical simulations showing the possibility of ground-state cooling and preparation of mechanical cat states using realistic parameters obtained from recent experiments.

Follow-up theoretical work on this topic could focus on some more practical aspects relevant for an experimental realisation such as, for example, modelling the readout scheme for verifying the prepared mechanical states. Additionally, one could further explore the tripartite system dynamics in the ultrastrong-coupling regime ($g > \omega_m$). We have done some preliminary simulations in this regime, assuming a stronger magnetic field (20 mT) and considering a beam that is five times longer than the one considered

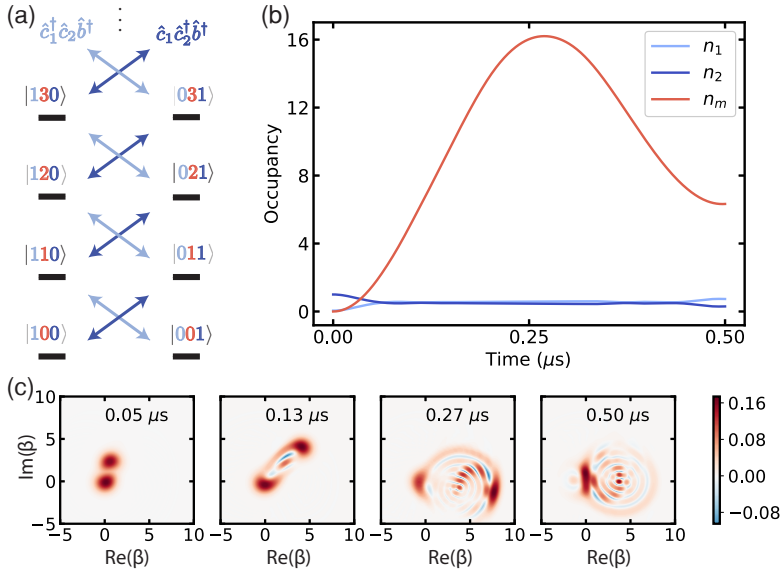


Figure 8.2: **Tripartite interaction dynamics of the system studied in chapter 5, in the USC coupling regime.** All parameters are similar to the ones in chapter 5, except for a five times lower mechanical frequency of 2 MHz (achieved with a five times longer beam) and two times stronger magnetic field, leading to a coupling strength of $g/2\pi \simeq 3 \text{ MHz} > \omega_m/2\pi$.

in chapter 5. This means five times smaller mechanical frequency (2 MHz) and ten times stronger coupling strength ($\sim 3 \text{ MHz}$). In this regime all terms in the tripartite interaction Hamiltonian $g(\hat{c}_1^\dagger \hat{c}_2 + \hat{c}_1 \hat{c}_2^\dagger)(\hat{b} + \hat{b}^\dagger)$ are resonant leading to very complex phenomena. The evolution of the excitations in the system, starting from one qubit in the excited state and assuming the mechanical ground state is reached, is plotted in Fig. 8.2(b). The evolution of the Wigner function of the mechanical resonator (obtained from the reduced density matrix without conditioning) is also plotted in Fig. 8.2(c). Remarkably the created state up to maximum phonon occupation features positive and negative fringes, reminiscent of the fringes in cat states. It is a complex “distorted cat” state resulting from the interplay of all the tripartite interaction terms and the individual radiation-pressure coupling terms with each qubit, and is therefore hard to interpret in terms of well-known quantum states. One could further explore this regime to controllably create desired states on demand after appropriate conditioning, for example. Further interesting results could be obtained by considering the case with more than one embedded beams on the SQUID, or including additional modes of the mechanical resonator, especially in the ultrastrong-coupling regime.

8.3. Thermally-populated resonators

In chapter 7 we examined the possibility of quantum control in a thermally-populated superconducting resonator in the radio-frequency regime. This was enabled by dispersively coupling it to a gigahertz superconducting qubit which was naturally cooled

down by a dilution refrigerator. Using reservoir engineering protocols we demonstrated ground-state cooling, preparation of Fock states and observed the dynamics of the thermalisation process in time domain.

In the future one could expand this work, using coherent population transfer techniques [252, 253], to determine the dephasing time of the resonator or even prepare superposition states. Moreover engineering the readout circuitry similar to QND measurements, i.e. by using a dispersively coupled readout resonator, may enable further quantum manipulation in time-domain. Furthermore, a natural step forward would be to resonantly couple the resonator to other quantum systems in the radio-frequency domain. One could for example resonantly couple to mechanical resonators, realised by metallic drumheads forming part of the electrical capacitor (or SQUID-embedded beams), that can typically be controlled only via parametric optomechanical coupling. Additionally, one could use the radio-frequency resonator to couple to and gain control over spin systems, as in Ref. [254]. Finally, extending the circuit to include coupled radio-frequency resonators, with sufficient individual control, could enable the study of thermodynamical effects in Bose-Hubbard models, in specially designed quantum simulators [242, 243].

8.4. Epilogue

The journey has come to an end. We wandered through mathematical derivations, fabricated microchips and measurements, wondering upon possibilities of harnessing the nonlinearity of Josephson elements in order to tame the elementary excitations of light and motion. We explored mainly three research directions, which compared to a typical PhD thesis might seem like exploring three disconnected faraway islands. They are, however, parts of a much wider scope of developing well-controlled quantum systems and contributing to quantum technologies. As such there is a lot of room for building on the answers we found and combining them to realise new research directions.

For example, well-controlled radio-frequency resonators (such as the one studied in chapter 7) could be employed to resonantly interface mechanical resonators (such as the ones studied in chapters 5 and 6), opening new avenues in interacting electromechanical systems. Additionally, one could use the techniques developed in chapter 5 as an alternative for controlling radio-frequency electrical resonators in time-domain using three-body interactions with high-frequency qubits. Another interesting avenue would be to explore analog quantum simulators of extended Bose-Hubbard models (using the couplings developed in chapter 4), where radio-frequency resonators with fast thermal control take the role of the primary components in the circuit, replacing the qubits. The possibilities are numerous, bound only by human imagination.

Acknowledgements

This thesis is the result of four very exciting years of research. The level of diversity in the topics, ranging from purely experimental to purely theoretical, reflects the diversity of all these brilliant minds I had the luck to be exposed to. Here I want to thank them all, knowing how faulty my memory can be and how difficult it is to properly express my gratitude in such a confined space.

First, I would like to thank the people that supervised me during these four years, making the ladder of knowledge easier to scale. **Gary** I am grateful for your supervision. I have learned a lot of things from you and I have always enjoyed our discussions both concerning science and life. Most importantly you taught me how to apply intuition before mathematics when tackling physical problems, which was one of my main objectives when starting this PhD. I have always come out of our meetings more excited and more motivated. I really appreciate your constant quest for developing as a supervisor and always being open to discuss literally all kinds of topics. **Leo** you introduced me to the fascinating world of quantum information and superconducting circuits and guided me during my first steps of becoming an independent researcher. My stay in your lab resulted in a great deal of added knowledge and set the ground for this PhD for which I am deeply grateful. **Nathan** I owe you a lot for teaching me how to approach scientific problems step by step and the importance of documenting my research, but also for your support at all levels. Your consistency and exceptional eye for the detail have always been very inspiring to me. I am very happy that you started your own group in Australia and I am sure great scientific discoveries lie ahead. All the best to Mim and your girls! Dear **Yaroslav**, the door in your office was always open for me and you were willing to discuss my numerous questions despite your busy schedule. Your meticulous way of approaching problems has been very influential. I am very glad that you are part of my committee. Many thanks also to my second promotor, **Kobus**, for his crucial contributions during my yearly evaluation meetings and for his excellent job as the head of our department. Finally, I want to thank all my committee members for evaluating this dissertation and taking part in the defence ceremony.

I would now like to thank all my team players for adding their own colour to the canvas. Let me begin with my two friends and paranymphes who also had the biggest scientific impact on this thesis.

One of them is a very special case of a naturalised German with a deeply Balkan soul. **Chris**, you always kept the excitement high and motivated me to work more. You were there in every step: from design and fabrication to setting up my first experiments and measuring, to providing endless comments on the thesis and even helping me with the cover design! Apart from our discussions I enjoyed the late music nights where *Dylan* somehow combined with *Maiden* on the guitar and violin. What counts the most is having earned a very good friend that I can trust. I am happy that you and Jasmin got a fresh start in Cologne and I wish you both the best of luck!

The other one is my **Mario** brother, mon mec principal! From the moment I sat next to you in the office I knew great things were lying ahead. Our interactions, mainly in the form of a and b daggers, helped put forward many ideas that may otherwise have been lost in my head. You made time in the lab very productive and at the same time very enjoyable! Thank you for the endless discussions on quantum circuits, the amazing experiments and all the musical discoveries of weird time signatures! But most importantly, thank you for your strong and honest friendship. You are a bright young researcher and I am sure one day you will crack the mysteries of quantum gravity!

I want to thank all the people from the DiCarlo lab for their vital support especially in the beginning of this journey. **Ale** you took me by the hand to a wonderful journey in the world of fabrication as my cleanroom mentor. You have been like a bigger brother to me, constantly challenging me with new (at times crazy) ideas and pushing my thinking out of the norm. I remember us searching for Tardigrades or going to the cleanroom to SEM at midnight about three years ago and I still cannot believe we are now responsible for little human beings! I wish you all the best for Karina and Nolanino! **Ramiro**, thank you for all the help during my fist measurements but most importantly for the inexhaustible enthusiasm that you brought every time we worked together. I am really glad to see great results coming out of your experiments and I am looking forward to your thesis! Thank you **Florian** for helping with many cooldowns as well as measurements in the beginning of my PhD. Your knowledge and skills are as solid as the Alps and you are one of the best instructors I had. I hear you are doing great at Intel but I think Academia really needs people like you to stay around. **Dave** you are the original gangsta! Thanks for all the help in the cleanroom and showing me the power of detailed and systematic study. I have always enjoyed our out-of-the-box political discussions. Also: keep rocking the world with your band, you guys are great! **Stefano**, thank you for your help with Maxwell simulations and the chip design code. I miss being at the same workspace with you because you understood the close link between productivity and humour. **Thijs**, many thanks for enlightening me on flux noise measurements. Those nanowires are in good hands with you. **Adriaan**, thanks for your help with the measurement code and merging my conflicts! Good luck with wrapping up and starting your company. **Niels**, I was always impressed with your sharpness when it comes to experiments. I would have liked to work with you on a project, especially now that I know you are a *Heavy Weather* fan! Good luck with your company and final preparations of your thesis. **Jacob, Nadia, Wouter** and **Xiang**, thank you all for improving my understanding concerning the hard-core engineering part of building a quantum computer. I also want to thank the Leiden theory team **Brian, Tom** and **Xavi**. It was always comforting to have theorists around to talk and share some fun. **Tom v.d.R** thank you for inspiring me to learn more about parametric amplification and for many interesting discussions revolving around life. **Nandini**, thanks for encouraging me in the early days in the cleanroom. We never overlapped in the same lab, although we did manage to keep the parity in our departments the same!

I owe a lot to all of Steelelab for making me feel at home in a very diverse and stimulating environment. **Mark** thank you for making sure that everything worked in the lab, from ensuring that all fridges were running to always being willing to help with the measurements. I miss our interactions and your sense of humour! **Felix**, your

organisational skills are unrivalled. Thank you for keeping the *wiki* alive and preventing a state collapse after Mark left. Your work is always very solid and you epitomise the ancient saying *nature has given us two ears, two eyes, and but one tongue...* I have always appreciated that. I wish you all the best for becoming daddy and wrapping up your thesis. **Sarwan** after all this hard work you made these membranes work and you should be really proud! I am looking forward to more exciting results coming out. Many thanks for sharing (and eventually taking up) the task of fabricating junctions for the group. Also thank you for your help with translating the summary in Dutch. **Ines**, thank you realising flux-mediated optomechanics! I probably wouldn't have pursued my theory work if it weren't for your experiment. Thanks for answering all my questions and contributing to a nice office atmosphere. **Daniel**, I want to equally thank you for the optomechanics experiments and for sharing your infinite knowledge on superconducting resonators and SQUIDs, as well as for the political and, at times, philosophical discussions. Good luck with your future position in Tübingen! **Nikos** thanks for bringing Greece to the department and making me feel less homesick. I am very happy for you becoming "daddy cool" and I wish you all the best for your family. **Byoung-Moo** you often surprised me with your knowledge of literature. Good luck with finishing your experiment and keep in mind that there is no such thing as the perfect device. **Adrian** thanks for enhancing the theoretical (and Mediterranean!) background in the group. **Martijn** thanks for keeping the fun levels high, be it in the lab, the cleanroom or Veldhoven. **Yildiz, Fatemeh** and **Hadi** we worked in very distant topics but I want to thank you for taking the effort to explain your work. I also owe a lot to my master students **Tim, Naimo** and **Damian** for constantly questioning the boundaries of my knowledge and helping me improve as supervisor. Also many thanks to all the MSc and BSc students that passed from our group for all the interesting work they exposed me to.

Stijn! I really miss batching jobs and discussing life with you. You are a rare original human being and a very good friend. I admire you for following your instincts and never compromising. Also: I promise I will make the sailing trip happen. **Sal** thanks for showing me the fun side of measurements during my MSc. Your enthusiasm and intuitive explanations of complex phenomena gave me a lot of inspiration and played an important role eventually in writing my PhD proposal. I really admire you for realizing your dream to start *Deft Circuits* and I am really proud of you for turning that VC deal down! **Gijs**, I always appreciated your ability to transform difficult concepts into simple and intuitive explanations, making each one of our scientific interactions very special. Also thanks for many life advices. **David** thank you for teaching me the secrets of etching and surface cleaning preparation, but also for providing us with high-quality superconducting thin films. **Rob** you always have a positive vibe and I could discuss everything with you from physics to politics without ever getting bored. Our pipe club meetings with Mario have always given me the boost I needed to fight the afternoon-induced dullness. Many thanks also to the rest of the Groeblacher lab, **Andreas, Igor, Moritz, Bas** et al. for the spontaneous discussions and for (re)initiating our journal club.

My dear **Marije**, you have been an instrumental force during these years. You were always there for advice when I needed it. You are an endless source of help and positive energy, which are the things that make the Casimir school and our platform so special.

I wish you all the best for your family, I know you will be a fantastic mom! My fellow *Casimir PhD platform*-ers: **Gesa, Orkide, Koen, Kirsten, Floris, Guoji** and **Nicole**. It was great to get to know all of you and very fulfilling to be part of this team. Organising the *Casimir Spring School* together was one of the best moments during my PhD.

A tribute to my office mates **Jan, Robbie, Ines** and **Mario** for keeping the office a cool and productive place; to the old MED/San Sebastian gang: **Rocco, Dejan**(Zdrava!), **Giordano, Emre, Holger** et al.; to the *Quantum III* teaching dream team: **Ad, Andrea, Jorrit, Nikos, Rasa, Marc**; to **Giannis** and **Esther** for giving me a food-induced time-travel to Greece on Wednesdays and Thursdays; to the **Kavli Nanolab** staff for keeping the standards very high in the cleanroom; to all the support staff **Marja, Maria, Marijke, Heleen, Erika** and **Etty** for helping me with ordering, conference bookings and getting through the bureaucracy during these four years.

A large source of strength stems from my friends back home, although many of them are now scattered around the globe. I want to thank **Giorgos** for being always there and for unpretentiously pushing my rational thinking out of the norm, **Manos** for believing in the same Utopia, **Nikos** (Korobos) for being a brother, **Vasilis** and **Stelian** for remaining original since high-school, and **Alex, Giorgos', Stella, Lampros, Antonis** for all the physics and fun in Athens. Also thanks to **Nikos** (Crypto) and **Kristel** for your friendship and support here in the Netherlands.

My beloved parents, a large part of my strength derives from a very fulfilling childhood. Thank you for your unconditional love and support and for always believing in me. **Alex**, I am very proud of you little brother, keep spiralling out! I also want to thank **Giorgos** and **Pola** for providing me with a second home all these years and for bringing up my other half.

Now here comes the most challenging part, where words become an insufficient means of expression. Love of my life, **Ilektra**. Our journey started before time begun, carrying us through cities of light with a single *Telos*: to unlock the mystery of life together. You complete me in the most wonderful way, enriching my (often intolerable) rational thinking with your emotional intelligence and creativity. But most importantly inspiring me to become a better person. *And now... the end is near...* My little **Antigoni**, you made the last two years the most exhausting and most fulfilling time of my life. You taught me already so many new wonderful aspects of life and gave me hope. I am eternally yours and I am looking forward to wherever this wind is taking us next.

Leiden, 20.11.2019

Curriculum Vitæ

Marios Kounalakis

05-01-1990 Born in Heraklion, Greece.

Education

- 2007–2012 “Ptychion” in Physics, University of Athens
Thesis: Study of quantum mechanics and quantum field theory under the path integral formalism
Advisor: Prof. dr. A. Karanikas
- 2012–2013 M2 Physics (NPAC), Paris Diderot University
Thesis: Phenomenological aspects of quarkonium production at the LHC
Advisor: Dr. J.-P. Lansberg
- 2013–2015 MSc Physics (*cum laude*), Leiden University
Selected for Casimir Pre-PhD program.
Thesis: Modelling digital quantum simulation of the Rabi model in circuit QED: Towards an experimental implementation of deep-strong coupling dynamics
Advisors: Dr. N. K. Langford & Prof. dr. L. DiCarlo
- 2015–2019 PhD Physics, Delft University of Technology
Funded by Casimir prize PhD position.
Thesis: Nonlinear couplings for quantum control of superconducting qubits and electrical/mechanical resonators
Advisor: Prof. dr. G. A. Steele

List of Publications

5. **M. Kounalakis**, Y. M. Blanter and G. A. Steele, *Flux-mediated optomechanics with a transmon qubit in the single-photon ultrastrong-coupling regime*, [arxiv:1911.05550](https://arxiv.org/abs/1911.05550) (under review).
4. **M. Kounalakis**, Y. M. Blanter and G. A. Steele, *Synthesizing multi-phonon quantum superposition states using flux-mediated three-body interactions with superconducting qubits*, [npj Quantum Information](https://doi.org/10.1038/s41534-019-0100-1) **5**, 100 (2019).
3. M. F. Gely, **M. Kounalakis**, C. Dickel, J. Dalle, R. Vatr e, B. Baker, M. D. Jenkins and G. A. Steele, *Observation and stabilization of photonic Fock states in a hot radio-frequency resonator*, [Science](https://doi.org/10.1126/science.1258000) **363**, 1072 (2019).
2. **M. Kounalakis**, C. Dickel, A. Bruno, N. K. Langford and G. A. Steele, *Tuneable hopping and nonlinear cross-Kerr interactions in a high-coherence superconducting circuit*, [npj Quantum Information](https://doi.org/10.1038/s41534-018-0038-1) **4**, 38 (2018).
1. N. K. Langford, R. Sagastizabal, **M. Kounalakis**, C. Dickel, A. Bruno, F. Luthi, D. J. Thoen, A. Endo and L. DiCarlo, , *Experimentally simulating the dynamics of quantum light and matter at ultrastrong coupling*, [Nature Communications](https://doi.org/10.1038/ncomms17151) **8**, 1715 (2017).

References

- [1] M. Planck, *The theory of heat radiation, translated by m, Masius*, P. Blackiston's Son & Co, Philadelphia, reprinted by Kessinger (1914).
- [2] N. Bohr, *Discussion with einstein on epistemological problems in atomic physics*, (1949).
- [3] A. Einstein, *Über einen die erzeugung und verwandlung des liches betreffenden heuristischen gesichtspunkt*, *Annalen der physik* **322**, 132 (1905).
- [4] A. Arons and M. Peppard, *Einstein's proposal of the photon concept—a translation of the annalen der physik paper of 1905*, *American Journal of Physics* **33**, 367 (1965).
- [5] N. Bohr, *Xxxvii. on the constitution of atoms and molecules*, *The London, Edinburgh, and Dublin Philosophical Magazine and Journal of Science* **26**, 476 (1913).
- [6] E. Rutherford, *Lxxix. the scattering of α and β particles by matter and the structure of the atom*, *The London, Edinburgh, and Dublin Philosophical Magazine and Journal of Science* **21**, 669 (1911).
- [7] B. Friedrich and D. Herschbach, *Stern and gerlach: How a bad cigar helped reorient atomic physics*, *Physics Today* **56**, 53 (2003).
- [8] A. H. Compton, *A quantum theory of the scattering of x-rays by light elements*, *Physical review* **21**, 483 (1923).
- [9] A. Einstein, B. Podolsky, and N. Rosen, *Can quantum-mechanical description of physical reality be considered complete?* *Phys. Rev.* **47**, 777 (1935).
- [10] D. Bohm, *Quantum theory* (Prentice-Hall, Englewood Cliffs, NJ, 1951) also as reprint ed.: New York, NY, Dover Publications, 1989.
- [11] G. Hermann and D. Lumma, *The foundations of quantum mechanics in the philosophy of nature*, *The Harvard Review of Philosophy* **7**, 35 (1999).
- [12] J. S. Bell, *On the einstein podolsky rosen paradox*, *Physics Physique Fizika* **1**, 195 (1964).
- [13] S. J. Freedman and J. F. Clauser, *Experimental test of local hidden-variable theories*, *Phys. Rev. Lett.* **28**, 938 (1972).
- [14] A. Aspect, J. Dalibard, and G. Roger, *Experimental test of bell's inequalities using time-varying analyzers*, *Phys. Rev. Lett.* **49**, 1804 (1982).
- [15] R. A. Bertlmann and A. Zeilinger, *Quantum (un) speakables: from bell to quantum information* (Springer Science & Business Media, 2013).
- [16] J. P. Dowling and G. J. Milburn, *Quantum technology: the second quantum revolution*, *Philosophical Transactions of the Royal Society of London. Series A: Mathematical, Physical and Engineering Sciences* **361**, 1655 (2003).
- [17] E. Schrödinger and J. D. Trimmer, *The present situation in quantum mechanics: a translation of schrödinger's 'cat paradox' paper*, *Proceedings of the American Philosophical Society* **124**, 323 (1980).

- [18] W. H. Zurek, *Decoherence, einselection, and the quantum origins of the classical*, Reviews of modern physics **75**, 715 (2003).
- [19] A. J. Leggett, *Macroscopic Quantum Systems and the Quantum Theory of Measurement*, Progress of Theoretical Physics Supplement **69**, 80 (1980), <http://oup.prod.sis.lan/ptps/article-pdf/doi/10.1143/PTP.69.80/5356381/69-80.pdf> .
- [20] A. Caldeira and A. J. Leggett, *Quantum tunnelling in a dissipative system*, Annals of physics **149**, 374 (1983).
- [21] B. D. Josephson, *Possible new effects in superconductive tunnelling*, Physics letters **1**, 251 (1962).
- [22] R. F. Voss and R. A. Webb, *Macroscopic quantum tunneling in 1- μ m nb josephson junctions*, Physical Review Letters **47**, 265 (1981).
- [23] M. H. Devoret, J. M. Martinis, and J. Clarke, *Measurements of macroscopic quantum tunneling out of the zero-voltage state of a current-biased josephson junction*, Physical review letters **55**, 1908 (1985).
- [24] J. Clarke, A. N. Cleland, M. H. Devoret, D. Esteve, and J. M. Martinis, *Quantum mechanics of a macroscopic variable: the phase difference of a josephson junction*, Science **239**, 992 (1988).
- [25] D. Deutsch and R. Jozsa, *Rapid solution of problems by quantum computation*, Proceedings of the Royal Society of London. Series A: Mathematical and Physical Sciences **439**, 553 (1992).
- [26] R. Cleve, A. Ekert, C. Macchiavello, and M. Mosca, *Quantum algorithms revisited*, Proceedings of the Royal Society of London. Series A: Mathematical, Physical and Engineering Sciences **454**, 339 (1998).
- [27] P. R. Tapster, J. G. Rarity, and P. Owens, *Violation of bell's inequality over 4 km of optical fiber*, Physical Review Letters **73**, 1923 (1994).
- [28] P. W. Shor and J. Preskill, *Simple proof of security of the bb84 quantum key distribution protocol*, Physical review letters **85**, 441 (2000).
- [29] D. Deutsch, *The fabric of reality* (Penguin UK, 1998).
- [30] S. Haroche, *Nobel lecture: Controlling photons in a box and exploring the quantum to classical boundary*, Reviews of Modern Physics **85**, 1083 (2013).
- [31] D. J. Wineland, *Nobel lecture: Superposition, entanglement, and raising schrödinger's cat*, Reviews of Modern Physics **85**, 1103 (2013).
- [32] V. Bouchiat, D. Vion, P. Joyez, D. Esteve, and M. Devoret, *Quantum coherence with a single cooper pair*, Physica Scripta **1998**, 165 (1998).
- [33] Y. Nakamura, Y. A. Pashkin, and J. Tsai, *Coherent control of macroscopic quantum states in a single-cooper-pair box*, nature **398**, 786 (1999).
- [34] D. Vion, A. Aassime, A. Cottet, P. Joyez, H. Pothier, C. Urbina, D. Esteve, and M. H. Devoret, *Manipulating the quantum state of an electrical circuit*, Science **296**, 886 (2002).
- [35] C. H. Van Der Wal, A. Ter Haar, F. Wilhelm, R. Schouten, C. Harmans, T. Orlando, S. Lloyd, and J. Mooij, *Quantum superposition of macroscopic persistent-current states*, Science **290**, 773 (2000).
- [36] J. R. Friedman, V. Patel, W. Chen, S. Tolpygo, and J. E. Lukens, *Quantum superposition of distinct macroscopic states*, nature **406**, 43 (2000).
- [37] J. M. Martinis, S. Nam, J. Aumentado, and C. Urbina, *Rabi oscillations in a large josephson-junction qubit*, Physical review letters **89**, 117901 (2002).

- [38] J. Clarke and F. K. Wilhelm, *Superconducting quantum bits*, *Nature* **453**, 1031 EP (2008).
- [39] M. H. Devoret, A. Wallraff, and J. Martinis, *Superconducting qubits: A short review*, arXiv preprint cond-mat/0411174 (2004).
- [40] P. Krantz, M. Kjaergaard, F. Yan, T. P. Orlando, S. Gustavsson, and W. D. Oliver, *A quantum engineer's guide to superconducting qubits*, *Applied Physics Reviews* **6**, 021318 (2019).
- [41] A. Blais, R.-S. Huang, A. Wallraff, S. M. Girvin, and R. J. Schoelkopf, *Cavity quantum electrodynamics for superconducting electrical circuits: An architecture for quantum computation*, *Phys. Rev. A* **69**, 062320 (2004).
- [42] G. Kurizki, P. Bertet, Y. Kubo, K. Mølmer, D. Petrosyan, P. Rabl, and J. Schmiedmayer, *Quantum technologies with hybrid systems*, *Proceedings of the National Academy of Sciences* **112**, 3866 (2015).
- [43] E. Gibney, *Quantum gold rush: the private funding pouring into quantum start-ups*, *Nature* **574**, 22 (2019).
- [44] J. Koch, T. M. Yu, J. Gambetta, A. A. Houck, D. I. Schuster, J. Majer, A. Blais, M. H. Devoret, S. M. Girvin, and R. J. Schoelkopf, *Charge-insensitive qubit design derived from the cooper pair box*, *Phys. Rev. A* **76**, 042319 (2007).
- [45] P. W. Anderson, *The resonating valence bond state in La_2CuO_4 and superconductivity*, *Science* **235**, 1196 (1987).
- [46] P. A. Lee, N. Nagaosa, and X.-G. Wen, *Doping a mott insulator: Physics of high-temperature superconductivity*, *Reviews of modern physics* **78**, 17 (2006).
- [47] K. G. Wilson, *Confinement of quarks*, *Physical Review D* **10**, 2445 (1974).
- [48] M. Lüscher and P. Weisz, *Quark confinement and the bosonic string*, *Journal of High Energy Physics* **2002**, 049 (2002).
- [49] A. Aspuru-Guzik, A. D. Dutoi, P. J. Love, and M. Head-Gordon, *Simulated quantum computation of molecular energies*, *Science* **309**, 1704 (2005).
- [50] T. Häner and D. S. Steiger, *0.5 petabyte simulation of a 45-qubit quantum circuit*, in *Proceedings of the International Conference for High Performance Computing, Networking, Storage and Analysis* (ACM, 2017) p. 33.
- [51] F. Arute, K. Arya, R. Babbush, D. Bacon, J. C. Bardin, R. Barends, R. Biswas, S. Boixo, F. G. Brandao, D. A. Buell, et al., *Quantum supremacy using a programmable superconducting processor*, *Nature* **574**, 505 (2019).
- [52] E. Pednault, J. A. Gunnels, G. Nannicini, L. Horesh, and R. Wisnieff, *Leveraging secondary storage to simulate deep 54-qubit sycamore circuits*, arXiv preprint arXiv:1910.09534 (2019).
- [53] R. P. Feynman, *Simulating physics with computers*, *International Journal of Theoretical Physics* **21**, 467 (1982).
- [54] I. M. Georgescu, S. Ashhab, and F. Nori, *Quantum simulation*, *Rev. Mod. Phys.* **86**, 153 (2014).
- [55] S. Lloyd, *Universal quantum simulators*, *Science* **273**, 1073 (1996).
- [56] M. Greiner, O. Mandel, T. Esslinger, T. W. Hänsch, and I. Bloch, *Quantum phase transition from a superfluid to a mott insulator in a gas of ultracold atoms*, *Nature* **415**, 39 (2002).

- [57] P. Roushan, C. Neill, J. Tangpanitanon, V. M. Bastidas, A. Megrant, R. Barends, Y. Chen, Z. Chen, B. Chiaro, A. Dunsworth, A. Fowler, B. Foxen, M. Giustina, E. Jeffrey, J. Kelly, E. Lucero, J. Mutus, M. Neeley, C. Quintana, D. Sank, A. Vainsencher, J. Wenner, T. White, H. Neven, D. G. Angelakis, and J. Martinis, *Spectroscopic signatures of localization with interacting photons in superconducting qubits*, *Science* **358**, 1175 (2017).
- [58] K. Xu, J.-J. Chen, Y. Zeng, Y.-R. Zhang, C. Song, W. Liu, Q. Guo, P. Zhang, D. Xu, H. Deng, K. Huang, H. Wang, X. Zhu, D. Zheng, and H. Fan, *Emulating many-body localization with a superconducting quantum processor*, *Phys. Rev. Lett.* **120**, 050507 (2018).
- [59] J. Jin, D. Rossini, R. Fazio, M. Leib, and M. J. Hartmann, *Photon solid phases in driven arrays of nonlinearly coupled cavities*, *Phys. Rev. Lett.* **110**, 163605 (2013).
- [60] J. Jin, D. Rossini, M. Leib, M. J. Hartmann, and R. Fazio, *Steady-state phase diagram of a driven qed-cavity array with cross-kerr nonlinearities*, *Phys. Rev. A* **90**, 023827 (2014).
- [61] D. Marcos, P. Widmer, E. Rico, M. Hafezi, P. Rabl, U.-J. Wiese, and P. Zoller, *Two-dimensional lattice gauge theories with superconducting quantum circuits*, *Annals of Physics* **351**, 634 (2014).
- [62] A. Ciani, B. M. Terhal, and D. P. DiVincenzo, *Hamiltonian quantum computing with superconducting qubits*, *Quantum Science and Technology* **4**, 035002 (2019).
- [63] M. Aspelmeyer, T. J. Kippenberg, and F. Marquardt, *Cavity optomechanics*, *Rev. Mod. Phys.* **86**, 1391 (2014).
- [64] M. Metcalfe, *Applications of cavity optomechanics*, *Applied Physics Reviews* **1**, 031105 (2014).
- [65] L. Susskind, *Dear qubitizers, $gr=qm$* , arXiv preprint arXiv:1708.03040 (2017).
- [66] R. Penrose, *On gravity's role in quantum state reduction: general relativity and gravitation*, *Gen. Relativ. Gravit.* **28**, 581 (1996).
- [67] W. Marshall, C. Simon, R. Penrose, and D. Bouwmeester, *Towards quantum superpositions of a mirror*, *Phys. Rev. Lett.* **91**, 130401 (2003).
- [68] D. Kleckner, I. Pikovski, E. Jeffrey, L. Ament, E. Eliel, J. Van Den Brink, and D. Bouwmeester, *Creating and verifying a quantum superposition in a micro-optomechanical system*, *New Journal of Physics* **10**, 095020 (2008).
- [69] A. N. Cleland and M. R. Geller, *Superconducting qubit storage and entanglement with nanomechanical resonators*, *Physical review letters* **93**, 070501 (2004).
- [70] F. Diedrich, J. C. Bergquist, W. M. Itano, and D. J. Wineland, *Laser cooling to the zero-point energy of motion*, *Phys. Rev. Lett.* **62**, 403 (1989).
- [71] E. Kapit, *The upside of noise: engineered dissipation as a resource in superconducting circuits*, *Quantum Science and Technology* **2**, 033002 (2017).
- [72] B. Yurke and J. S. Denker, *Quantum network theory*, *Phys. Rev. A* **29**, 1419 (1984).
- [73] U. Vool and M. Devoret, *Introduction to quantum electromagnetic circuits*, *International Journal of Circuit Theory and Applications* **45**, 897 (2017).
- [74] H. Goldstein, C. Poole, and J. Safko, *Classical mechanics* (AAPT, 2002).
- [75] H. Kleinert, *Path integrals in quantum mechanics, statistics, polymer physics, and financial markets* (World scientific, 2009).
- [76] J. Ulrich and F. Hassler, *Dual approach to circuit quantization using loop charges*, *Phys. Rev. B* **94**, 094505 (2016).

- [77] J. J. Sakurai, *Advanced quantum mechanics* (Pearson Education India, 1967).
- [78] Y. A. Pashkin, O. Astafiev, T. Yamamoto, Y. Nakamura, and J. Tsai, *Josephson charge qubits: a brief review*, *Quantum Information Processing* **8**, 55 (2009).
- [79] J. A. Schreier, A. A. Houck, J. Koch, D. I. Schuster, B. R. Johnson, J. M. Chow, J. M. Gambetta, J. Majer, L. Frunzio, M. H. Devoret, S. M. Girvin, and R. J. Schoelkopf, *Suppressing charge noise decoherence in superconducting charge qubits*, *Phys. Rev. B* **77**, 180502 (2008).
- [80] K. Likharev and A. Zorin, *Theory of the bloch-wave oscillations in small josephson junctions*, *Journal of Low Temperature Physics* **59**, 347 (1985).
- [81] L. Landau, *The damping problem in wave mechanics*, *Z. Phys* **45** (1927).
- [82] J. Von Neumann, *Wahrscheinlichkeitstheoretischer aufbau der quantenmechanik*, *Nachrichten von der Gesellschaft der Wissenschaften zu Göttingen, Mathematisch-Physikalische Klasse* **1927**, 245 (1927).
- [83] J. Johansson, P. Nation, and F. Nori, *Qutip: An open-source python framework for the dynamics of open quantum systems*, *Computer Physics Communications* **183**, 1760 (2012).
- [84] M. A. Nielsen and I. L. Chuang, *Quantum computation and quantum information* (Cambridge University Press, Cambridge, 2001).
- [85] D. Ristè, C. C. Bultink, M. J. Tiggelman, R. N. Schouten, K. W. Lehnert, and L. DiCarlo, *Millisecond charge-parity fluctuations and induced decoherence in a superconducting transmon qubit*, *Nature Communications* **4**, 1913 (2013).
- [86] K. Serniak, M. Hays, G. de Lange, S. Diamond, S. Shankar, L. D. Burkhardt, L. Frunzio, M. Houzet, and M. H. Devoret, *Hot nonequilibrium quasiparticles in transmon qubits*, *Phys. Rev. Lett.* **121**, 157701 (2018).
- [87] S. J. Bosman, M. F. Gely, V. Singh, A. Bruno, D. Bothner, and G. A. Steele, *Multi-mode ultra-strong coupling in circuit quantum electrodynamics*, *npj Quantum Information* **3**, 46 (2017).
- [88] M. Tinkham, *Introduction to superconductivity* (Courier Corporation, 2004).
- [89] M. Hutchings, J. B. Hertzberg, Y. Liu, N. T. Bronn, G. A. Keefe, M. Brink, J. M. Chow, and B. Plourde, *Tunable superconducting qubits with flux-independent coherence*, *Physical Review Applied* **8**, 044003 (2017).
- [90] D. M. Pozar, *Microwave engineering* (John Wiley & Sons, 2009).
- [91] M. Göppl, A. Fragner, M. Baur, R. Bianchetti, S. Filipp, J. Fink, P. Leek, G. Puebla, L. Steffen, and A. Wallraff, *Coplanar waveguide resonators for circuit quantum electrodynamics*, *Journal of Applied Physics* **104**, 113904 (2008).
- [92] L. S. Bishop, *Circuit quantum electrodynamics: volume II*, Ph.D. thesis, Yale University (2010).
- [93] J. Baselmans, S. Yates, P. De Korte, H. Hoevers, R. Barends, J. Hovenier, J. Gao, and T. Klapwijk, *Development of high-q superconducting resonators for use as kinetic inductance detectors*, *Advances in Space Research* **40**, 708 (2007).
- [94] A. Bruno, G. De Lange, S. Asaad, K. Van der Enden, N. Langford, and L. DiCarlo, *Reducing intrinsic loss in superconducting resonators by surface treatment and deep etching of silicon substrates*, *Applied Physics Letters* **106**, 182601 (2015).
- [95] A. F. Kockum, A. Miranowicz, S. De Liberato, S. Savasta, and F. Nori, *Ultrastrong coupling between light and matter*, *Nature Reviews Physics* **1**, 19 (2019).

- [96] J. Majer, J. Chow, J. Gambetta, J. Koch, B. Johnson, J. Schreier, L. Frunzio, D. Schuster, A. Houck, A. Wallraff, *et al.*, *Coupling superconducting qubits via a cavity bus*, *Nature* **449**, 443 (2007).
- [97] J.-M. Raimond, M. Brune, and S. Haroche, *Manipulating quantum entanglement with atoms and photons in a cavity*, *Reviews of Modern Physics* **73**, 565 (2001).
- [98] A. Wallraff, D. I. Schuster, A. Blais, L. Frunzio, R.-S. Huang, J. Majer, S. Kumar, S. M. Girvin, and R. J. Schoelkopf, *Strong coupling of a single photon to a superconducting qubit using circuit quantum electrodynamics*, *Nature* **431**, 162 (2004).
- [99] E. T. Jaynes and F. W. Cummings, *Comparison of quantum and semiclassical radiation theories with application to the beam maser*, *Proceedings of the IEEE* **51**, 89 (1963).
- [100] A. Wallraff, D. I. Schuster, A. Blais, L. Frunzio, J. Majer, M. H. Devoret, S. M. Girvin, and R. J. Schoelkopf, *Approaching unit visibility for control of a superconducting qubit with dispersive readout*, *Phys. Rev. Lett.* **95**, 060501 (2005).
- [101] D. Schuster, A. Houck, J. Schreier, A. Wallraff, J. Gambetta, A. Blais, L. Frunzio, J. Majer, B. Johnson, M. Devoret, *et al.*, *Resolving photon number states in a superconducting circuit*, *Nature* **445**, 515 (2007).
- [102] N. K. Langford, R. Sagastizabal, M. Kounalakis, C. Dickel, A. Bruno, F. Luthi, D. J. Thoen, A. Endo, and L. DiCarlo, *Experimentally simulating the dynamics of quantum light and matter at deep-strong coupling*, *Nature Communications* **8**, 1715 (2017).
- [103] A. A. Houck, J. Schreier, B. Johnson, J. Chow, J. Koch, J. Gambetta, D. Schuster, L. Frunzio, M. Devoret, S. Girvin, *et al.*, *Controlling the spontaneous emission of a superconducting transmon qubit*, *Physical review letters* **101**, 080502 (2008).
- [104] M. Boissonneault, J. M. Gambetta, and A. Blais, *Dispersive regime of circuit qed: Photon-dependent qubit dephasing and relaxation rates*, *Physical Review A* **79**, 013819 (2009).
- [105] D. I. Schuster, *Circuit quantum electrodynamics*, Ph.D. thesis (PhD Thesis Yale University, 2007).
- [106] J. Gambetta, W. A. Braff, A. Wallraff, S. M. Girvin, and R. J. Schoelkopf, *Protocols for optimal readout of qubits using a continuous quantum nondemolition measurement*, *Phys. Rev. A* **76**, 012325 (2007).
- [107] R. Barends, *Photon-detecting superconducting resonators*, Ph.D. thesis (2009).
- [108] E. U. Manual, *Sonnet software*, Inc., Liverpool, NY (2008).
- [109] M. ANSYS, *3d software, 2010, version 13.0. 0*, ANSYS Inc (2010).
- [110] D. Rosenberg, D. Kim, R. Das, D. Yost, S. Gustavsson, D. Hover, P. Krantz, A. Melville, L. Racz, G. Samach, *et al.*, *3d integrated superconducting qubits*, *npj quantum information* **3**, 42 (2017).
- [111] B. Foxen, J. Mutus, E. Lucero, R. Graff, A. Megrant, Y. Chen, C. Quintana, B. Burkett, J. Kelly, E. Jeffrey, *et al.*, *Qubit compatible superconducting interconnects*, *Quantum Science and Technology* **3**, 014005 (2017).
- [112] M. Brinson and S. Jahn, *Qucs: A gpl software package for circuit simulation, compact device modelling and circuit macromodelling from dc to rf and beyond*, *International Journal of Numerical Modelling: Electronic Networks, Devices and Fields* **22**, 297 (2009).
- [113] M. F. Gely and G. A. Steele, *Qucat: Quantum circuit analyzer tool in python*, arXiv preprint arXiv:1908.10342 (2019).

- [114] D. Thoen, B. Bos, E. Haalebos, T. Klapwijk, J. Baselmans, and A. Endo, *Superconducting nb_{1n} thin films with highly uniform properties over a 100 mm wafer*, *IEEE Trans. Appl. Supercond.* **27**, 1 (2017).
- [115] G. Dolan, *Offset masks for lift-off photoprocessing*, *Applied Physics Letters* **31**, 337 (1977).
- [116] V. Ambegaokar and A. Baratoff, *Tunneling between superconductors*, *Physical Review Letters* **10**, 486 (1963).
- [117] D. Ristè, S. Poletto, M.-Z. Huang, A. Bruno, V. Vesterinen, O.-P. Saira, and L. DiCarlo, *Detecting bit-flip errors in a logical qubit using stabilizer measurements*, *Nature Communications* **6** (2015).
- [118] M. A. Broome, A. Fedrizzi, S. Rahimi-Keshari, J. Dove, S. Aaronson, T. C. Ralph, and A. G. White, *Photonic boson sampling in a tunable circuit*, *Science* **339**, 794 (2013).
- [119] J. B. Spring, B. J. Metcalf, P. C. Humphreys, W. S. Kolthammer, X.-M. Jin, M. Barbieri, A. Datta, N. Thomas-Peter, N. K. Langford, D. Kundys, J. C. Gates, B. J. Smith, P. G. R. Smith, and I. A. Walmsley, *Boson sampling on a photonic chip*, *Science* **339**, 798 (2013).
- [120] H. Bernien, S. Schwartz, A. Keesling, H. Levine, A. Omran, H. Pichler, S. Choi, A. S. Zibrov, M. Endres, M. Greiner, V. Vuletić, and M. D. Lukin, *Probing many-body dynamics on a 51-atom quantum simulator*, *Nature* **551**, 579 (2017).
- [121] J. Zhang, G. Pagano, P. W. Hess, A. Kyprianidis, P. Becker, H. Kaplan, A. V. Gorshkov, Z. X. Gong, and C. Monroe, *Observation of a many-body dynamical phase transition with a 53-qubit quantum simulator*, *Nature* **551**, 601 (2017).
- [122] J. I. Cirac and P. Zoller, *Goals and opportunities in quantum simulation*, *Nat Phys* **8**, 264 (2012).
- [123] A. A. Houck, H. E. Tureci, and J. Koch, *On-chip quantum simulation with superconducting circuits*, *Nat Phys* **8**, 292 (2012).
- [124] C. Noh and D. G. Angelakis, *Quantum simulations and many-body physics with light*, *Reports on Progress in Physics* **80**, 016401 (2017).
- [125] M. J. Hartmann, *Quantum simulation with interacting photons*, *Journal of Optics* **18**, 104005 (2016).
- [126] J. Li, M. P. Silveri, K. S. Kumar, J. M. Pirkkalainen, A. Vepsäläinen, W. C. Chien, J. Tuorila, M. A. Sillanpää, P. J. Hakonen, E. V. Thuneberg, and G. S. Paraoanu, *Motional averaging in a superconducting qubit*, *Nature Communications* **4** (2013).
- [127] Y. Chen, P. Roushan, D. Sank, C. Neill, E. Lucero, M. Mariantoni, R. Barends, B. Chiaro, J. Kelly, A. Megrant, *et al.*, *Emulating weak localization using a solid-state quantum circuit*, *Nature Communications* **5** (2014).
- [128] Y. Salathé, M. Mondal, M. Oppliger, J. Heinsoo, P. Kurpiers, A. Potočnik, A. Mezzacapo, U. Las Heras, L. Lamata, E. Solano, S. Filipp, and A. Wallraff, *Digital quantum simulation of spin models with circuit quantum electrodynamics*, *Phys. Rev. X* **5**, 021027 (2015).
- [129] C. Eichler, J. Mlynek, J. Butscher, P. Kurpiers, K. Hammerer, T. J. Osborne, and A. Wallraff, *Exploring interacting quantum many-body systems by experimentally creating continuous matrix product states in superconducting circuits*, *Phys. Rev. X* **5**, 041044 (2015).
- [130] P. Roushan, C. Neill, A. Megrant, Y. Chen, R. Babbush, R. Barends, B. Campbell, Z. Chen, B. Chiaro, A. Dunsworth, A. Fowler, E. Jeffrey, J. Kelly, E. Lucero, J. Mutus, P. J. J. O'Malley, M. Neeley, C. Quintana, D. Sank, A. Vainsencher, J. Wenner, T. White, E. Kapit, H. Neven, and J. Martinis, *Chiral ground-state currents of interacting photons in a synthetic magnetic field*, *Nat Phys* **13**, 146 (2017).

- [131] J. Braumüller, M. Marthaler, A. Schneider, A. Stehli, H. Rotzinger, M. Weides, and A. V. Ustinov, *Analog quantum simulation of the rabi model in the ultra-strong coupling regime*, *Nature Communications* **8**, 779 (2017).
- [132] M. Fitzpatrick, N. M. Sundaresan, A. C. Y. Li, J. Koch, and A. A. Houck, *Observation of a dissipative phase transition in a one-dimensional circuit qed lattice*, *Phys. Rev. X* **7**, 011016 (2017).
- [133] A. Potočník, A. Bargerbos, F. A. Y. N. Schröder, S. A. Khan, M. C. Collodo, S. Gasparinetti, Y. Salathé, C. Creatore, C. Eichler, H. E. Türeci, A. W. Chin, and A. Wallraff, *Studying light-harvesting models with superconducting circuits*, *Nature Communications* **9**, 904 (2018).
- [134] A. Kandala, A. Mezzacapo, K. Temme, M. Takita, M. Brink, J. M. Chow, and J. M. Gambetta, *Hardware-efficient variational quantum eigensolver for small molecules and quantum magnets*, *Nature* **549**, 242 (2017).
- [135] P. Bertet, C. J. P. M. Harmans, and J. E. Mooij, *Parametric coupling for superconducting qubits*, *Phys. Rev. B* **73**, 064512 (2006).
- [136] T. Hime, P. A. Reichardt, B. L. T. Plourde, T. L. Robertson, C.-E. Wu, A. V. Ustinov, and J. Clarke, *Solid-state qubits with current-controlled coupling*, *Science* **314**, 1427 (2006).
- [137] R. Harris, A. J. Berkley, M. W. Johnson, P. Bunyk, S. Govorkov, M. C. Thom, S. Uchaikin, A. B. Wilson, J. Chung, E. Holtham, J. D. Biamonte, A. Y. Smirnov, M. H. S. Amin, and A. Maassen van den Brink, *Sign- and magnitude-tunable coupler for superconducting flux qubits*, *Phys. Rev. Lett.* **98**, 177001 (2007).
- [138] A. O. Niskanen, K. Harrabi, F. Yoshihara, Y. Nakamura, S. Lloyd, and J. S. Tsai, *Quantum coherent tunable coupling of superconducting qubits*, *Science* **316**, 723 (2007).
- [139] S. H. W. van der Ploeg, A. Izmalkov, A. M. van den Brink, U. Hübner, M. Grajcar, E. Il'ichev, H.-G. Meyer, and A. M. Zagoskin, *Controllable coupling of superconducting flux qubits*, *Phys. Rev. Lett.* **98**, 057004 (2007).
- [140] M. S. Allman, F. Altomare, J. D. Whittaker, K. Cicak, D. Li, A. Sirois, J. Strong, J. D. Teufel, and R. W. Simmonds, *rf-squid-mediated coherent tunable coupling between a superconducting phase qubit and a lumped-element resonator*, *Phys. Rev. Lett.* **104**, 177004 (2010).
- [141] R. C. Bialczak, M. Ansmann, M. Hofheinz, M. Lenander, E. Lucero, M. Neeley, A. D. O'Connell, D. Sank, H. Wang, M. Weides, J. Wenner, T. Yamamoto, A. N. Cleland, and J. M. Martinis, *Fast tunable coupler for superconducting qubits*, *Phys. Rev. Lett.* **106**, 060501 (2011).
- [142] S. J. Srinivasan, A. J. Hoffman, J. M. Gambetta, and A. A. Houck, *Tunable coupling in circuit quantum electrodynamics using a superconducting charge qubit with a v-shaped energy level diagram*, *Phys. Rev. Lett.* **106**, 083601 (2011).
- [143] F. Wulschner, J. Goetz, F. R. Koessel, E. Hoffmann, A. Baust, P. Eder, M. Fischer, M. Haerberlein, M. J. Schwarz, M. Pernpeintner, E. Xie, L. Zhong, C. W. Zollitsch, B. Peropadre, J.-J. Garcia Ripoll, E. Solano, K. G. Fedorov, E. P. Menzel, F. Deppe, A. Marx, and R. Gross, *Tunable coupling of transmission-line microwave resonators mediated by an rf squid*, *EPJ Quantum Technology* **3**, 10 (2016).
- [144] S. J. Weber, G. O. Samach, D. Hover, S. Gustavsson, D. K. Kim, A. Melville, D. Rosenberg, A. P. Sears, F. Yan, J. L. Yoder, W. D. Oliver, and A. J. Kerman, *Coherent coupled qubits for quantum annealing*, *Phys. Rev. Applied* **8**, 014004 (2017).
- [145] Y. Chen, C. Neill, P. Roushan, N. Leung, M. Fang, R. Barends, J. Kelly, B. Campbell, Z. Chen, B. Chiaro, A. Dunsworth, E. Jeffrey, A. Megrant, J. Y. Mutus, P. J. J. O'Malley, C. M. Quintana, D. Sank, A. Vainsencher, J. Wenner, T. C. White, M. R. Geller, A. N. Cleland, and J. M. Martinis, *Qubit architecture with high coherence and fast tunable coupling*, *Phys. Rev. Lett.* **113**, 220502 (2014).

- [146] D. C. McKay, S. Filipp, A. Mezzacapo, E. Magesan, J. M. Chow, and J. M. Gambetta, *Universal gate for fixed-frequency qubits via a tunable bus*, *Phys. Rev. Applied* **6**, 064007 (2016).
- [147] Y. Lu, S. Chakram, N. Leung, N. Earnest, R. K. Naik, Z. Huang, P. Groszkowski, E. Kapit, J. Koch, and D. I. Schuster, *Universal stabilization of a parametrically coupled qubit*, *Phys. Rev. Lett.* **119**, 150502 (2017).
- [148] A. van Otterlo, K.-H. Wagenblast, R. Baltin, C. Bruder, R. Fazio, and G. Schön, *Quantum phase transitions of interacting bosons and the supersolid phase*, *Phys. Rev. B* **52**, 16176 (1995).
- [149] G. Mazzarella, S. M. Giampaolo, and F. Illuminati, *Extended bose hubbard model of interacting bosonic atoms in optical lattices: From superfluidity to density waves*, *Phys. Rev. A* **73**, 013625 (2006).
- [150] M. R. Geller, E. Donate, Y. Chen, M. T. Fang, N. Leung, C. Neill, P. Roushan, and J. M. Martinis, *Tunable coupler for superconducting xmon qubits: Perturbative nonlinear model*, *Phys. Rev. A* **92**, 012320 (2015).
- [151] S. Richer and D. DiVincenzo, *Circuit design implementing longitudinal coupling: A scalable scheme for superconducting qubits*, *Phys. Rev. B* **93**, 134501 (2016).
- [152] F. W. Strauch, P. R. Johnson, A. J. Dragt, C. J. Lobb, J. R. Anderson, and F. C. Wellstood, *Quantum logic gates for coupled superconducting phase qubits*, *Phys. Rev. Lett.* **91**, 167005 (2003).
- [153] J. Tangpanitanon, V. M. Bastidas, S. Al-Assam, P. Roushan, D. Jaksch, and D. G. Angelakis, *Topological pumping of photons in nonlinear resonator arrays*, *Phys. Rev. Lett.* **117**, 213603 (2016).
- [154] G. Corrielli, A. Crespi, G. Della Valle, S. Longhi, and R. Osellame, *Fractional bloch oscillations in photonic lattices*, *Nature Communications* **4**, 1555 (2013).
- [155] M. Sameti, A. Potočnik, D. E. Browne, A. Wallraff, and M. J. Hartmann, *Superconducting quantum simulator for topological order and the toric code*, *Phys. Rev. A* **95**, 042330 (2017).
- [156] L. Neumeier, M. Leib, and M. J. Hartmann, *Single-photon transistor in circuit quantum electrodynamics*, *Phys. Rev. Lett.* **111**, 063601 (2013).
- [157] D. J. Thoen, B. G. C. Bos, E. A. F. Haalebos, T. M. Klapwijk, J. J. A. Baselmans, and A. Endo, *Superconducting nbtin thin films with highly uniform properties over a \varnothing 100 mm wafer*, *IEEE Transactions on Applied Superconductivity* **27**, 1 (2017).
- [158] M. Devoret, *Les Houches, Session LXIII* (Elsevier Science, Amsterdam, 1997).
- [159] R. Barends, J. Wenner, M. Lenander, Y. Chen, R. C. Bialczak, J. Kelly, E. Lucero, P. O'Malley, M. Mariantoni, D. Sank, et al., *Minimizing quasiparticle generation from stray infrared light in superconducting quantum circuits*, *Applied Physics Letters* **99**, 113507 (2011).
- [160] M. Blencowe, *A light sounding drum*. *Nature* **469**, 168 (2011).
- [161] M. P. Blencowe and E. Buks, *Quantum analysis of a linear dc squid mechanical displacement detector*, *Phys. Rev. B* **76**, 014511 (2007).
- [162] K. Stannigel, P. Komar, S. J. M. Habraken, S. D. Bennett, M. D. Lukin, P. Zoller, and P. Rabl, *Optomechanical quantum information processing with photons and phonons*, *Phys. Rev. Lett.* **109**, 013603 (2012).
- [163] J. Bochmann, A. Vainsencher, D. D. Awschalom, and A. N. Cleland, *Nanomechanical coupling between microwave and optical photons*, *Nature Physics* **9**, 712 (2013).

- [164] R. W. Andrews, R. W. Peterson, T. P. Purdy, K. Cicak, R. W. Simmonds, C. A. Regal, and K. W. Lehnert, *Bidirectional and efficient conversion between microwave and optical light*, *Nature Physics* **10**, 321 (2014).
- [165] A. D. O'Connell, M. Hofheinz, M. Ansmann, R. C. Bialczak, M. Lenander, E. Lucero, M. Neeley, D. Sank, H. Wang, M. Weides, *et al.*, *Quantum ground state and single-phonon control of a mechanical resonator*, *Nature* **464**, 697 (2010).
- [166] Y. Chu, P. Kharel, T. Yoon, L. Frunzio, P. T. Rakich, and R. J. Schoelkopf, *Creation and control of multi-phonon fock states in a bulk acoustic-wave resonator*, *Nature* **563**, 666 (2018).
- [167] J. Chan, T. M. Alegre, A. H. Safavi-Naeini, J. T. Hill, A. Krause, S. Gröblacher, M. Aspelmeyer, and O. Painter, *Laser cooling of a nanomechanical oscillator into its quantum ground state*, *Nature* **478**, 89 (2011).
- [168] J. D. Teufel, T. Donner, D. Li, J. W. Harlow, M. S. Allman, K. Cicak, A. J. Sirois, J. D. Whittaker, K. W. Lehnert, and R. W. Simmonds, *Sideband cooling of micromechanical motion to the quantum ground state*, *Nature* **475**, 359 (2011).
- [169] E. E. Wollman, C. Lei, A. Weinstein, J. Suh, A. Kronwald, F. Marquardt, A. Clerk, and K. Schwab, *Quantum squeezing of motion in a mechanical resonator*, *Science* **349**, 952 (2015).
- [170] R. Riedinger, A. Wallucks, I. Marinković, C. Löschnauer, M. Aspelmeyer, S. Hong, and S. Gröblacher, *Remote quantum entanglement between two micromechanical oscillators*, *Nature* **556**, 473 (2018).
- [171] C. Ockeloen-Korppi, E. Damskäg, J.-M. Pirkkalainen, M. Asjad, A. Clerk, F. Massel, M. Woolley, and M. Sillanpää, *Stabilized entanglement of massive mechanical oscillators*, *Nature* **556**, 478 (2018).
- [172] A. Reed, K. Mayer, J. Teufel, L. Burkhart, W. Pfaff, M. Reagor, L. Sletten, X. Ma, R. Schoelkopf, E. Knill, *et al.*, *Faithful conversion of propagating quantum information to mechanical motion*, *Nature Physics* **13**, 1163 (2017).
- [173] J. J. Viennot, X. Ma, and K. W. Lehnert, *Phonon-number-sensitive electromechanics*, *Physical review letters* **121**, 183601 (2018).
- [174] S. Hong, R. Riedinger, I. Marinković, A. Wallucks, S. G. Hofer, R. A. Norte, M. Aspelmeyer, and S. Gröblacher, *Hanbury brown and twiss interferometry of single phonons from an optomechanical resonator*, *Science* **358**, 203 (2017).
- [175] J.-M. Pirkkalainen, S. Cho, F. Massel, J. Tuorila, T. Heikkilä, P. Hakonen, and M. Sillanpää, *Cavity optomechanics mediated by a quantum two-level system*, *Nature communications* **6**, 6981 (2015).
- [176] P. Rabl, *Photon blockade effect in optomechanical systems*, *Phys. Rev. Lett.* **107**, 063601 (2011).
- [177] A. Nunnenkamp, K. Børkje, and S. M. Girvin, *Single-photon optomechanics*, *Phys. Rev. Lett.* **107**, 063602 (2011).
- [178] P. D. Nation, *Nonclassical mechanical states in an optomechanical micromaser analog*, *Phys. Rev. A* **88**, 053828 (2013).
- [179] J.-Q. Liao and L. Tian, *Macroscopic quantum superposition in cavity optomechanics*, *Phys. Rev. Lett.* **116**, 163602 (2016).
- [180] A. D. Armour, M. P. Blencowe, and K. C. Schwab, *Entanglement and decoherence of a micromechanical resonator via coupling to a cooper-pair box*, *Phys. Rev. Lett.* **88**, 148301 (2002).

- [181] M. Abdi, M. Pernpeintner, R. Gross, H. Huebl, and M. J. Hartmann, *Quantum state engineering with circuit electromechanical three-body interactions*, *Physical review letters* **114**, 173602 (2015).
- [182] P. D. Nation, M. P. Blencowe, and E. Buks, *Quantum analysis of a nonlinear microwave cavity-embedded dc squid displacement detector*, *Phys. Rev. B* **78**, 104516 (2008).
- [183] P. D. Nation, J. Suh, and M. P. Blencowe, *Ultrastrong optomechanics incorporating the dynamical casimir effect*, *Phys. Rev. A* **93**, 022510 (2016).
- [184] O. Shevchuk, G. A. Steele, and Y. M. Blanter, *Strong and tunable couplings in flux-mediated optomechanics*, *Phys. Rev. B* **96**, 014508 (2017).
- [185] I. Rodrigues, D. Bothner, and G. Steele, *Coupling microwave photons to a mechanical resonator using quantum interference*, arXiv preprint arXiv:1907.01418 (2019).
- [186] M. Kounalakis, C. Dickel, A. Bruno, N. Langford, and G. Steele, *Tuneable hopping and nonlinear cross-kerr interactions in a high-coherence superconducting circuit*, *npj Quantum Information* **4**, 38 (2018).
- [187] M. C. Collodo, A. Potočnik, S. Gasparinetti, J.-C. Besse, M. Pechal, M. Sameti, M. J. Hartmann, A. Wallraff, and C. Eichler, *Observation of the crossover from photon ordering to delocalization in tunably coupled resonators*, *Phys. Rev. Lett.* **122**, 183601 (2019).
- [188] S. Etaki, M. Poot, I. Mahboob, K. Onomitsu, H. Yamaguchi, and H. Van der Zant, *Motion detection of a micromechanical resonator embedded in a dc squid*, *Nature Physics* **4**, 785 (2008).
- [189] M. F. Gely, M. Kounalakis, C. Dickel, J. Dalle, R. Vatré, B. Baker, M. D. Jenkins, and G. A. Steele, *Observation and stabilization of photonic fock states in a hot radio-frequency resonator*, *Science* **363**, 1072 (2019).
- [190] R. Lescanne, L. Verney, Q. Ficheux, M. H. Devoret, B. Huard, M. Mirrahimi, and Z. Leghtas, *Escape of a driven quantum josephson circuit into unconfined states*, *Phys. Rev. Applied* **11**, 014030 (2019).
- [191] D. Ristè, C. C. Bultink, K. W. Lehnert, and L. DiCarlo, *Feedback control of a solid-state qubit using high-fidelity projective measurement*, *Phys. Rev. Lett.* **109**, 240502 (2012).
- [192] P. Campagne-Ibarcq, E. Flurin, N. Roch, D. Darson, P. Morfin, M. Mirrahimi, M. H. Devoret, F. Mallet, and B. Huard, *Persistent control of a superconducting qubit by stroboscopic measurement feedback*, *Phys. Rev. X* **3**, 021008 (2013).
- [193] P. Magnard, P. Kurpiers, B. Royer, T. Walter, J.-C. Besse, S. Gasparinetti, M. Pechal, J. Heinsoo, S. Storz, A. Blais, and A. Wallraff, *Fast and unconditional all-microwave reset of a superconducting qubit*, *Phys. Rev. Lett.* **121**, 060502 (2018).
- [194] R. Lescanne, S. Deléglise, E. Albertinale, U. Réglade, T. Capelle, E. Ivanov, T. Jacqmin, Z. Leghtas, and E. Flurin, *Detecting itinerant microwave photons with engineered non-linear dissipation*, arXiv preprint arXiv:1902.05102 (2019).
- [195] R. Meservey and P. Tedrow, *Properties of very thin aluminum films*, *Journal of Applied Physics* **42**, 51 (1971).
- [196] A. Schneider, T. Wolz, M. Pfirrmann, M. Spiecker, H. Rotzinger, A. V. Ustinov, and M. Weides, *Transmon qubit in a magnetic field: Evolution of coherence and transition frequency*, *Phys. Rev. Research* **1**, 023003 (2019).
- [197] R. Cleve and H. Buhrman, *Substituting quantum entanglement for communication*, *Phys. Rev. A* **56**, 1201 (1997).

- [198] D. Bruß, D. P. DiVincenzo, A. Ekert, C. A. Fuchs, C. Macchiavello, and J. A. Smolin, *Optimal universal and state-dependent quantum cloning*, *Phys. Rev. A* **57**, 2368 (1998).
- [199] D. M. Greenberger, M. A. Horne, and A. Zeilinger, *Going beyond bell's theorem*, in *Bell's theorem, quantum theory and conceptions of the universe* (Springer, 1989) pp. 69–72.
- [200] S. G. Hofer, K. W. Lehnert, and K. Hammerer, *Proposal to test bell's inequality in electromechanics*, *Physical review letters* **116**, 070406 (2016).
- [201] V. C. Vivoli, T. Barnea, C. Galland, and N. Sangouard, *Proposal for an optomechanical bell test*, *Phys. Rev. Lett.* **116**, 070405 (2016).
- [202] P. Rabl, S. J. Kolkowitz, F. Koppens, J. Harris, P. Zoller, and M. D. Lukin, *A quantum spin transducer based on nanoelectromechanical resonator arrays*, *Nature Physics* **6**, 602 (2010).
- [203] S. Camerer, M. Korppi, A. Jöckel, D. Hunger, T. W. Hänsch, and P. Treutlein, *Realization of an optomechanical interface between ultracold atoms and a membrane*, *Phys. Rev. Lett.* **107**, 223001 (2011).
- [204] O. Arcizet, V. Jacques, A. Siria, P. Poncharal, P. Vincent, and S. Seidelin, *A single nitrogen-vacancy defect coupled to a nanomechanical oscillator*, *Nature Physics* **7**, 879 (2011).
- [205] J. T. Hill, A. H. Safavi-Naeini, J. Chan, and O. Painter, *Coherent optical wavelength conversion via cavity optomechanics*, *Nature communications* **3**, 1196 (2012).
- [206] M. Hofheinz, H. Wang, M. Ansmann, R. C. Bialczak, E. Lucero, M. Neeley, A. O'connell, D. Sank, J. Wenner, J. M. Martinis, *et al.*, *Synthesizing arbitrary quantum states in a superconducting resonator*, *Nature* **459**, 546 (2009).
- [207] C. Law and J. Eberly, *Arbitrary control of a quantum electromagnetic field*, *Physical review letters* **76**, 1055 (1996).
- [208] A. H. Ghadimi, S. A. Fedorov, N. J. Engelsen, M. J. Beryhi, R. Schilling, D. J. Wilson, and T. J. Kippenberg, *Elastic strain engineering for ultralow mechanical dissipation*, *Science* **360**, 764 (2018).
- [209] P. Kumar, S. Sendelbach, M. A. Beck, J. W. Freeland, Z. Wang, H. Wang, C. C. Yu, R. Q. Wu, D. P. Pappas, and R. McDermott, *Origin and reduction of $1/f$ magnetic flux noise in superconducting devices*, *Phys. Rev. Applied* **6**, 041001 (2016).
- [210] L. DiCarlo, J. M. Chow, J. M. Gambetta, L. S. Bishop, B. R. Johnson, D. I. Schuster, J. Majer, A. Blais, L. Frunzio, S. M. Girvin, and R. J. Schoelkopf, *Demonstration of two-qubit algorithms with a superconducting quantum processor*, *Nature* **460**, 240 (2009).
- [211] D. W. Brooks, T. Botter, S. Schreppler, T. P. Purdy, N. Brahms, and D. M. Stamper-Kurn, *Non-classical light generated by quantum-noise-driven cavity optomechanics*, *Nature* **488**, 476 (2012).
- [212] A. H. Safavi-Naeini, S. Gröblacher, J. T. Hill, J. Chan, M. Aspelmeyer, and O. Painter, *Squeezed light from a silicon micromechanical resonator*, *Nature* **500**, 185 (2013).
- [213] T. P. Purdy, P.-L. Yu, R. Peterson, N. Kampel, and C. Regal, *Strong optomechanical squeezing of light*, *Physical Review X* **3**, 031012 (2013).
- [214] T. A. Palomaki, J. D. Teufel, R. W. Simmonds, and K. W. Lehnert, *Entangling mechanical motion with microwave fields*, *Science* **342**, 710 (2013).
- [215] S. M. Meenehan, J. D. Cohen, S. Gröblacher, J. T. Hill, A. H. Safavi-Naeini, M. Aspelmeyer, and O. Painter, *Silicon optomechanical crystal resonator at millikelvin temperatures*, *Physical Review A* **90**, 011803 (2014).

- [216] M. Yuan, V. Singh, Y. M. Blanter, and G. A. Steele, *Large cooperativity and microkelvin cooling with a three-dimensional optomechanical cavity*, *Nature communications* **6**, 8491 (2015).
- [217] J. Qian, A. A. Clerk, K. Hammerer, and F. Marquardt, *Quantum signatures of the optomechanical instability*, *Phys. Rev. Lett.* **109**, 253601 (2012).
- [218] X. Zhou and A. Mizel, *Nonlinear coupling of nanomechanical resonators to josephson quantum circuits*, *Phys. Rev. Lett.* **97**, 267201 (2006).
- [219] J. Clarke and A. I. Braginski, *The SQUID handbook* (Wiley Online Library, 2004).
- [220] M. Kounalakis, Y. M. Blanter, and G. A. Steele, *Synthesizing arbitrary mechanical quantum states using flux-mediated three-body interactions with superconducting qubits*, arXiv preprint arXiv:1905.10225 (2019).
- [221] A. Nunnenkamp, K. Børkje, and S. M. Girvin, *Cooling in the single-photon strong-coupling regime of cavity optomechanics*, *Phys. Rev. A* **85**, 051803 (2012).
- [222] M. Brune, S. Haroche, J. M. Raimond, L. Davidovich, and N. Zagury, *Manipulation of photons in a cavity by dispersive atom-field coupling: Quantum-nondemolition measurements and generation of “schrödinger cat” states*, *Phys. Rev. A* **45**, 5193 (1992).
- [223] B. Vlastakis, A. Petrenko, N. Ofek, L. Sun, Z. Leghtas, K. Sliwa, Y. Liu, M. Hatridge, J. Blumoff, L. Frunzio, et al., *Characterizing entanglement of an artificial atom and a cavity cat state with bell’s inequality*, *Nature communications* **6**, 8970 (2015).
- [224] K. E. Khosla, M. R. Vanner, N. Ares, and E. A. Laird, *Displacement electromechanics: How to detect quantum interference in a nanomechanical resonator*, *Phys. Rev. X* **8**, 021052 (2018).
- [225] P. T. Cochrane, G. J. Milburn, and W. J. Munro, *Macroscopically distinct quantum-superposition states as a bosonic code for amplitude damping*, *Phys. Rev. A* **59**, 2631 (1999).
- [226] H. Jeong and M. S. Kim, *Efficient quantum computation using coherent states*, *Phys. Rev. A* **65**, 042305 (2002).
- [227] Z. Leghtas, G. Kirchmair, B. Vlastakis, R. J. Schoelkopf, M. H. Devoret, and M. Mirrahimi, *Hardware-efficient autonomous quantum memory protection*, *Phys. Rev. Lett.* **111**, 120501 (2013).
- [228] U. L. Andersen, J. S. Neergaard-Nielsen, P. Van Loock, and A. Furusawa, *Hybrid discrete-and continuous-variable quantum information*, *Nature Physics* **11**, 713 (2015).
- [229] D. Gottesman, A. Kitaev, and J. Preskill, *Encoding a qubit in an oscillator*, *Physical Review A* **64**, 012310 (2001).
- [230] D. J. Weigand and B. M. Terhal, *Realizing modular quadrature measurements via a tunable photon-pressure coupling in circuit-qed*, arXiv preprint arXiv:1909.10075 (2019).
- [231] S. O. Valenzuela, W. D. Oliver, D. M. Berns, K. K. Berggren, L. S. Levitov, and T. P. Orlando, *Microwave-induced cooling of a superconducting qubit*, *Science* **314**, 1589 (2006).
- [232] K. Geerlings, Z. Leghtas, I. M. Pop, S. Shankar, L. Frunzio, R. J. Schoelkopf, M. Mirrahimi, and M. H. Devoret, *Demonstrating a driven reset protocol for a superconducting qubit*, *Phys. Rev. Lett.* **110**, 120501 (2013).
- [233] U. Vool, A. Kou, W. C. Smith, N. E. Frattini, K. Serniak, P. Reinhold, I. M. Pop, S. Shankar, L. Frunzio, S. M. Girvin, and M. H. Devoret, *Driving forbidden transitions in the fluxonium artificial atom*, *Phys. Rev. Applied* **9**, 054046 (2018).
- [234] K. W. Murch, U. Vool, D. Zhou, S. J. Weber, S. M. Girvin, and I. Siddiqi, *Cavity-assisted quantum bath engineering*, *Phys. Rev. Lett.* **109**, 183602 (2012).

- [235] S. Shankar, M. Hatridge, Z. Leghtas, K. M. Sliwa, A. Narla, U. Vool, S. M. Girvin, L. Frunzio, M. Mirrahimi, and M. H. Devoret, *Autonomously stabilized entanglement between two superconducting quantum bits*, *Nature* **504**, 419 (2013).
- [236] Z. Leghtas, S. Touzard, I. M. Pop, A. Kou, B. Vlastakis, A. Petrenko, K. M. Sliwa, A. Narla, S. Shankar, M. J. Hatridge, *et al.*, *Confining the state of light to a quantum manifold by engineered two-photon loss*, *Science* **347**, 853 (2015).
- [237] N. Ofek, A. Petrenko, R. Heeres, P. Reinhold, Z. Leghtas, B. Vlastakis, Y. Liu, L. Frunzio, S. M. Girvin, L. Jiang, M. Mirrahimi, M. H. Devoret, and R. J. Schoelkopf, *Extending the lifetime of a quantum bit with error correction in superconducting circuits*, *Nature* **536**, 441 (2016).
- [238] C. Eichler and J. R. Petta, *Realizing a circuit analog of an optomechanical system with longitudinally coupled superconducting resonators*, *Phys. Rev. Lett.* **120**, 227702 (2018).
- [239] M. F. Gely, G. A. Steele, and D. Bothner, *Nature of the lamb shift in weakly anharmonic atoms: From normal-mode splitting to quantum fluctuations*, *Physical Review A* **98**, 053808 (2018).
- [240] B. Baker, A. C. Li, N. Irons, N. Earnest, and J. Koch, *Adaptive rotating-wave approximation for driven open quantum systems*, *Physical Review A* **98**, 052111 (2018).
- [241] S. Rips, M. Kiffner, I. Wilson-Rae, and M. J. Hartmann, *Steady-state negative wigner functions of nonlinear nanomechanical oscillators*, *New Journal of Physics* **14**, 023042 (2012).
- [242] M. Rigol, V. Dunjko, and M. Olshanii, *Thermalization and its mechanism for generic isolated quantum systems*, *Nature* **452**, 854 (2008).
- [243] S. Sorg, L. Vidmar, L. Pollet, and F. Heidrich-Meisner, *Relaxation and thermalization in the one-dimensional bose-hubbard model: A case study for the interaction quantum quench from the atomic limit*, *Physical Review A* **90**, 033606 (2014).
- [244] N. Ares, F. Schupp, A. Mavalankar, G. Rogers, J. Griffiths, G. Jones, I. Farrer, D. Ritchie, C. Smith, A. Cottet, *et al.*, *Sensitive radio-frequency measurements of a quantum dot by tuning to perfect impedance matching*, *Physical Review Applied* **5**, 034011 (2016).
- [245] S. E. Nigg, H. Paik, B. Vlastakis, G. Kirchmair, S. Shankar, L. Frunzio, M. H. Devoret, R. J. Schoelkopf, and S. M. Girvin, *Black-box superconducting circuit quantization*, *Phys. Rev. Lett.* **108**, 240502 (2012).
- [246] C. W. Gardiner and M. J. Collett, *Input and output in damped quantum systems: Quantum stochastic differential equations and the master equation*, *Phys. Rev. A* **31**, 3761 (1985).
- [247] A. A. Clerk, M. H. Devoret, S. M. Girvin, F. Marquardt, and R. J. Schoelkopf, *Introduction to quantum noise, measurement, and amplification*, *Reviews of Modern Physics* **82**, 1155 (2010).
- [248] L. S. Bishop, J. Chow, J. Koch, A. Houck, M. Devoret, E. Thuneberg, S. Girvin, and R. Schoelkopf, *Nonlinear response of the vacuum rabi resonance*, *Nature Physics* **5**, 105 (2009).
- [249] D. M. Abrams, N. Didier, S. A. Caldwell, B. R. Johnson, and C. A. Ryan, *Methods for measuring magnetic flux crosstalk between tunable transmons*, arXiv preprint arXiv:1908.11856 (2019).
- [250] M. Mališ, P. K. Barkoutsos, M. Ganzhorn, S. Filipp, D. J. Egger, S. Bonella, and I. Tavernelli, *Local control theory for superconducting qubits*, *Phys. Rev. A* **99**, 052316 (2019).
- [251] M. Sameti and M. J. Hartmann, *Floquet engineering in superconducting circuits: From arbitrary spin-spin interactions to the kitaev honeycomb model*, *Physical Review A* **99**, 012333 (2019).
- [252] C. G. Yale, B. B. Buckley, D. J. Christle, G. Burkard, F. J. Heremans, L. C. Bassett, and D. D. Awschalom, *All-optical control of a solid-state spin using coherent dark states*, *Proceedings of the National Academy of Sciences* **110**, 7595 (2013), <https://www.pnas.org/content/110/19/7595.full.pdf>.

-
- [253] Y.-I. Sohn, S. Meesala, B. Pingault, H. A. Atikian, J. Holzgrafe, M. Gündoğan, C. Stavrakas, M. J. Stanley, A. Sipahigil, J. Choi, *et al.*, *Controlling the coherence of a diamond spin qubit through its strain environment*, *Nature communications* **9**, 2012 (2018).
- [254] B. Albanese, S. Probst, V. Ranjan, C. Zollitsch, M. Pechal, A. Wallraff, J. Morton, D. Vion, D. Esteve, E. Flurin, *et al.*, *Radiative cooling of a spin ensemble*, *arXiv preprint arXiv:1910.11092* (2019).